Realistic shear assessment and novel strengthening of existing concrete bridges

Valerio, Pierfrancesco

Award date:
2009

Awarding institution:
University of Bath

REALISTIC SHEAR ASSESSMENT AND NOVEL STRENGTHENING OF EXISTING CONCRETE BRIDGES

Pierfrancesco Valerio

A Thesis Submitted for the Degree of Doctor of Philosophy

University of Bath

Department of Architecture and Civil Engineering

November 2009

Table of Contents

Acknowledgements

First and foremost I would like to thank my supervisor Prof. Tim Ibell and Dr. Antony Darby for their help, encouragement and friendship throughout the course of my PhD study.

I gratefully acknowledge the funding for the research, obtained from the Engineering and Physical Sciences Research Council (EPSRC) with additional support from Network Rail.

Very special thanks go to the technicians in the laboratory of the Department of Architecture and Civil Engineering of University of Bath, in particular to Brian Purnell, Neil Price, William Bazeley and Graham Mott, for their help and guidance throughout the experimental programme.

I would also like to mention Vasilios Maniatidis and Frederick Ellul, whom I had the pleasure of working with in the research office and who made my time spent at University very enjoyable.

This thesis is dedicated to my parents and, most of all, to my wife Pin-Hui, whose love, patience and support throughout these years have been invaluable.

Abstract

The actual shear capacity of existing concrete structures is often unable to meet current standard requirements. This may be attributable to increased load requirements, inadequate shear provisions in the original design or increased demand in shear capacity owing to flexural strengthening. However, available methods of assessment are often conservative, and the actual strength may be sufficient to sustain the specified assessment load. Therefore, it is important that realistic assessment methods are employed.

This research comprises an investigation into the shear capacity of prestressed concrete bridges and into the feasibility of a novel strengthening approach, both through comprehensive laboratory experimentation and theoretical analyses. The laboratory testing indicates that the shear capacity of prestressed concrete bridges, post-tensioned transversely to form a deck, can be significantly greater than suggested by the relevant standards. The strengthening method proposed, namely deep embedment of steel or fibre-reinforced polymer (FRP) bars, is found to be feasible and very effective for reinforced concrete (RC) and prestressed concrete (PSC) beams of any size.

Analytical models based on the upper-bound theorem of plasticity theory are successfully developed and applied, resulting in much more realistic predictions than those from current standards and codes when assessing shear capacity. For the strengthened beams, in addition to an upper-bound model, a strengthening design method based on a truss analogy is developed, which can be directly implemented into codes of practice.

The analytical methods permit the assessment of existing longitudinally and laterally prestressed concrete bridges for shear capacity in a rational manner, and then to determine the capacity of a practical shear strengthening system if the bridge turns out to actually be understrength. Use of the proposed methodology will allow significant savings, as the costs associated with replacing or strengthening the structure can be avoided or minimised, encouraging a sustainable approach.

Chapter 1
Introduction

1.1 Background and motivation

Due to increased traffic, higher allowable truck weights, higher train speeds and deterioration of materials, most bridges in the UK are being assessed for both bending and shear capacity. An area of concern, identified by various bridge owners including Network Rail, is the actual shear strength of prestressed concrete rectangular bridge beams when post-tensioned together transversely and made contiguous within a deck; this is a common typology used for railway bridges, with simply supported spans ranging between 6 and 20 metres. These bridges in particular, better described in Chapter 3, are the focus of the research project, as they have been repeatedly flagged as being apparently of insufficient shear capacity.

Traditional methods of analysis, which neglect the lateral prestressing, have led to many shear assessment failures as these beams often contain a low percentage of stirrups. Furthermore, yield line methods for flexural strength assessment are becoming ever more popular, so the demand on shear strength in concrete bridges increases. If a bridge is judged by the assessment process to be substandard there are various options available, including monitoring, weight or speed restrictions and propping; ultimately, it is necessary to strengthen or replace the bridge. The reassessment of a supposedly substandard structure using more appropriate methods may show the structure is adequate, meaning the life of the bridge is extended, resulting in significant cost savings for the community.

The priority is therefore to ensure that a realistic shear assessment tool is in place, which is able to predict the real strength of such bridges adequately. Thereafter, if it turns out that the bridge has inadequate shear strength, a viable shear strengthening scheme is sought, which ensures minimal disruption to the bridge users. Such a scheme would ensure a cost effective solution. By combining these two aspects (realistic shear assessment and practical shear strengthening) in one

project, a powerful management tool for owners of concrete bridges with shear concerns can be produced.

1.2 Assessment and strengthening

When assessing concrete bridges with little or no shear reinforcement, the dilemma for code writers has been in allowing these bridges to remain standing, particularly in the absence of any distress. BD 44/95 (1995) therefore allows the absence of shear stirrups in existing beams and loosens many of the specific shear reinforcement requirements of modern design codes of practice. Ibell et al. (1999) found that while BD 44/95 is accurate for individual bridge beams, its predictions for beam-and-slab bridges underestimate the shear capacity by around 30% on average, due to internal restraint and arching. As part of the same research, it was found that initial cracking of contiguous bridge beams occurred at less than 2/3 of the ultimate shear capacity in 95% of cases, implying that bridges in service which show no distress have probably not been loaded to 2/3 of their shear capacity in the past (Ibell et al., 1998a).

Many approaches to the problem of shear in reinforced concrete structures have been developed since Ritter (1899) and Mörsch (1909) first pioneered the concept of the truss analogy, and it cannot be claimed that any is entirely satisfactory in all situations. It is evident that a unified methodology of analysis for these bridges is needed, being capable of considering the effect of both longitudinal and lateral prestressing in a rational manner. Elastic analyses are favoured in design as they generally provide safe and conservative solutions. However, concrete bridges have the capability of redistributing the way loads are carried, and global collapse only occurs when a collapse mechanism can be formed. Therefore, an analysis method that models plastic redistribution can provide a more accurate ultimate capacity prediction than an elastic analysis.

Plasticity theory is a powerful tool in predicting the strength of a concrete structure and plasticity-based approaches have been shown experimentally to provide quick and accurate shear capacity predictions; plastic solutions have already been implemented in many codes, such as Eurocode 2 (2004). Nielsen (1999) and his research group in Denmark have successfully employed the lower-bound and upper-bound theorems to many problems of shear in concrete. A generalised

upper-bound model has been developed by Ibell et al (1997a, 1997b, 1997c) for the shear capacity of beam-and-slab concrete bridges. This thesis presents analytical models, based on plasticity theory, resulting in realistic predictions for the shear capacity of this type of prestressed bridge.

There are several approaches to retrofitting existing concrete bridges in shear, often involving the use of fibre-reinforced polymer (FRP) laminates externally bonded (EB) to the webs of the bridge beams or the near surface mounted (NSM) system, where FRP bars are inserted near the surface of the webs (Concrete Society TR55, 2004). However, in this particular case, the webs of the beams are inaccessible and an altogether new approach is adopted and validated in the thesis, namely the so-called 'deep embedment' system: vertical holes are drilled into the web of the beams from the soffit in the shear spans, high-viscosity epoxy resin is injected from the bottom and then FRP or steel bars are embedded into place. A pilot study at the University of Bath (Valerio and Ibell, 2003) has found that the use of vertically embedded steel or FRP bars in the shear zones of RC beams which were originally under-strength in shear could lead to a ductile flexural behaviour of the beams.

Shear strengthening schemes involving vertical steel bars with end plates have been adopted in the past, but such schemes carry with them problems such as maintenance liability, installation issues (top surface of concrete deck must be accessible), time and the possible use of stainless steel, which carries with it expense and the need for isolation from existing carbon-steel reinforcement.

The reason for wishing to study both steel and FRP as possible strengthening materials in the deep embedment system is that steel is a well-understood material and bridge owners might prefer to use steel in this situation initially. FRP, on the other hand, has far better corrosion resistance, is light to handle on site and is becoming mainstream in bridge strengthening projects. Both materials therefore deserved attention in the project.

1.3 Methodology and research objectives

This project aimed to formulate a realistic assessment tool for contiguous-beam concrete bridges and to develop a minimal-disruption shear strengthening scheme for these bridges. This was achieved through an extensive series of large- and small-

scale laboratory tests in the unstrengthened and strengthened situation combined analytically with plasticity-based shear assessment models. It has been found previously (Ibell et al., 1997b) that small-scale tests, combined with a limited number of larger-scale tests, are extremely cost-effective and useful in aiding understanding of shear in concrete bridges.

With this in mind, a total of 43 specimens were tested in shear under a four-point loading arrangement in both the unstrengthened and strengthened situation. The unstrengthened tests comprised 16 small-scale beams, 4 large-scale beams and 9 small-scale bridges; the strengthened specimens comprised 10 small-scale beams and 4 large-scale beams. All specimens were replica of scaled-down models of typical bridges in service at present, so that prestressing and reinforcement layouts were fully representative of reality.

The variables studied included the level of the longitudinal and transverse prestressing force, the presence of internal stirrups, the shear span to depth ratio, the percentage of strengthening and the type of strengthening material. As part of the process of validation of the deep embedment strengthening technique, 65 pull out bond tests were performed where the performance of five different strengthening bars and three types of epoxies were compared.

On the basis of a large experimental investigation on small-scale and large scale specimens, this thesis develops a series of models based on plasticity theory for the shear assessments of prestressed concrete bridges, resulting in more realistic predictions than those due to current codes. A novel shear strengthening technique is shown to be feasible and effective that will allow a viable solution for all concrete structures found to be actually understrength in shear. In addition to an upper-bound model, a simplified strengthening method based on a lower-bound truss analogy is proposed which could be implemented into codes of practice.

Thus, this project covers both the question of a need for a more realistic shear assessment technique in prestressed concrete bridges as well as the question of how best to strengthen such structures practically, if deemed necessary. Also, the deep embedment strengthening technique can be successfully used in all cases when only the top or bottom faces of a shear-deficient concrete member are accessible.

Chapter 2
Literature Review

2.1 Introduction

The first part of this Chapter contains a review on the shear behaviour of reinforced and prestressed concrete beams with or without shear reinforcement. The development of the theoretical models and research findings leading to the current code provisions for shear design and assessment are examined and discussed.

In the second part, an overview of the use of fibre-reinforced polymer (FRP) materials in concrete is presented, with special emphasis on the research and development of the techniques of shear strengthening of concrete beams with FRP.

2.2 Shear in reinforced and prestressed concrete beams

2.2.1 The behaviour of concrete beams subjected to shear

In a beam subject to pure bending tensile stresses exceeding the concrete strength cause vertical cracks to form, which extend up to the neutral axis. The presence of the shear stresses, which are maximum at the centroid of the elastic region, cause the flexural cracks to rotate; these flexural-shear cracks are commonly found in slender reinforced concrete beams subject to shear. In flanged beams, deep beams and prestressed beams, where the prestressing delays the formation of flexural cracks, web-shear cracks are more likely to occur, which develop at the centroid of the beam when the principal elastic tensile stress exceeds the concrete strength and then extend towards both the load area and the support.

Cracks propagate in a direction normal to the principal tensile stress. Kotsovos and Bobrowski (1993) suggested that the direction of the compressive force path could describe the propagation of shear cracks (see Figure 2.1). They assumed that the tri-axial compressive state beneath the load plate and above the support plate can

significantly increase the local concrete strength preventing the shear cracks from penetrating these regions; therefore, in a beam subject to concentrated loads the cracks beneath the load plate propagate into the constant moment zone where the compression state is uni-axial and extend to the surface to an angle approaching 26.5° to the horizontal, in accordance with the Mohr-Coulomb failure criterion for pure compression (see Figure 2.5).

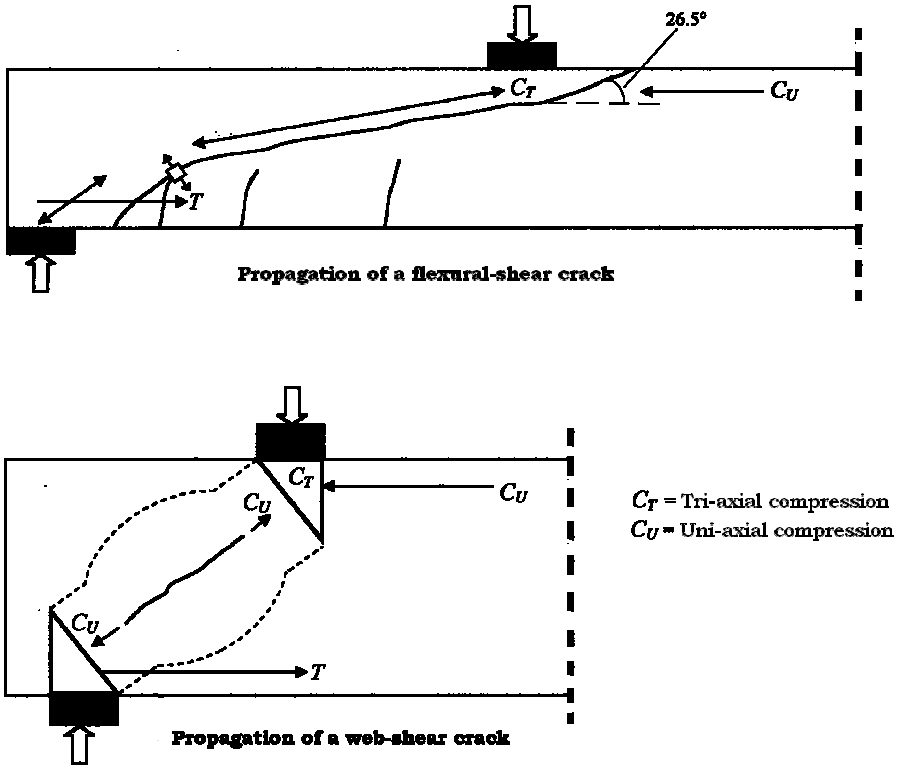

Figure 2.1: Path of compressive force in the shear span (after Whitehead, 2002)

2.2.1.1 Shear transfer mechanisms

Experimental evidence gathered over the years by the researchers showed that in a concrete beam the shear forces can be carried through the mechanisms of stress transfer in the compression zone above the neutral axis, aggregate interlock, dowel action, arch action and tension in the transverse stirrups, which act as ties between the concrete zone above and below the shear cracks and come into play only after the formation of these cracks. Figure 2.2 shows the equilibrium of the internal forces due to the aforementioned possible transfer mechanisms in a slender reinforced concrete beam with stirrups (where arch action is negligible) after an inclined crack has developed.

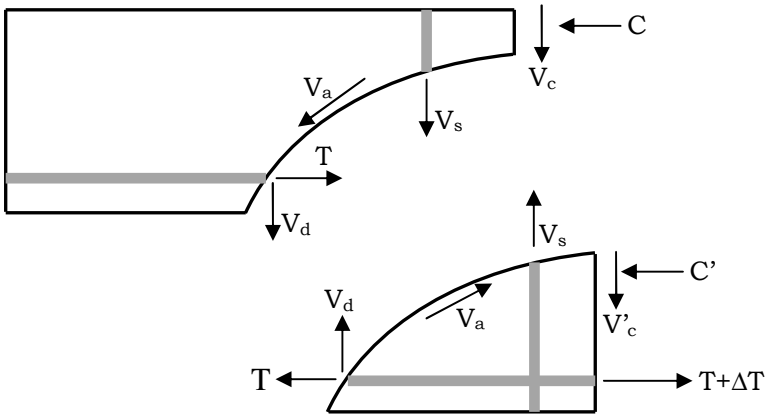

Figure 2.2: Equilibrium of forces in a slender RC beam with stirrups

Stress transfer in the compression zone

Although the exact stress distribution of compressive and shearing forces in the compression zone at failure is not fully understood, most researchers considered this to be the limiting criterion for the shear resistance. Kotsovos (1988, 2007) suggested that dowel effects and aggregate interlock do not exist and designers should ignore such mechanisms and focus on the compression zone only. Generally, a Mohr's circle analysis can be conducted to determine the interaction of the shear and compressive stresses and the Rankine criterion (where failure is assumed to occur when the principal stresses reach the maximum capacity in tension or compression) or the Mohr-Coulomb criterion, described later in the chapter, may be used to predict the capacity of the uncracked concrete zone above the neutral axis.

Aggregate interlock

Aggregate interlock is the shear transfer along a crack caused by the aggregates protruding from the crack surface and providing resistance against slip. According to Walraven (1981) the parameters involved are the shear stress, the normal stress, the crack width and the crack slip. Walraven (1981) developed a mechanical model idealising the aggregate particles as spheres projected from the concrete matrix at the shear crack interface; as slip develops, normal and shear stresses in the contact zones are activated and are related to crack slip and width. He considered the aggregate interlock compromised for crack widths and crack slips in excess of about 1.5mm and 2mm, respectively.

Swamy and Andriopoulas (1974) considered the shear resistance supplied by aggregate interlock and dowel effects to contribute between 50 and 80% of the total shear resistance of beams without stirrups. For beams containing stirrups they found that aggregate interlock and dowel effects together contributed up to 30% of the total shear resistance, claiming that the presence of stirrups reduces the aggregate interlock effects because of the wider crack openings near to failure.

In a parametric study on the sensitivity to shear friction of reinforced and prestressed concrete beams with varying degrees of shear reinforcement (0.12 to 1.11%), Duthinh (1999) found that the normal stresses across the cracks are negligible and that, although the aggregate interlock contribution increases as the shear reinforcement decreases, the beams with low degrees of shear reinforcement are more sensitive to changes in shear friction, and the values of the crack width after which the capacity due to aggregate interlock drops are significantly reduced.

Nagle and Kuchma (2007) conducted a series of shear-friction tests on specimens containing transverse reinforcement and measured crack slips and widths during testing. They found that the ultimate shear capacity was, on average, 50% in excess of the ACI 318-05 (2005) predictions for the shear resistance across a crack. Also, the shear capacity was always in excess of Walraven's model predictions for crack widths exceeding 1mm.

Dowel action

The longitudinal reinforcement can provide direct resistance against shear by dowel action. Paulay et al. (1974) described three types of failure modes associated with dowel action: tensile splitting, concrete crushing and dowel failure. Tensile splitting is the horizontal cracking in the concrete that develops along the level of longitudinal reinforcement, because steel is stiff and isotropic and can transfer large transverse loads to the thin layer of concrete cover. Concrete crushing occurs when tensile splitting cracks are prevented by a thick cover or by the web reinforcement. The dowel failure of the bar is due to a reduction in its axial capacity because of the combination of the high axial and shear stresses, but only lightly reinforced sections subject to large kinking deformations are subjected to this form of failure.

Taylor (1974) assumed that dowel action contributes to the shear capacity of a concrete beam by 15 to 25%, while the contribution of the compression zone is 20

to 40% and the contribution of the aggregate interlock 35 to 50%. Jelic et al. (1999) noted that if dowel action did exist, then beams reinforced with larger diameter bars would exhibit higher shear loads. As the results from all their tests on beams with different diameter bars were about the same, they concluded that dowel action cannot be a viable component in the shear mechanism of a cracked concrete section.

El-Ariss (2007) compared the load-displacement response of a series of shear tests in literature with the predictions of a non-linear computer model where the dowel action was modelled considering the reinforcing bars as beams on an elastic foundation; he found that the predictions were generally more accurate when dowel action was included in the analysis (especially for beams with low amounts of transverse reinforcement) and concluded that ignoring the dowel action may result in too conservative predictions. Sonnenberg and Al-Mahidi (2007) used photogrammetry to measure the movements of concrete and flexural reinforcement as shear cracking developed in a series of shear tests of RC beams. They compared the measurements with the formula for the dowel capacity proposed by Taylor (1974) and found that the dowel contribution to shear capacity was around 20%.

Arch action

Near the supports, beam theory is not applicable and arch action is dominant. The compressive force is angled directly to the support point and the flexural reinforcement resists the horizontal component of this force (see Figure 2.1).

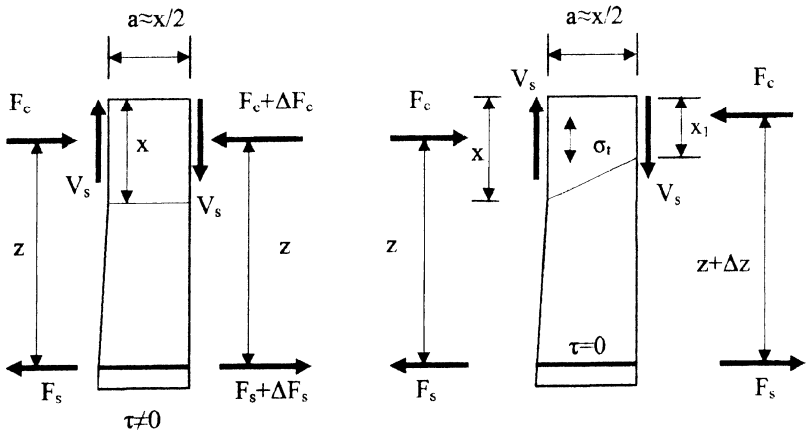

Figure 2.3*:* Equilibrium of cantilever teeth before and after bond failure (after Kotsovos, 2007)

Arch action also describes the variation in the compressive force path that generally occurs as a result of loss of bond between the concrete and the longitudinal bars after extensive cracking (Kotsovos, 2007). Figure 2.3 shows equilibrium of a cantilever tooth within a concrete beam. Debonding starts from the centre of the beam where the axial force is greater; after debonding, the right-hand flexural crack widens, leading to a reduction in depth of the neutral axis and an extension in the lever arm to satisfy equilibrium, so the shear forces are transmitted in the compression zone only.

2.2.1.2 Shear failure modes

Kani (1967) noted that the type of shear failure that developed in rectangular RC beams without web reinforcement was strongly related to the shear span to depth ratio (a/d). He formulated a relationship between the shear span to depth ratio and the failure load, expressed as a percentage of the maximum theoretical capacity of the section, known as 'Kani's shear valley' (see Figure 2.4).

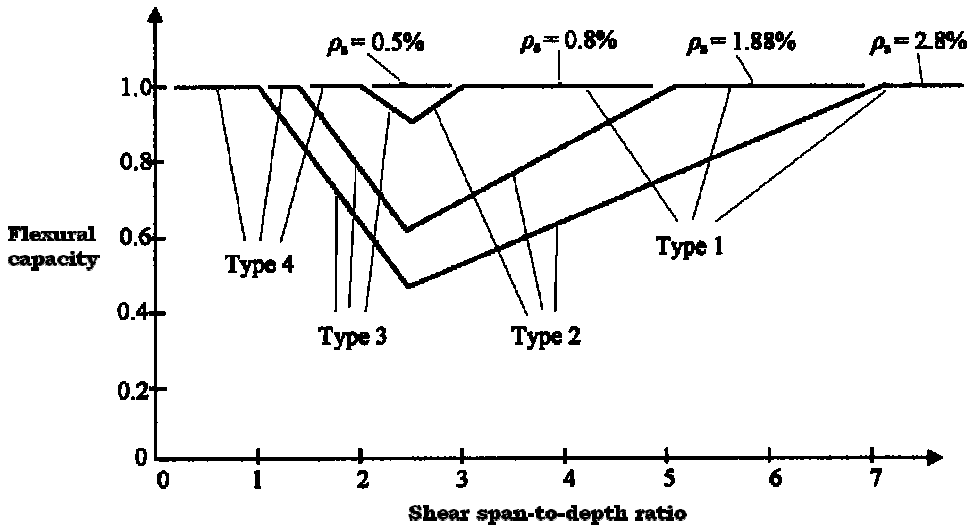

Figure 2.4: Kani's 'shear valley' diagram

The failure modes were categorised into four types: flexural failure (Type 1), diagonal tension failure (Type 2), shear-compression failure (Type 3) and web-crushing failure (Type 4). Kani found that the ultimate shear strength was increased by a factor of 6 as the a/d ratio decreased from 7 to 1 and that the increase rate rose dramatically when $a/d < 2.5$ due to arch action.

Slender beams normally fail in shear in diagonal tension, although the presence of vertical reinforcement can change the type of shear failure mode or even change the collapse mode from shear to flexure. Concrete beams with a sufficient amount of stirrups typically fail in flexure or shear-compression in the compression zone. In heavily prestressed concrete beams web-crushing is more likely to happen, although the a/d ratio remains the primary factor governing the failure mode.

Size effect

Kani (1967) showed that as the depth of the beam increases, the shear stress at failure decreases because the crack widths at points above the main reinforcement tend to increase, leading to a reduction in aggregate interlock. Collins and Kuchma (1999) showed that the size effect is greatly reduced in beams containing well-distributed longitudinal reinforcement along the beam height.

Cladera Bohigas (2002) showed that the ultimate shear capacity of RC beams 900mm deep did not increase with increasing concrete strengths, while in 250mm deep beams the shear capacity increased almost linearly with the concrete strength, and in beams 500mm deep the increase with concrete strength had a lower gradient. He then pointed out that the influence of the size effect becomes bigger when the concrete compressive strength increases, to such an extent that, for deep beams, the benefit of having a higher concrete compressive strength can be more than outweighed by the loss caused by the size effect.

Size effects are usually associated with brittle failures and a Weibull analysis is often used in the codes to describe the effect, with a factor in the form of $(d/d_0)^{-m}$, where d is the effective beam depth, d_o is the reference effective depth and m is the Weibull root. However, Bazant et al. (2007) pointed out that Weibull theories work well only for structures failing right at the initiation of fracture growth from a smooth surface, which is not the case for concrete beams, where a large cracking zone develops before the maximum load is reached. Therefore, they proposed an energetic formula for the size effect of shear in concrete where the shear stress of a beam v_c equals $v_0/(1+d/d_o)^{0.5}$, where v_0 and d_o are the shear strength and effective depth of the reference specimen, respectively.

2.2.2 Existing theories for the analysis of shear in concrete

2.2.2.1 Development of the principal theories

The first formula for calculating the shear stress in a beam prior to cracking was developed in the 19th century by Jourawski (Timoshenko, 1983):

$$\tau = \frac{V S}{I b} \tag{2.01}$$

where V is the applied shear force, I is the second moment of area of the cross section, S is the first moment of area at the point where shear stresses are calculated and b is the beam width. When a beam is cracked in flexure, Mörsch (1909) assumed that the shear stress is maximum at the neutral axis and is constant down to the flexural steel, with the maximum value equal to:

$$\tau = \frac{V}{b_w z} \tag{2.02}$$

where b_w is the web width and z the flexural lever arm.

For the analysis of beams with transverse reinforcement (i.e. vertical), truss models were developed by Ritter (1899) and Mörsch (1909). A concrete beam cracked in shear can be idealised as a truss with the top chord in compression, the bottom chord in tension, the diagonal struts in compression inclined at 45° to the longitudinal axis and the vertical ties in tension. From equilibrium of a 45° truss, the shear stress in a beam is:

$$\tau = \frac{V}{b_w z} = \frac{A_v \sigma_y}{b_w s} = \rho_v \sigma_y \tag{2.03}$$

where A_v is the area of the transverse reinforcement, σ_y is the stress in the transverse steel, s is the spacing of the transverse reinforcement and $\rho_v = A_v/(b_w s)$. Kupfer (1964) proposed a truss model with variable angle of inclination for the compressive struts providing an elastic solution for the inclination of the diagonal struts by neglecting the concrete tensile strength. Truss models, which are still the basis of design in most codes, will be examined in more detail later.

Leonhardt and Walther (1962), after an extensive experimental campaign on RC and PRC beams, showed that beam and arch effects interact and that the shear capacity of PRC beams is highly dependent on the beam slenderness. Kani (1967) treated the concrete teeth between two adjacent flexural cracks as cantilevers that

would break when the tension due to bending at the root of the cantilevers reached the tensile strength. The resulting expression gave the shear capacity in terms of the crack spacing and the crack height above the longitudinal steel; aggregate interlock and dowel effects were neglected.

In the UK, CP 110 (1972) introduced the concept of an empirical 'concrete contribution' to sum to the 'steel contribution' from a 45° truss, an approach considered sensible following experimentation but without theoretical justification, because the concrete would be cracked prior to full truss contribution and the concrete contribution is essentially based on tensile strength, now lost. Nonetheless, this approach is still present in several codes of practice. The formula proposed, which forms the basis of the current code BS 5400-4 (1990), was:

$$V = \xi_s v_c b d + \frac{A_{sv} f_{yv} d}{s} \tag{2.04}$$

where ξ_s is a size effect factor and the concrete contribution v_c is of the form:

$$v_c = K\left(\frac{100A_s}{bd}\right)^{1/3} (f_{cu})^{1/3} \tag{2.05}$$

where K is a constant and f_{cu} is the characteristic concrete cube strength.

The CEB-FIP Model Code (1993) adopted a formula for the concrete contribution based on the equation derived by Zsutty (1971), where additional factors to account for enhancement at short shear spans, size effect and prestressing force are considered:

$$\frac{V_c}{b\,d} = 0.12 \left(1 + \sqrt{\frac{200}{d}}\right)\left(\frac{3d}{a_s}\right)^{1/3} (100\rho_s f_{ck})^{1/3} + 0.15\frac{N_d}{A_c} \tag{2.06}$$

where A_c is the cross-sectional area of concrete, N_d is the applied compression force, ρ_s is the percentage of longitudinal reinforcement and f_{ck} is the characteristic compressive cylinder strength of concrete.

The aggregate interlock model originally proposed by Walraven (1981) was adapted by Reineck (1991) to derive a tooth model which takes all shear-carrying mechanisms into account, leading to an explicit formula for beams with and without shear reinforcement. Kotsovos (1988, 2007) developed the compression force path theory, in which beams are modelled as a frame with an uncracked compression zone transferring shear loads to the support by arch action and it is assumed that the capacity is limited by the failure of one of the compressive struts;

for prestressed concrete beams or beams carrying axial loads the frame is increased in size to account for the additional compression. The shear strength of beams without web reinforcement is evaluated using Kani's shear valley and vertical reinforcement is added to prevent diagonal tension failure, and the contribution made by the vertical reinforcement is added separately.

Regarding the stirrups' effectiveness, Brestler and Scordelis (1963) published results from tests conducted on shear critical concrete beams containing low to medium quantities of web reinforcement. They found that even slender beams containing very small amounts of web reinforcement could provide enhanced shear resistances. Krefeld and Thurston (1966) confirmed that lightly reinforced web sections could provide enhanced shear capacity up to a stirrup spacing of $1.14d$. Swamy and Qureshi (1974) showed that the most efficient spacing for normal strength stirrups was $0.75d$ and that stirrups spaced closer than $0.75d$ had little effect on the width of shear cracks, although the average stress levels in the stirrups that intercepted diagonal cracks were reduced. Batchelor and Kwun (1981) showed that low percentages of stirrups were effective in resisting shear provided that the stirrup spacing was less than d.

Anderson and Ramirez (1989) noted that although all the stirrups crossing a discontinuity were activated, only those that the discontinuity passed through near their centre were effective in resisting shear. They also showed the benefit of interior stirrup legs for wide beams with multiple longitudinal bars per layer, as the outside longitudinal bars had reduced strains in specimens containing interior stirrups, and these specimens exhibited higher shear capacity. The Concrete Society TR49 (1998) proposed the following equation for the minimum amount of stirrups to be placed in a concrete beam:

$$A_{sv} \geq 0.4 \left(\frac{f_{cu}}{40}\right)^{2/3} \frac{b_v s_v}{0.95 f_{yv}} \qquad (2.07)$$

Plasticity theory

Plasticity theory may be successfully used for the ultimate limit state analysis of concrete structures. Its main assumptions are that the yield surface is convex, that a normality condition between strain increments and stress states exists, that displacements of the structure at failure are small and that materials are perfectly plastic; these can be met by concrete when the compressive strength is reduced by

an appropriate effectiveness factor υ, which takes into account the fact that not all the concrete zones crossed by cracks reach their peak value at the same time, so the compression strength at collapse is reduced (Nielsen, 1999).

The lower-bound and upper-bound theorems can be used to obtain the load that will cause collapse of a structure. In the lower-bound approach, a lower-bound on the collapse load is found from a system of internal resultants that is in equilibrium with the applied load without exceeding the yield stress anywhere in the structure. An upper-bound load is found by considering a compatible collapse mechanism in which the rate of internal energy dissipation (when the mechanism is displaced by an arbitrary amount) is equated to the work done by the external loads. Although the upper-bound solutions are potentially unsafe, it is often possible to minimize the upper-bound solution to identify the critical load capacity, termed the exact solution and equal, in fact, to the highest lower-bound solution.

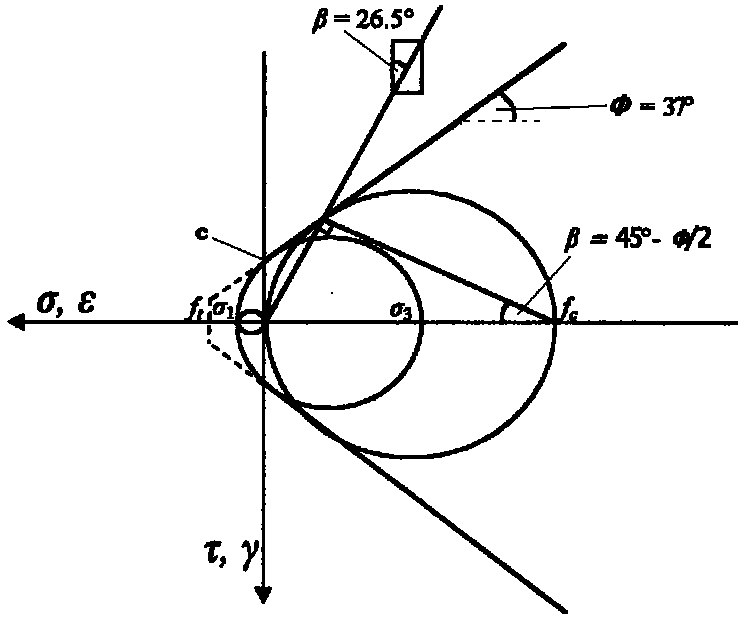

Figure 2.5: The modified Mohr-Coulomb failure criterion

Concrete is usually modelled as a Mohr-Coulomb material. The Mohr-Coulomb criterion was originally developed by Coulomb for granular materials and was refined by Mohr for materials which slip along their planes with the introduction of a failure surface. The separation failure is recognised by including a tension cut-off surface (the 'modified' Mohr-Coulomb criterion); the concrete tensile strength is often neglected, conservatively. Any Mohr's circle derived from the normal and

shear stresses that touches the failure surface represents a critical situation and failure by sliding or separation can occur (see Figure 2.5); because the sliding failure is influenced by direct stress, the failure surface is inclined at the internal angle of friction for the material, assumed to be φ = 37° for normal concrete (Nielsen, 1999). With c the cohesion and σ the normal tensile stress, the equation for the failure surface is:

$$\tau = c - \sigma tan\varphi \tag{2.08}$$

Under conditions of uni-axial compression the sliding failure plane forms an angle of (45°-φ/2) = 26.5° with the direction of the compression force.

Early works employing plasticity theory to analyse the shear failure of plain and reinforced concrete beams were conducted by Nielsen and Bræstrup (1975), Nielsen et al. (1978), Jensen et al. (1978) and Nielsen and Bræstrup (1978). Although the shear failure of concrete is often brittle, good correlation has been obtained with shear test data using both lower-bound and upper-bound approaches by choosing the appropriate value for the effectiveness factor ν (Ibell et al., 1998b).

Strut-and-tie models, which are based on the lower-bound theorem of plasticity, have been applied to members without web reinforcement by Marti (1985) and Schlaich et al. (1987), who suggested a refined strut-and-tie approach that includes concrete tension ties. Provisions for the design of structural members using strut-and-tie models are being introduced in codes worldwide (AASHTO LFRD, 2008; ACI 318-05, 2005; ACI 318-08, 2008). Park and Kuchma (2007) developed an interesting strut-and-tie model for calculating the strength of RC deep beams that employs constitutive laws for cracked concrete and considers the strain compatibility. When compared with the results of 214 tests on deep beams in the literature, the model proved to be more accurate than the strut-and-tie models suggested by ACI 318-05 (2005) for the design of deep beams.

Truss models

Truss analogies have been applied to concrete shear design since Ritter and Mörsch's 45° truss models. If the truss is seen as a stress field in equilibrium according to the lower-bound theorem of plasticity, solutions can be optimized varying the angle θ. Assuming that the web of the beam carries an homogeneous stress field consisting of a uni-axial principal compressive stress f_2 forming a constant angle θ with the beam axis (see Figure 2.6), equilibrium of the stress field

with the applied shear force $\tau = V/b_w z$ gives, assuming that the stirrups are sufficiently closely spaced so that the stirrup forces can be distributed over a concrete area $b_w z$:

$$f_2 = \frac{V}{b_w z}(tan\theta + cot\theta) \tag{2.09}$$

$$\frac{A_v f_y}{b_w s} = \frac{V}{b_w z} tan\theta \tag{2.10}$$

$$N_v = V cot\theta \tag{2.11}$$

In a 45° truss the shear capacity of a beam is usually determined by (2.10) assuming that at failure the angle θ equals 45° and the stirrups yield, checking that the diagonal concrete struts and the longitudinal reinforcement are able to withstand the correspondent loads given by (2.09) and (2.11), where the concrete compressive strength is reduced by an appropriate effectiveness factor υ.

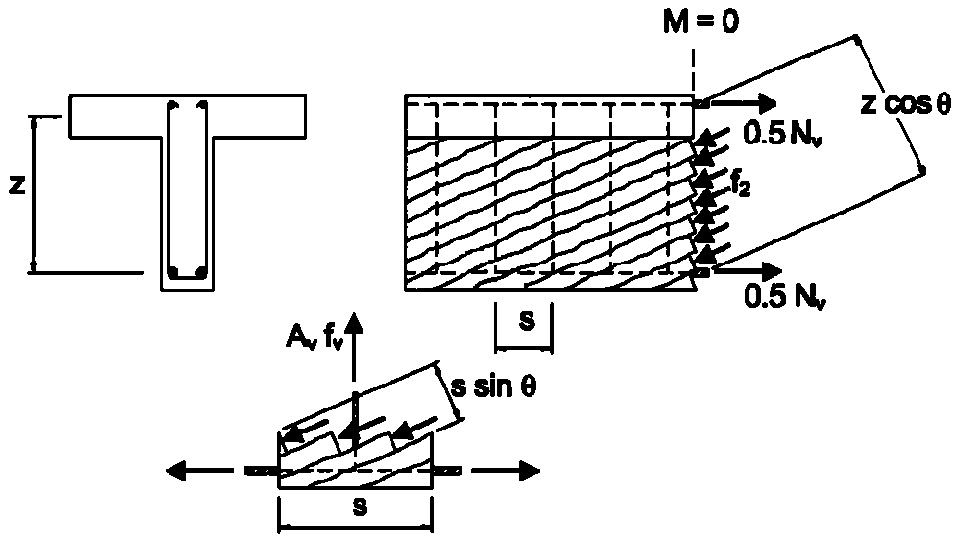

Figure 2.6: Diagonal compression field in a variable angle truss model
(after Cladera Bohigas, 2002)

However, it is only with a variable angle truss that optimised solution can be obtained. In the so-called 'web-crushing criterion' it is assumed that at failure stirrups yield and concrete reaches its factored ultimate compressive strength, so the angle θ and the shear capacity V are obtained from (2.09) and (2.10), again checking through (2.11) that the longitudinal reinforcement is not yielding.

Alternatively, it could be assumed that both the longitudinal reinforcement and the stirrups yield at failure, determine θ and V, and check the concrete in compression.

Some codes assume the shear capacity to be the sum of a concrete contribution (equal to the shear cracking strength of a beam without stirrups) plus the capacity of the stirrups at yielding in a 45° truss. However, when a variable angle truss is used with a flatter inclination of the diagonal field, the contribution due to the shear strength at cracking of a beam without transverse reinforcement is lower and is conservatively disregarded in most codes.

The modified compression field theory

The modified compression field theory (MCFT) is a non-linear model for the response of reinforced concrete subjected to shear (Vecchio and Collins, 1986). The average stresses, average strains and the inclination of the diagonal stress field are determined by compatibility of the deformations of the transverse reinforcement, the longitudinal reinforcement and the diagonally stressed concrete. The concrete stress-strain relationships were originally derived from tests performed by Collins and his team in Toronto.

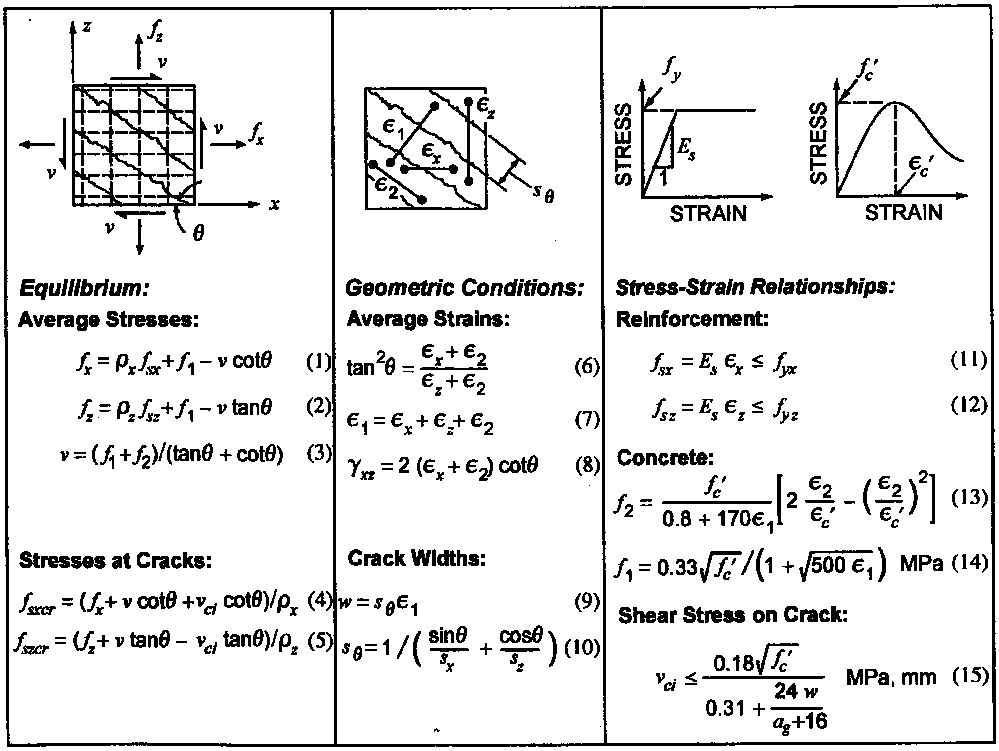

Figure 2.7: Equations of the modified compression field theory (after Bentz et al., 2006)

At each step of the analysis, the loss of tensile stresses in the concrete at the crack is replaced by an increase in the steel stresses or, after the steel has yielded, by average shear stresses on the crack interface. In members without transverse reinforcement the local stresses at a crack control the capacity and the average stresses are used for estimating the inclination of the critical diagonal crack. The 15 equations which need to be satisfied at each step are summarized in Figure 2.7.

As pointed out by Cladera Bohigas (2002), the MCFT can be seen as a truss model in which the shear strength is the sum of the steel contribution from a truss V_s and a concrete contribution V_c, represented by the vertical component of the shear stress transferred across the cracks v_{ci}, rather than by the diagonal cracking strength:

$$V_c = v_{ci} b_w d_v \tag{2.12}$$

$$V_s = \frac{A_v}{s} f_y d_v \cot\theta \tag{2.13}$$

Figure 2.8 shows a section cut halfway between two cracks (left) and at a crack (right). As the average tensile stress transverse to the struts equals f_1 and the two sets of stresses must equilibrate to the same vertical shear in both cases, then:

$$V_c = v_{ci} b_w d_v = f_1 b_w d_v \cot\theta \tag{2.14}$$

and therefore

$$f_1 = v_{ci} \tan\theta \tag{2.15}$$

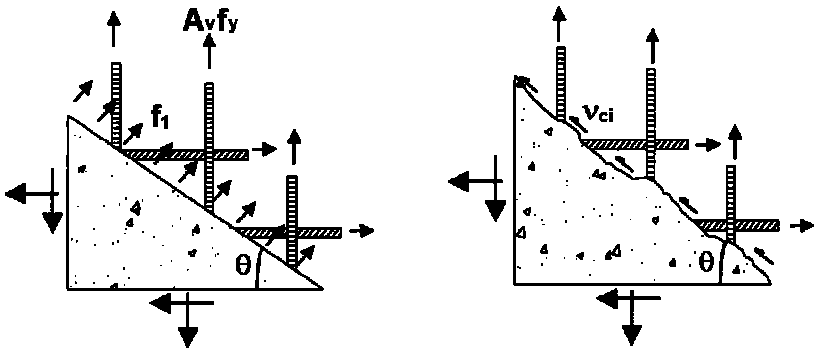

Figure 2.8: Average stresses and stresses at a crack in the MCFT
(after Cladera Bohigas, 2002)

After the stirrups yield, the beam will not collapse if the shear friction can increase, so the angle θ decreases and the failure of the beam will be governed by the crushing of the compression struts or by crack slip; the more shear reinforcement the lesser the crack width and the greater the concrete contribution will be. The iteration required for the solution of several non-linear equations is a lengthy process, so the use of aptly-developed computer programs may be needed.

Collins et al. (1996) introduced a design model based on the MCFT in which the shear stress is assumed to remain constant over the web depth. This method is the basis of the design model of the AASHTO LFRD Bridge Design Specifications (AASHTO LFRD, 2008), where the shear strength of a section is a function of the two parameters β and θ:

$$V = V_c + V_s = \beta\sqrt{f'_c}\, b_w d_v + \frac{A_v}{s} f_y d_v \cot\theta \tag{2.16}$$

For both members with and without transverse reinforcement, β and θ are given in a table as a function of the longitudinal straining of the web ε_x at the level of the main longitudinal reinforcement (calculated for the applied M, V and N) and of the crack spacing s_{xe}, a function of the longitudinal bar spacing and aggregate size. The range of values in the table were chosen to ensure that the stirrups yield and the concrete does not exceed its crushing strength.

Although the MCFT has generally been proven to be very accurate for sufficiently reinforced concrete elements, its ability to predict the shear capacity of beams with no shear reinforcement or lightly reinforced (ρ_v =0.05-0.10%) has been questioned (Vecchio, 2000). Such beams are likely to fail in shear after the formation of a critical single crack, while the MCFT is a theory based on a smeared crack approach. The introduction of a lower limit on the residual tensile stresses in the cracks and of an upper limit to the maximum crack width was proposed by Vecchio (2000) to address the problem.

More recently, Bentz et al (2006) proposed a simplified method, adopted by the Canadian Code (CSA Committee A23.3, 2004), in which two explicit equations for β and θ are derived, which are the product of a strain factor and a size factor:

$$\beta = \frac{0.4}{1 + 1500\varepsilon_x} \frac{1300}{1000 + s_{xe}} \tag{2.17}$$

$$\theta = (29^\circ + 7000\varepsilon_x)(0.88 + \frac{s_{xe}}{2500}) \leq 75^\circ \quad (2.18)$$

For beams with stirrups, a value of ε_x is estimated and a first value of V is found. If the longitudinal reinforcement is not yielding, Equations (1) and (11) of Figure 2.7 are used to determine the value of ε_x corresponding to this shear stress level and the calculations are repeated until convergence is reached; checks are made to ensure that the shear stress found lies below the proposed limit of $0.25f'_c$ (to ensure transverse reinforcement is yielding at failure) and that, from Equation (4) in Figure 2.7, the longitudinal reinforcement can transmit the stresses across cracks without yielding, as assumed. If the longitudinal reinforcement is found to be yielded, the value of ε_x which will correspond to the yield stress in Equation (4) shall be used instead in a trial and error process. For beams without stirrups the same procedure applies, starting with an estimate of ε_x. If the longitudinal steel does not yield, the axial tension at failure f_x is found by Equations (1) and (11) in Figure 2.7; again, if the longitudinal steel yields, Equation (4) in Figure 2.7 sets an upper limit to f_x and then to the maximum shear stress, and dictates the value of ε_x. In predicting the shear strength of over 100 pure shear tests on RC panels, where the MCFT resulted in an average shear strength ratio of 1.01 and Coefficient of Variation (CoV) of 12.2%, this simplified method proved to be similarly accurate, with an average prediction ratio of 1.11 and a CoV of 13.0%.

Kuchma et al. (2006) compared the predictions for the shear capacity of a series of high-strength PSC beams with stirrups subjected to uniformly distributed loads of the AASHTO LRFD (2004) code, based on the MCFT design method proposed by Collins et al. (1996), with those of the ACI 318-02 (2002), based on the superposition of a concrete contribution and a 45° truss model. They found that ACI predictions were generally very conservative while AASHTO was more accurate, and the measured inclination of the shear cracks at failure was around 25-30° for all beams. However, they observed that designing a member for the higher shear stresses ($0.25f'_c$) permitted by the MCFT can lead to significant shear cracking at 40-50% of the design strength of the member, which can cause concerns in terms of serviceability. They suggested the maximum design shear stress to be limited to $0.18f'_c$ and the simplified MCFT design method (Bentz et al., 2006) to be adopted. Also, they proposed that the ACI approach may still be retained but a variable angle truss model, which is less conservative, may be adopted in the code. Kuchma et al (2008) described the changes in the AASHTO LFRD code (2008) which resulted in the implementation of the simplified MCFT design method for the shear design of

both prestressed and non-prestressed beams, where the longitudinal strain at mid-depth ε_x needed in (2.17) and (2.18) is taken equal to one half of the tensile strain in the flexural tensile reinforcement, calculated from the design moment, shear and axial force as the ratio between the expressions $(M_u/d_v)+0.5N_u+V_u-V_p-A_{ps}f_{p0}$ and $E_sA_s+E_pA_{ps}$.

2.2.2.2 Other approaches for RC beams

Zink (2000) proposed a model for the evaluation of the shear capacity of slender RC beams without transverse reinforcement in which the main contribution is given by the shear force V_0 carried in the compression zone (see Figure 2.9):

$$V_0 = \iint \tau(z)dydz = \frac{2}{3} b_w k_x d\, f_{ct} \tag{2.19}$$

where f_{ct} is the tensile concrete strength and $k_x d$ is the height of the flexural compression zone, itself a function of the longitudinal reinforcement ratio ρ and the ratio a_E between the elastic modulus of steel and concrete:

$$k_x = \sqrt{(\rho a_E)^2 + 2\rho a_E} - \rho a_E \tag{2.20}$$

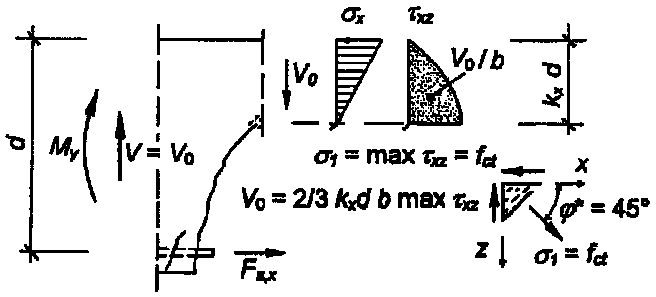

Figure 2.9: Distribution of shear stresses in the compression zone (after Zink, 2000)

According to Zink the shear force V_0 carried in the flexural compression zone has a dominant role in the overall shear capacity of the beam, but factors which take into account size effect, aggregate interlock and tension stiffening need to be included, leading to a shear capacity at cracking V_{sr} of:

$$V_{sr} = V_0 \left(\frac{4d}{a}\right)^{1/4} \left(\frac{5l_{ch}}{d}\right)^{1/4} \tag{2.21}$$

where a is the shear span length and l_{ch} is the characteristic length according to Hillerborg (1983):

$$l_{ch} = \frac{E_c G_f}{f_{ct}^{\ 2}} \tag{2.22}$$

where G_f is the fracture energy needed for a complete crack opening. The contribution $(5l_{ch}/d)^{1/4}$ takes into account the size effect and the aggregate interlock (see Figure 2.10). The term $(4d/a)^{1/4}$ accounts for the different shear capacities at different shear spans, related to the tension stiffening that causes the depth of the compression zone to increase towards the support. Leonhardt and Walter (1962) had observed a 20% drop in the height of the compression zone under the load when the shear span varied from 3.5 to 8 times the effective depth. The model by Zink could predict the shear capacity of 233 tests on RC beams with a mean value of 0.99 and a CoV of 12.5%.

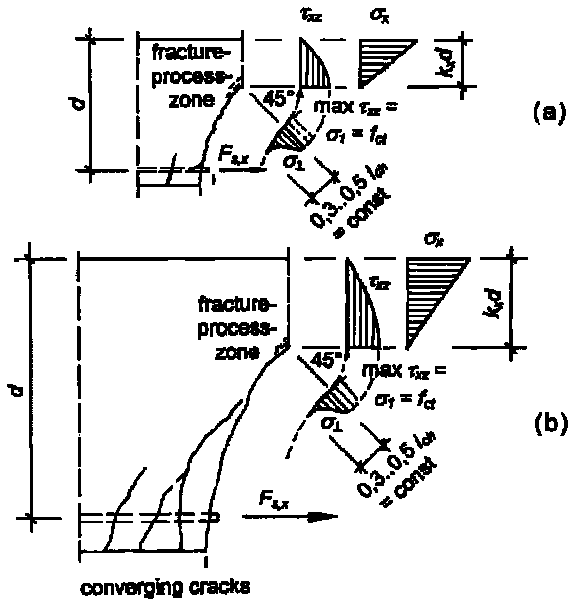

Figure 2.10: Influence of size effect for (a) small and (b) large beams loaded in shear, according to Hillerborg (after Zink, 2000)

Gastebled and May (2001) used fracture mechanics in combination with an assumed failure mechanism derived from test observations to produce an empirical formula for the shear capacity of RC beams without transverse reinforcement that is similar in form and magnitude to that adopted by the CEB-FIP Model Code (1993).

Zararis and Papadakis (2001), Zararis (2003) and Zararis et al. (2006) developed a theory for the shear resistance of RC rectangular and T-beams with and without stirrups.

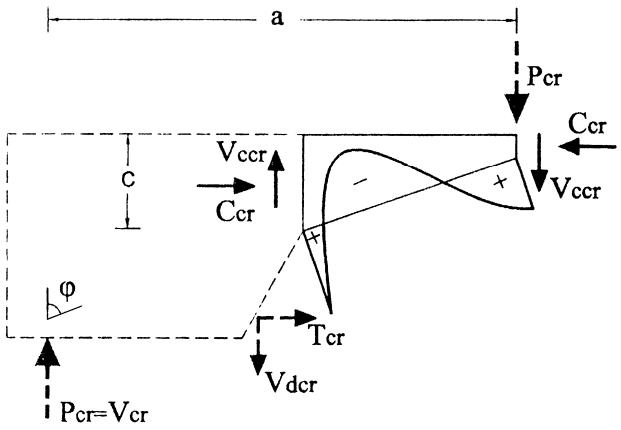

Figure 2.11: First and second branch of a critical diagonal shear crack (after Zararis, 2003)

The theory is based on the observation that the critical shear crack leading to collapse involves two branches: the first is a slightly inclined crack of approximately the same height as the flexural cracks, while the second initiates from the tip of the first and propagates across the compression zone (see Figure 2.11).

Shear failure is predicted to occur when the splitting tensile strength of concrete in the compression zone of the second branch reaches its limit value $f_{ct} = 0.3 f_c^{2/3}$, resulting in the expression (which includes a size effect factor):

$$V_{cr} = (1.2 - 0.2\frac{a}{d})\ \frac{c}{d} f_{ct} b_w d \tag{2.23}$$

where the depth of the compression zone c is a function of the effective depth, the concrete cylinder compression strength f'_c and the percentages of longitudinal reinforcement ρ and ρ':

$$(\frac{c}{d})^2 + 600\frac{\rho+\rho'}{f'_c}\frac{c}{d} - 600\frac{\rho+(d'/d)\rho'}{f'_c} = 0 \tag{2.24}$$

In beams with transverse reinforcement, the gradual opening of the second branch activates the stirrup force V_s and causes an increase of the shear force in the longitudinal bars ΔV_d (see Figure 2.12) so the total shear capacity of the beam equals $V_u = V_{cr} + V_s + \Delta V_d$. The force in the stirrups along the diagonal crack V_s is equal to $0.25(a/d)\rho_v f_{yv} b_w d$ and the increase of dowel force ΔV_d is $0.5\rho_v f_{yv} b_w d$ (Zararis,

2003). For T-beams with and without stirrups the approach is identical, but a suitable expression for the effective width b_{ef} replaces the web width b_w to take into account the increased capacity of the compression zone due to the presence of the upper flange (Zararis et al., 2006). The model is shown to perform satisfactorily in predicting the shear strength of a database comprising over 300 tests on shear critical beams with and without transverse reinforcement.

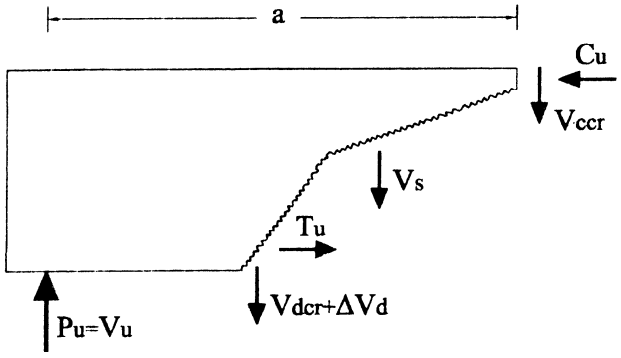

Figure 2.12: Distribution of forces in beams with stirrups (after Zararis, 2003)

Tureyen and Frosch (2003) and Tureyen et al. (2006) suggested that a RC beam without transverse reinforcement fails in shear when the principal tensile stresses in the compression zone in a cracked region within the shear span exceed the concrete tensile strength f_t, so the shear capacity V_c is expressed by:

$$V_c = \frac{2}{3}\sqrt{f_t^2 + f_t \frac{\sigma_m}{2}} b_w c \tag{2.25}$$

where σ_m is the maximum compressive flexural stress at cracking and c is the neutral axis depth at cracking. They found that this simple formula provides more accurate predictions than the ACI 318-05 (2005) expression:

$$V_c = \frac{1}{6}\sqrt{f_c'}\, b_w d \tag{2.26}$$

and it can be satisfactorily applied to T-beams when the neutral axis depth is calculated disregarding the contribution of the flange.

Brown et al. (2006) compiled a database of over 1200 tests to examine the effects of loading type and position on the shear strength of RC beams. They found that the shear strength is strongly affected by the type of loading. A significant number of beams subjected to concentrated loads failed below the nominal strength predicted

by the ACI 318-05 (2005), while the code predictions for beams subjected to uniform loads were always on the safe side. They also found that the a/d ratio is the major parameter affecting the shear capacity of RC beams subjected to concentrated loads.

Choi et al. (2007) and Choi and Park (2007) introduced a unified theoretical model able to predict the shear capacity of both slender (a/d > 2.5) and deep (a/d ≤ 2.5) RC beams with and without transverse reinforcement. The model is based on the assumption that only the compression zone, which is subject to combined shear and normal stresses, contributes to the shear capacity. The shear capacity, derived using Rankine's failure criterion, is governed by diagonal tension in slender beams and a combination of diagonal tension and compression crushing in deep beams, where the critical diagonal tensile crack is not long enough to penetrate the entire depth of the compression zone (see Figure 2.13).

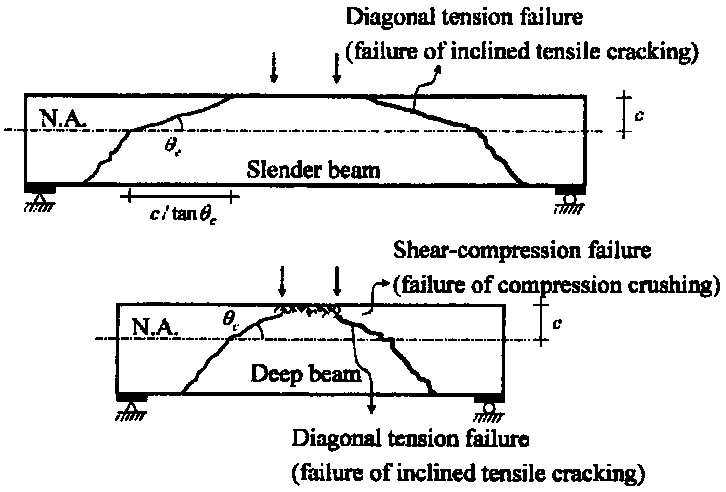

Figure 2.13: Shear failure of slender and deep beams (after Choi et al., 2007)

The shear strength of a beam is defined as the sum of the contribution of concrete V_c and transverse reinforcement V_s, where the shear strength of concrete is the sum of the contributions of tensile cracking V_{ct} and compression crushing V_{cc}, and the shear strength of the transverse reinforcement is given by a 45° truss analogy:

$$V_{ct} = \lambda_s \sqrt{f_t [f_t + \bar{\sigma}_{ct}]}\ b[c(a_{x1}\varepsilon_0) - c_c] \tag{2.27}$$

$$V_{cc} = \sqrt{f_t [f_t + \bar{\sigma}_{cc}]}\ bc_c \tag{2.28}$$

$$V_s = \rho_w f_{vy} b(d - 2c_c) \tag{2.29}$$

where λ_s is a size effect factor, σ_{cc} and σ_{ct} are the average compressive normal stresses in the failure surfaces of compression crushing and tensile cracking respectively, c is the depth of the compression zone at the critical section, $\alpha_{x1}\varepsilon_0$ is the maximum compressive strain at the critical section and c_c is the depth of the failure surface at compression crushing (see Figure 2.14). All parameters are expressed as a function of $\alpha_{x1}\varepsilon_0$, and an iterative calculation is needed to solve the equation, although a simplified method is proposed where α_{x1} is expressed as a function of the shear span to depth ratio only. When compared with shear test results from over 1000 RC beams in the literature, a mean value of the ratios of experimental to predicted capacity of 0.99 and a CoV of 14.7% was obtained by the model.

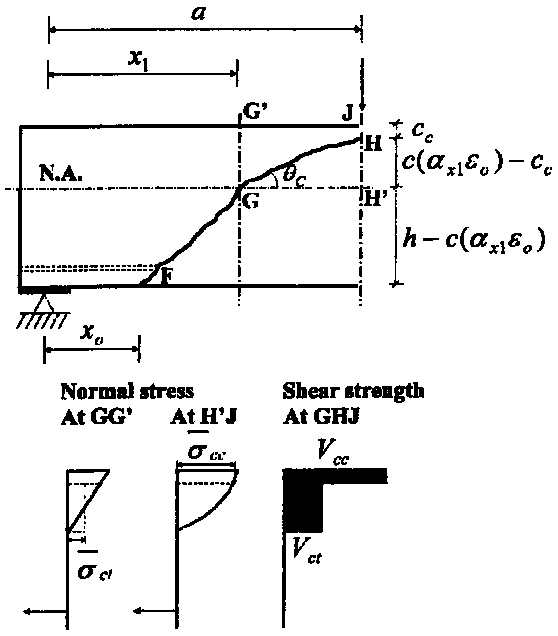

Figure 2.14: Average compression stresses in the compression zone (after Choi et al, 2007)

Muttoni and Fernandez Ruiz (2008) proposed a model to predict the shear strength of concrete beams without stirrups based on the arching action of a beam after the opening of the critical shear crack. The model, implemented by the Swiss SIA Code 262 (2003), assumes that the shear capacity depends on the concrete compressive strength, the maximum aggregate size and the maximum crack width, taken as proportional to the product of the longitudinal strain at 0.6d and the effective depth d.

An interesting approach was proposed by Li and Tran (2008), who evaluated the shear capacity of a RC beam with stirrups using an indeterminate truss model which has struts at various angles (including struts that go directly from the point load to the support, to simulate arch action) and includes the concrete contribution, normally neglected in the truss models, by converting the concrete contribution term V_c into an equivalent stirrup reinforcement term. Unfortunately, the solution is somewhat dependent on the predefined shape of the truss and it is impractical to be solved by hand, rendering the model unusable for design.

2.2.2.3 Other approaches for prestressed concrete (PSC) beams

The influence of prestressing forces on the shear capacity of prestressed concrete beams with and without stirrups was investigated by Keller et al. (2002a, 2002b) and Keller (2004). They pointed out that a pure sectional analysis is not appropriate because often prestressed beams exhibit a residual shear capacity after the formation of the inclined crack, and this is explained with the existence of an alternative shear transfer mechanism in the form of a lattice model with struts and ties (see Figure 2.15) whose capacity is influenced by the shape of the critical inclined crack that depends on the level of the prestressing forces.

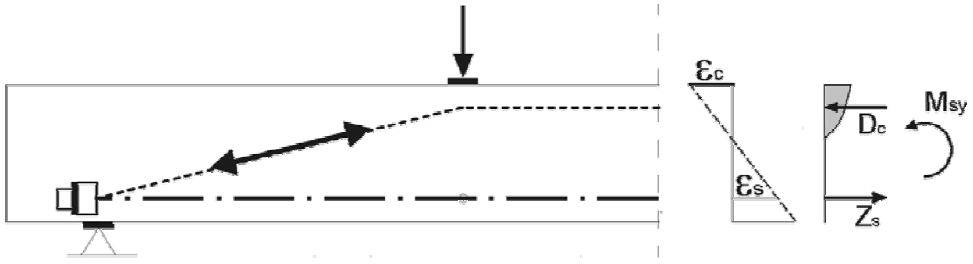

Figure 2.15: Lattice model with no bond between reinforcement and concrete (after Keller, 2004)

Therefore, according to Keller (2004), beams subject to shear have two different shear bearing mechanisms with corresponding capacities: the shear capacity at inclined cracking V_{sr} and the capacity of the lattice V_{sp}. The shear failure of the beams will occur at inclined cracking only if $V_{sp}<V_{sr}$, which is usually the case for RC beams. In prestressed beams it is likely that the contribution of the prestressing force would render $V_{sp}>V_{sr}$ hence leading to a higher ultimate capacity.

The inclined cracking load V_{sr} is calculated using the German code DIN 1045-1 (2001), where 0.10 has been replaced by 0.168 to disregard any safety factor and k is the size effect factor equal to $1+(200/d)^{0.5}$:

$$V_{sr} = 0.168k\left(100\rho_l f_{ck}\right)^{1/3} + 0.12\frac{P}{A_c} b_w d \tag{2.30}$$

The shear capacity of the lattice, with no bond between the longitudinal tensile reinforcement and the concrete in the shear zone, is considered equal to (see Figure 2.15):

$$V_{sp} = \frac{min(D_{max}, Z_{max})z}{a}\left(\frac{M_{cr}}{M_u}\right) \tag{2.31}$$

where $D_{max} = 0.81 f_c bx$ is the strength of the compression strut and $Z_{max} = E_s A_s \varepsilon_{s,y,max}$ is the ultimate strength of the tensile reinforcement. The ratio M_{cr}/M_u between the cracking moment and ultimate moment of the beam accounts for the capacity of the lattice at different prestressing levels.

Keller et al. (2002a) found the shear span to effective depth ratio a/d had a substantial influence over the shear capacity of prestressed beams without stirrups, after comparing a large database of test results using the predictions of the DIN code (see Figure 2.16).

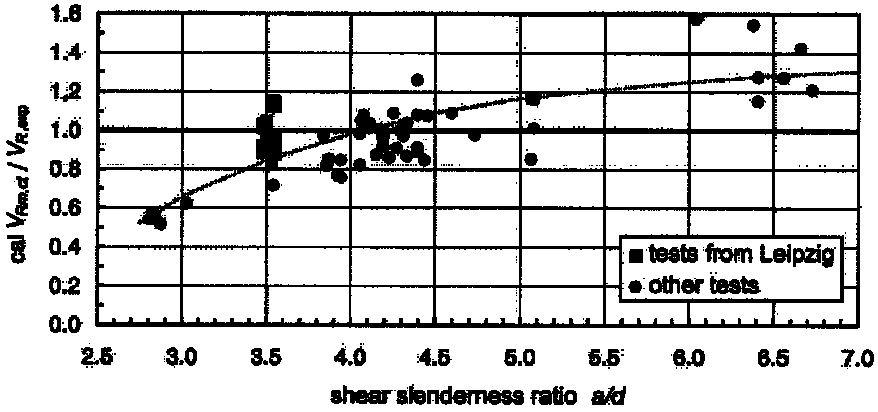

Figure 2.16: DIN predictions and test results at varying slenderness ratio (after Keller et al., 2002a)

They observed (see Figure 2.17) that the change in position of the compressive force P inside the section gives a contribution to the lattice model and creates a shear resistance $V_\lambda = P(\Delta z_p/a)$. A small slenderness ratio increases significantly the

inclination λ of the strut and therefore the contribution to the shear capacity is enhanced. For high slenderness ratios the compressive strut is flatter and the capacity is also reduced by extensive flexural crack growth, leading to premature shear cracking in the web, which may explain why the capacity of PSC beams with slenderness ratios higher than 5d can be very similar to that of RC beams.

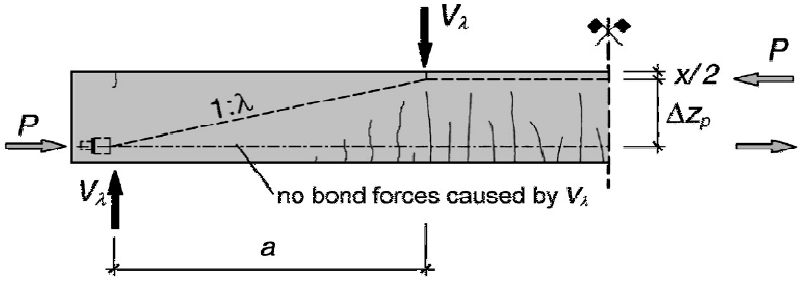

Figure 2.17: Shear component due to arch action of the prestressing force (after Keller et al., 2002a)

Keller et al. (2002b) also compared the test results of a series of PSC beams with stirrups with the predictions of DIN 1045-1 (2001), which adopts a model proposed by Reineck (2001) where the capacity is a sum of a concrete contribution and a truss-based steel contribution, where the axial forces have influence on the angle θ and on the concrete contribution term $V_{Rd,c}$:

$$V_{Rd,c} = 0.24 f_{ck}^{1/3} \left(1 + 1.2 \frac{\sigma_{cd}}{f_{cd}} \right) b_w z \tag{2.32}$$

$$\tan\theta = \frac{1 \quad (V_{Rd,c}/V_{Ed})}{1.2 - 1.4(\sigma_{cd}/f_{cd})} \tag{2.33}$$

$$V_{Rd,s} = \frac{A_{sw}}{s} z f_{ywd} \cot\theta \tag{2.34}$$

and V_{Ed} is the design value of the acting shear force. In the experimental campaign the inclination of the diagonal cracks in the middle of the shear region was measured between 26° and 29° while the DIN approach gave values of around 36°.

Figure 2.18 shows that after the beginning of diagonal cracking the shear reinforcement was activated and the load-bearing mechanisms active before cracking were replaced by a redistributed truss action with a crack inclination approaching 45° until the yielding strength was reached in the stirrups, at which point the theoretical strut inclination was close to the measured crack inclination.

The code approach was conservative in these tests. Similarly to beams without transverse reinforcement, should the shear capacity of the lattice model described previously be higher than the code prediction, the shear capacity will be higher and will depend on the lattice mechanism.

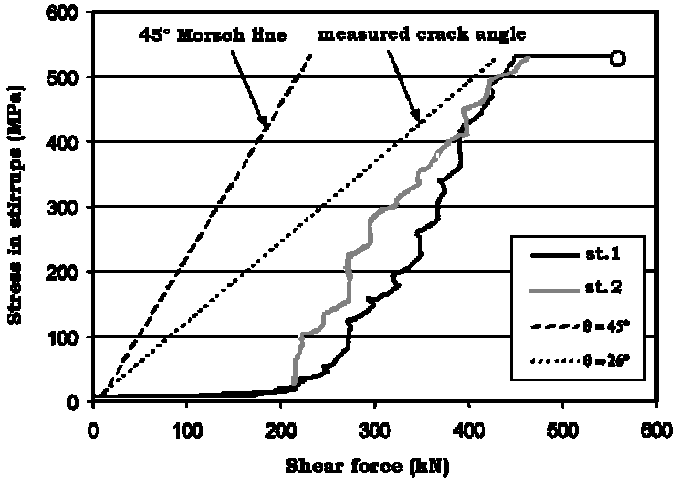

Figure 2.18: Measured stress in the web reinforcement in PRC beams with stirrups (after Keller et al., 2002b)

von Ramin and Matamoros (2006) proposed a comprehensive model for RC and PSC concrete members with and without transverse reinforcement where the shear capacity is calculated as a weighted superposition of contributions from arch action (V_a), truss action (V_t), compression zone and friction (V_{cz}+V_f). The concept stems from a formula proposed by Watanabe and Kabeyasawa (1998) where the shear strength of concrete beams with transverse reinforcement is given by the sum of the contributions of a varying angle truss model and the arch action of a strut-and-tie lower-bound plasticity solution given by Nielsen (1999). In the von Ramin and Matamoros model, the arch contribution contains a reduction factor to account for additional stress demand due to the concurrent truss action, and a transition function to describe the decreasing influence of arch action with the a/d ratio. The truss action is calculated using a variable angle truss model where the inclination of the compression field is limited by the beam depth and loading configuration. The contribution from the compression zone depends on the concrete tensile strength and the depth of the neutral axis, while the contribution of friction, calculated similarly to that presented by Reineck (1991), depends on the crack width which is a function of the strain in the longitudinal reinforcement. The axial forces influence the strain in the longitudinal reinforcement and the depth of the

neutral axis. The model is shown to be slightly over-conservative but has the advantage of being applicable to all cases of RC and PSC beams, deep, slender and with and without transverse reinforcement.

Oh and Kim (2006) performed a series of shear tests on full-scale post-tensioned beams of varying concrete strengths. They found that in all cases the inclination of the compressive struts, measured through a series of strain gauges applied to the concrete surface in the shear zone, was about 50° before cracking and approached 25° at failure; also, they found no difference in the shear capacity at failure when concrete strengths varied from 40 to 60MPa.

Wolf and Frosch (2007), on the basis of the previously described model of Tureyen and Frosch (2003), found that a lower bound for the shear capacity of both RC and PSC beams without stirrups, but still giving more accurate and less conservative predictions than the ACI 318-05 (2005) formulae for the capacity of slender RC and PSC beams, is:

$$V_c = 0.42\sqrt{f_c'}\, b_w c \tag{2.35}$$

where c is the neutral axis depth at cracking. They found that, for prestressed beams, it is safe to assume the depth to the neutral axis equal to the smallest along the span length (corresponding to the section of maximum bending moment), because for prestressed beams the shear capacity is often minimum further away from the support in the zones near the mid-span.

Cladera and Marì (2006), based on a parametric study performed using a neural network over a large series of experimental results, proposed a formulation for the shear capacity of prestressed beams with and without stirrups. For beams without stirrups cracked in flexure, a formulation similar to that of Eurocode 2 (2004) is adopted, but modified to take into account a diverse contribution of the amount of longitudinal reinforcement to the capacity and to the size effect:

$$V_u = [0.225\,\xi(100\rho_l)^{1/2} f_{ck}^{\ 0.2} + 0.15\sigma_{cp}]b_w d \tag{2.36}$$

where the size effect factor $\xi = 1+(200/s_x)^{0.5}$ depends on the vertical distance between the longitudinal reinforcement. For beams with stirrups, the shear capacity is defined as the sum of the contribution of concrete and of the transverse reinforcement (from a variable angle truss):

$$V_c = [0.17\,\xi(100\rho_l)^{1/2} f_{ck}^{\ 0.2}\tau_d^{\ 1/3} + 0.15\sigma_{cp}]b_w d \tag{2.37}$$

$$V_s = d_v \frac{A_w}{s} f_{ywd} \cot\theta \tag{2.38}$$

The term $\tau_d = 3.5\,(200/s_x)^{0.5}\,(f_{ywd}/b_w)(A_w/s)^{0.5}$ takes into account the influence of the stirrups on the shear friction, while the angle θ is derived from the AASHTO LFRD (2004) procedure, that implements the MCFT, and equals $20+15\varepsilon_x+45(\tau_d/f_{cd})$, where the longitudinal strain at mid-height of the beam ε_x equals 0.001 (having assumed the maximum longitudinal strain in the reinforcement equal to 0.002). Predictions from the model were compared with the predictions of Eurocode 2 (2004), ACI 318-02 (2002) and BS 8110 (1997) over a series of shear tests from various researchers on PSC beams and were shown to perform satisfactorily particularly for deep beams without stirrups (where codes were proven to be potentially unsafe) and for all beams with stirrups with high prestressing forces, where code predictions were excessively conservative.

2.2.3 Code provisions for assessment and design

2.2.3.1 The assessment of concrete bridges in the UK

In the UK, bridge assessment is part of a management strategy designed to minimise the risk of a possible bridge collapse. For railway bridges, the whole process including the management strategy, the requirements for the assessment, the methods available and the actions to be taken are defined in the Network Rail company standards NR/CS/CIV/032 (2004) "Managing existing structures", NR/SP/CIV/035 (2004) "Assessment of structures" and NR/GN/CIV/025 (2006) "The structural assessment of underbridges". For highway bridges, the document BD 79/06 (2006) "The management of sub-standard highway structures" provides guidance for procedures to be taken following the failure of an initial assessment, which is carried out in accordance with the BD 21/01 (2001) "The assessment of highway bridges and structures" and the BD 44/95 (1995) "The assessment of concrete highway bridges and structures".

As summarised in the flowchart of Figure 2.19, for railway bridges the process starts with a Level 1 assessment, which comprises a desk study, inspection and analysis based on the most conservative distribution of loads. The use of refined analysis, bridge-specific loads, worst credible strengths, load testing and reliability analyses are part of the subsequent levels of assessment, if deemed necessary.

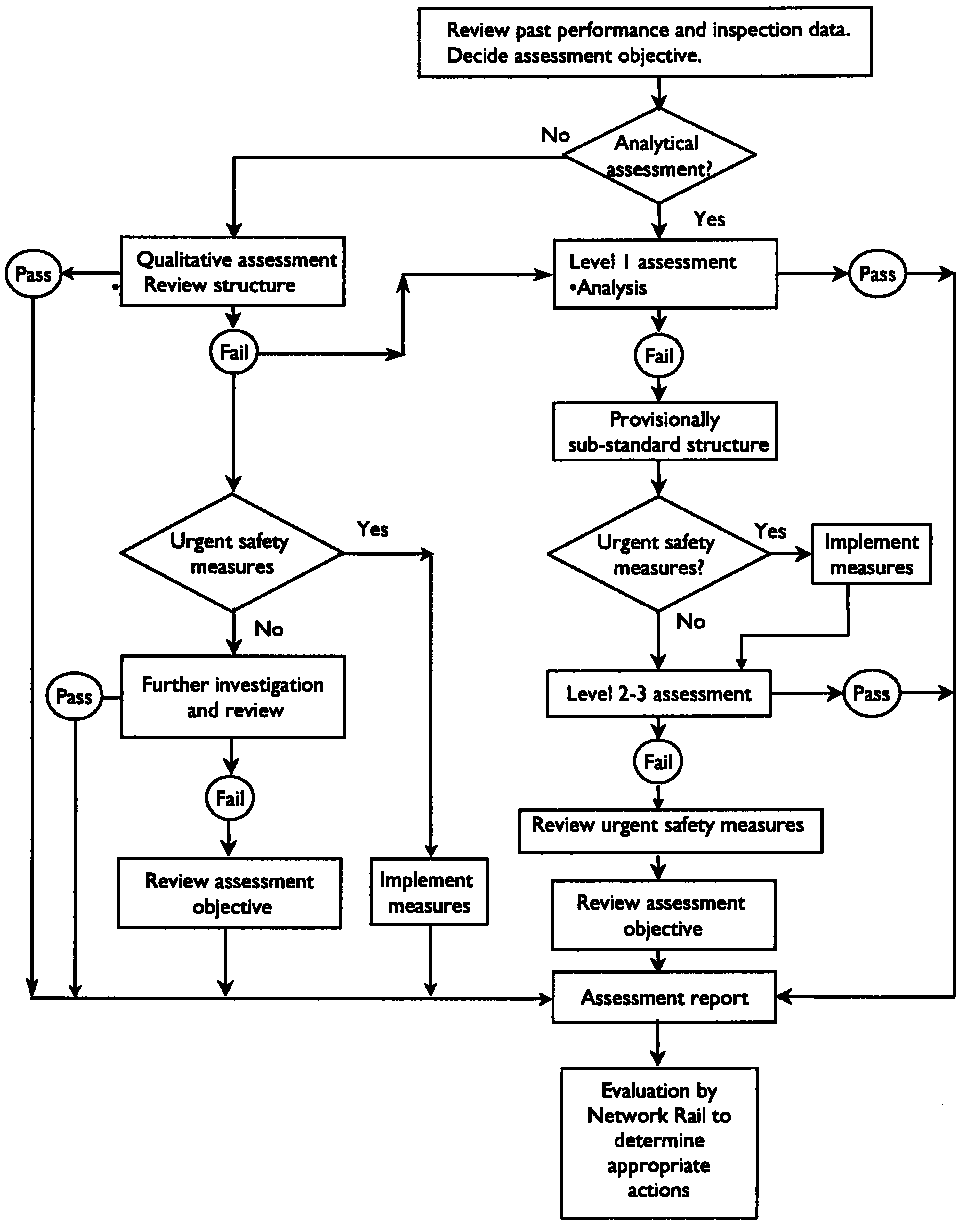

Figure 2.19: Assessment process flowchart for railway bridges (after NR/GN/CIV/025, 2006)

When a bridge is classified as sub-standard following the failure of a Level 1 assessment, a refined analysis is undertaken and interim measures are imposed; if further assessments cannot prove the structural adequacy then the bridge will have to be strengthened or replaced. Therefore, realistic assessment methods showing that the structure is adequate can result in significant savings.

Assessment loading for railway bridges

The load-carrying capacity of a railway bridge is defined by the RA (Route Availability) number of the most critical element of the bridge (in terms of bending strength, shear capacity, etc…) when subject to a load associated with the

permissible speed required at the bridge location; this represents the safe rail traffic load capacity of the bridge.

The RA number of a bridge is derived by applying the type RA1 static load model defined in GE/RT8006 (2000), comprised of point and uniformly distributed loads equivalent to one British Standard Unit (BSU), such as to give the most severe effect for the element under consideration. The maximum number of units of such loading which the critical element of the bridge has the capacity to carry is determined, rounded down to the next smaller integer and ten is subtracted to obtain the RA number of the bridge. RA numbers generally range from the lowest capacity RA0 to the highest RA15, represented by 25 British Standard Units of load. The type RA1 static load model excludes dynamic effects, which are dependent upon train speed and bridge characteristics, and take the form of static load multipliers.

For simply supported spans, the type RA1 loading may be represented by an Equivalent Uniformly Distributed Load (EUDL); the maximum moment or shear force, at a location, of the RA1 loading travelling across a span is calculated and the UDL required to produce the same effect is called the EUDL. EUDL tables are usually employed for obtaining the maximum bending moment at mid-span (where the EUDL equals M_{max}*8/span length) and for obtaining the maximum end shear (where the EUDL equals twice the end shear force). The RA number of a rail vehicle at a certain speed is derived dividing its EUDL value by the EUDL value of the RA1 loading over the same span length, rounded up to the next large integer, and ten is subtracted. To permit a train to run without restriction on a route, its RA number shall not exceed the RA number of each bridge on the route.

For each level of assessment the load carrying capacity of a bridge is determined according to the flowchart of Figure 2.20.

Assessed categories for railway bridges

The assessed category of a railway bridge is obtained with reference to the 'utilisation factor' U, which is derived for the traffic applicable to the route concerned at speeds pertaining to the bridge location. The utilisation factor is

$$U = \frac{S^*_A (1 + r)}{R^*} \tag{2.39}$$

where S^*_A is the assessment load effect due to live load including the dynamic factor, r is the ratio between dead load and live load effects and R^* is the corresponding assessment resistance. A value of U less than 1.0 (categories A1 if <0.8 and A2 if >0.8) indicates that the bridge is able to safely carry the traffic for the route at the permissible speed at the bridge location and that no safety measures are necessary. A value of U greater than 1.0 (categories A3, B, C, D, E and F for increasing values of U) indicates that the bridge is a sub-standard structure and that safety measures of increased criticality are to be imposed.

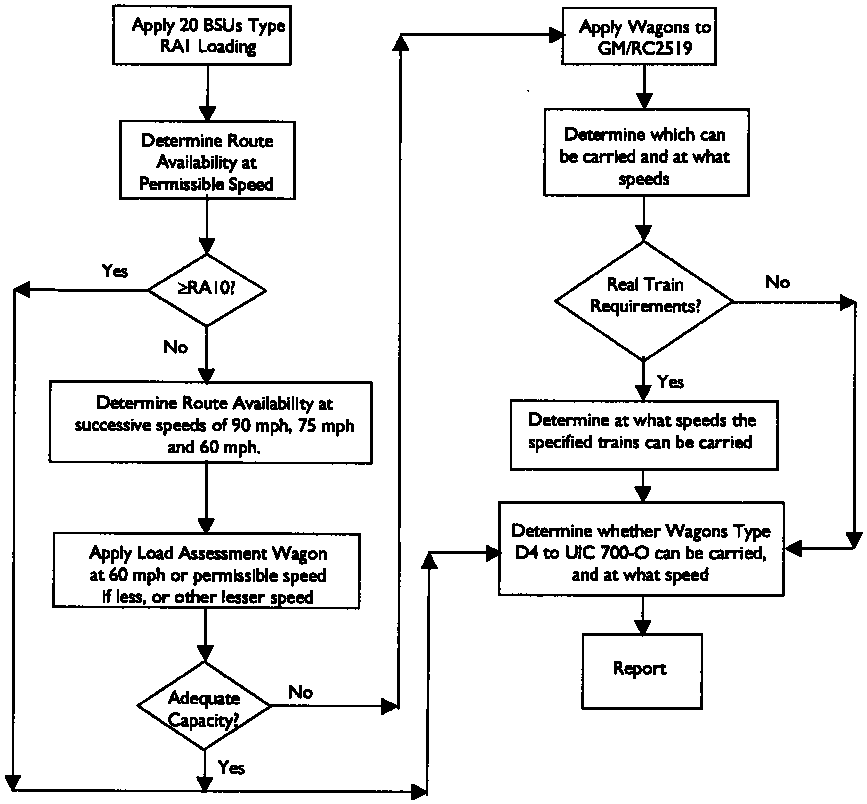

Figure 2.20: Live loading flowchart for the assessment of railway bridges (after NR/GN/CIV/025, 2006)

The assessment loads, Q^*_A, are derived from the nominal loads Q^*_K multiplied by the load partial factor γ_{fL} for each type of loading. The assessment load effects, S^*_A, are derived from the assessment loads Q^*_A multiplied by the load partial factor γ_{f3} which takes account of inaccurate assessment of the effects of loading. The assessment resistance, R^*, is the calculated resistance of a structural element, fundamentally a function of f_k/γ_m, the material characteristic strength and the partial factor for material strength.

Shear capacity of beams

The document NR/GN/CIV/025 (2006) states that concrete bridges should be assessed using limit state principles at the Ultimate Limit State (ULS) and, only when specified in the Assessment Remit, at the Serviceability Limit State (SLS). Elastic methods may be used to determine the distribution of forces and deformations throughout the structure, while non-linear and plastic methods of analysis may be used where agreed during the Technical Approval Process.

In the absence of effective shear reinforcement, the ultimate shear resistance of a section of a RC beam is given by:

$$V_u = \xi_s v_c b_w d = \left(\frac{550}{d}\right)^{1/4} \left(\frac{0.24}{\gamma_{mv}}\right) \left(\frac{100A_s}{b_w d}\right)^{1/3} \left(f_{cu}\right)^{1/3} b_w d \qquad (2.40)$$

where d is the effective depth to tension reinforcement, b_w is the web width, A_s is the area of the longitudinal tensile reinforcement (adequately anchored), f_{cu} is the characteristic compressive cubic strength of concrete in MPa and γ_{mv} is the partial factor for concrete in shear , equal to 1.25; the term $(550/d)^{0.25}$ should not be taken as less than 0.7 and the term $(100A_s/b_w d)$ should not be taken less than 0.15 or greater than 3. An enhancement in the shear capacity is considered when the shear span length is $a_v \leq 3d$ by increasing the allowable shear stress $\xi_s v_c$ to $3d\xi_s v_c/a_v$, on condition that adequate anchorage of the longitudinal tensile reinforcement is provided. In any case, the shear stress $\xi_s v_c$ (or $3d\xi_s v_c/a_v$) should not exceed the lesser of $0.92(f_{cu}/\gamma_{mc})^{0.5}$ or $7/(\gamma_{mc})^{0.5}$, with γ_{mc} equal to 1.50.

The ultimate shear resistance of PSC beams without shear reinforcement is treated differently for sections that are uncracked ($M < M_{cr}$) and sections that are cracked ($M \geq M_{cr}$) in flexure, with the cracking moment defined as:

$$M_{cr} = \left(0.49\sqrt{f_{cu}/\gamma_{mc}} + f_{pt}\right) I/y \qquad (2.41)$$

where γ_{mc} is the partial factor for concrete in bending, equal to 1.50, and f_{pt} is the stress due to prestress only at the tensile fibre distance y from the centroid of the concrete section which has a second moment of area I, after all the prestressing losses have occurred. At uncracked sections the shear resistance is:

$$V_{c0} = 0.67\, bh\sqrt{f_t^2 + f_{cp} f_t} \qquad (2.42)$$

where h is the beam depth, b is the web width, f_{cp} is the compressive stress at the centroidal axis due to prestress after all the losses have occurred and f_t =

$0.32(f_{cu}/\gamma_{mc})^{0.5}$ is the maximum design principal tensile stress at the centroidal axis of the section. At cracked sections, (2.43) below is used when $f_{pe} > 0.6f_{pu}$ and the greater of (2.43) and (2.44) is used when $f_{pe} \le 0.6f_{pu}$ (f_{pu} and f_{pe} are the characteristic strength of the prestressing wires and the design effective prestress in the tendons, respectively), unless (2.42) gives a smaller value:

$$V_{cr} = 0.045bd\sqrt{f_{cu}/\gamma_{mc}} + \frac{M_{cr}}{(\frac{M}{V} - \frac{d}{2})} \tag{2.43}$$

$$V_{cr} = (1 - 0.55\frac{f_{pe}}{f_{pu}})\ v_c bd_s + \frac{M_0}{(\frac{M}{V} - \frac{d_s}{2})} \tag{2.44}$$

where d is the distance from the extreme compression fibre to the centroid of the tendons at the section considered (but not less than $0.625h$), v_c is the design value for the shear stress of RC beams, M and V are the values of the bending moment and shear force at the considered section due to ultimate loads, $M_0 = f_{pt}I/y$ is the moment necessary to produce zero stress in the concrete at the depth d and d_s is the distance from the compression face to the centroid of the steel area A_s. The values resulting from (2.43) and (2.44) should not be taken as less than $0.12bd(f_{cu}/\gamma_{mc})^{0.5}$ and $0.12bd_s(f_{cu}/\gamma_{mc})^{0.5}$ respectively. In any case, the shear force due to the ultimate load should not exceed $0.36(0.7-f_{cu}/250)(f_{cu}/\gamma_{mc})\ bd_s$.

Where effective vertical links are present, the ultimate shear resistance of a RC member section is taken as:

$$V_u = \xi_s v_c b_w d + \frac{f_{yv}d}{\gamma_{ms}s_v}A_{sv} \tag{2.45}$$

where A_{sv} is the cross-sectional area of the links, f_{yv} is the characteristic tensile strength of links (not to be taken greater than 480 MPa), s_v is their spacing and γ_{ms} is the partial factor for steel, equal to 1.15. For PSC beams, the ultimate shear resistance is the sum of the resistances of the concrete alone V_c, given by (2.42), (2.43) or (2.44) and of the shear reinforcement, V_s:

$$V_s = \frac{f_{yv}d_t}{\gamma_{ms}s_v}A_{sv} \tag{2.46}$$

where d_t is the depth from the extreme compression fibre either to the longitudinal bars or to the centroid of the tendons, whichever is the greater. Links are considered effective in resisting shear if the spacing of the legs of links in the

direction of the span and at the right angles to it does not exceed the effective depth d (d_t for PSC beams) and if $A_{sv}(f_{yv}/\gamma_{ms}) \geq 0.2 b_w s_v$. Furthermore, for vertical links to be effective, the tensile capacity of the longitudinal reinforcement at a section, $A_s f_y/\gamma_{ms}$ for RC beams and $(A_{s(t)}f_{pu(t)}+A_{s(u)}f_{yL(u)})/\gamma_{ms}$ for PSC beams, must be greater than:

$$\frac{M}{z} + \frac{V - \xi_s v_c b_w d}{2} \tag{2.47}$$

where M and V are the co-existent ultimate bending moment and shear force at the section under consideration and z is the lever arm which may be taken as $0.9d$. However, within an individual sagging or hogging region, the assessed tensile capacity should not exceed M_{max}/z, where M_{max} is the maximum ultimate moment within that region.

As an alternative method, RC and PSC beams with links may be assessed in shear using the varying angle truss model. For elements with vertical links, the shear strength is the lesser value obtained from the following expressions:

$$V_u = \frac{f_{yv} d}{\gamma_{ms} s_v} A_{sv} \cot\theta \tag{2.48}$$

$$V_u = \frac{0.72\, b_w d v\, (f_{cu}/\gamma_{mc})}{(\cot\theta + \tan\theta)} \tag{2.49}$$

where θ is the angle of the assumed concrete struts to the horizontal, taken such that $\cot\theta$ lies in the range 0.4 to 2.5 for members with constant reinforcement and 0.5 to 2.0 for members with curtailed reinforcement, and $v = 0.7(1-f_{cu}/250) \geq 0.5$ is the effectiveness factor for concrete. The area of links A_{sv} should not be taken as greater than $(0.4 b_w s_v v f_{cu})/(f_{yv}\ \gamma_{mc})$ and the flexural reinforcement at any section should be capable of resisting the bending moment at a distance $0.9d\cot\theta/2$ in the direction of increasing moment from the section considered, provided effective anchorage is present.

In the assessment code NR/GN/CIV/025 (2006), originally based on BD 44/95 (1995), the variable angle truss model approach for beams with links has been adopted after recognising that in beams with small areas of links the 'addition' approach can over-estimate the shear capacity because such links may actually have very little effect. This problem is overcome in the 'addition' approach by specifying minimum link areas below which they are considered ineffective. The advantage of a variable angle optimised truss is that it has a theoretical justification

in plasticity theory and can offer increased shear strength for the same amount of links, although this implies a greater force in the main flexural reinforcement.

2.2.3.2 Design codes for shear in concrete

In the UK, the design documents containing provisions for shear in concrete are BS 5400-4 (1990) "Steel, concrete and composite bridges – Part 4: Code of practice for design of concrete bridges" and BS 8110-1 (1997) "Structural use of concrete – Part 1: Code of practice for design and construction". The rules of the assessment code NR/GN/CIV/025 (2006) previously reported originate from the formulae contained in the BS codes through BD 44/95 (1995), where the variable angle truss approach has been added and a certain degree of conservatism has been removed through the relaxation of some safety factors. It is therefore considered unnecessary to detail the BS provisions here.

Eurocode 2 (2004)

The design value for the shear resistance of RC or PSC beams without shear reinforcement in regions cracked in bending is given by:

$$V_{Rd,c} = \frac{0.18}{\gamma_c} k \left(100 \rho_l f_{ck}\right)^{1/3} + 0.15 \frac{N_{Ed}}{A_c} \; b_w d \tag{2.50}$$

with a minimum value of:

$$V_{Rd,c} = 0.035 k^{3/2} f_{ck}^{1/2} + 0.15 \frac{N_{Ed}}{A_c} \; b_w d \tag{2.51}$$

where A_c is the cross-sectional area of concrete, N_{Ed} is the axial force in the cross-section due to loading or prestressing (positive in compression), d is the effective depth, b_w is the web width, $\rho_l = A_{sl}/b_w d$ is the percentage of longitudinal reinforcement, A_{sl} is the area of the tensile reinforcement adequately anchored, f_{ck} is the characteristic compressive cylinder strength of concrete in MPa, $k = 1+(200/d)0.5 \leq 2$ is the size effect factor (with d in mm) and γ_c is the partial factor for concrete, equal to 1.50 for persistent and transient actions and 1.20 for accidental actions.

For PSC beams in regions uncracked in bending (defined as the sections in regions where the flexural tensile stress is smaller than $f_{ctk,0.05}/\gamma_c$, where $f_{ctk,0.05} = 0.7 f_{ctm} = 0.7 \text{x} 0.3 f_{ck}^{2/3}$ is the characteristic axial tensile strength of concrete at the 5% fractile) the shear resistance is derived fromm the Mohr's circle:

$$V_{Rd,c} = \frac{I\, b_w}{S}\sqrt{(f_{ctd})^2 + a_l \frac{N_{Ed}}{A_c} f_{ctd}} \tag{2.52}$$

where I is the second moment of area of the cross-section, S the first moment of area about the centroidal axis, b_w is the width of the cross-section at the centroidal axis and $a_l = l_x/l_{pt2} \le 1$ for pretensioned tendons and equal to 1 for other types of prestressing, where l_x is the distance of the section considered from the starting point of the transmission length and $l_{pt2} = 1.2 l_{pt}$ is the upper bound value of the transmission length of the prestressing element. The basic value of the transmission length l_{pt} is defined in the code as a function of the type of tendon, type of tendon release, concrete tensile strength and cement class.

An enhancement in the shear capacity is considered when the shear span length a_v is smaller than $2d$, by means of a reduction factor $\beta = a_v/d$ applied to the design shear force V_{Ed}, which should however always satisfy the condition (disregarding the reduction):

$$V_{Ed} \le 0.5\, b_w\, d\nu\, f_{cd} \tag{2.53}$$

where $f_{cd} = (a_{cc} f_{ck})/\gamma_c$ is the design value of the concrete compressive strength, $a_{cc} = 1$, and $\nu = 0.6(1\text{-}f_{ck}/250)$ is the effectiveness factor for concrete cracked in shear.

For RC and PSC beams with vertical shear reinforcement (and with no inclined tensile or compressive chords) the design is based on a variable angle truss model and the shear resistance is the smaller value of the two expressions:

$$V_{Rd,s} = \frac{A_{sw}}{s} z\, f_{ywd} \cot\theta \tag{2.54}$$

$$V_{Rd,max} = \frac{a_{cw} b_w z \nu_1 f_{cd}}{\cot\theta + \tan\theta} \tag{2.55}$$

where A_{sw} is the cross-sectional area of the shear reinforcement, z is the inner lever arm corresponding to the maximum bending moment in the element under consideration, f_{ywd} is the design yield strength of the shear reinforcement (with the partial safety factor for steel γ_s equal to 1.15 for persistent and transient actions and 1 for accidental actions), s is the stirrup spacing, θ is the angle between the concrete compression strut and the beam axis perpendicular to the shear force limited by $1 \le \cot\theta \le 2.5$, ν_1 is the effectiveness factor for concrete cracked in shear which equals 0.6 if the design stress of the shear reinforcement is below 80% of the characteristic yield stress f_{yk} and f_{ck} is not to be over 60MPa, otherwise $\nu_1 = \nu = 0.6(1\text{-}$

$f_{cu}/250$); a_{cw} is a coefficient taking account of the interaction between the stress in the compression chord and the axial stress, which equals 1 for non-prestressed members, $1+(\sigma_{cp}/f_{cd})$ for $0<\sigma_{cp}\leq 0.25f_{cd}$, 1.25 for $0.25f_{cd}<\sigma_{cp}\leq 0.5f_{cd}$ and $2.5(1-\sigma_{cp}/f_{cd})$ for $0.5f_{cd}<\sigma_{cp}\leq 1.0f_{cd}$ where σ_{cp} is the mean compressive stress in the concrete due to the design axial force.

The maximum cross-sectional area of the shear reinforcement that can be considered to be effective for $cot\theta = 1$ is given by:

$$\frac{A_{sw,max} f_{ywd}}{b_w s} \leq \frac{1}{2} a_{cw} v_1 f_{cd} \tag{2.56}$$

Furthermore, the longitudinal reinforcement should be able to resist the total force:

$$\frac{M_{Ed}}{z} + \frac{V_{Ed} cot\theta}{2} \tag{2.57}$$

which should not exceed $M_{Ed,max}/z$, where $M_{Ed,max}$ is the maximum moment along the beam.

Jackson and Salim (2006) commented that the increase in the capacity of web crushing (likely to be the critical shear failure mode for PSC beams) allowed by the Eurocode through the coefficient a_{cw} can be theoretically justified only if low values of the strut inclination θ are assumed because, due to prestressing, the initial direction of the principal compression is closer to horizontal and less rotation of the cracks is needed to reach the optimum value of θ, which for a prestressed beam is usually 25 to 35°. However, if higher values of θ are selected to increase the web compression capacity, more rotation would be needed to get to the optimum θ and the proposed increase in web crushing capacity may not be justified. Nevertheless, comparisons with shear tests on PSC beams showed that, when the design stress of the shear reinforcement is assumed to be over 80% of f_{yk}, the provisions were reasonably accurate and always on the safe side.

Cladera and Marì (2007) compared the provisions of the new Eurocode for RC and PSC beams with stirrups to empirical tests and to the provisions of other codes and formulations. They stated that, "although the varying truss angle procedure is very simple and justified by the lower bound theory of plasticity, it neglects a number of variables that may be primary in some cases and offers a great scatter of results. Moreover, the benefit of prestressing is not taken into account". In particular, they found that the Eurocode procedure may be too conservative for PSC beams failing

due to stirrups yielding or with high levels of prestressing force and for beams slightly reinforced in shear, while it may be unconservative for heavily reinforced members.

German code DIN 1045-1 (2001)

The shear capacity of RC and PSC beams without shear reinforcement is given by:

$$V_{Rd,ct} = 0.10k\left(100\rho_l f_{ck}\right)^{1/3} - 0.12\frac{P}{A_c}\ b_w d \tag{2.58}$$

where P is the value of the applied axial force (positive in tension), f_{ck} is the characteristic compressive cylinder strength of concrete and $k = 1+(200/d)0.5 \le 2$ is the size effect factor with d in mm; in this formula the partial factor for concrete is included in the 0.10 constant. A formula analogous to (2.52) applies for PSC beams in regions uncracked in bending.

The flexural shear capacity of RC and PSC beams with vertical shear reinforcement is given by a variable angle truss model in which the value of the strut inclination to the horizontal is calculated by means of (2.59) and (2.60), while (2.61) provides the value of the design shear force in the stirrups:

$$V_{Rd,c} = 0.24 f_{ck}^{1/3}\left(1 + 1.2\frac{\sigma_{cd}}{f_{cd}}\right) b_w z \tag{2.59}$$

$$0.58 \le \cot\theta = \frac{1.2 - 1.4(\sigma_{cd}/f_{cd})}{1 - (V_{Rd,c}/V_{Ed})} \le 3 \tag{2.60}$$

$$V_{Rd,s} = \frac{A_{sw}}{s} z\, f_{ywd} \cot\theta \tag{2.61}$$

where σ_{cd} is the design value of the axial concrete stress in the beam axis (positive in tension), f_{cd} is the design value of the characteristic compressive cylinder strength of concrete f_{ck} and θ is the angle of the assumed concrete struts to the horizontal (to be taken as 40° for non-prestressed beams).

ACI 318-08 (2008)

The shear strength of rectangular RC and PSC beams made of normal concrete is the sum of a concrete contribution V_c and a contribution from stirrups V_s from a 45° truss analogy.

The nominal shear strength of a RC beam with no stirrups is given by the two alternative expressions:

$$V_c = 0.17\sqrt{f_c'}b_w d \tag{2.62}$$

$$V_c = (0.16\sqrt{f_c'} + 17\rho_w \frac{V_u}{M_u} d)b_w d \tag{2.63}$$

where d is the effective depth to tension reinforcement, b_w is the web width, ρ_w is the percentage of tensile longitudinal reinforcement, f_c' is the characteristic cylinder compressive strength of concrete in MPa and V_u and M_u are the external shear and moment at the section; $\sqrt{f_c'}$ should not exceed 8.3MPa, V_c should not exceed $0.29\sqrt{f_c'}b_w d$ and $(V_u/M_u)d$ should not exceed 1.

The nominal shear resistance of a PSC beam with an effective prestress force not less than 40% of the tensile strength of tensile reinforcement is equal to:

$$V_c = (0.05\sqrt{f_c'} + 4.8\frac{V_u}{M_u} d_p)\, b_w d \tag{2.64}$$

where d_p is the effective depth to the centroid of the prestressed reinforcement and d is not less than $0.8h$; V_c needs to be taken not less than $0.17\sqrt{f_c'}b_w d$ nor greater than $0.42\sqrt{f_c'}b_w d$, and $(V_u/M_u)d_p$ should not exceed 1. If a more accurate calculation is undertaken, V_c should be equal to the lesser of V_{ci} and V_{cw}:

$$V_{ci} = 0.05\sqrt{f_c'}b_w d_p + \frac{V_i}{M_{max}} M_{cre} \tag{2.65}$$

$$V_{cw} = (0.29\sqrt{f_c'} + 0.3f_{pc})b_w d_p + V_p \tag{2.66}$$

where V_i is the shear acting in the section subject to the maximum moment M_{max}, f_{pc} is the compressive stress due to prestressing at the centroid of the section, V_p is the vertical component of the prestressing force and the cracking moment M_{cre} equals:

$$M_{cre} = \frac{I}{y_t}(0.5\sqrt{f_c'} + f_{pe}) \tag{2.67}$$

where y_t and f_{pe} are the distance to the extreme tensile fibre and the prestressing stress at that fibre of the section, respectively. V_{ci} need not be taken as less than $0.17\sqrt{f_c'}b_w d$ and V_{cw} may be calculated, alternatively, as the load giving a tensile stress of $0.33\sqrt{f_c'}$ at the centroid of the section.

For RC and PSC beams the additional shear capacity due to the transverse reinforcement equals:

$$V_s = \frac{f_{yt} d}{s} A_v (\sin a + \cos a) \tag{2.68}$$

where the yield stress of stirrups f_{yt} shall not exceed 420MPa and the stirrup spacing s shall not exceed $d/2$ for RC beams or $0.75h$ for PSC beams, limits increased by 1.5 times when V_s exceeds $0.33\sqrt{f_c'}$, while the shear capacity V_s is not to be taken greater than $0.66\sqrt{f_c'}b_w d$. In RC beams the minimum area of stirrups is the lower value between $0.062\sqrt{f_c'}b_w s/f_{yt}$ and $0.35 b_w s/f_{yt}$, while in PRC beams the additional limit of $(A_{ps} f_{pu} s/80 f_{yt} d)(d/b_w)^{0.5}$ is introduced, where A_{ps} and f_{pu} are the area and ultimate tensile strength of the prestressing steel in the tension zone, respectively.

2.3 Strengthening of concrete structures with FRP

2.3.1 FRP composites for structural strengthening

Fibre reinforced polymer (FRP) materials have been successfully used for many years in the aerospace and automotive industries; the aerospace industry has used FRP composite sheets to form aircraft wings, while the design of modern Formula 1 cars and high-tech racing sailboats now almost entirely relies on FRP properties.

In the construction industry, they have been widely used across the world for the retrofit, repair and strengthening of existing concrete, masonry, steel, iron and timber structures since the late 1980s. Their use is now the preferred choice over traditional techniques, primarily due to their light weight, high strength and high durability, leading to simpler and quicker strengthening processes and reduced maintenance costs. Several guidelines have been produced worldwide for the structural strengthening with FRP materials (fib Bulletin 14, 2001; fib Bulletin 35, 2006; ACI 440.2R, 2008; ACI 440R, 2007; Concrete Society TR55, 2004; Concrete Society TR57, 2003; BD 84/02, 2002; BD 85/08; CIRIA Report C595, 2004; CNR DT-200, 2004; CNR DT-201, 2005; CNR DT-202, 2005).

In the past, concrete structures were strengthened by casting additional concrete (topping slabs) and dowelling in steel bars; this technique was particularly messy, disruptive and expensive. In the 1960s, steel plates began to be used, usually glued

to the tension zones of concrete structures; however, due to the weight of steel plates, temporary support was necessary to keep the plates in position during curing of the adhesive. Subsequently, from the 1990s, the use of FRP sheets, plates, tapes and bars grew rapidly due to their aforementioned advantages, which are particularly important for bridges because of the high costs of lane closures and possession times on major highways and railway lines. In most cases it is only possible to increase the live load capacity of a structure. However, by jacking and propping the structure prior to the application of the FRP, or by prestressing the structure with FRP, it is possible to resist dead load as well.

2.3.1.1 Properties of FRP components

FRP materials are made from thousands of high strength, high modulus continuous fibres encased within a resin matrix. Fibres provide the strength, stiffness and stability to the composite, while the matrix binds the fibres together and transfers load between them. The most suitable fibres are glass, carbon and aramid (better known by the trade name of Kevlar). Each is a family of fibre types in general, with individual fibre types within the families that may vary. The selection of the type of fibre to use will therefore depend on many factors, especially the type of loading they will need to sustain and the environmental conditions surrounding the strengthening system.

The fibres have a linear elastic response up to ultimate load, with no significant yielding. Carbon fibres can have tensile strengths in excess of 5500MPa, while aramid and glass fibres do not usually exceed 4000MPa. Compressive strengths of carbon and glass are close to the tensile equivalent, while that of aramid is significantly lower. The elastic modulus of carbon fibres is similar or greater than that of steel, while the stiffness of aramid is lower (around 130GPa) and that of glass significantly lower, generally not higher than 85GPa. However, the maximum elongation of carbon fibres at failure (2%) is generally less than half that of aramid and a quarter that of glass fibre (ACI 440R, 2007).

Carbon and aramid fibres are resistant to most forms of chemical attack, while many types of glass fibres are attacked by alkalis, except for the specially formulated AR (alkali-resistant) type. Glass and carbon fibres are not affected by ultraviolet light, while aramid needs to be coat-painted to avoid strength reduction. Aramid and glass fibres are non-conducting, while carbon fibres should be used with care in the vicinity of electricity supplies for risk of becoming live due to

induced currents (i.e. in the presence of AC overhead electrification systems). When subjected to fire, glass fibres retain strength up to 1000°C, carbon up to 650°C and aramid up to 200°C (Concrete Society TR55, 2004).

Epoxies are generally used as the resin matrix. Polyester, vinylester and polyurethanes are also adopted, but they generally have inferior properties to those of epoxies, which have excellent strength, strong adhesion to the fibres and good chemical and solvent resistance. The modulus of elasticity of the resins is 3-3.5GPa, while tensile strength is in the region of 50-90MPa. Maximum elongation can range from 2 to 8%, depending on the particular matrix used; Poisson's ratio of the matrix materials is between 0.35 and 0.40 (Moukwa, 1996).

The overall strength and stiffness of the FRP composite is significantly lower than those of the fibres alone, due to the resin matrix. The density of the FRP composites is 1.5 to 2.5 t/m^3, about four times less than steel.

2.3.1.2 Types of FRP composites

There are many types of commercially available FRP products in various forms, such as rods, plates, fabrics, shells, etc., which may be bonded to concrete through an adhesive or combined with the resin in-situ as part of the strengthening application process.

Plates and rods are usually manufactured by the pultrusion process. The process allows high fibre contents to be achieved (typically 70%), so high strength and stiffness are possible. Continuous fibre rovings are drawn through a bath that contains the resin matrix and additives. The fibres are pulled through a heated die, and the composite consolidates; the pultruded section is then cut to the desired length using an abrasive wheel. Plates are usually 1 to 5mm thick and up to 150mm wide, but the dimensions can be varied to suit the particular application. Rods are usually in the form of circular or square bars of diameter up to 20mm or rectangular strips of thickness less than 2mm (Concrete Society TR55, 2004).

Fabrics are available in the form of sheet material, usually a woven or stitched cloth, or in the form of prepreg material, consisting of fibres pre-impregnated with resin which is cured in place. The arrangement of the fibres in the fabrics can be unidirectional or bidirectional, where a percentage of fibres are in the transverse direction and offer strength and stiffness in both directions.

Shells are usually manufactured through filament winding, a process where resin-impregnated fibres are wound round a mandrel in the appropriate pattern to form, once cured, a cylindrical shell. Other manufacturing processes include hand lay-up inside or outside a suitable mould.

2.3.2 Design of strengthening schemes

There are four basic forms of concrete strengthening which can be achieved using FRP materials:

- Flexural resistance can be increased in beams, slabs and columns by adding longitudinal FRP to the tensile face
- Ultimate shear resistance can be increased in beams, slabs and columns by adding transverse FRP material, either to the surface or internally
- The axial resistance and strain capacity can be increased in columns by wrapping FRP material circumferentially around the member
- The seismic performance and ductility of a structure can be increased by adding FRP material to the joints.

FRP composites can be applied in several ways to obtain the desired strengthening effect:

- Uni-directional plates glued to the concrete with an adhesive (to increase flexural and shear capacity)
- Uni- or bi-directional fabrics resined to the concrete in a wet lay-up process (to increase flexural, shear and axial capacity)
- Preformed shells fitted around concrete columns (to increase axial capacity)
- Near surface mounted (NSM) bars or strips resined into grooves (to increase flexural and shear capacity)
- Deep embedment of FRP bars for shear strengthening, a technique developed as part of this research project which will be treated in detail in the following chapters.

Pultruded plates have excellent uni-axial properties (but poor transverse strength) and they can be placed in multiple layers. Fabrics are normally placed in many layers to make up the required thickness and they are usually preferred to plates when the concrete substrate is in poor condition or whenever their flexible nature may be advantageous over the plates. In the NSM system, grooves are cut in the

concrete surface and FRP bars or strips are inserted into the holes and bonded in place with an adhesive; this technique is advantageous over the plate bonding or wet lay-up when the surface is undulating, the concrete has a poor quality outer layer or when the FRP material would otherwise be exposed to external damage (Concrete Society TR55, 2004).

Epoxy resins are the most common type of adhesive for bonding the FRP composites to concrete, due to their superior structural performance and their ability to cure at ambient temperature. The adhesive should be able to withstand a maximum temperature of at least 50°C in service and have an adequately high glass transition temperature. In confined spaces the resin should be selected so as to minimise toxic fumes in the event of fire (Concrete Society TR55, 2004).

Strengthening against one mode of failure may increase the probability of occurrence of another mode, which may need to be considered in design (Concrete Society TR55, 2004).

The design of FRP strengthening schemes is based on limit state principles; design is usually carried out at the ultimate limit state and it is checked at the serviceability limit state. The ultimate limit states to be checked include bending, shear, compression, FRP anchorage, FRP plate separation and fire resistance, while serviceability limit state checks include deflection, cracking, fatigue, creep, creep rupture and durability. In addition, a serviceability check must be undertaken on the existing steel reinforcement to ensure that it does not yield under the new service load conditions, which may lead to unacceptable permanent deformations. FRP composites exhibit a linear stress-strain response to ultimate failure with no yielding. The mechanical properties of the FRP composite, obtainable from manufacturer's data or from direct testing, are usually the tensile strength, the Young's modulus and the maximum elongation at failure, preferably in the form of characteristic values or mean values and standard deviation.

Three different partial material safety factors are applied to the FRP materials for strengthening, namely γ_E (related to loss in elastic stiffness over time), γ_{mm} (related to the manufacturing process) and γ_ε (related to long-term reductions in ultimate strain capacity). The design elastic modulus E_{fd} and the design ultimate strain ε_{fd} are then given by the expressions:

$$E_{fd} = E_{fk} / (\gamma_E \gamma_{mm}) \tag{2.69}$$

$$\varepsilon_{fd} = \varepsilon_{fk} / (\gamma_\varepsilon \gamma_{mm}) \tag{2.70}$$

where E_{fk} and ε_{fk} are the characteristic values of the elastic modulus and ultimate strain of the FRP composite, respectively. The design tensile strength f_{fd} can be derived from:

$$f_{fd} = \varepsilon_{fd} E_{fd} \tag{2.71}$$

The values of the partial safety factors depend on the fibre type and on the different application or manufacturing process. Higher safety factors are recommended for glass FRPs and for hand lay-up processes. For the adhesives, it is recommended that a minimum partial safety factor of 4 is adopted to account for the long term strength losses (Concrete Society TR55, 2004).

2.3.3 Shear strengthening using FRP

2.3.3.1 Overview

Figure 2.21 shows how a structural member may be strengthened in shear using FRP materials. A review of the recent theories and developments related to the externally bonded (EB) and near surface mounted (NSM) applications, together with the provisions of existing guidelines, is presented in the following paragraphs; details of the deep embedment (DE) technique, developed in the present research project, are given in subsequent chapters.

To increase the shear capacity of a member, externally bonded (EB) plates or fabrics ideally should be wrapped around the whole perimeter of the member. Full wrapping is the most efficient scheme and is commonly used in column applications where access to all four sides of the member is usually available. In beam applications, where an integral slab makes it impractical to completely wrap the member, U-wrapping or side bonding are normally adopted, but the effectiveness of these two systems is highly reduced by the fact that they are prone to debonding failure, because the maximum anchorage capacity of the strips to the concrete face can be substantially lower than the ultimate capacity of the FRP; therefore, the contribution that FRP makes to the shear capacity in these systems is governed by separation of the FRP from the concrete, often associated with the propagation of a failure plane in the concrete close to the surface (Concrete Society TR55, 2004). Prestressed straps wrapped around the beams have been successfully

employed to enhance the shear capacity of concrete rectangular and T-beams, although the techniques for installing a strap without requiring access to the top surface of the beam may be quite disruptive (Hoult and Lees, 2009).

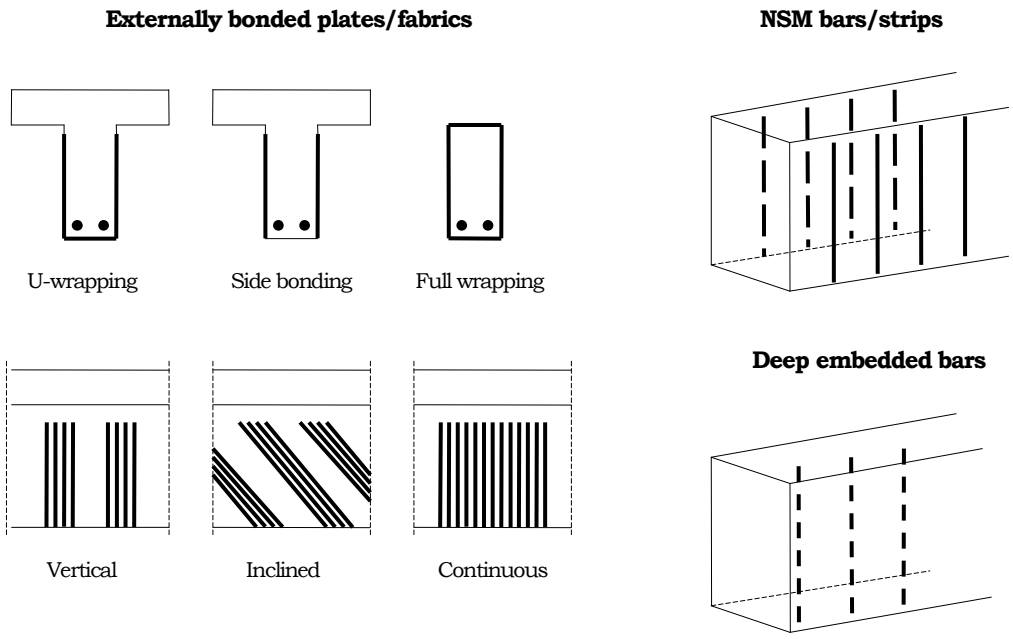

Figure 2.21: Shear strengthening techniques

The use of NSM bars or strips glued into concrete slots offer potentially superior bond performances because the FRP rods are resined on 3 sides and the bond capacity can benefit from a restraint offered by the concrete substrate to the pull out.

When the top surface and the webs are inaccessible (as is the case for most precast concrete beams for highway and railway bridges), the use of deep embedded FRP bars has been proposed by the Author in a pilot study at the University of Bath (Valerio and Ibell, 2003), showing that the technique is feasible and can prevent shear failure while leading to more ductile flexural failures.

Most of the design guidelines for evaluating the shear capacity of concrete beams strengthened with FRP assume that the contribution of the FRP, V_f, can be added to the concrete and steel contributions V_c and V_s in a 45° truss arrangement. As will be discussed later, however, this approach can lead to unconservative predictions because it relies on the fact that the steel has yielded when the full capacity of the FRP has been reached, which may not always be the case.

2.3.3.2 Existing theories for externally bonded (EB) applications

After observation that the contribution of the FRP to the shear strength of a beam is less than its ultimate tensile strength, Triantafillou (1998) proposed that the FRP contribution should rely on an effective strain at shear failure rather than on its ultimate strain capacity. The expression for V_f is:

$$V_f = \frac{A_f E_f \varepsilon_{fe} d_f}{s_f} (\sin\beta + \cos\beta) \tag{2.72}$$

where A_f is the total area of one FRP sheet wrapped or bonded, d_f is its effective depth (taken as $0.9d$), s_f is the sheet spacing, β is the inclination of the sheets to the horizontal, E_f is the Young's modulus of the FRP and ε_f is the effective strain, which is given in a formula as a function of the axial rigidity of the FRP sheet ($\rho_f E_f$), and was evaluated from a regression analysis based on experimental results.

Khalifa et al. (1998) proposed a modification to Triantafillou's model in which the ratio R of effective stress (or strain) in the FRP to its ultimate strength (or strain) is used instead of the effective strain itself. The resulting expression, which is a best fit to the experimental data for $\rho_f E_f$ < 1.1GPa is:

$$R = \frac{\varepsilon_{fe}}{\varepsilon_{fu}} = 0.5622(\rho_f E_f)^2 - 1.2188(\rho_f E_f) + 0.778 \leq 0.5 \tag{2.73}$$

where the 0.5 limit is introduced to maintain the FRP strain below 0.004, a limit value based on testing (Priestley et al., 1996). A further limit on R is proposed that quantifies the ultimate capacity of the sheets at debonding based on a bond strength model by Maeda et al. (1997), who proposed an expression to evaluate the effective length L_e (i.e. the active length where the bond is transferred, which corresponds to the maximum tensile force that an FRP sheet can carry) and the average bond stress as a function of $E_f t_f$. The resulting expression for R is:

$$R = \frac{0.0042(f'_c)^{2/3} w_{fe}}{(E_f t_f)^{0.58} \varepsilon_{fu} d_f} \tag{2.74}$$

where f'_c is the concrete cylinder compressive strength, t_f is the sheet thickness and w_{fe} is the effective width of FRP, equal to d_f-L_e or to d_f-$2L_e$ for the U-jacket and side bonded configurations, respectively. The term V_f is then calculated from Equation (2.72) where the effective strain is the least of the values of R derived from (2.73) and (2.74). The design procedure in ACI 440.2R (2002, 2008) is based on this model.

Triantafillou and Antonopoulos (2000) proposed a modification to Triantafillou's (1998) model introducing different expressions for the effective strain based on a regression analysis from a larger database, this time distinguishing between different FRP types and between full wrapping and U-wrapping/side bonding. The design procedure recommended by the fib Bulletin 14 (2001) is based on this model. A further modification to the model was proposed by Matthys and Triantafillou (2001) to incorporate the effect of the shear span to depth ratio; according to this model, the effective strains are expressed by:

$$\varepsilon_{fe} = 0.72\varepsilon_{fu}e^{-0.0431\Gamma_f} \tag{2.75}$$

$$\varepsilon_{fe} = 0.56\varepsilon_{fu}e^{-0.0455\Gamma_f} \tag{2.76}$$

for fully wrapped or U-wrapped/side bonded CFRP respectively, with the factor Γ_f given by:

$$\Gamma_f = \frac{E_f \rho_f}{f_c^{2/3}(a/d)} \tag{2.77}$$

Teng et al (2003) pointed out that the vast majority of beams with fully wrapped FRPs, and some U-wrapped, failed by diagonal tension (with or without FRP rupture), causing the FRP to tear along a line corresponding to the critical shear crack in the concrete. However, all beams with FRPs bonded on the side and many with U-wrapping failed by debonding of the FRP from the concrete. The main drawback of the above models is that the possible failure modes (FRP rupture and FRP debonding) are not clearly distinguished from each other.

Chen and Teng (2003a) proposed a model for the FRP rupture which explicitly includes the effect of the strain non-uniformity of the FRP along the beam height to explain why the ultimate FRP strength is not reached at failure; this accounts for the fact that the FRP intersected by the shear crack is not stressed at the same ultimate tensile strength at any instant of the failure process, unlike the case of steel, which can yield. The FRP contribution V_f in the 45° truss model contains an effective stress $f_{FRP,e} = D_{FRP}\,\sigma_{FRP,max}$, where $\sigma_{FRP,max}$ is the maximum stress (function of the maximum FRP strain) and D_{FRP} is a stress (or strain) distribution factor, which is the ratio of the average strain to the maximum strain within the effective FRP height, found to vary from a minimum of 0.5 (the value suggested for design) to a maximum of 0.75 for different possible strain distributions. The FRP sheets should

not be spaced in excess of half the horizontal distance spanned by the shear crack to ensure that at least two sheets will cross the diagonal crack.

For the FRP debonding, a model was proposed (Chen and Teng, 2003b) where the effective stress is again the product of a stress distribution factor D_{frp} and a maximum stress $\sigma_{frp,max}$, but in this case they are derived based on a bond strength model developed from the observation that debonding failure of EB sheets is in fact a failure of the concrete just beneath the FRP-to-concrete interface (Chen and Teng, 2001). The stress distribution factor is a function of the ratio between the maximum bond length L_{max} (equal to the FRP effective height or to half the effective height for U-wrapped and side-bonded vertical sheets, respectively) and the effective bond length L_e; this ratio can vary from 0.5 to over 0.9, while the maximum stress in the FRP at debonding is given by:

$$\sigma_{frp,max} = 0.427 \beta_w \beta_L \sqrt{\frac{E_{frp} \sqrt{f'_c}}{t_{frp}}} \tag{2.78}$$

where the factor β_w represents the width ratio of the bonded sheet to the concrete and the factor β_L is a function of the actual bonded length. The FRP spacing has to be limited to ensure that in all cases there are fibres intercepting the more effective half (lower half for U-wrapping and middle half for side plates) of the assumed diagonal crack. The model relies on the fact that all the FRPs intersected by the critical shear crack can develop their full bond strength at ultimate (whose value depends on the location of the shear crack relative to the end of the sheet); indeed, the bonded interface generally experiences a certain slip (with maximum values of the order of 0.2mm) after the peak stress, leading to a pseudo-plastic behaviour which may justify this assumption. Chen and Teng's (2003a, 2003b) models performed well when compared to a database of FRP-strengthened beams which failed due to FRP rupture or FRP debonding, with average test to predicted ratios of 1.06 and 1.11, respectively. The respective coefficients of variation in each case were 21.5% and 20.9%.

In order to verify the assumption that all FRP sheets can reach the full bond strength at the ultimate condition, Lu et al. (2009) created a FE model where four potential slip fields were analysed to simulate different propagation patterns of the critical shear crack crossing an FRP sheet, where the sum of the interfacial slips on both sides of the crack equals the crack width. The FRP sheets were modelled by a series of truss elements and the interface with the concrete was modelled as

nonlinear springs linked to a rigid substrate (the concrete); the bond-slip model proposed by Lu et al. (2005) was used to derive the properties of the springs. Imposing an increasing boundary displacement (corresponding to the considered slip field) to the trusses the stress in the trusses and the slips could be found at any point for increasing values of the crack width. Results showed that although the different critical shear crack models result in significantly different average stress-to-slip responses in the FRP sheet, their effect on the stress distribution factor and on the effective stress of Chen and Teng's (2003b) model is much less significant, with a maximum discrepancy of 15% found for a slip field corresponding to beams with light flexural reinforcement. This confirms that the hypothesis that all FRP intersected by a crack can reach the full bond capacity is reasonably accurate.

Colotti et al. (2004) proposed an analytical model to evaluate the shear capacity of RC beams strengthened with FRP plates based on the plasticity theory. According to the lower-bound theorem of plasticity theory, the shear capacity of a beam with stirrups having sufficient longitudinal reinforcement is related to the simultaneous occurrence of web crushing and stirrup yield, and depends on the percentage of vertical stirrups $\psi = A_{sf}f_y/(bsf_c)$ (Nielsen, 1999). Assuming that the effectiveness of the FRP strengthening can be evaluated in a similar way as for stirrups, they proposed that the total degree of shear reinforcement is the sum of a term for the internal stirrups (ψ_i) and one for the external FRP (ψ_e). In the case of bond failures (U-wrapping and side bonding), the degree of FRP strengthening equals p_b/bf_c, where p_b is the distributed force per horizontal unit length sustained by the FRP; from the hypothesis that the global bond force is resisted by the area of FRP sheets above or below a critical crack and equals $0.5A_b\tau_u$ (τ_u being the average bond strength of the FRP to concrete interface at the ultimate condition), the force p_b equals $w_f h_f \tau_u/s_f$, where w_f, h_f and s_f are the width, height and spacing of the FRP sheets. For tensile failures of the FRP (full wrapping) the degree of FRP strengthening equals p_f/bf_c, where $p_f = A_f f_{fe}/s_f$ and the effective stress is the ultimate stress f_{fu} multiplied by an effectiveness factor v_f. Assuming an average bond strength of $\tau_u = 2.77 + 0.06\,(f_c\text{-}20)$ for bond failures and an effectiveness factor equal to 1 for the rupture failures, they found that the model performed better than ACI 440.2R (2002), Triantafillou and Antonopoulos (2000) and Matthys and Triantafillou (2001) models when compared with 73 RC beam tests from literature, with a mean ratio of 1.02 and a CoV of 16.5%.

Mosallam and Banerjee (2007) conducted a series of tests on RC beams with stirrups strengthened with EB carbon and glass FRPs. They found that the models of Colotti et al (2004) and Matthys and Triantafillou (2001) offered the best correlations, while ACI 440.2R (2002) and Triantafillou and Antonopoulos (2000) models were always unconservative. They considered that the effect of the a/d ratio, disregarded in the latter models, was a key parameter in the overall capacity.

Monti and Liotta (2007), following an extensive experimental campaign into RC beams strengthened with EB FRPs, proposed a series of design equations for the evaluation of the V_f contribution to shear capacity. For full wrapping and U-wrapping the resisting mechanism is based on the truss analogy while in the case of side bonding a crack-bridging mechanism is considered to develop. The expressions for V_f, implemented in the Italian guidelines CNR DT-200 (2004), are a function of the effective debonding strength f_{fed}, which is different for the three cases. The effective debonding strength, which represents the maximum FRP effective stress, depends on the debonding strength at the FRP-concrete interface (related to the available and effective bond lengths and the fracture energy, similarly to the debonding model of Chen and Teng, 2003b), on the ultimate FRP strength (for full wrapping) and on parameters related to the effective height of the FRP, which in the case of side bonding is taken equal to the vertically projected length of the sheet minus the effective bond length plus the bonded length that would be necessary at the debonding slip s_f, assumed equal to 0.2mm.

A formulation for V_f based on the truss model was given by Taljsten and Carolin (2007), where the two key parameters are the limiting value of effective strain (function of the strengthening configuration) and effective length of FRP, represented by the effective depth of the sheet minus its anchorage length.

Lima and Barros (2007) compared the results of a large database of tests in the literature with the provisions of the fib Bulletin 14 (2001), ACI 440.2R (2002), CNR DT-200 (2004) and the Australian guidelines CIDAR (2006), based on the model of Chen and Teng previously described. They found that no code was statistically satisfactory, with CoVs varying from 54% to 73% and a large population of unconservative results, especially for the beams containing stirrups.

In an experimental campaign to investigate the size effect on FRP-strengthened RC beams, Leung et al. (2007) showed that beams with the U-wrapped configuration

are prone to size effect while the ones fully wrapped are not. They explained this with the observation that the debonding capacity of U-wrapped beams is a function of the square root of the FRP area, while for the fully wrapped configuration the capacity is directly proportional to the FRP area, so with U-wrapping a linear increase in the beam size and FRP area does not lead to a proportional increase in ultimate capacity. Also, they showed that for large scale U-wrapped beams code predictions are unsafe.

Lee and Al-Mahidi (2008) used photogrammetry to measure crack widths, slips and strains in three RC beams strengthened in shear with L-shaped CFRP plates. They found that both the control specimen and the strengthened beams reached their peak load for average crack width values of 1.5 to 2mm, while the average strains in FRP at failure were of the order of 4000 to 6000με. Slip measurements showed that when FRP debonded at failure, values of slip of 0.8 to 1mm were reached.

Interaction between FRP and stirrups

Mohamed Ali et al. (2006) studied the interaction between internal stirrups and external FRP strengthening and pointed out that, because stirrups are anchored and can yield, there is no guarantee that the peak shear forces that can be resisted by the stirrups and FRP coincide. As shown in Figure 2.22 (a), forces in the internal stirrups and external FRP plates are caused by the opening w of the diagonal crack, which induces the stirrups to stretch and have a strain $\varepsilon_s = w/D$, while in the FRP w equals the two crack face slips δ_{up} and δ_{lw}, and the capacity of the two sides of the FRP is related to the bond-slip characteristics of the FRP to concrete interface, usually idealised with bilinear branches as shown in Figure 2.22 (b).

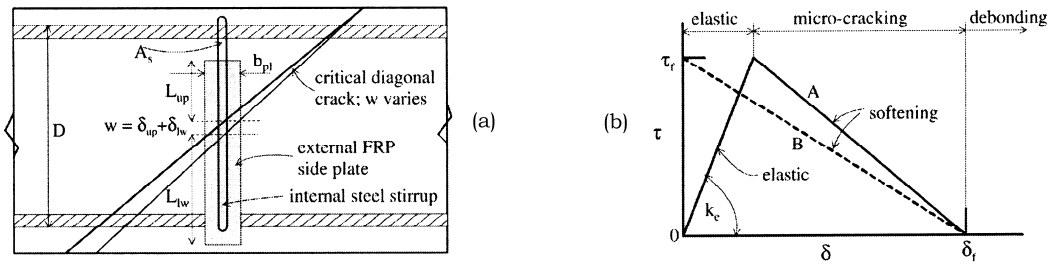

Figure 2.22: (a) Stirrups-FRP interaction and (b) Idealised bond-slip models (after Mohamed Ali et al., 2006)

After initial debonding occurs at the FRP-to-concrete interface, the slip at a crack face is the sum of the maximum slip δ_f at debonding and a contribution from the uniform strain of the remaining unbonded part of FRP; for different values of the imposed crack width w, assumed to open either uniformly or pivoted at the top surface, Mohamed Ali et al. (2006) derived the force-width response for different strengthening configurations with similar amount of stirrups.

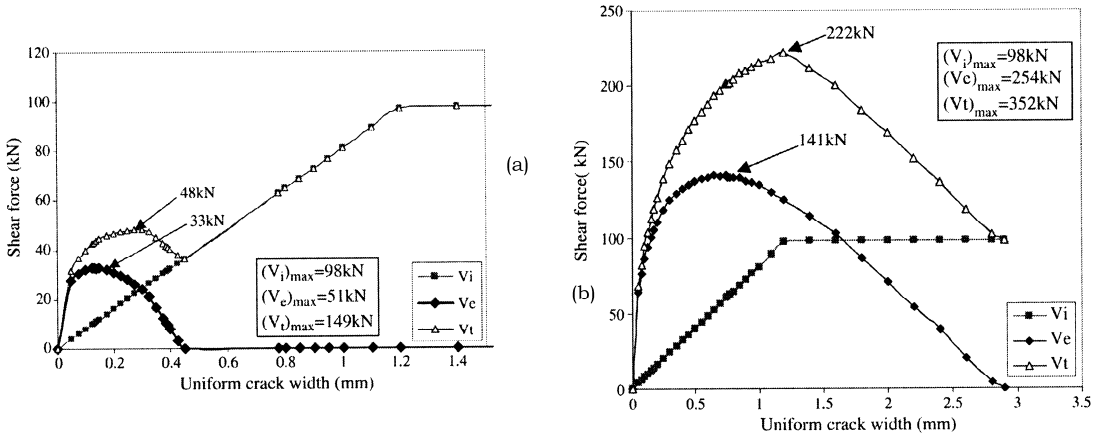

Figure 2.23: Shear force-crack width response for (a) side bonded and (b) NSM (after Mohamed Ali et al., 2006)

Figure 2.23 shows the results for an EB (side bonded) and an NSM configuration with strips, where peak bond stresses and maximum slips of 7MPa/0.16mm and 13MPa/1.54mm were used respectively based on tests in the literature; it is evident that when the peak resistance of FRP is reached the stirrups may not have yielded and that the ductility of the bond-slip response, that is higher in NSM systems, plays a key role in defining the proportions of the interaction. In side bonding, when the peak capacity of the FRP is lower than the capacity of the stirrups alone, the overall capacity of the beam is not increased at all by the presence of the FRP, while in a U-wrapping configuration the reduction in strength of the FRP after the peak will be more gradual and may still contribute to the capacity at stirrup yield. In any case, it is unlikely that the shear capacity will reach the sum of the maximum contribution from stirrups and FRP, as suggested by the codes and most existing guidelines, which may be dangerously unconservative in the case of beams containing stirrups.

Grande et al. (2007) performed a series of tests on RC beams with stirrups strengthened with full wrapping, U-wrapping and side bonding. They compared

their results with the Italian CNR DT-200 (2004) and found that the code provision was always unconservative, especially for side bonding. They studied the interaction between stirrups and FRP and found that the contribution of FRP reduces when the amount of stirrups increases, concluding that it is not realistic to neglect the interaction.

Pellegrino and Modena (2008) proposed a model for the shear capacity of beams strengthened with EB FRP that considers the interaction between stirrups and FRP. In the model, the term V_f is a function of the effective FRP strain ε_{fe}, while the stirrup contribution V_s is reduced by multiplying it by 0.75, and the stress in the stirrups is limited by the maximum stress in the FRP $\varepsilon_{fe}E_f$ and is equal to the yield stress only when $\varepsilon_{fe}E_f > f_y$. However, limiting the stress of FRP based on the stress level in steel does not appear completely justified.

Bousselham and Chaallal (2008) performed a series of shear tests on full size RC T-beams with and without stirrups strengthened with EB FRP sheets and measured the strain response of both stirrups and FRP up to failure. They found that yielding of the stirrups occurred in most cases; however, the contribution of the FRP sheets to the shear capacity was relatively low and the maximum strains reached were only a small fraction of the FRP failure strain, of the order of 15-20%.

2.3.3.3 Existing theories for near surface mounted (NSM) applications

The existing knowledge on NSM applications, which consist of cutting grooves into the concrete cover and gluing FRP bars or strips using an adhesive, is more limited than that on the externally bonded methods. However, several experimental studies have proven that NSM systems are effective for both flexural and shear strengthening of concrete structures (De Lorenzis and Teng, 2007).

Bond capacity in NSM applications

The performance of the bond between NSM FRP and the substrate plays a key role in the effectiveness of the system; it depends on a series of parameters such as the dimension of the grooves, the properties of concrete and the adhesive, and the dimension and surface configuration of the bars, which can be smooth, ribbed, sanded, spirally wound or roughened with a pre-ply treatment. Possible bond failure modes for NSM systems include splitting of the concrete cover, failure at the epoxy-concrete or epoxy-bar interface (pull-out failures), shear failure of the epoxy

(occurring when the shear strength of the epoxy is exceeded), interlaminar shear failure within the FRP bar (whose resistance is highly dependent on the surface configuration) or bar rupture.

The bond stress-slip response of various forms of reinforcing can be determined by pull-out tests. These tests are often categorised as short embedment length (direct pull out tests on prisms) or long embedment length (beam tests). Tension in the FRP bar at various degrees of slippage may be found, leading to generic load-slip plots for FRP bars. In short embedment length tests, the reinforcement is bonded over a short region and therefore the bond stresses are distributed fairly evenly over the bonded length. In the case of long embedment length tests larger forces are developed, the bond stress distribution can vary substantially along the bar, and the peak bond stress generally develops further away from the loaded end as the load increases. Various authors (De Lorenzis and Teng, 2007) have studied the local bond strength of the NSM system where the local bond-slip curve is expressed as the average bond stress versus the loaded end slip (for short embedment length) or is found from strain measurements along the bond (for long embedment length).

From pull-out tests using round bars, De Lorenzis and Nanni (2002) and De Lorenzis et al. (2004) found that most failures occurred by splitting of the epoxy cover (for deformed or spirally wound bars) or by pull out at the bar-epoxy interface (for sanded bars), with an optimum groove size to bar diameter ratio of 2. De Lorenzis et al. (2004) found that the bond strength ranged from 5 to 22MPa, with the better performance obtained with CFRP sand-coated spirally wound bars, where bond strength in excess of 20MPa and a relatively ductile response of the bond-slip curve was attained. De Lorenzis and Galati (2006) studied the effect of two different types of epoxies on the bond capacity of round spirally-wound sand-coated CFRP bars. They found that the epoxy with the higher tensile strength and modulus of elasticity (23MPa and 13GPa versus 19MPa and 4GPa, respectively) gave a higher bond strength (14MPa versus 8MPa) but a lower ductility in the bond-slip response.

From bond tests on NSM rectangular strips, which maximise the surface area to sectional area ratio for a given volume when compared to round bars, Sena Cruz and Barros (2002) and Blaschko (2003) found local bond strengths of the order of 16 to 20MPa. In Blaschko's (2003) tests, failure occurred in the epoxy and he proposed a formula which relates the bond strength to the shear strength of the

epoxy and the distance from the NSM strip to the nearest concrete edge, considered to have a detrimental effect when less than 150mm. Shield et al. (2005) studied the effect of different adhesive types on the bond capacity of NSM strips to concrete; they found big differences in the bond capacity even when using adhesives with similar nominal tensile and shear ultimate strength, concluding that other material properties such as ultimate shear strain and shear modulus of the adhesive may play an important role.

From the equilibrium of forces in the bonded length of an NSM to concrete joint, it is found (De Lorenzis and Teng, 2007) that the maximum stress that can be resisted in the joint is:

$$\sigma_{max} = \sqrt{\frac{2\,E\,\Pi\,G_f}{A}} \tag{2.79}$$

where E and A are the elastic modulus and area of the FRP, Π is the perimeter over which the bond stress acts and G_f is the fracture energy of the bonded joint, equal to the area underneath the bond-slip curve. When the value of the maximum stress is below the tensile strength of the FRP, its full capacity cannot be reached and an increase in bond length does not increase capacity. When the maximum stress is larger than the FRP tensile strength, the full capacity can be developed. Experimental evidence (De Lorenzis and Teng, 2007) showed that in the case of NSM systems the bond behaviour is more similar to that of internal rebars because the fracture energy is much higher than in EB systems; therefore, a full development length is often achievable.

Seracino et al. (2007) performed a series of push-pull tests on NSM strips where the FRP size, concrete strength and bond length were varied. They observed debonding failures due to cracking in the concrete (for long bonded lengths), pull-out failure in the adhesive (for short bonded lengths) and also bar rupture in some cases. They confirmed that an idealized bilinear model can be adopted for the NSM bond-slip curve similar to those typically used for the EB technique, but a great improvement in strength (2 to 3 times) and ductility (of an order of magnitude) can be obtained with NSM compared with EB systems (see Figure 2.24). They concluded that the improved efficiency of the NSM technique is a result of the confinement of the interface debonding crack by the surrounding concrete cover.

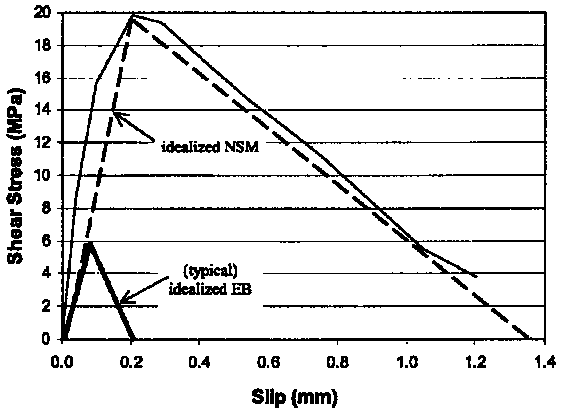

Figure 2.24: Bond slip relations for EB and NSM systems (after Seracino et al., 2007)

Mohamed Ali et al. (2008) compared the effectiveness of NSM and EB strips in increasing the shear capacity of concrete blocks with stirrups subject to push off (pure shear) tests. They found that in the case of FRP EB specimens failure occurred by debonding of the plates with very limited ductility, as the recorded FRP strains at failure were about 10-15% of the rupture value. However, the blocks with NSM FRP strips exhibited a more ductile behaviour, with FRP strains at failure of the order of 55 to 90% of rupture, confirming the superior effectiveness of the NSM system. An analytical model was proposed where the contribution of the stirrups (in terms of yield stress) and the NSM strips (in terms of bond strength) could be added, giving good predictions.

Shear strengthening with NSM applications

De Lorenzis and Nanni (2001) carried out eight tests on RC beams with and without stirrups strengthened in shear with CFRP ribbed round bars, varying parameters such as bar spacing and inclination angle. They found increases in shear capacity as high as 106% in beams containing no stirrups and 35% in beams with a limited amount of stirrups. The failure modes observed were debonding of the FRP bars by splitting of the epoxy cover or separation of the concrete cover from the longitudinal steel reinforcement. They proposed a model to compute the FRP contribution V_f to the shear capacity based on the 45° truss analogy, in which the basic assumption is that at failure the bond stresses are evenly distributed along the bars crossed by the critical shear crack and are equal to the average bond strength; as discussed previously, the assumption is acceptable if the bond-slip behaviour is ductile enough to allow such a redistribution.

According to the model, the V_f contribution is equal to the bond capacity of the bars intersected by the critical crack, limited by a maximum strain of 0.004 imposed on the FRP to maintain the integrity of the concrete in shear. The shear contribution of the FRP bars is therefore:

$$V_f = 2\pi d_b \tau_b (\sum_{i=1}^{n} l_{emb,i}) \tag{2.80}$$

where $l_{emb,i}$ is the minimum embedment length of the i-th bar (i.e. the minimum between the two lengths of each bar at both sides of the crack); this value depends on the bar spacing s, their inclination and the effective length of the FRP bar h_{net}, equal to the height of the strengthened part minus the concrete cover to the longitudinal reinforcement. The embedment length $l_{i,lim}$ of a bar crossed by the crack corresponding to the strain $\varepsilon_{f,max}$ is given by:

$$l_{i,lim} = \frac{A_f E_f \varepsilon_{f,max}}{2\pi d_b \tau_b} \tag{2.81}$$

where A_f and E_f are the area and modulus of elasticity of the FRP bar, respectively. When the value given by (2.81) is lower than the embedment length $l_{emb,i}$ of a bar crossed by the critical crack, then $l_{i,lim}$ would be the limiting value for that bar. De Lorenzis and Nanni (2001) proposed a value of τ_b = 6.9MPa for the average bond stress.

Nanni et al. (2004) tested a full-scale PRC girder strengthened in shear with NSM strips and found that the capacity was very close to that predicted by the model of De Lorenzis and Nanni (2001). Dias and Barros (2005) tested a series of RC beams without stirrups strengthened in shear with both the EB and NSM techniques using FRP strips. They found that, although both techniques were able to increase the ultimate shear capacity, the NSM technique was more efficient, offering an average increase of capacity of 83% (versus the 54% of EB) and a more ductile behaviour at failure. They found good correlation between the shear capacity of the NSM-strengthened beams and the model of De Lorenzis and Nanni (2001), where values of 16.1MPa and 0.0059 were adopted for the average bond stress and limit strain of the FRP respectively according to previous bond tests on NSM strips (Sena Cruz and Barros, 2002). In a further experimental programme on real-scale T-beams with and without stirrups with varying amount and inclination of NSM strengthening, Dias and Barros (2006) found an increase in shear capacity ranging from 13% to 29%, confirming the effectiveness of the system.

Rizzo and De Lorenzis (2009a) proposed a refinement to the original model in which the angle formed by the critical crack and the FRP bars with the horizontal can be varied, making the model more general. From geometric considerations they found a closed form equation for the minimum total embedment length $l_{emb,tot,min}$ of (2.80), expressed as a function of the bar spacing, inclination and effective length. When the longest among the minimum embedment lengths of all the bars crossed by the crack is higher than the value in (2.81), the bond stress in (2.80) is reduced by the ratio $l_{i,lim}/l_{emb,max}$ to represent the upper limit on V_f. They used five different bond-slip models (including the rigid plastic model employed in the truss analogy, where the value of the bond stress is selected so to give the same fracture energy G_f) to derive the load-slip response of an NSM-strengthened RC beam with stirrups following the method of Mohamed Ali et al (2006) previously described, where the crack width is gradually increased and the corresponding slip in the FRP and load in the FRP and stirrups are calculated. They found that the difference in response between the bond-slip models was less than 5%, confirming that the rigid-plastic models can be employed when an appropriate value of the bond stress is chosen. Most importantly, they found that the FRP and stirrup contribution could be added because the peak of the FRP contribution is reached when the steel has already yielded; this happens because the fracture energy in the NSM system is much larger than in EB applications.

Oehlers et al (2008), following a series of push-pull tests, reported that closely spaced NSM strips can interact with each other and fail as a group at a reduced strength when compared with the sum of the single resistance. Dias and Barros (2006) and De Lorenzis and Rizzo (2009b) observed that, rather than debonding of the FRP from concrete, the prevalent failure mechanism for RC beams with high strengthening ratio of NSM FRP bars or strips involves the detachment of the side concrete cover containing the strengthening laminates. Such a failure mode is influenced by the spacing of the FRP because NSM bars located at large spacing tend to debond from the concrete substrate independently from each other, while when they are closely spaced the bond stresses transferred to the concrete mutually interact and create an out of plane tensile stress envelope in the concrete substrate. This is exacerbated by the presence of internal steel stirrups, that create two vertical planes of weakness, which facilitate the detachment of the side concrete covers.

Bianco et al. (2009) proposed an analytical approach to evaluate the capacity due to this failure mode based on the analogy with the failure of concrete in bonded anchors, where conical fracture surfaces are formed with critical tensile stresses normal to the surface. In the model, the maximum contribution to shear by the FRP for side concrete separation is expressed as the sum of the tensile resistance of each semi-conical surface associated with the shortest length of the two sides of a bar intersected by the critical shear crack; when the bars are closely spaced the semi-conical surfaces intersect with each other so the overall capacity is lower than the sum of the capacity of the single surface, and the effectiveness of the system is reduced.

Clearly, because in beams strengthened with NSM the full debonding capacity assumed in the proposed models may not be reached because of the early separation of the side concrete cover, further experimental and analytical evidence needs to be gathered before a safe and reliable design procedure may be implemented.

2.3.4 Guidelines for the shear strengthening of concrete using FRP

The design formulae for the shear strengthening of concrete structures using FRP, developed for the EB system, are presented in the following with reference to the American ACI 440.2R (2008), the British Concrete Society TR55 (2004) and Italian CNR DT-200 (2004) guidelines. All guidelines assume that the shear capacity from the FRP may be summed to that of the concrete and steel contribution following a 45° truss analogy.

ACI 440 2R (2008)

The contribution of the FRP strengthening to the shear capacity is given by $\psi_f V_f$, where ψ_f is a reduction coefficient equal to 0.95 or 0.85 for fully wrapped or U-wrapping/side-bonding respectively and V_f is given by:

$$V_f = \frac{A_{fv} E_f \varepsilon_{fe} d_f}{s_f} (\sin a + \cos a) \tag{2.82}$$

where A_{fv} is the total area of the FRP sheet wrapped or bonded, d_f is the effective depth of the sheets (taken as their total depth minus the cover to the tension steel), s_f is the sheet spacing, a is the inclination of the sheets to the horizontal, E_f is the

Young's modulus of the FRP and ε_{fe} is the effective strain that can be achieved at the ultimate limit state by the sheets.

The effective strain for the fully wrapped case is equal to the lesser of 0.004 and $0.75\varepsilon_{fu}$ while for U-wrapping and side bonding this equals the lesser of 0.004 and $k_v\varepsilon_{fu}$, where ε_{fu} is the ultimate strain of the FRP sheet and the reduction factor k_v equals:

$$k_v = \frac{k_1 k_2 L_e d_f}{11900\varepsilon_{fu}} \leq 0.75 \tag{2.83}$$

with the active bond length L_e and the reduction factors equal to:

$$L_e = \frac{23300}{(t_f E_f)^{0.58}} \tag{2.84}$$

$$k_1 = \left(\frac{f_c'}{27}\right)^{2/3} \tag{2.85}$$

$$k_2 = \frac{d_f - L_e}{d_f} \quad \text{(for U-wrapping)} \tag{2.86}$$

$$k_2 = \frac{d_f - 2L_e}{d_f} \quad \text{(for side bonding)} \tag{2.87}$$

The spacing of the FRP sheets should comply with the limits for stirrups given in ACI 318-08 (2008), and the total shear reinforcement V_s+V_f should not exceed $0.66\sqrt{f_c'}b_w d$.

Concrete Society TR55 (2004)

The contribution of the FRP to the shear capacity is:

$$V_f = E_{fd}\varepsilon_{fse}A_{fs}\left(d_f - \frac{n}{3}l_{t,max}\right)(\cos\beta + \sin\beta)/s_f \tag{2.88}$$

where A_{fs} is the total area of the FRP sheet wrapped or bonded, d_f is the effective depth of the sheets (taken as their total depth minus the cover to the tension steel), s_f is the sheet spacing, β is the inclination of the sheets to the horizontal, E_{fd} is the design Young's modulus of the FRP, ε_{fe} is the effective strain that can be achieved at the ultimate limit state by the sheets and $l_{t,max}$ is the anchorage length required to develop full anchorage capacity, with n = 0,1 or 2 for fully wrapped, U-wrapped and side bonded beams respectively.

The effective strain is taken to be the minimum of 0.004, ε_{fd} /2 and 0.64 $(f_{ctm}/E_{fd}t_f)^{0.5}$, where f_{ctm} is the concrete tensile strength and ε_{fd} is the design strain capacity of the FRP. The anchorage length $l_{t,max}$ is equal to $0.7(E_{fd}t_f/f_{ctm})^{0.5}$. The spacing of the sheets should not be so wide as to allow the formation of a crack without intercepting a strip, so the spacing should not exceed the least of $0.8d_f$, d_f-$(n/3)l_{t,max}$ and $b_f+d_f/4$. Also, irrespective of the amount of FRP provided, the shear strength of a section V_u is limited by the shear stress leading to diagonal compression failure in the concrete, equal to the lesser of $0.75(f_{cu})^{0.5}$ or 4.75MPa according to the UK code for bridge design BS 5400-4 (1990). The ultimate bending capacity should then be checked assuming the area of the tensile longitudinal reinforcement is reduced by the additional demand in shear due to the strengthening.

CNR DT-200 (2004)

The contribution to the shear capacity of side bonded FRP sheets is:

$$V_{Rd,f} = \frac{min\,[0.9d, h_w]}{\gamma_{Rd}} f_{ed} 2t_f \frac{\sin\beta}{\sin\theta} \frac{w_f}{p_f} \tag{2.89}$$

where w_f and p_f are the sheet width and spacing orthogonal to the sheet axis respectively, d is the beam effective depth, h_w is the beam web depth, t_f is the sheet thickness, γ_{Rd} is a safety factor equal to 1.2, β is the inclination of the sheets to the horizontal, θ is the inclination of the shear cracks (assumed equal to 45°) and f_{ed} is the effective FRP design strength, calculated from:

$$f_{fed} = f_{fdd} \frac{z_{rid,eq}}{min[0.9d, h_w)} (1 - 0.6\sqrt{\frac{l_{eq}}{z_{rid,eq}}})^2 \tag{2.90}$$

where $z_{rid,eq}$ equals $min[0.9d,\ h_w]$-$l_e \sin\beta$, l_e is the effective bonded length $(E_f t_f/2f_{tcm})^{0.5}$, f_{ctm} is the mean concrete tensile strength and $l_{eq} = s_f E_f \sin\beta/f_{dd}$, where E_f is the Young's modulus of the FRP, s_f is the ultimate debonding slip assumed to be equal to 0.2mm and the ultimate design strength f_{dd} is:

$$f_{fdd} = \frac{1}{\gamma_{f,d}\sqrt{\gamma_c}} \sqrt{\frac{2E_f G_{fk}}{t_f}} \tag{2.91}$$

where $\gamma_{f,d}$ and γ_c are the partial factors for bond and concrete, and G_{fk} is the fracture energy of the FRP to concrete interface, equal to 0.03 k_b $(f_{ck}\ f_{ctm})^{0.5}$; f_{ck} is the characteristic cylinder compressive strength and k_b is a geometric coefficient depending on the width of the concrete element and the width of the FRP sheet.

The contribution to the shear capacity of fully wrapped or U-wrapped FRP sheets is:

$$V_{Rd,f} = \frac{0.9d}{\gamma_{Rd}} f_{ed} 2t_f (\cot\theta + \cot\beta) \frac{w_f}{p_f} \tag{2.92}$$

where the effective FRP design strength f_{ed} for the U wrap configuration equals:

$$f_{fed} = f_{fdd}\left(1 - \frac{1}{3}\frac{l_e \sin\beta}{\min[0.9d, h_w]}\right) \tag{2.93}$$

while for fully wrapped members the expression is also function of the corner radius of the section to be wrapped and the rupture strength of the sheet.

The value of the sheet width w_f shall be limited between 50 and 250mm and the spacing p_f shall not exceed the lesser of $0.5d$, $3w_f$ and w_f+200mm. In any case, the shear capacity of the strengthened member shall not exceed the ultimate strength of the concrete strut $V_{Rd,max}$.

2.4 Concluding remarks

In this chapter, existing literature outlining the various types of shear analyses and design methods for RC and PSC beams, with and without transverse reinforcement, has been presented. In addition, a comprehensive overview of recent developments in shear strengthening techniques using FRP materials has been given.

Although in the past decades numerous methods of shear analysis have been proposed by the research community with different degrees of complexity, there is still no unanimous consensus on the best way forward, which is reflected by the fact that codes worldwide still employ different approaches. The main problem is that parameters that are considered critical in one theory are disregarded in another; for example, test evidence suggests that the slenderness ratio a/d has a substantial influence over the shear capacity of prestressed beams, a fact which is disregarded in some codes. On the other hand, the most comprehensive approaches are often too complex to be easily implemented by practising engineers.

At present, shear assessment of concrete bridges does not consider the actual manner in which a bridge behaves during collapse. Therefore, approaches based on plasticity theory may be the most appropriate for assessment, as a series of realistic

failure mechanisms can be analysed for the structure as a whole, rather than considering a pure sectional analysis.

In recent years, many researchers have focused their attention on the shear strengthening of concrete beams using FRP, leading to the production of a number of guidelines worldwide. The important issue of bond between the FRP and the concrete has been the subject of several studies. It has been shown that NSM applications offer better bond performance than EB applications as their bond-slip response is much more ductile, increasing the likelihood that the FRP contribution to the shear enhancement can be additive to that of the internal stirrups. However, the effectiveness is potentially compromised by the occurrence of a failure mode involving the detachment of the side concrete cover containing the NSM laminates.

As will be discussed in detail in the following chapters, the deep embedment technique, developed as part of the present research project, aims to overcome the drawbacks of some of the existing shear strengthening methods, by being applicable when only the soffit of the member is accessible, exhibiting a very ductile bond-slip response and being internal, so that the full bond capacity can always be obtained.

Chapter 3
Test Philosophy and Preparation

3.1 Introduction

As mentioned in Chapter 1, this research aims to formulate a realistic shear assessment tool for contiguous concrete beam bridges and to develop a novel shear strengthening scheme for such bridges, if found to be under strength.

The experimental investigation comprised 34 large- and small-scale tests on single beams, in both the unstrengthened and strengthened configuration, and 9 small-scale tests on entire bridge models, which are replica scaled-down models of bridges in service at present. In addition, 65 bond tests were performed to assess the bond capacity of bars glued into concrete for the newly proposed deep embedment strengthening technique.

The tests were planned in order to investigate the numerous variables that affect the shear behaviour of these structures (and, in general, of RC and PSC beams), including the level of the longitudinal and transverse prestressing, the amount of internal stirrups, the shear span to depth ratio, the amount of strengthening and the effectiveness of FRP versus steel in the strengthening approach.

This chapter describes the details of all specimens, explaining how tests were designed starting from the existing reference bridges. The test programme and the casting, strengthening and testing procedure are also presented.

3.2 Design of the test specimens

3.2.1 Existing reference bridge

An existing bridge has been taken as a reference in the construction of the test specimens. The bridge is a simply supported railway underbridge consisting of ten

pretensioned rectangular concrete beams transversely prestressed together to form a deck of total length of 14.6 metres, with a distance of 13.72 metres between the centres of the support bearings (see Figures 3.1 and 3.2).

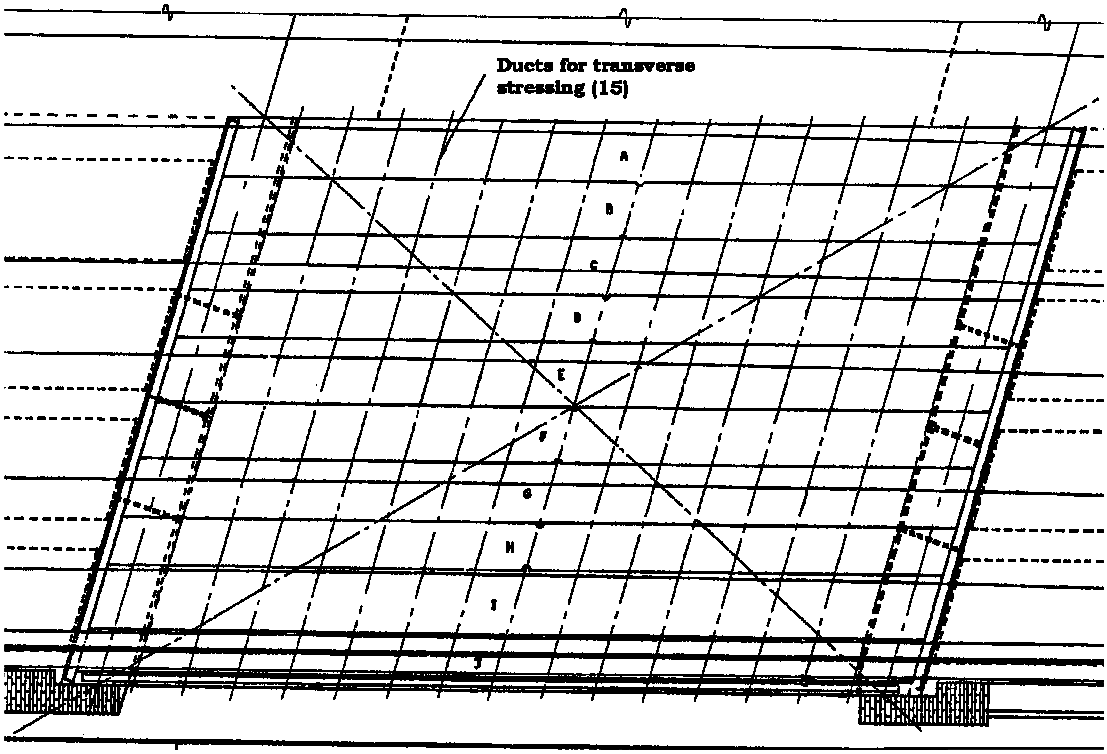

Figure 3.1: Plan of the existing reference bridge

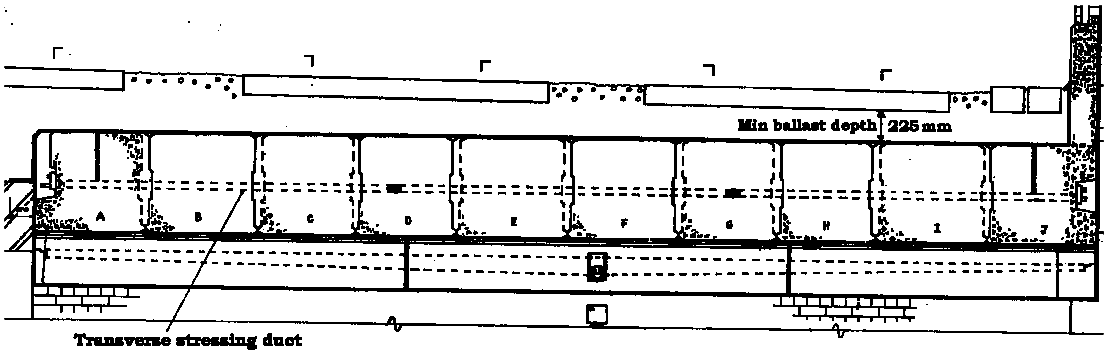

Figure 3.2: Cross section of the reference bridge (section at support)

Each beam was typically 900mm wide and 762mm deep (see Figure 3.3) and was pre-tensioned longitudinally with a total of 38 tendons at mid-span, 21 of which were not bonded towards the supports, where 17 tendons remained fully effective.

Each pre-tensioning tendon was a nominal 15.2mm diameter 7-wire strand (139mm^2 nominal area) stressed at an initial force of 159kN.

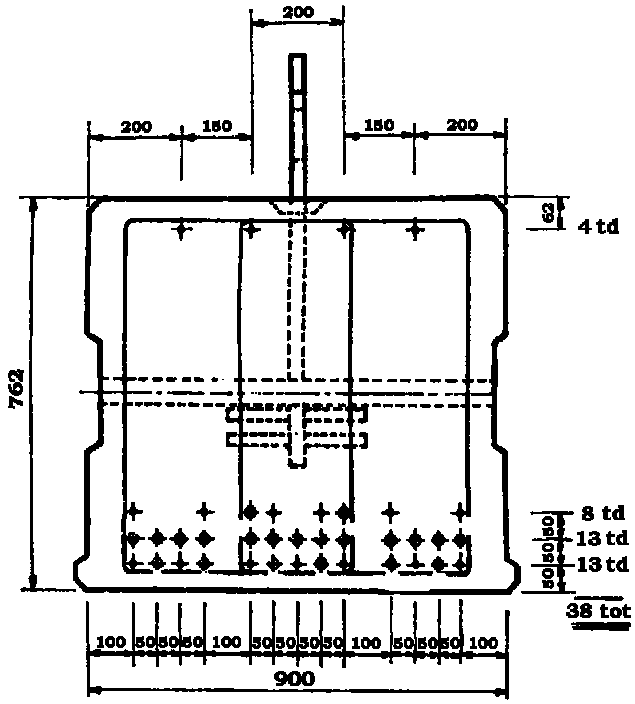

Figure 3.3: Typical cross section of the reference bridge beams at mid-span (in mm)

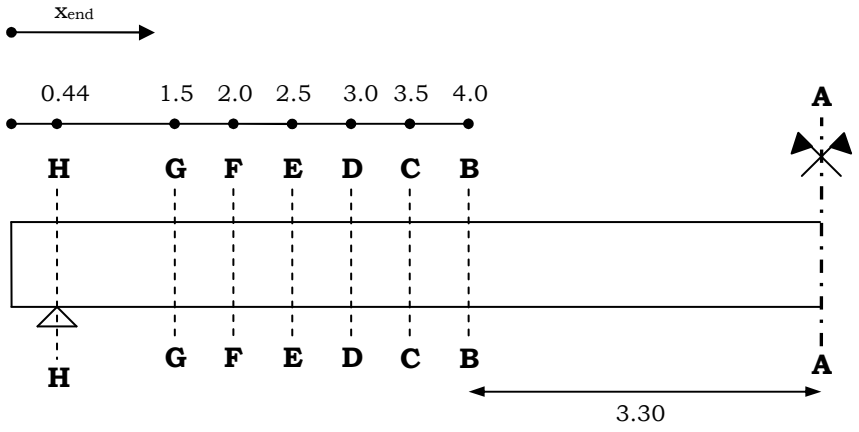

Figure 3.4: Elevation of the reference beam showing debonding points (in m)

The beams were transversally prestressed together, in situ, with 15 post-tensioned tendons spaced 900mm apart. Each tendon comprised four 7-wire strands of 12.5mm nominal diameter and 93mm^2 nominal area each stressed at an initial force of 105kN, so that the total initial force at transfer was 420kN for each tendon. The specified characteristic compressive cubic strength of the concrete at 28 days

was 60MPa. The geometric characteristics differed along the span at each debonding section (see Figure 3.4) and they are summarized in Table 3.1 with reference to Figure 3.5, where A_t is the transformed area of the cross section (with a Young's modulus ratio equal to 6), y_c is the distance from the centroid C of the cross section to the bottom edge, I_t is the transformed second moment of area, y_{ct} is the distance from the centroid of the prestressing tendons Ct to the bottom edge, e is the eccentricity of the tendons, d is the effective depth to the centroid of the prestressing tendons and d_s is the effective depth to the longitudinal tension reinforcement.

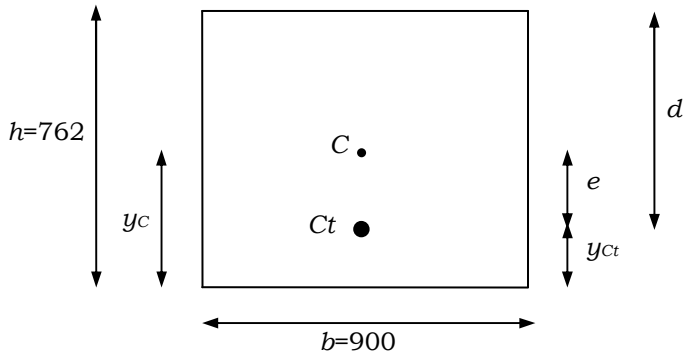

Figure 3.5: Geometric characteristics of the reference beam (in mm)

Table 3.1: Geometric properties of the reference beam

Section	**A-A B-B**	**C-C**	**D-D**	**E-E**	**F-F**	**G-G**	**H-H**
Tendons	38	36	34	31	27	23	17
A_t (cm^2)	7174	7158	7142	7116	7083	7050	7000
y_C (mm)	371	372	372	374	375	376	378
I_t (cm^4)	3.47E6	3.46E6	3.44E6	3.42E6	3.40E6	3.37E6	3.35E6
y_{Ct} (mm)	157	162	169	179	191	207	238
e (mm)	214	210	203	195	184	169	140
d (mm)	605	600	593	583	571	555	524
d_s *(mm)*	669	667	660	660	660	659	666

As discussed in Chapter 2, for prestressed beams the length of the span where shear is critical may well extend to distances of over 6d from the support. For this reason, the average values of the geometrical characteristics in the zone between the support and the section at 6d from the support were used as a design basis for

the small- and large-scale test beams, as it was impractical to provide such detailed debonding patterns for these beams.

The average value of the effective depth in the shear zone was 576mm and the ratio d/h between the effective depth and the total depth was equal to 0.756 in the shear zone, 0.688 at support and 0.794 at mid-span. The degree of longitudinal reinforcement Φ is defined as $(A_{sl}/bh)(f_y/f_c)$, where f_y is the steel yield stress and f_c the characteristic cylinder strength of the concrete. With f_y taken equal to the characteristic 0.1% proof stress (approximately 1500MPa) and f_c equal to 50MPa, Φ was equal to 0.170 in the shear zone, 0.103 at support and 0.231 at mid-span. In the shear zone, the average value of the effective depth to the longitudinal tension reinforcement was equal to d_s = 663mm.

The beams were provided with 10mm diameter high yield steel stirrups whose layout varied in three zones along the 14.60 meter length of the beam length. At the support, for a total length of 1 metre from the end of the beam, there are four–leg links at 100mm c/c giving a percentage of transverse reinforcement $\rho_{sv} = A_{sv}/bs$ = 0.35%. In the shear zone, extending for approximately 5m beyond the support, there are four-leg links at 300mm c/c plus two-leg links at 300mm c/c, giving a total ρ_{sv} = 0.175%. In the remaining zone at mid-span there are four-leg links at 900mm c/c plus two-leg links at 300mm c/c giving a total ρ_{sv} = 0.098%. The degree of vertical reinforcement ψ is defined as $\rho_{sv}(f_y/f_c)$. With f_y = 410MPa and f_c = 50MPa, ψ was equal to 0.014 in the shear zone, 0.029 at support and 0.008 at mid-span. It must be noted, however, that the assessment code NR/GN/CIV/025 (2006) states that links are not effective in resisting shear when their spacing in the direction of the span or at right angles to it exceeds d_s; this means that the two-leg links should be disregarded as their lateral spacing within the beam section exceeds 700mm. Therefore, the effective percentage of transverse reinforcement in the shear zone is equal to 0.117%, with a degree of vertical reinforcement ψ = 0.010.

Analysis of the stress state

For 15.2mm diameter tendons pre-tensioned to 159kN, the initial stress is 1145MPa. Following NR/GN/CIV/025 (2006) and Eurocode 2 (2004) a total loss of prestressing of approximately 30% is given as sum of the instantaneous and time-dependant losses, leading to a residual effective tendon stress of around 800MPa in service.

The nominal permanent loads acting on the bridge are the dead weight of the beams and the weight of the ballast and track. According to the assessment code NR/GN/CIV/025 (2006), the dead weight of the beam is 24*0.9*0.762 = 16.46kN/m, the weight of ballast (with average depth of 250mm to the underside of the sleepers) over a beam is 18*0.9*0.25 = 4.05kN/m and the weight of the track with timber sleepers over the width of a beam is equal to (8.50kN/m*0.9m)/3.2m = 2.40kN/m.

The stress state due to the actions described above is then assessed under the bridge service load condition. The stresses, regarding compression as positive, due to the prestressing are:

$$\sigma_c = \frac{N}{A_t} + \frac{Ne}{I_t} y \tag{3.01}$$

and those due to the permanent loads are:

$$\sigma_c = \frac{M}{I_t} y \tag{3.02}$$

where N is the total prestressing force at a section after all the losses, y is the distance from the centroid to the fibre under consideration (see Figure 3.6) and M is the moment at the section due to the permanent loads. The average shear stress on the cross sections due to the permanent loads is:

$$\upsilon = \frac{V}{b_w d} \tag{3.03}$$

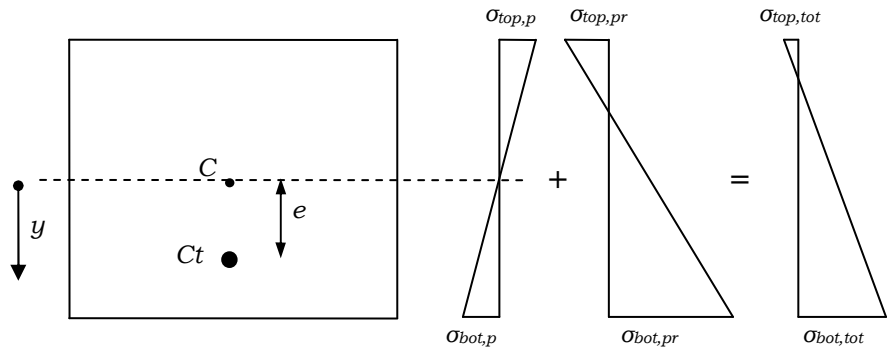

Figure 3.6: Stress state in the reference bridge beam (p = permanent, pr = prestressing)

Table 3.2 summarizes the stress state in the reference bridge beam in service under the permanent and prestressing forces after all losses. The average values in the shear zone for the top and bottom normal stresses are 0.4MPa and 8.7MPa respectively, with a mean value through the section of 4.5MPa; the average value of the shear stress is 0.25MPa.

Table 3.2: Stresses in the reference beam (p = permanent, pr = prestressing)

Section	N (kN)	$\sigma_{bot,pr}$ (MPa)	$\sigma_{top,pr}$ (MPa)	$\sigma_{bot,p}$ (MPa)	$\sigma_{top,p}$ (MPa)	$\sigma_{bot,tot}$ (MPa)	$\sigma_{top,tot}$ (MPa)	v (MPa)
A-A	4229	15.6	-4.3	-6.0	6.3	9.6	2	0.0
B-B	4229	15.6	-4.3	-4.6	4.8	11.0	0.5	0.17
C-C	4007	14.7	-3.9	-4.2	4.4	10.5	0.5	0.20
D-D	3784	13.6	-3.4	-3.7	3.8	9.9	0.4	0.22
E-E	3450	12.2	-2.8	-3.1	3.3	9.1	0.5	0.25
F-F	3005	10.3	-2.1	-2.5	2.6	7.8	0.5	0.28
G-G	2560	8.4	-1.3	-1.8	1.8	6.6	0.5	0.30
H-H	1892	5.7	-0.3	0.0	0.0	5.7	-0.3	0.36

A total loss of prestressing of around 30% is assumed for the lateral post-tensioning tendons spaced at 900mm c/c along the deck. Therefore, a transverse force of 0.7*420 = 294kN acts over each lateral area of 0.9*0.762 = 0.686m^2, giving an average compressive stress between beams of 0.43MPa in service.

3.2.2 Small- and large-scale beam specimens

Within the shear zone, the scaled-down beams were designed to match with the values of the real beams in terms of the ratio of effective depth to real depth (d/h), degree of longitudinal and transverse reinforcement and the stress state due to permanent loads and prestressing after all losses. A scaled-down size of approximately a quarter and a half of the dimensions of the reference was selected for the small-scale and large-scale specimens, respectively. The large-scale beams, in particular, are identical to those used for short span bridges of this type, so could be considered to be directly representative of full-scale specimens. The chosen cross sections and reinforcement layout, constant along the beam length, are shown in Figures 3.7 and 3.8.

The small-scale beams were 110mm wide, 190mm deep and 3000mm long, with four 7mm diameter prestressing wires of 38.5mm^2 nominal area (two of them pre-tensioned to 45kN each in the prestressed specimens) as longitudinal reinforcement and two-leg 3mm diameter mild steel vertical stirrups spaced at 100mm c/c in the shear zone (in the specimens with transverse reinforcement). The large-scale beams were 450mm wide, 350mm deep and 4000mm long, with fourteen 12.5mm diameter prestressing tendons of 93mm^2 nominal area pre-tensioned to 70kN as longitudinal reinforcement and four-leg 8mm diameter high yield steel stirrups spaced at 225mm c/c in the shear zone.

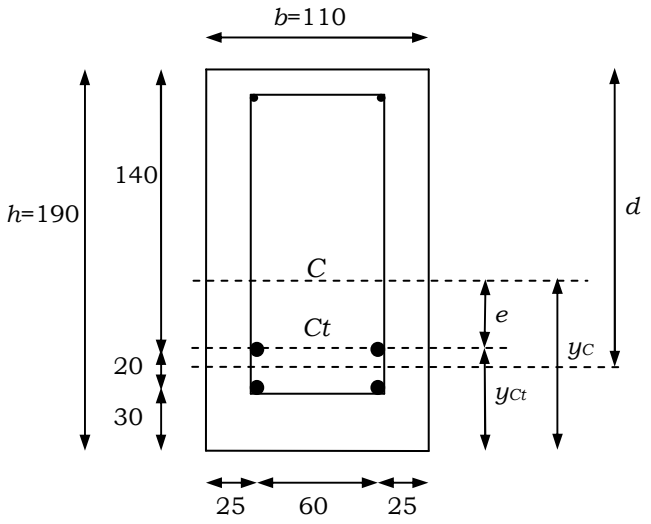

Figure 3.7: Cross section of the small-scale beams (in mm)

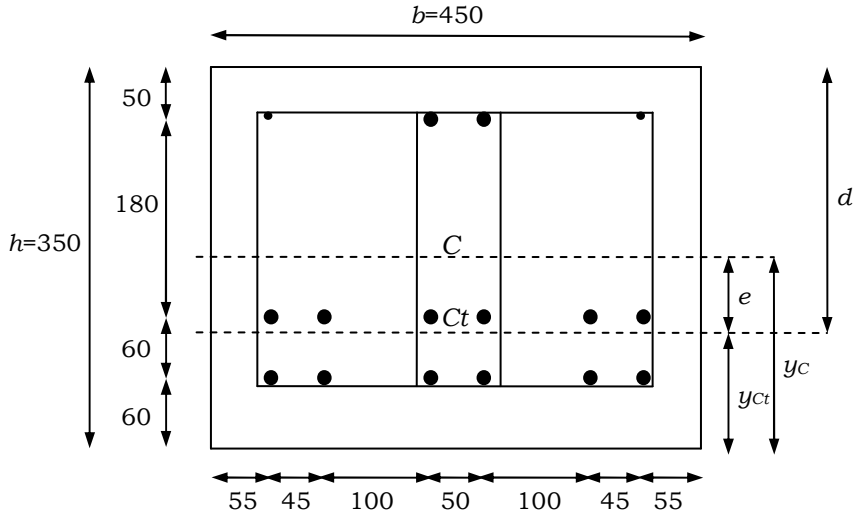

Figure 3.8: Cross section of the large-scale beams (in mm)

The geometric characteristics are summarized in Figures 3.7, 3.8 and 3.9 and the section properties are given in Table 3.3 where, for the small-scale beams, d is the effective depth to the centroid of the four wires (including the two not prestressed); d_s is the effective depth to the tension reinforcement.

Table 3.3: Section properties of the test beams

Beam	A_t (cm^2)	y_c (mm)	I_t (cm^4)	y_{ct} (cm^4)	e (mm)	d (mm)	d_s (mm)
S-scale	214	94	6405	50	44	150	150
L-scale	1653	172	164E3	105	67	245	260

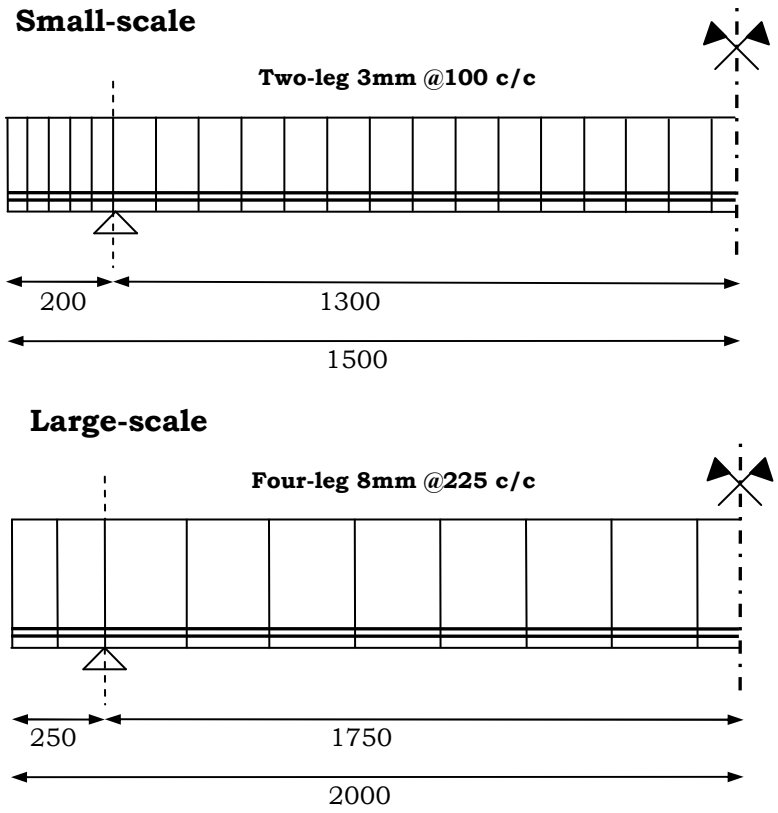

Figure 3.9: Elevation of the test beams showing the layout of stirrups (in mm)

The ratio d/h between the effective depth and the total depth was equal to 0.789 and 0.700 for the small-scale and large-beams respectively, with a maximum deviation of 8% when compared with the 0.756 of the real beams. As no debonding was provided in the test beams, the degree of longitudinal reinforcement Φ =

(A_{sl}/bh) (f_y/f_c) was constant along the span and equal to 0.199 for the small-scale and 0.213 for the large-scale beams, values that lie between the 0.170 (shear zone) and 0.231 (mid-span) of the real beams; this ensured that, in relative terms, the shear capacity of the test beams could not greatly be enhanced by the increase of longitudinal reinforcement and, at the same time, the flexural capacity was not excessively reduced.

In the shear zone, the degree of vertical reinforcement $\Psi = \rho_{sv}$ (f_y/f_c) was equal to 0.012 and 0.019 for the small- and large-scale beams respectively. The degree of vertical reinforcement of the large-scale beams was 35% higher than the real ones. However, as a bar size smaller than 8mm was not available for the high yield steel bars and the adopted stirrups spacing was already $0.85d_s$ (a value beyond which the links may well be ineffective), this is considered a reasonable approximation.

Analysis of the stress state

The total initial prestressing force was 90kN in the small-scale beams and 980kN in the large-scale beam. The stress state in the beams at testing is found by summing the dead weight stresses and the prestressing after losses, with the instantaneous and time-dependent losses calculated in accordance with NR/GN/CIV/025 (2006) and Eurocode 2 (2004), assuming the beams tested two months after casting. Similarly to the real beams, the average stresses in the shear zone from the support to the section at $6d$ were calculated. For the small-scale beams, the top and bottom stresses were -1.1MPa and 7.8MPa, with a mean value through the section of 3.4MPa. For the large-scale beams, the top and bottom stresses resulted -0.5MPa and 9.9MPa, with a mean value through the section of 4.7MPa. When compared to the 0.4MPa (top), 8.7MPa (bottom) and 4.5MPa (average) stresses of the real beams, it is seen that the discrepancy was never higher than 1.5MPa, which is considered reasonably accurate.

3.2.3 Small-scale bridge specimens

The replica scaled-down models of the existing bridge were reproduced by five of the small-scale beams prestressed together transversely by equally spaced external loads (see Figure 3.10) transferred to the sides of the beams via multi-directional Teflon bridge bearings, in order to minimise the friction. Measurements of friction losses showed a vertical restraint of only 2% of the lateral prestressing force.

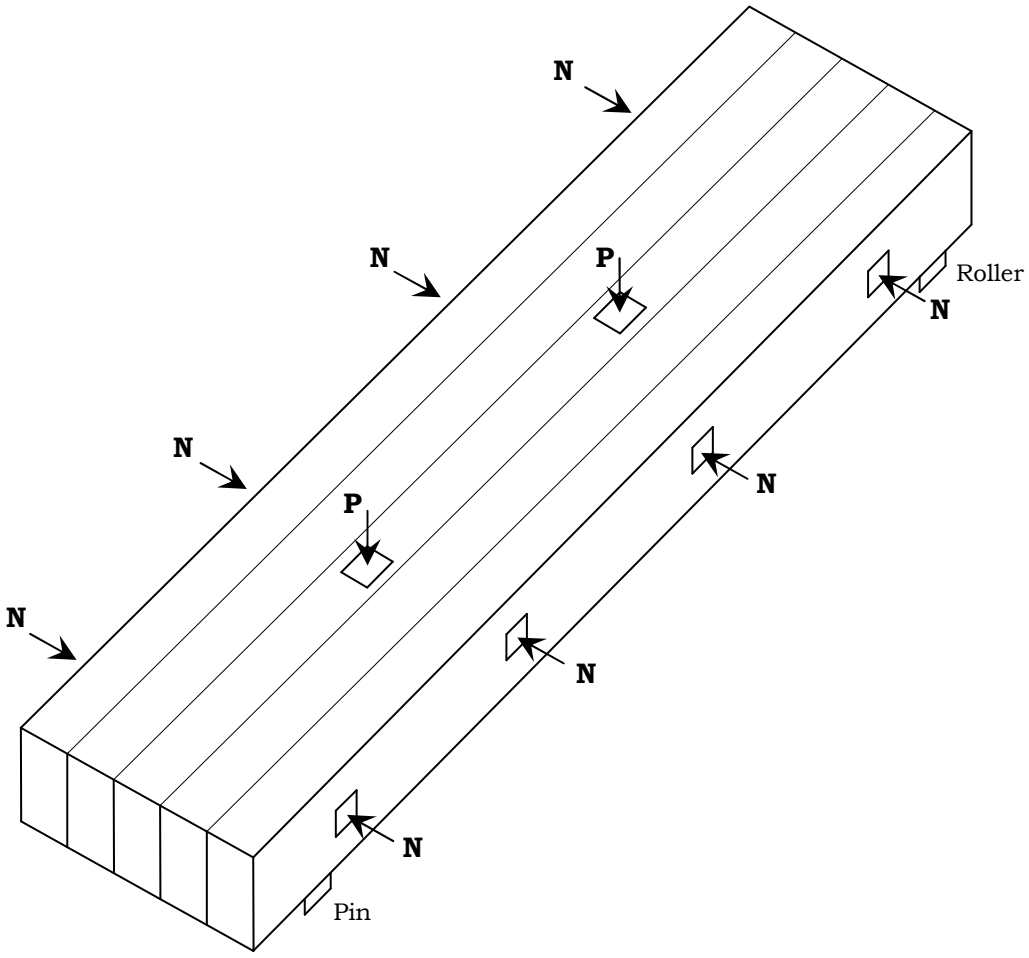

Figure 3.10: General layout of the small-scale bridges

This arrangement could provide a fairly uniform lateral pressure on the central beam, as confirmed by an elastic FE model of the deck (described in Chapter 6) and therefore reproduced well the conditions of the internal beams in the real bridges under lateral prestressing. As the purpose of the test was to investigate the contribution to the capacity offered by the lateral prestressing, a 2mm layer of fine sand was placed between the beams as a conservative representation of the actual filling material, which is cast-in concrete with better cohesive and frictional properties.

Test loads were applied on the central beam only, which is not dissimilar from the real situation, where the train load under one rail (distributed through the ballast at 15° from the vertical according to the assessment code) covers the width of one entire beam.

3.3 Test programme

3.3.1 Unstrengthened specimens

All specimens were loaded under a four-point loading system to provide constant shear within the shear span. Figure 3.11 shows the test layout for all unstrengthened specimens.

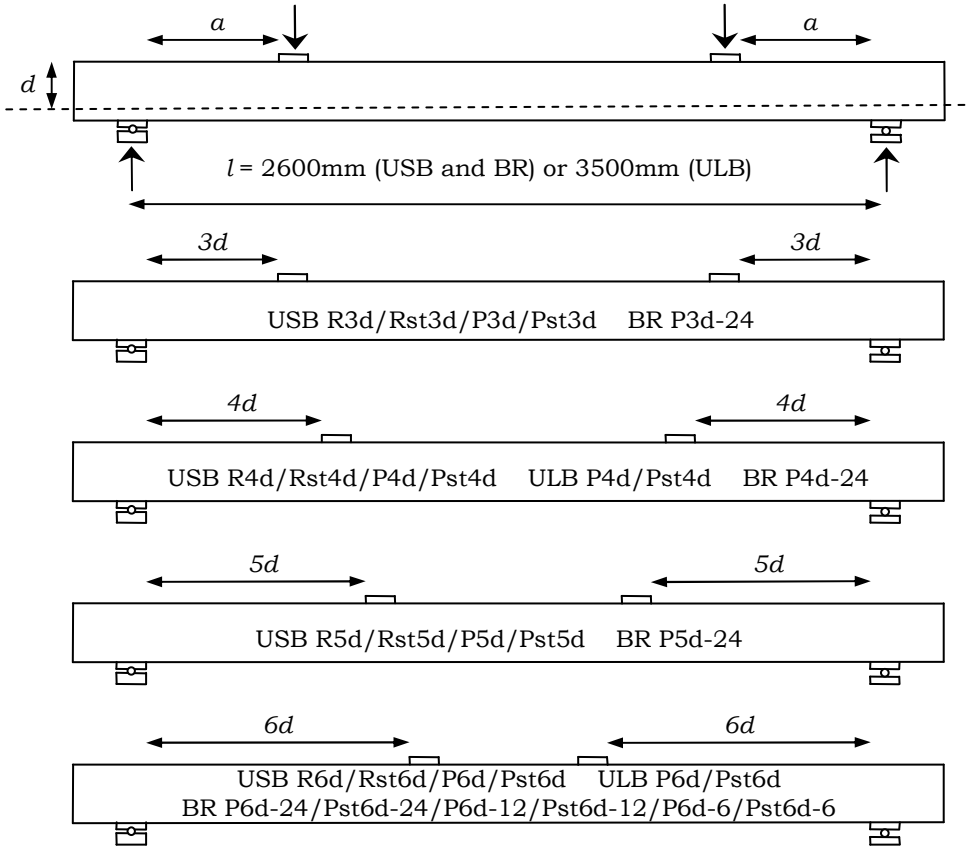

Figure 3.11: Test layout for the unstrengthened specimens

Initially, to investigate the numerous parameters involved in the shear behaviour of concrete beams, sixteen unstrengthened small-scale beams (USB) were tested at shear span lengths of 3, 4, 5 and 6 times *d* in all possible configurations, i.e. prestressed, non-prestressed, with and without stirrups, where the test notations are: P for the prestressed beams, Pst for the prestressed beams with stirrups, R for the reinforced non-prestressed beams and Rst for the reinforced non-prestressed

beams with stirrups. Four unstrengthened large-scale beams (ULB), two of them containing stirrups, were tested at 4*d* and 6*d*.

Finally, nine small-scale bridges (BR) were tested in the arrangement previously described and shown in Figure 3.10, using five prestressed small-scale beams in each case. Four bridges containing beams without stirrups were tested at 3, 4, 5 and 6*d* with a total lateral applied load of 240kN, which corresponds to a lateral stress of 0.42MPa, equal to the full level of lateral prestress in the real bridges after all losses. Three bridges containing beams with stirrups and two with beams without stirrups were then tested at 6*d*, which turned out to be the critical position from the previous tests, but with lateral pressures reduced to half (120kN) and one quarter (60kN) to simulate loss of lateral prestress on such bridges due to possibility of post-tensioning tendons becoming ineffective.

3.3.2 Bond tests for deep embedment bars

To assess the bond characteristic of the bars deeply embedded into concrete for the newly proposed strengthening technique, a series of bond tests were performed using 5 different bar types and 3 different types of adhesive.

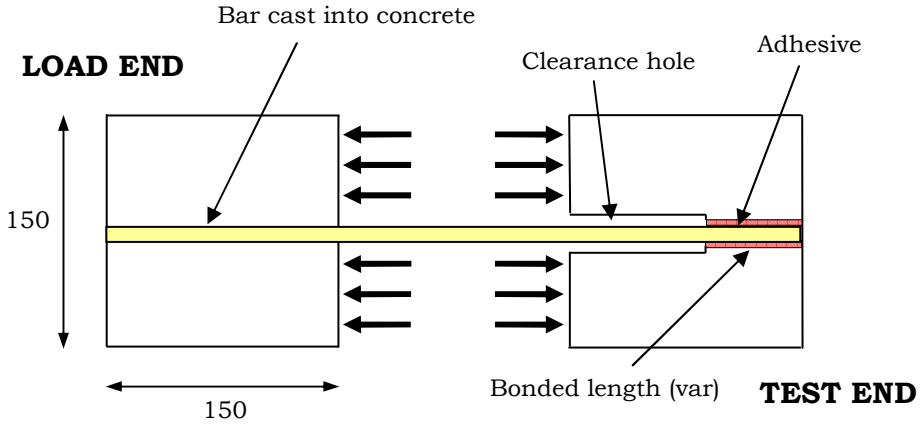

Figure 3.12: Pull out test layout

The chosen arrangement was a pull out test on cubes (see Figure 3.12), a type of short embedment anchorage length test that allows easy restraint of the loaded end of the bar without the need for a large testing unit. It is recognised that such an arrangement creates a stress state in the concrete that may be different to that in

the shear zone of the strengthened beams and may lead to slightly enhanced bond capacities. However, due to its simplicity, the ease of measurement of the bar slip and the fact that a comparison between several different parameters was sought, this test arrangement was a pragmatic compromise.

3.3.1.1 Bar types

The FRP bars used were 7.5mm diameter Arapree rods, 7.5mm Carbopree rods, 9mm Aslan GFRP rods and 6mm Aslan CFRP rods together with 8mm diameter high yield deformed steel bars (see Figure 3.13).

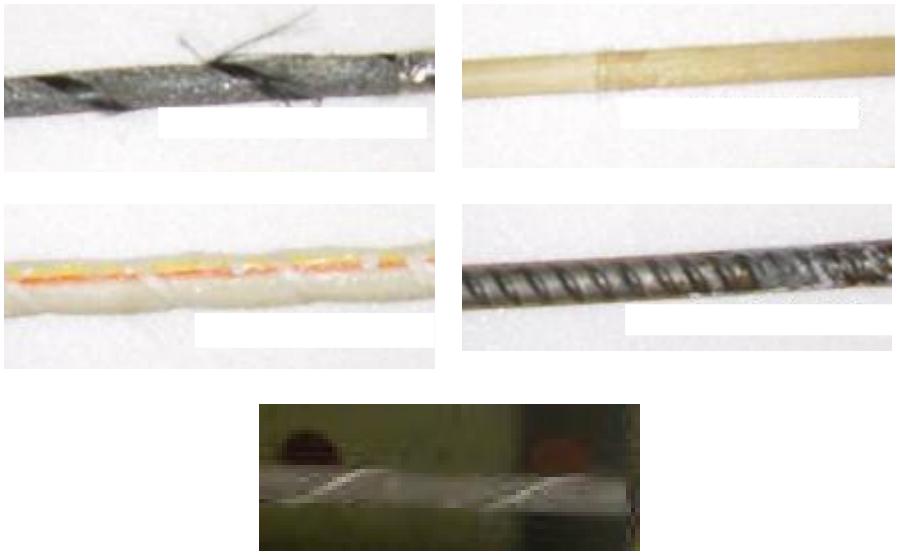

Figure 3.13: Carbopree, Arapree, Aslan GFRP, Steel and Aslan CFRP bars (Top to bottom, left to right)

Arapree and Carbopree rods are respectively aramid- and carbon-based straight bars produced by Sireg S.p.A. (2008). The surface of Arapree bars is slightly sand-coated, while Carbopree bars are spirally wound with a fibre tow and sand-coated. Aslan GFRP and CFRP rods are respectively glass- and carbon-based straight bars produced by Hughes Brothers Inc. (2008). Aslan GFRP bars are spirally wound with a fibre-tow and sand-blasted, while the CFRP bars have a surface roughened with a pre-ply treatment. Table 3.4 summarizes the properties of all FRP strengthening bars adopted as specified by the manufacturers, where f_u is the ultimate tensile strength and ε_u the ultimate strain of the bar, whose stress-strain response is linear up to failure. Properties of the steel bars used for strengthening are summarized in Table 4.1 in Chapter 4.

Table 3.4: Properties of the FRP and steel strengthening bars

Bar type	***Diameter*** (mm)	***Area*** (mm^2)	f_u (MPa)	***E*** (GPa)	ε_u (%)	***Density*** (g/m^3)
Arapree	7.5	44	1400	60	2.4	1.7
Carbopree	7.5	44	2300	130	1.8	1.7
Aslan GRFP	9	64	760	40.8	1.6	2.0
Aslan CFRP	6	28	2060	124	1.7	1.6

From laboratory tests on bar samples (described in Chapter 5) it was found that the 8mm high yield deformed steel bars adopted have a yield strength of 530MPa, elastic modulus of 200GPa and ultimate strain of 13%.

3.3.1.2 Adhesive types

Three commercially available adhesives were used for the bond tests: the Araldite LY 5052/Aradur 5052 epoxy system (Huntsman Advanced Materials, 2007), the Hilti RE-500 system (Hilti Inc., 2008a) and the Hilti HY-150 hybrid adhesive (Hilti Inc., 2008b).

Figure 3.14: Adhesive systems

The Araldite/Aradur system is a combination of a low viscosity epoxy resin and hardener normally used in the wet lay-up, moulding or filament winding processes of aerospace and industrial composites. The two components come in separate containers (see Figure 3.14) and need to be accurately weighed and mixed in the

correct proportion before application. Although the very low viscosity of this adhesive makes its application from the bottom side of a beam impractical (it will pour out before setting), it was used for comparison as it was the one adopted in a successful pilot study (Valerio and Ibell, 2003). Hilti 150 is an adhesive consisting of a methacrylate resin, hardener, cement and water that comes in a two-pack cartridge. It is applied through a mixing nozzle via an appropriate dispenser gun. It is designed for the fastening of threaded steel bars into concrete, grout or stone materials. Hilti 500 is a non-sag, high strength, two part epoxy adhesive, also supplied in a two-pack cartridge with dispenser gun and mixing nozzle (see Figure 3.14).

Table 3.5 summarizes the properties of the adhesives at room temperature as specified by the manufacturers, where σ_u is the ultimate tensile strength, ε_u is the elongation at failure and T_G is the glass transition temperature. Note that the elastic modulus E is the tensile modulus for the Araldite, the flexural modulus for the Hilti 150 and the compressive modulus for the Hilti 500.

Table 3.5: Properties of the structural adhesives (values from manufacturers)

Adhesive type	$\boldsymbol{\sigma_u}$ (MPa)	$\boldsymbol{E}$ (MPa)	$\boldsymbol{\varepsilon_u}$ (%)	$\boldsymbol{T_G}$ (°C)
Araldite (AR)	60	3450	2.0	60
Hilti 150 (H150)	15.9	7032	N/A	N/A
Hilti 500 (H500)	43.5	1493	2.0	63

3.3.1.3 Bond test programme

The pull-out tests (see Figure 3.12) were performed at five different embedment lengths for each of the five bars and the various adhesives.

Table 3.6: Programme of bond tests

Test No	**Bar type**	**Adhesive type**	**Bonded length** (mm)
1-15	7.5mm Aramid	AR/H150/H500	15/30/45/60/75
16-30	7.5mm Carbon	AR/H150/H500	15/30/45/60/75
31-45	8mm Steel	AR/H150/H500	15/30/45/60/75
46-60	9mm Glass	AR/H150/H500	15/30/45/60/75
60-65	6mm Carbon	H500	15/30/45/60/75

The selected lengths were 15, 30, 45, 60 and 75mm, a range of values that would allow assessment of the effectiveness of the system for relatively short bonded lengths and provide reassurance about the minimum bond capacities which can be relied upon in strengthening schemes. Table 3.6 shows the details of the bond test programme.

3.3.3 Strengthened specimens

Ten small-scale (SSB) and four large-scale (SLB) beams were strengthened in the shear zone with the deep embedment technique, where the choice of the adhesive (non-sag Hilti 500) and the strengthening bar type (carbon or steel) was dictated by the findings of the bond tests, discussed in Chapter 5. Figure 3.15 shows the test layout for the strengthened specimens, where the key for the layout of each specimen is described below.

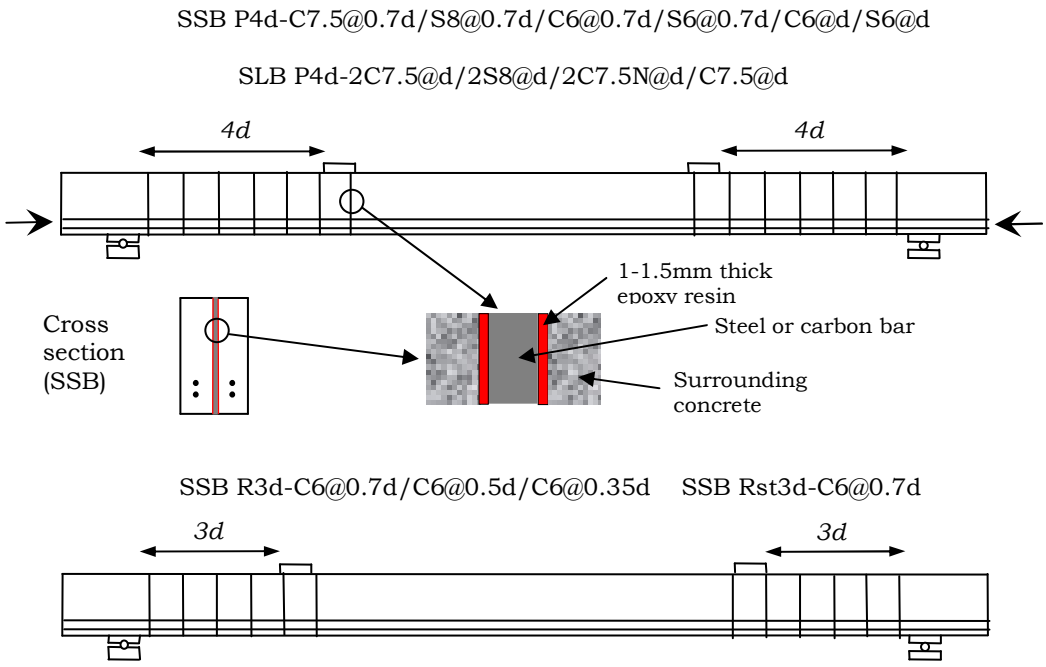

Figure 3.15: Test layout for the strengthened specimens

Six small-scale prestressed beams without stirrups (P) were strengthened with carbon (C) or steel (S) bars of 6, 7.5 or 8mm diameter spaced at 0.7*d* or *d*; four small-scale non-prestressed beams (R), one of which containing stirrups (Rst), were

strengthened using 6mm carbon bars spaced at 0.7, 0.5 and 0.35 times *d*. Four large-scale prestressed beams without stirrups (P) were strengthened using 7.5mm carbon or 8mm steel bars spaced at *d*, one of which using the near-surface mounted technique (N) for comparison.

In all the small-scale beams, only one bar was placed in each cross-section but in the case of the large-scale beams, where the width was 450 mm, the solutions with either two or one bar in each cross-section were considered. The non-prestressed beams were tested at a shear span of 3*d* where the gap between the shear and flexural capacity is greatest; the prestressed beams, for which the shear capacity may be substantially enhanced for short shear spans, were loaded at 4*d*.

3.4 Specimen preparation and testing procedure

3.4.1 Casting procedure

The small-scale specimens were cast in the laboratory of the University of Bath. The concrete mix chosen was such to obtain a mean value of the compressive cube strength of 60-65MPa, representative of the 60MPa characteristic cube strength specified for the actual bridges. As most specimens were prestressed, the concrete mix was selected to have a minimum compressive cube strength of 40MPa 3 days after casting, when the pre-tensioned wires are released, i.e. at transfer. The mix proportions were, in percentage of weight:

- Ordinary Portland cement (CEM 42.5N class) 30.0 %
- Coarse aggregate (12mm class limestone) 26.9 %
- Fine aggregate (4mm class grit) 26.9 %
- Sand 8.0 %
- Water 8.0 %
- Super Plasticizer 0.2 %

The beams were cast using a 0.3m^3 pan mixer, where one batch of concrete per beam was required (see Figure 3.16). Four control specimens were taken from each batch of concrete, consisting of 100mm cubes for the determination of the compressive strength.

Figure 3.16: Pan mixer for the casting of small-scale specimens

Figure 3.17: Static end of the casting and prestressing rig

The same formwork and casting rig were used for both the reinforced and prestressed small-scale beams. The formwork was constructed using standard lengths of steel channel sections ensuring a straight beam, a high quality surface finish and possibility of unlimited usage. For prestressing, the static end assembly of the rig was composed of an end plate and a 50mm wedge plate that was allowed to move back and forth. Two 100kN load cells were placed inside the assembly to indicate the load distribution in each wire (see Figure 3.17). The pre-tensioning

system was composed of two 75mm thick tension blocks secured together by two 30mm diameter shafts (see Figure 3.18). The load was applied by a 200kN hydraulic jack bearing against the end plate. Each wire could be stressed individually by adjusting the pre-tensioning screws.

Figure 3.18: Pre-tensioning zone of the casting and prestressing rig

Before the casting of each beam, the formwork was cleaned, all the joint edges are waxed and the surface of the formwork was greased with mineral oil. The longitudinal wires were inserted and held in place under minimum tension by using the tensioning system previously described, with the load transferred to the wires by barrel and wedge anchors. In the beams with stirrups, two 3mm diameter mild steel lengths were placed in the top zone of the formwork (passing through holes in the end plates and secured by steel barrels) to provide longitudinal support to the stirrups. Soon after pouring and compacting of the concrete with an internal vibrator, for the prestressed beams two wires were pre-tensioned to 45kN each with the hydraulic jack; the beams were left to cure under polythene sheeting for three days, the two wires were released and the beams were covered with damp cloth for another week before being removed from the casting rig and painted white the day before testing, to aid identification of cracks.

The large-scale prestressed beams were supplied by Tarmac, a UK precast manufacturer, and delivered to the laboratory of University of Bath a month after

casting. The concrete mix was selected to have a mean concrete cube strength equal to 60-65MPa after 28 days. Four 100mm cubes were taken from each beam for the determination of the compressive strength.

The 150mm cubes used for the bond tests were cast using the same pan mixer and with the same mix proportions as the beam specimens, with four 100mm cubes taken from each batch of concrete to determine the compressive strength. The two cubes required for each bond test specimen were cast into 150mm steel moulds and 450mm long strengthening bars were fully embedded in the centre of one wet cube and kept vertical until concrete has set (see Figure 3.19).

Figure 3.19: Pair of cubes for bond test after curing

3.4.2 Strengthening procedure

In the beams to be strengthened, vertical holes 2 to 3mm wider than the diameter of the strengthening bar were manually-drilled upwards from the soffit of the beam in the shear span with a diamond core rotary drill. As the maximum diameter of the holes was 12mm and the spacing of the internal prestressing reinforcement was never less than 50mm for both test specimens and actual beams, it is easy to avoid damaging the internal bars. Furthermore, it has been observed in a test sample that if the diamond core accidentally hits a reinforcing bar the sound changes and the resistance to drilling increases enormously making it virtually impossible to

proceed, so tendons can not be severed in any case. Figures 3.20 to 3.23 summarize the strengthening procedure.

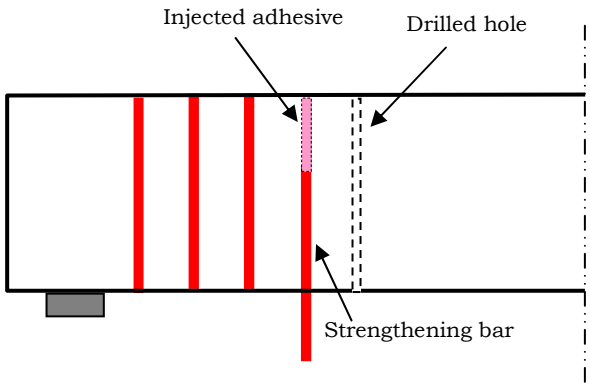

Figure 3.20: Strengthening procedure

The holes were cleaned from dust with pressurized air, the Hilti 500 non-sag adhesive was injected from the soffit with a gun dispenser and bars were inserted manually until the excess adhesive started to slowly flow out of the bottom, providing confidence that the hole was filled (see Figure 3.21). Figure 3.22 shows the strengthening layout of a large-scale beam with two bars in the cross-section, while Figure 3.23 is a close-up view of the soffit of a strengthened small-scale beam, where the bars and the surrounding adhesive are shown.

Figure 3.21: Strengthening of a small-scale beam –
Resin injection (left) and bar insertion (right)

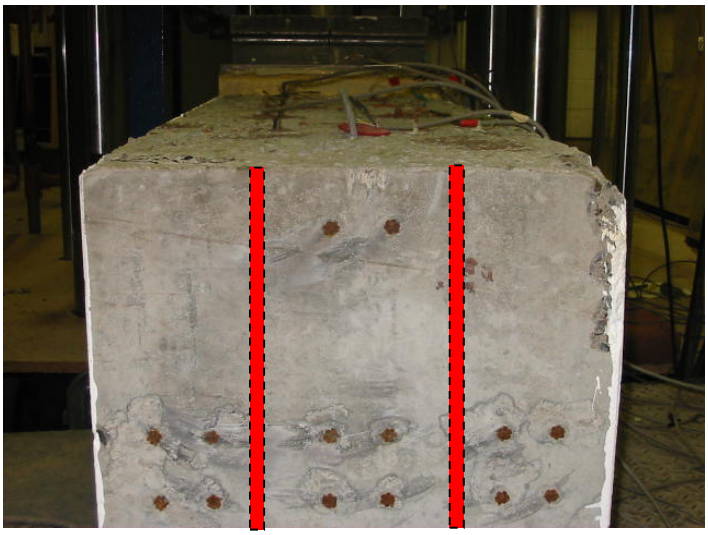

Figure 3.22: Position of the strengthening bars in the large-scale beam with two bars in the cross-section

Figure 3.23: Beam soffit after strengthening

The strengthening procedure was particularly quick and easy, especially with FRP bars due to their light weight; the bars could remain in position soon after their insertion without the need of any external support during the curing process. Hilti 500 adhesive sets after approximately 12 hours, according to the manufacturer's data (Hilti Inc., 2008a).

Harris (2004), in a research project investigating the fire resistance of epoxy-grouted steel connections in laminated veneer lumber, used the Hilti 500 adhesive to glue steel rods into timber. The examination of the rods after pull out tests showed that

sometimes air bubbles were trapped within the injected resin, thus preventing a proper load transfer between the rod and the timber and leading to reduced capacities. The problem was successfully overcome by fitting a plastic sleeve around the tip of the nozzle extension with the outer diameter slightly smaller than the diameter of the hole, so as the resin is pumped it presses onto the sleeve and forces the nozzle back out leaving no air bubbles along the hole depth. Figure 3.24 shows the arrangement used by Harris.

Figure 3.24: Custom nozzle with plastic sleeve for preventing air bubbles (after Harris, 2004)

Although in the present project this problem was not encountered in the small cubes used for the bond tests, this may be an issue in beam specimens, where it is not possible to check the presence of air bubbles in the hole. Therefore, it would be desirable that such arrangement or a similarly manufacturer-approved system is adopted in real applications to avoid this problem.

3.4.3 Testing procedure

3.4.3.1 Concrete and steel samples

All 100mm concrete cubes were tested in a Controls compression machine approximately 28 days after casting. Samples of the 7mm prestressing wires and 3mm mild steel bars used in the small-scale beams and samples of the 6mm and 8mm high yield deformed bars used for strengthening were strain-gauged and

tested in tension at a controlled constant displacement rate with a 100kN capacity Dartec tension machine (see Figure 3.25).

3.4.3.2 Bond tests

Figures 3.26 shows the setup for the 65 bond tests, also tested in the 100kN capacity Dartec machine, (with a controlled displacement rate of 3mm/min), where the two cubes were restrained by 20mm thick steel shoes. To control the bonded length of each bar, holes were drilled into the test end cubes; the diameter of the holes was 2 to 3mm wider than the bar diameter for the desired bonded length with 16mm clearance holes for the remaining unbonded length (see Figure 3.12). The depth of this clearance hole was checked using a marked rod before each test.

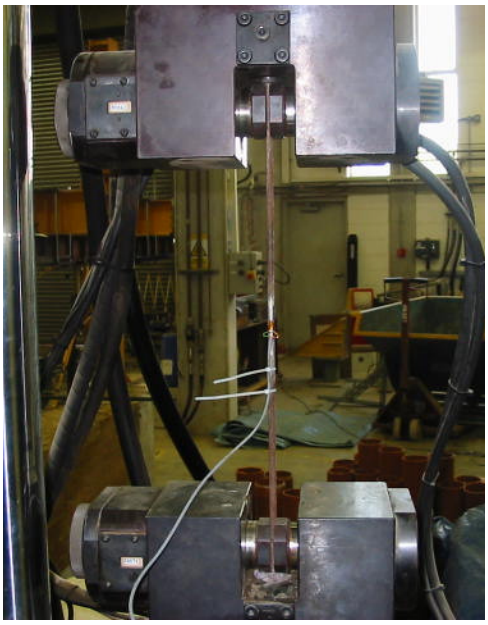

Figure 3.25: Tension test of steel samples

Figure 3.26: Bond tests setup

To further ensure that the bar remained unbonded in the clearance hole, cling film was wrapped around the bar along the length of clearance hole to provide a layer with very low interlaminar shear resistance. Strain gauges were applied at the middle of each bar and within the clearance hole length to measure the bar strain along its whole unbonded length. The bar slip at the test end was measured from the reading of a displacement transducer over a bracket attached to the bar 30mm above the top face of the cube at the test end (see Figure 3.26) after subtracting the component due to the elastic strain of the bar along the unbonded length.

3.4.3.3 Small-scale beams

The loading arrangement for the small-scale beam tests is shown in Figures 3.27 and 3.28.

Figure 3.27: Loading arrangement for the small-scale beams

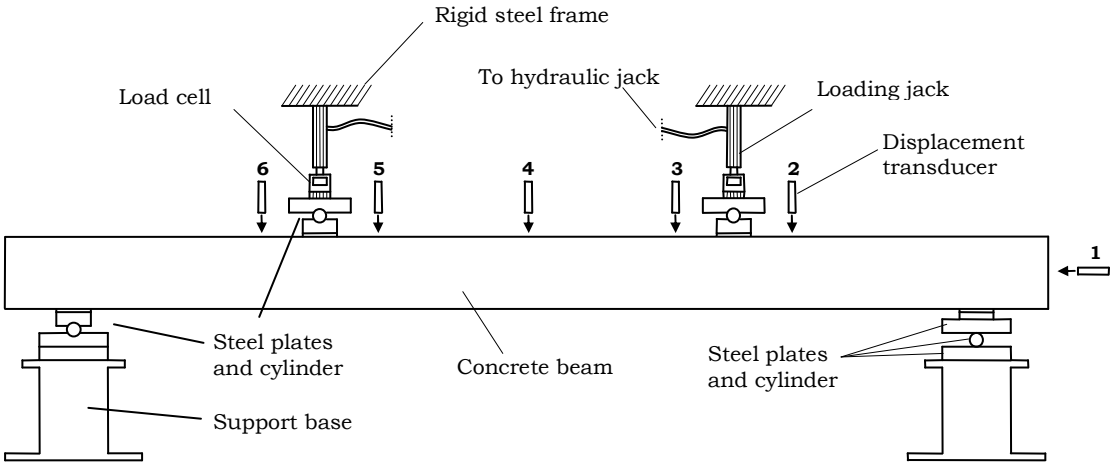

Figure 3.28: Test setup with position of the displacement gauges

The beams were supported on a pin at one end and a roller at the other. The loads were applied via 100mm wide steel plates loaded by two 100kN hydraulic jacks, whose reactions were provided by a rigid steel beam, itself supported by two rigid transverse steel frames. Two rigid steel platforms formed the base for the pinned and roller supports.

Prior to testing, six displacement transducers were positioned on each specimen, four in the proximity of the two loads, one in the middle of the beam and one at the roller (see Figure 3.28). The beams were loaded monotonically until failure and crack patterns were marked at intervals throughout the testing procedure. Readings from the displacement transducers were taken every second with a Measurement Group data logger connected to a computer.

3.4.3.4 Small-scale bridges

As previously described, each small-scale bridge consisted of five simply supported prestressed small-scale beams stressed together laterally through eight free sliding Teflon bearings, which were loaded by hydraulic jacks on one side and, on the other side, reacted against the wall through a rigid steel box beam (see Figures 3.29 and 3.30). The lateral loads were kept constant during each test providing a fairly uniform pressure on the central beam, as confirmed by a FE analysis (see Chapter 6), and therefore reproducing the stress state of an internal beam in the actual bridges.

Prior to lateral prestressing, the small lateral gaps between the beams, of the order of 2-3 millimetres, were filled with fine sand (see Figure 3.30) which was poured from the top before the lateral stressing and was prevented from dropping through by a thin strip of silicon applied longitudinally along the bottom of the gaps between beams. A preliminary test on a small-scale bridge with no lateral loads applied confirmed that the thin silicon strips failed at low loads and therefore did not offer any additional unwanted restraint to the system. The vertical loads were applied on the central beam via 100mm wide steel plates loaded by two 200kN hydraulic jacks. Twelve displacement transducers were positioned on each specimen; six were placed on the central beam, in a similar arrangement to the single beams, and the other six were placed in the middle of the remaining four beams and in the proximity of the applied load to investigate the distribution of the vertical deflections both longitudinally and transversely.

Figure 3.29: Test setup for the small-scale bridges

Figure 3.30: Lateral view of the setup for the small-scale bridges

3.4.3.5 Large-scale beams

The large-scale beams were tested in a four point loading arrangement using a 2000kN Dartec machine with load applied under displacement control (see Figures

3.31 and 3.32). A steel spreader beam was used to transfer the loads between the load machine reaction plates and the concrete beam. Six displacement transducers were positioned in the middle and in the proximity of the two loads at both sides of the spreader beam, to assess differential displacements, if any, across the beam width.

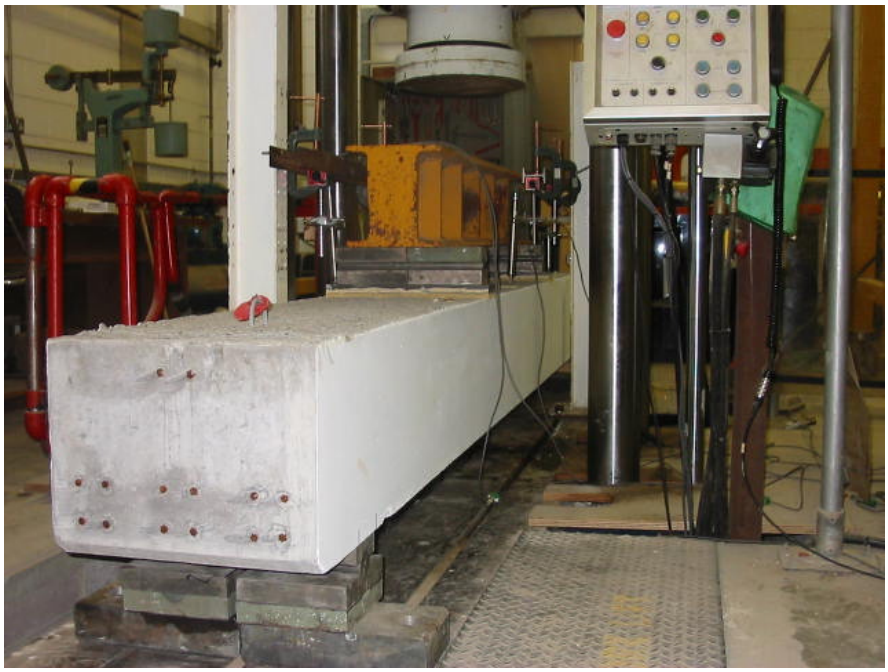

Figure 3.31: Test setup for the large-scale beams

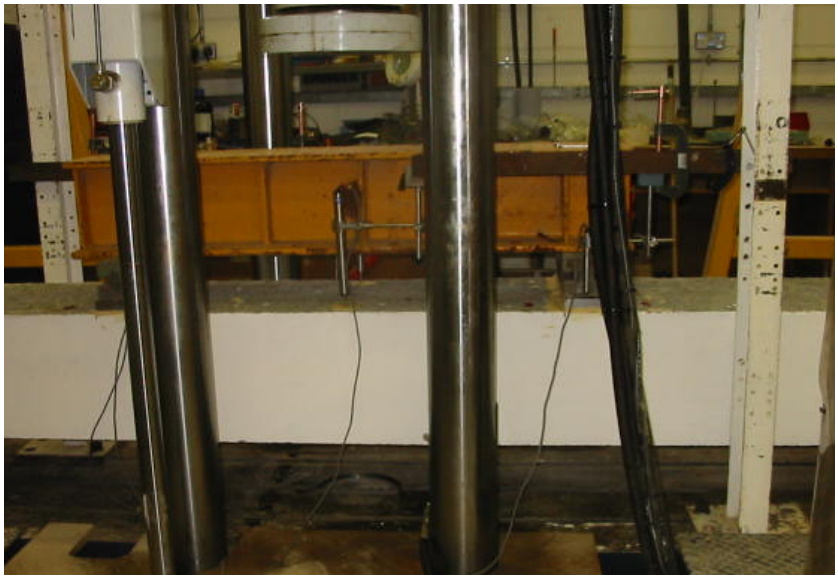

Figure 3.32: Steel spreader beam and displacement transducers

For the case of both the NSM- and deep embedment-strengthened large-scale beams, each strengthening bar was provided with three strain gauges along its length connected, together with the displacement transducers, to a Measurement Group data logger with readings taken every second (see Figures 3.33 to 3.36).

Figure 3.33: Strain gauges in the carbon bars

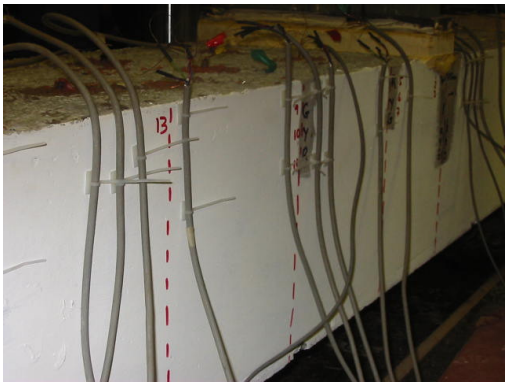

Figure 3.34: Strain gauge connections

Figure 3.35: NSM bar

Figure 3.36: Strain gauges in the NSM test

Chapter 4
Test Results and Discussion - Unstrengthened Specimens

4.1 Introduction

The results of the laboratory testing on the unstrengthened specimens designed and described in Chapter 3 are summarised in the following sections, with accompanying photographs and plots. They comprise the material tests on concrete and steel samples and the main tests on the unstrengthened small-scale beams, large-scale beams and bridges.

A quantitative analysis of the data is also provided, by comparing the test results with the predictions according to the current Network Rail assessment standard NR/GN/CIV/025 (2006) and the Eurocode 2 (2004), whose equations have been described in detail in Chapter 2.

4.2 Tests on concrete and steel samples

Four 100mm cube control specimens were taken from each batch of concrete used for the 150mm bond test cubes and from each batch used for the small-scale and large-scale beams. They were tested in compression on the same day of the corresponding main specimen test. The mean compressive strength of the cubes laid between 58 and 64MPa for all tests, in good agreement with the value of 60MPa originally planned.

Tensile tests were carried out on the 7mm prestressing wires and 3mm mild steel bars used in the small-scale beams and the 6mm and 8mm high yield deformed bars used for strengthening. Figure 4.1 shows the results of all tensile tests on the steel samples. Table 4.1 summarises the average values of the stress at rupture, the stress at yield, the ultimate strain and yield strain for the different bar types. Note that, for the prestressing wires, f_y is the 0.1% proof stress.

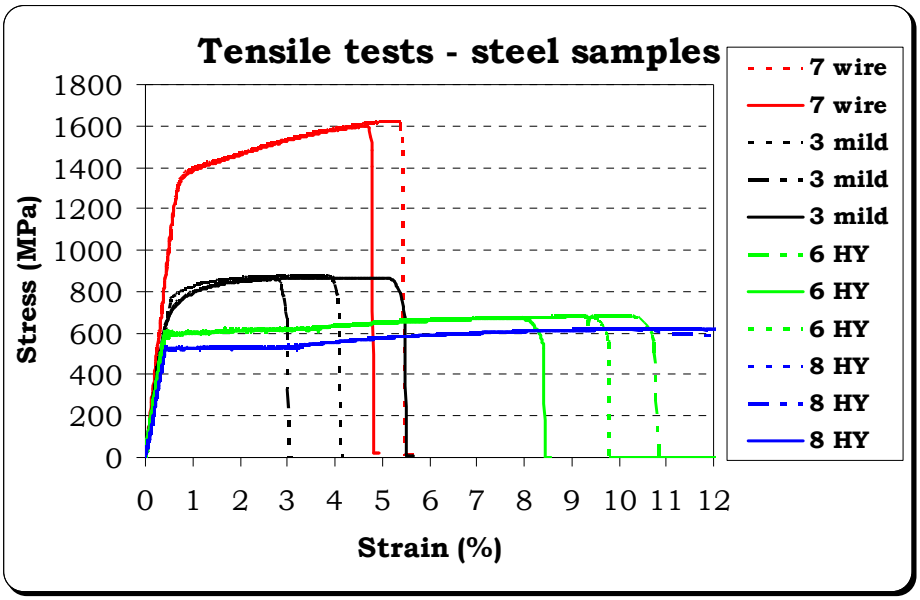

Figure 4.1: Stress-strain plots for the steel samples tested in tension

Table 4.1: Average properties of the steel bars from tensile test

Steel Type	7mm wire	3mm mild	6mm HY bar	8mm HY bar
f_u (MPa)	1610			
f_y (MPa)	1350	700	575	530
ε_u (%)	5.3	4.0	9.8	13.0
ε_y (%)	0.78	0.35	0.2875	0.265

4.3 Small-scale beams (USB)

As described in Chapter 3, sixteen small-scale beams, prestressed and non-prestressed and with and without stirrups, were tested in shear at 3, 4, 5 and 6 times the effective depth. All specimens were loaded under a four-point loading system and the value of the 'applied load' is always per jack; therefore, the total load applied on each specimen was actually double of the value reported in the following description and plots.

4.3.1 Specimens tested at 3d

Figures 4.2 to 4.5 show the failure of the four specimens tested at a shear span equal to 3*d*. In the non-prestressed specimens, the first flexural cracks started to appear in the middle constant moment zone at an applied load of about 6kN,

propagating upwards as load was increased. Flexural cracks then formed over a wider area until a load of 22.5kN, when diagonal shear cracks appeared in both shear zones. Specimen USB R3d, without stirrups, failed in brittle shear at 23.5kN on the left side span (see Figure 4.2), while specimen USB Rst3d, containing stirrups, sustained load until shear failure occurred at 31.5kN (see Figure 4.3).

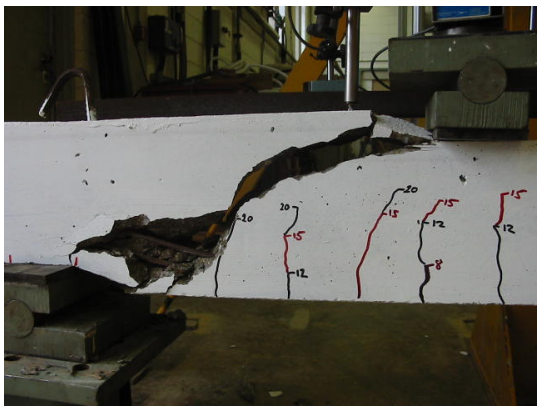

Figure 4.2: USB R3d at failure

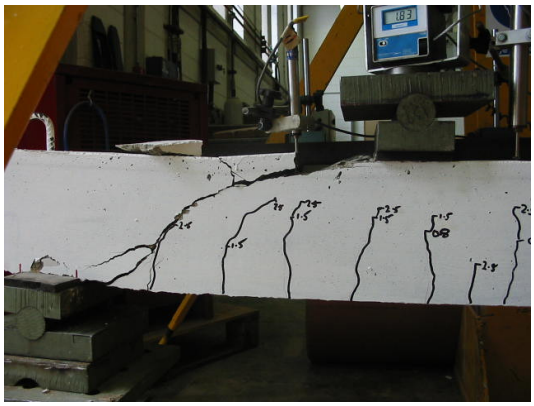

Figure 4.3: USB Rst3d at failure

Figure 4.4: USB P3d at failure

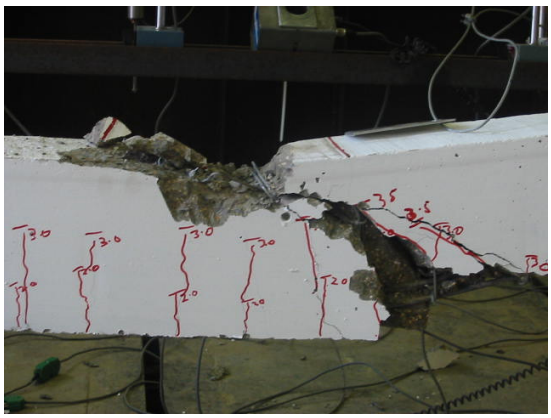

Figure 4.5: USB Pst3d at failure

In both prestressed specimens, flexural cracks appeared at a load of approximately 18kN in the middle zone and diagonal shear cracks formed in the shear spans at 34.5kN. In contrast to the non-prestressed case, collapse did not occur suddenly after the shear cracking. The critical shear cracks on each of the shear spans increased considerably in width and both beams kept sustaining load and substantial deflections until brittle shear failure occurred at 54.4kN and 54.5kN for the USB P3d and USB Pst3d, respectively (see Figures 4.4 and 4.5).

Figure 4.6 shows the load-deflection plot at mid-span for the four specimens, where the loss of stiffness due to the flexural cracking and the brittleness of the failure are evident.

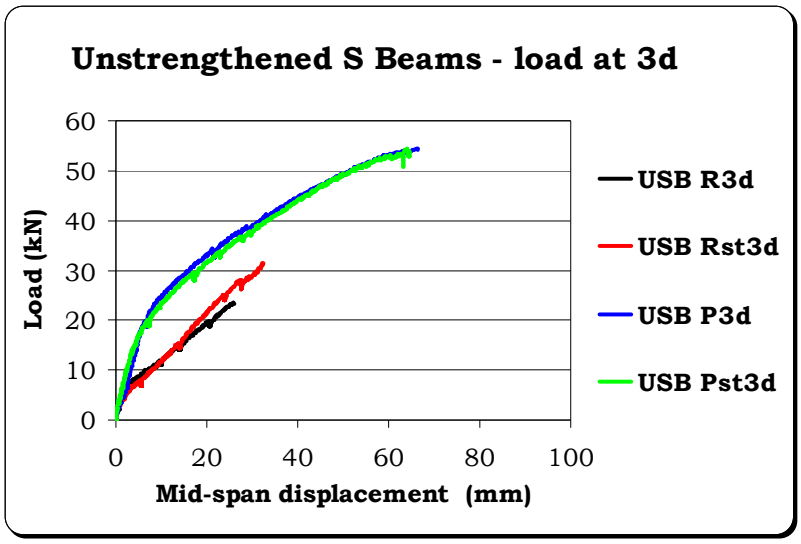

Figure 4.6: Load-displacement plot for the USB specimens loaded at 3d

4.3.2 Specimens tested at 4d

Photographs of the specimens tested at a shear span of 4*d* are shown in Figures 4.7 to 4.10, with Figure 4.11 showing the load-displacement plot. In the non-prestressed specimens, the first flexural cracks formed at an applied load of about 5.5kN, increasing in width and number as load was increased. Diagonal shear cracks appeared in the shear spans at 23kN for both specimens.

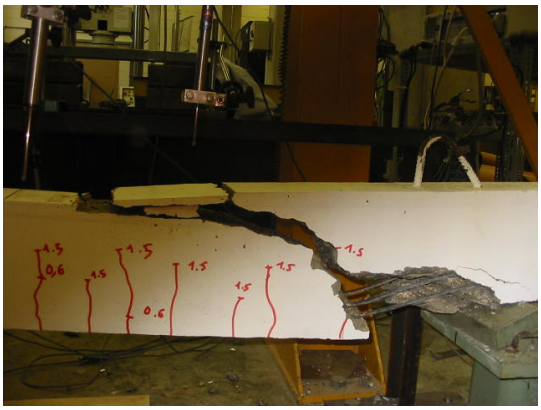

Figure 4.7: USB R4d at failure

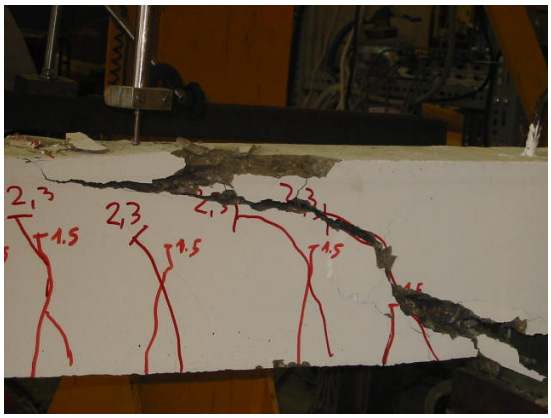

Figure 4.8: USB Rst4d at failure

Specimen USB R4d failed in brittle shear at 25.2kN on the right side span (see Figure 4.7), while the shear cracks in specimen USB Rst4d grew in width until shear failure occurred at 33.8kN (see Figure 4.8). In the two prestressed specimens, the first flexural cracks formed at 15kN in the central zone, with diagonal shear cracks appearing at 30kN. Brittle shear failure occurred on the right side of specimen USB P4d at 37.9kN (see Figure 4.9). Specimen USB Pst4d sustained load until it failed in ductile flexure at an applied load of 46.4kN (see figure 4.10).

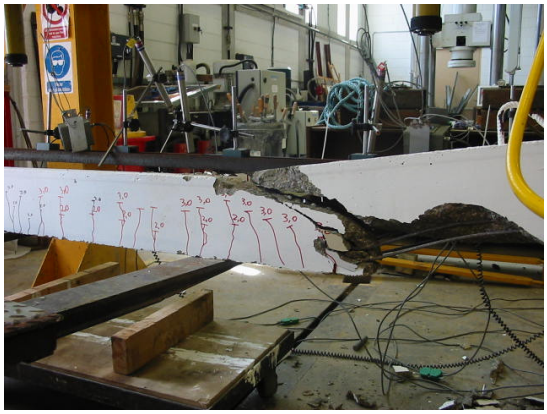

Figure 4.9: USB P4d at failure

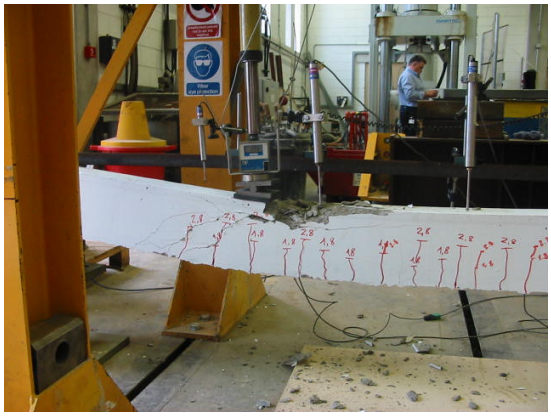

Figure 4.10: USB Pst4d at failure

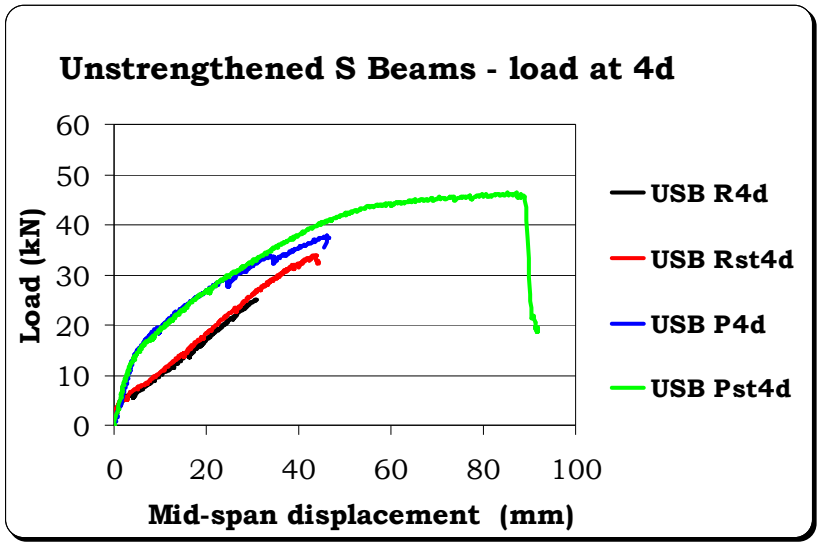

Figure 4.11: Load-displacement plot for the USB specimens loaded at 4d

4.3.3 Specimens tested at 5d

In the RC specimens with a shear span of 5*d* (see Figures 4.12 and 4.13), the first flexural cracks appeared in the central zone at an applied load of 4kN, while the

first shear cracks were noted after the load reached approximately 20kN. Both specimens failed in shear; USB R5d, without stirrups, reached a peak load of 21.4kN while USB Rst5d, with stirrups, failed at 28.3kN.

Figure 4.12: USB R5d at failure

Figure 4.13: USB Rst5d at failure

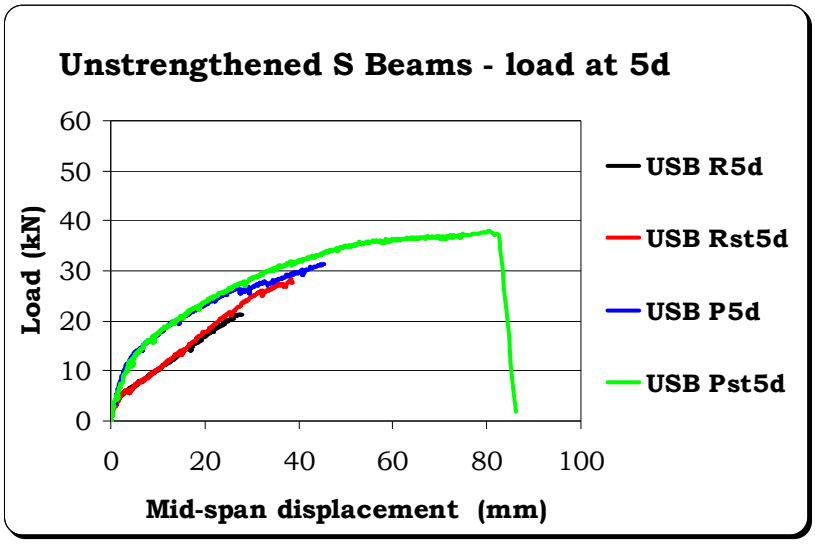

Figure 4.14: Load-displacement plot for the USB specimens loaded at 5d

In the prestressed beams USB P5d and USB Pst5d (see Figures 4.15 and 4.16), the flexural cracks in the constant moment central zone appeared at an applied load of 12kN. In both specimens, the first diagonal shear cracks formed when the load approached 26kN. Diagonal shear failure occurred in the left side span of specimen USB P5d at 31.4kN, while the stirrups in specimen USB Pst5d were effective in leading the beam to a ductile flexural failure at an applied load of 37.9kN. Figure 4.14 shows the load-deflection plot for the four beams.

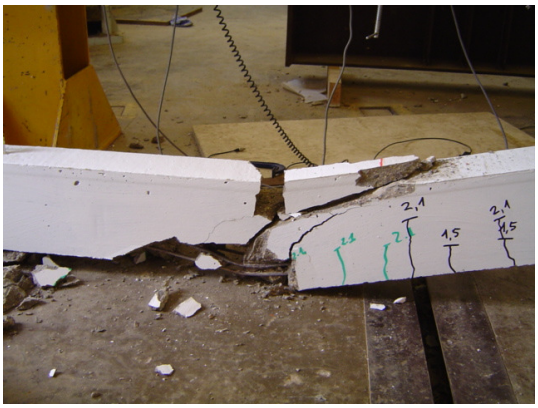

Figure 4.15: USB P5d at failure

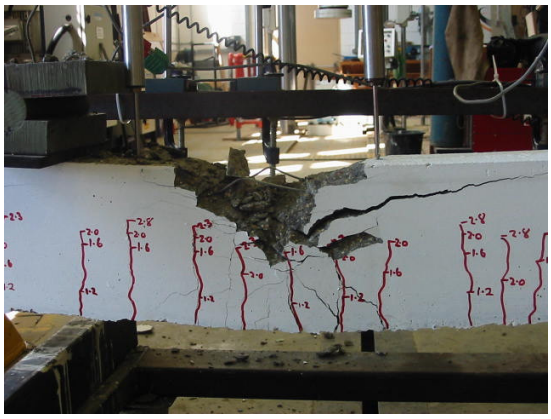

Figure 4.16: USB Pst5d at failure

4.3.4 Specimens tested at 6d

The specimens tested at 6*d* are shown after failure in Figures 4.17 to 4.20, while Figure 4.21 shows their load-displacement behaviour. Flexural cracks in the non-prestressed specimens formed at an applied load of just 3kN, increasing in width and number as load was increased. Diagonal shear cracks appeared in the shear spans at 20kN for both specimens. Specimen USB R6d then failed in shear at a applied load on the jack of 21.7kN (see Figure 4.17), while the stirrups in specimen USB Rst6d increased the beam shear capacity up to 28.4kN (see Figure 4.18).

In the prestressed beams, the first flexural cracks formed at 10kN; at load of 23kN diagonal shear cracks started to form in both shear spans. Specimen USB P6d failed in shear at 28.5kN in a very brittle fashion (see Figure 4.19), while specimen USB Pst6d, containing stirrups, failed in a mixed flexural-shear mode, in a much more ductile manner, at a load of 31.2kN (see Figure 4.20).

Figure 4.17: USB R6d at failure

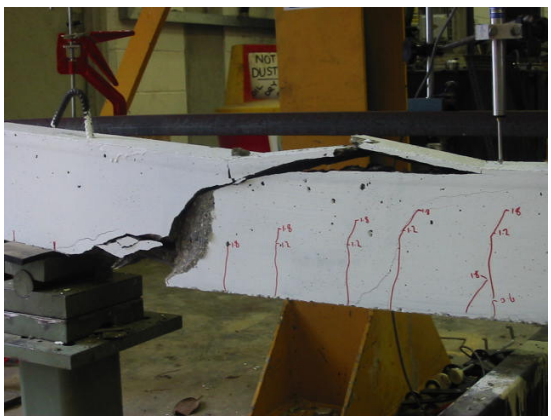

Figure 4.18: USB Rst6d at failure

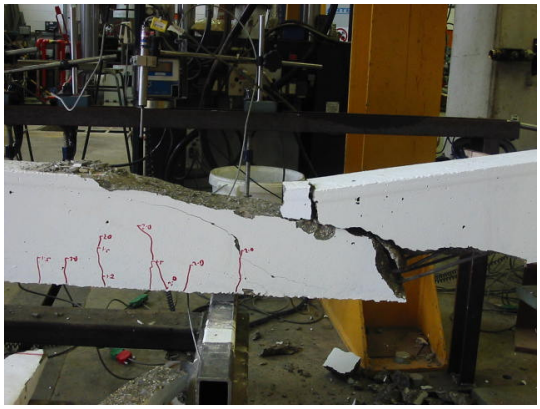

Figure 4.19: USB P6d at failure

Figure 4.20: USB Pst6d at failure

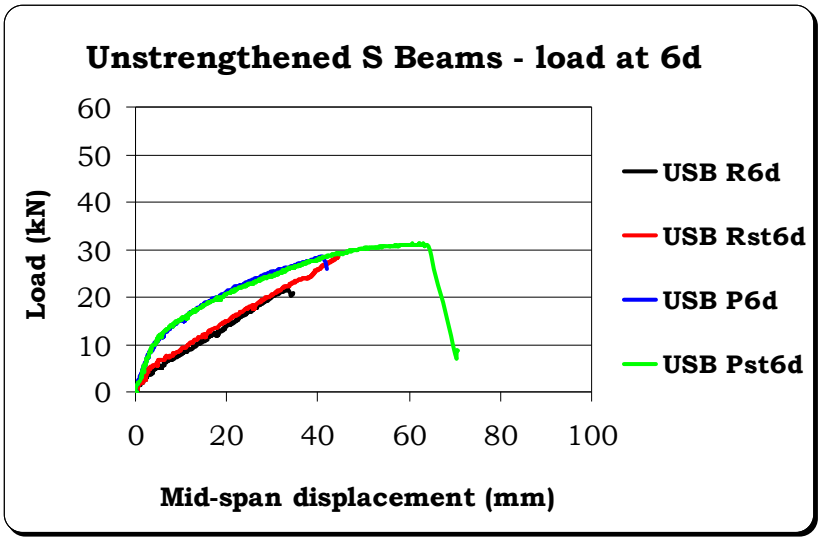

Figure 4.21: Load-displacement plot for the USB specimens loaded at 6d

4.3.5 Discussion

Figures 4.22 to 4.25 show the load-displacement plots grouped to represent all specimens of a similar type (RC, RCst, PSC and PSCst), at each shear span.

From the observation of the test results and plots the following remarks can be made:

- In each pair of beams, with and without stirrups, loaded at the same span to depth ratio, whether prestressed or not, the first flexural cracks (in the

central zone) and diagonal shear cracks (in the shear spans) always occurred at the same value of the applied load. The stiffness of the pairs of specimens was also the same until the first diagonal shear cracking occurred. This confirms that the presence of stirrups does not affect the cracking pattern and the stiffness of the beams before diagonal shear cracking, i.e. they only come into play once shear cracks occur acting as a tie to the shear cracks and delaying ultimate failure.

- The four RC beams without stirrups, which all failed in shear, behaved similarly in terms of peak load and maximum deflection. The failure load in all cases was only slightly higher (less than 10%) than the first shear cracking load, demonstrating that for a non-prestressed beam without stirrups the first shear cracks initiate beam collapse. A reduction in the failure load of about 15% was noted for the beams loaded at 5*d* and 6*d* when compared to the ones loaded at 3*d* and 4*d*, showing a tendency for the ultimate shear failure load to decrease with the increase of the shear span length (see Figure 4.22).

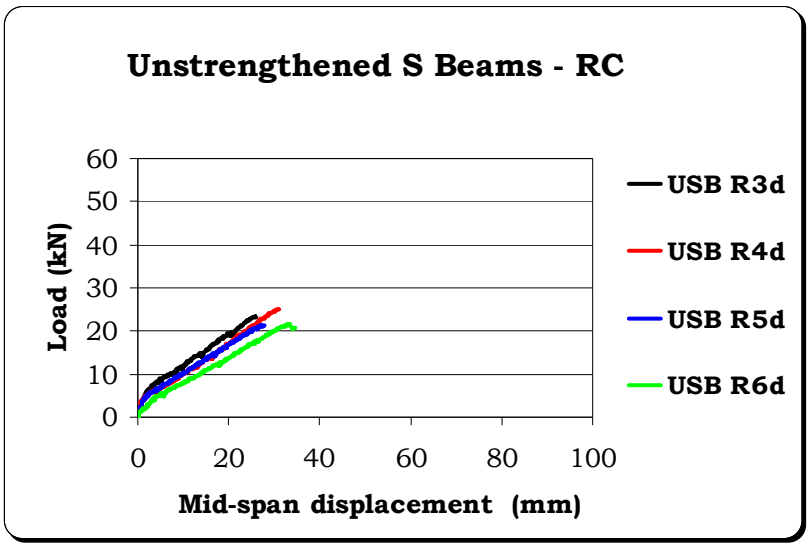

Figure 4.22: Load-displacement plot for the USB RC specimens

- The four RC beams with stirrups, which again failed in shear, behaved similarly in terms of peak load and maximum deflection and showed an average increase of shear capacity of 7.6kN when compared to the plain specimens, due to the presence of stirrups. A slight reduction in stiffness

was observed in the specimens with longer shear spans, as expected (see Figure 4.23).

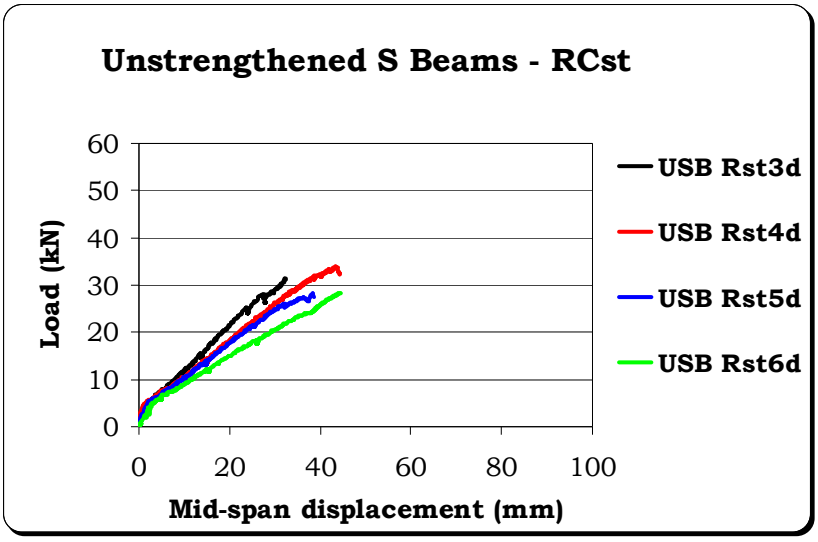

Figure 4.23: Load-displacement plot for the USB RCst specimens

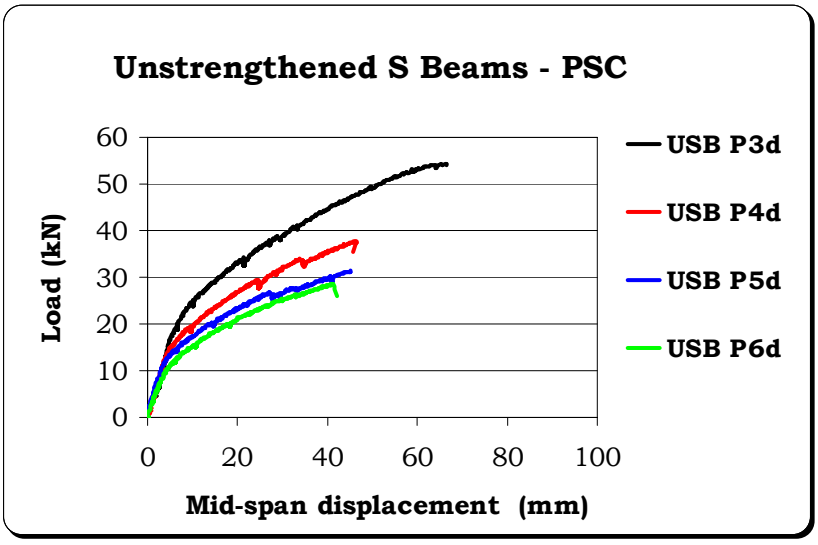

Figure 4.24: Load-displacement plot for the USB PSC specimens

- The PSC beams without stirrups all failed in shear, but with notable differences in terms of peak load and stiffness (see Figure 4.24). A greater enhancement in stiffness and load capacity was observed as the shear span length reduced. The peak load ranged from 28.5kN for a shear span length $a = 6d$ to 54.4kN for $a = 3d$, a remarkable 90% increase. When compared

with the equivalent non-prestressed beams, the enhancement in shear capacity due to the prestressing was 32% at 6*d* and 131% at 3*d*. In contrast to the RC beams, the shear capacity for these PSC beams was higher than the first diagonal shear cracking load (especially for short shear spans), showing that for prestressed beams the arching action described in Chapter 2 can be substantial even for slender members.

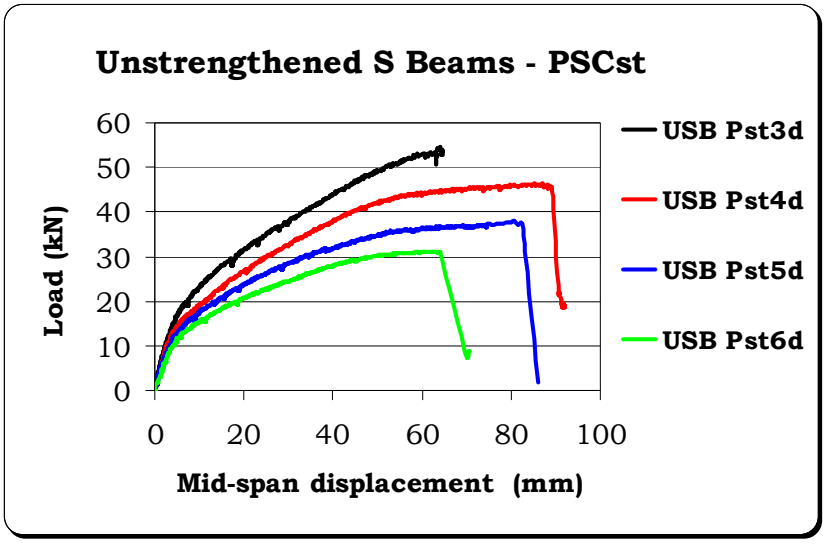

Figure 4.25: Load-displacement plot for the USB PSCst specimens

- The PSC beams with stirrups all failed in flexure apart from the one loaded at 3*d*, which failed in shear at the same ultimate load of the equivalent beam with no stirrups. Despite their low percentage, the effectiveness of the stirrups in the specimens loaded at 4, 5 and 6*d* is proved by the fact that the failure mode changed from brittle shear to ductile flexure (see Figure 4.25). The lack of enhancement of capacity in specimen USB Pst3d was due to the fact that, for prestressed beams, at a shear span of 3*d* the arching action proved to be dominant and at such high levels of load the stirrup contribution is not additive, as the stirrups come into play soon after formation of the diagonal shear cracks; the gap between the diagonal shear cracking load and the ultimate load was about 20kN, in excess of the capacity of the stirrups. Specimen USB Pst6d confirmed the criticality of slender beams in shear, as the failure of this specimen was in fact of a mixed flexural-shear type.

4.4 Small-scale bridges (BR)

Nine small-scale bridges, each made of five prestressed small-scale beams, were tested in shear as described in Chapter 3. These tests allowed the investigation of parameters such as the shear span length and the presence of stirrups in relation to the level of lateral prestressing.

4.4.1 Shear tests on the filling material between the beams

As discussed in Chapter 3, a 2-3mm layer of fine sand was placed between the small-scale beams to render the contact surface and the lateral pressure between beams as even as possible. This represents a conservative approximation of the real situation where cast-in concrete is present between beams and the dowel action of the post-tensioning bars contributes to the resistance of the shear key.

In the laboratory of soil mechanics of the University of Bath, direct shear tests were performed using the 'shear box' apparatus on the sand adopted for four different level of applied normal stress, to obtain the internal friction angle of this filling material for the various levels of lateral prestressing present on the side face of the central beam. The angle of friction was found to vary from 28° (for a normal stress corresponding to the full lateral loading) to 36° (for a normal stress corresponding to the lateral load reduced to a quarter), with an average value of 32°.

4.4.2 Specimens with full lateral prestressing

The four specimens without stirrups and the one with stirrups were prestressed laterally with a total force of 24t (giving an average lateral stress in the central beam equal to the full stress in the real bridges after all losses) and loaded on the central beam at 3, 4, 5 and 6*d*. Generally, all specimens behaved elastically as a whole slab until the loss of static friction between the central beam and its two neighbouring beams took place; after that, the stiffness of the central beam began to decrease and the failure mechanism developed in the central beam only. In all specimens, the four beams either side of the central beam recovered elastically after the vertical load was released and appeared to be virtually undamaged.

Figures 4.26 shows specimen BR P3d-24, loaded 3*d* from the support, at failure, while Figure 4.27 depicts the shear-failed central beam after the two neighbouring

beams on the right hand side have been removed. The load-displacement plot for the five beams of this specimen is presented in Figure 4.28.

Figure 4.26: BR P3d-24 at failure

Figure 4.27: Central beam of BR P3d-24 after failure

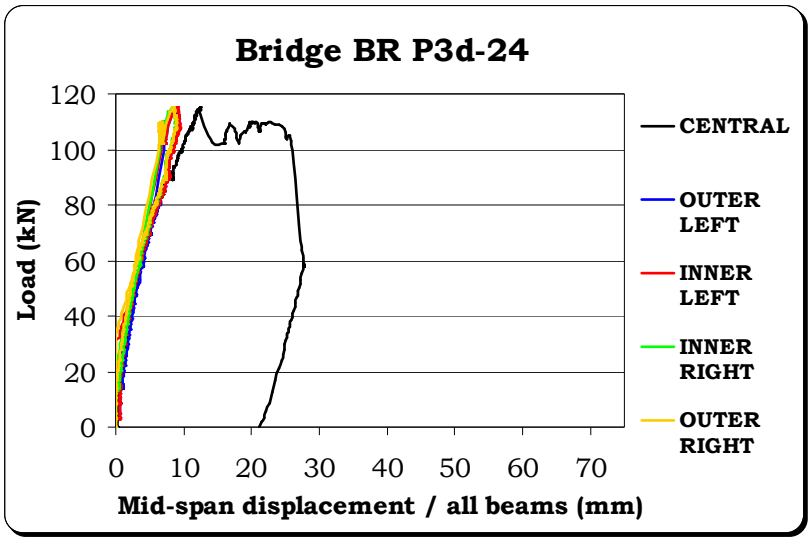

Figure 4.28: Load-displacement plot for the BR P3d-24 specimen

The five beams of specimen BR P3d-24 all behaved similarly until the first sound of cracking could be heard at a load level on each jack of about 80kN, due to the peeling off of the top concrete surface of the central beam. At a load of 91.7kN the central beam started to deflect independently after the loss of static friction with its two neighbouring beams (see Figure 4.28); this led to a loss of stiffness and increased deflection rate until a relatively ductile shear failure, with signs of crushing in the compression zone, occurred in the central beam at 115.4kN, with

an increase of 112% over the shear capacity of the equivalent single beam loaded at 3*d* (USB P3d).

Figures 4.29 to 4.31 show the load-deflection plots and photographs at failure for the other three specimens without stirrups with full lateral prestressing.

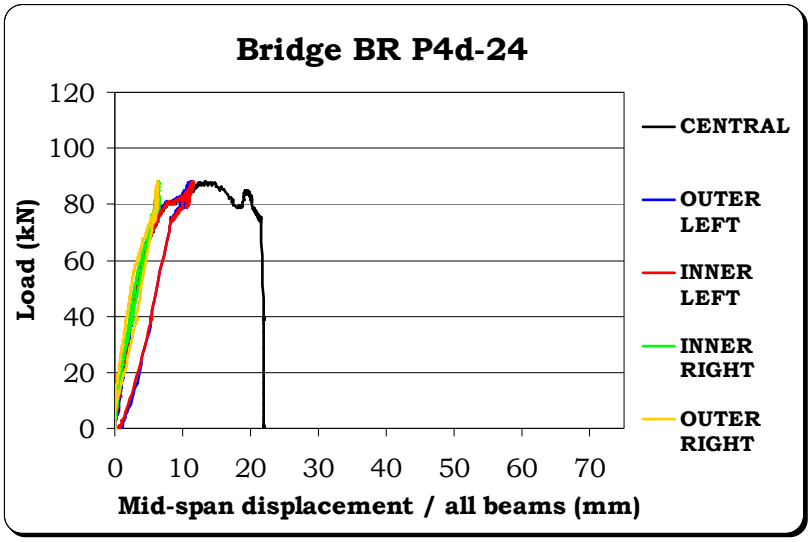

Figure 4.29: Load-displacement plot for the BR P4d-24 specimen

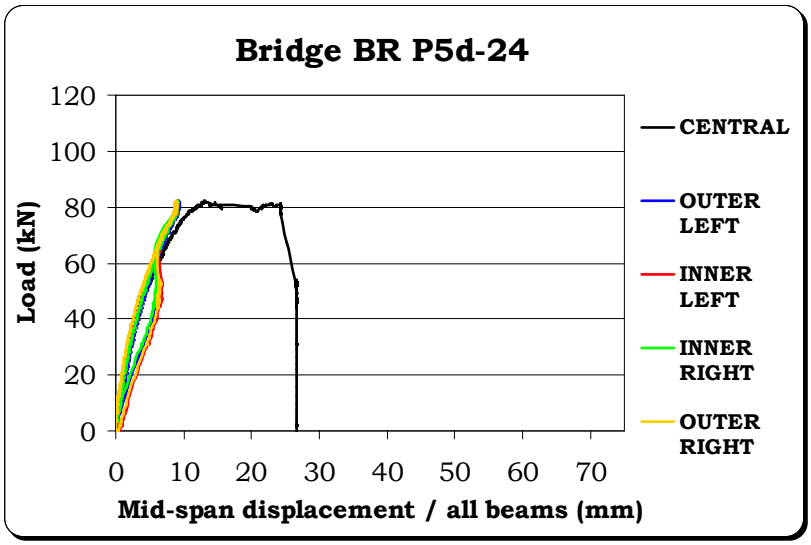

Figure 4.30: Load-displacement plot for the BR P5d-24 specimen

In specimen BR P4d-24, loaded 4*d* from support, the loss of static friction between the central beam and its neighbouring beams occurred at 79.8kN, followed by the central beam failing in shear at 88.0kN (see Figure 4.32), with an increase in shear

capacity of 132% over the equivalent single beam (USB P4d). In BR P5d-24, loaded 5*d* from the support, the central beam began to deflect independently from the others at 63.9kN and failed in shear at 82.0kN, although the peak load was sustained in a ductile manner and the beam's maximum displacement was almost 30mm (see Figures 4.33 and 4.34). This represented a remarkable 162% increased capacity compared to the equivalent single beam (USB P5d).

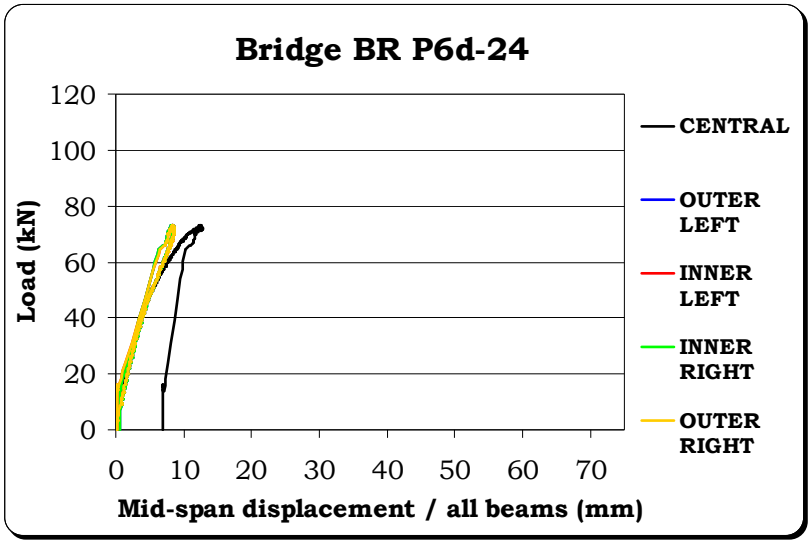

Figure 4.31: Load-displacement plot for the BR P6d-24 specimen

Figure 4.32: Central beam of BR P4d-24 after failure

Figure 4.33: Central beam deflection in BR P5d-24

The central beam in specimen BR P6d-24, loaded 6*d* from the support, suffered loss of friction at 55.4kN and collapsed in a mixed flexural-shear mode at a load of 73.1kN, a 156% increase over the single beam (USB P6d). It should be noted that the failure was ductile and not brittle as it appears on the load-deflection plot of

Figure 4.31; the post-peak behaviour could not be plotted properly as the transducer became stuck under a concrete fragment which was considered dangerous to remove just before the explosive collapse of the specimen. When the load approached 67kN, the top concrete surface of the central beams started to crush in compression, but the beam was able to sustain increased loading until an explosive shear collapse occurred in the right hand span (see Figure 4.35).

Figure 4.34: Central beam of BR P5d-24 after failure

Figure 4.35: Central beam of BR P6d-24 after failure

Figures 4.36 to 4.38 refer to the specimen BR Pst6d-24, loaded at 6*d* and containing stirrups, whose behaviour was very similar to the equivalent bridge specimen without stirrups, with the loss of static friction to the central beam occurring at a load of 57.5kN and the top concrete surface starting to crush in compression at 66kN.

Figure 4.36: Central beam of BR Pst6d-24 at failure

Figure 4.37: Shear crack in BR Pst6d-24 after failure

When the load reached 67.5kN, the beam suddenly collapsed explosively due to the formation of an extremely wide shear crack in the left span (see Figure 4.37), of the order of 20mm, which could not be contained by the stirrups. The increase of capacity over the equivalent single beam (USB Pst6d) was 117%.

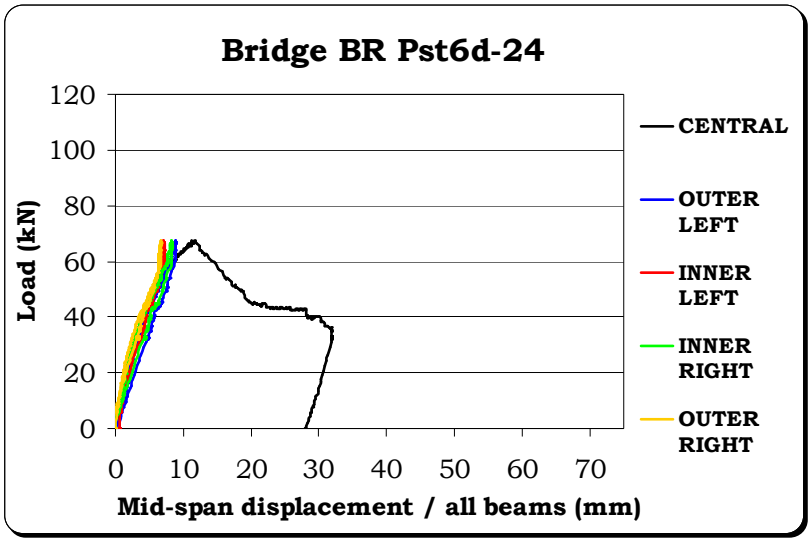

Figure 4.38: Load-displacement plot for the BR P6d-24 specimen

4.4.3 Specimens with reduced lateral prestressing

To assess the effect of a loss of the lateral pressure in the real beams due to the eventuality of some of the post-tensioning tendons becoming ineffective, four tests were performed with load applied at 6*d*, the critical span length, with the lateral load reduced to half (12t) and a quarter (6t) of the full load. Bridges both with and without stirrups were tested.

Figure 4.39: BR P6d-12 at failure

Figure 4.40: Central beam of BR P6d-12 after failure

Figures 4.39 to 4.48 show photographs at failure and the load-displacement plots for all four specimens with reduced lateral pressure.

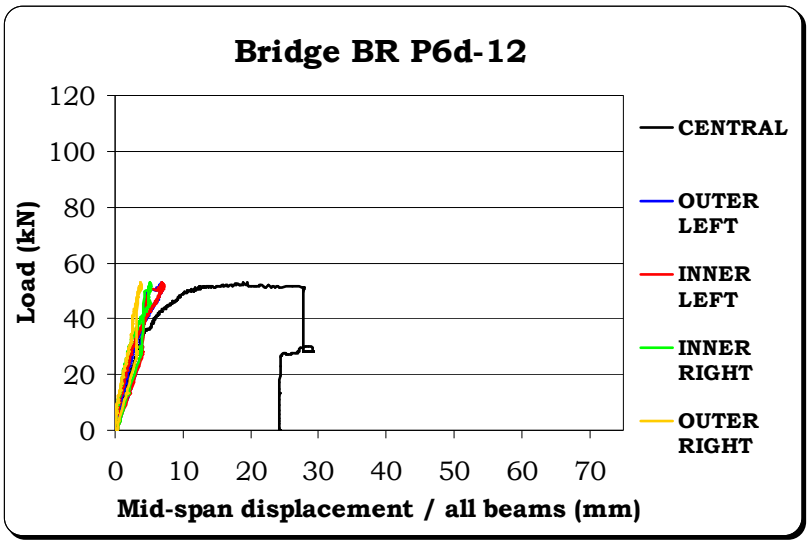

Figure 4.41: Load-displacement plot for the BR P6d-12 specimen

Specimens BR P6d-12 and BR Pst-6d-12 behaved very similarly until the static friction was fully mobilized and slipping occurred between the central beam and the two neighbouring beams at about 37.5kN in both cases. The crushing of the top concrete surface of the central beam after slipping occurred was much less evident in these specimens than in those with the full lateral load, a sign of a significant reduction in lateral confinement.

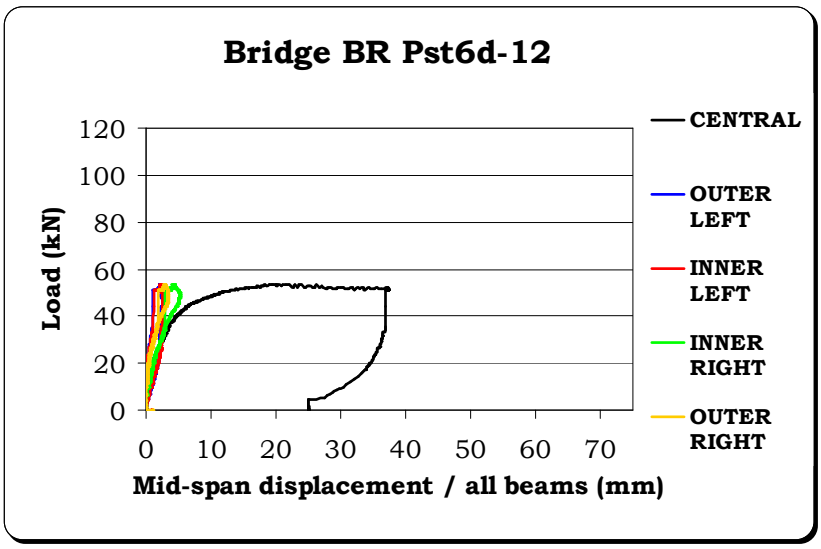

Figure 4.42: Load-displacement plot for the BR Pst6d-12 specimen

After the slipping the central beam of specimen BR P6-12 started to deflect considerably, and when the displacement was around 30mm it failed in shear in the right span at a load of 52.9kN (see Figures 4.40 and 4.41).

The central beam of the specimen with stirrups (BR Pst-6d-12) had a very ductile behaviour and after the peak load of 53.5kN was reached it failed in flexure with a maximum displacement close to 40mm (see Figures 4.42 and 4.43). The increase of capacity over the single beams was 85% and 72%, respectively.

Figure 4.43: Central beam of BR Pst6d-12 after failure

Figure 4.44: Central beam of BR P6d-6 after failure

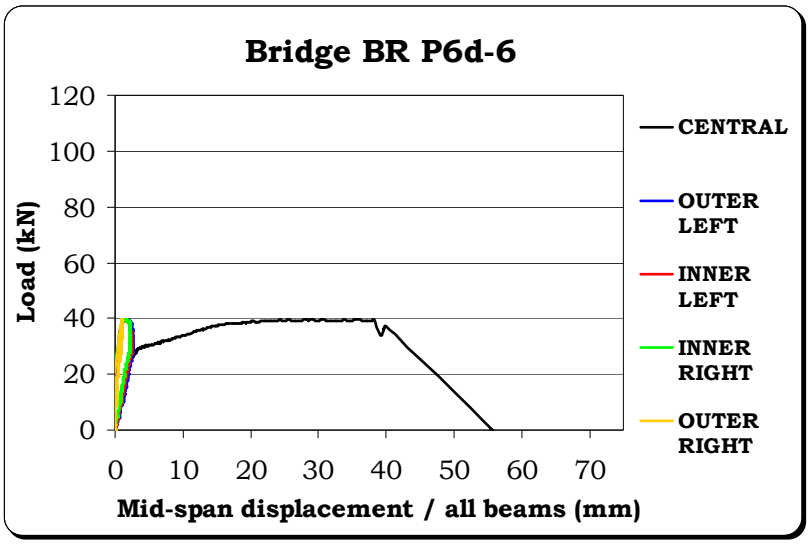

Figure 4.45: Load-displacement plot for the BR P6d-6 specimen

In specimens BR P6d-6 and BR Pst6d-6, with only 25% of the lateral full load applied, the central beams began to deflect independently at approximately 27.5kN and 22.0kN, respectively. However, the specimen without stirrups failed in shear at a maximum load of 39.6kN (see Figures 4.44 and 4.45), while the specimen with stirrups could sustain a higher load until the central beam failed in flexural compression mixed with shear at a load of 47.1kN (see Figures 4.46 to 4.48).

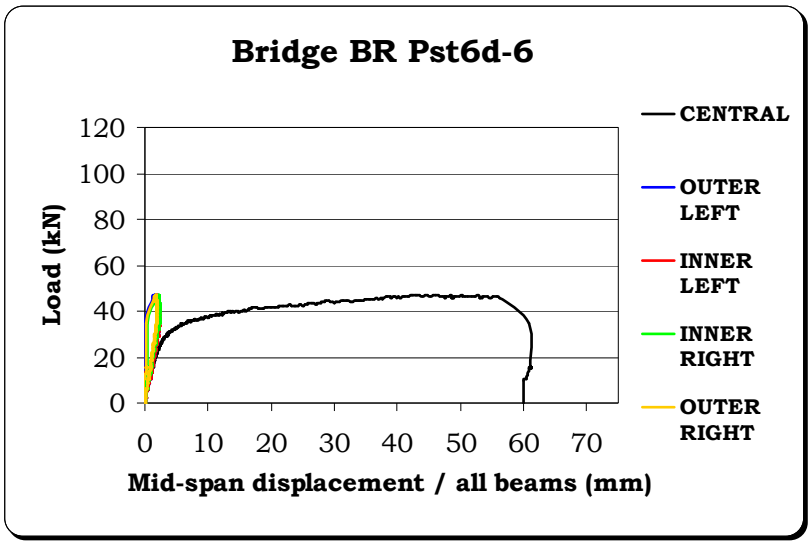

Figure 4.46: Load-displacement plot for the BR Pst6d-6 specimen

Both failures were ductile, especially in the case of the specimen with stirrups, with a maximum displacement of the central beam of 60mm. Despite the presence of a much reduced lateral prestressing, the increase of capacity over the single beams was 39% and 51%, respectively.

Figure 4.47: BR Pst6d-6 after failure

Figure 4.48: Central beam of BR Pst6d-6 after failure

4.4.4 Discussion

The following comments can be made after the examination of the test results on the small-scale bridges:

- All specimens behaved elastically as a whole slab until the static friction was mobilized between the loaded central beam and its two neighbours, with the failure mechanism involving the central beam only. This represents, in the real laterally prestressed bridges, a conservative scenario involving the failure of the shear keys provided between the beams and the beginning of a load-carrying pattern where the capacity of the single beam can be enhanced by the lateral confinement due to the post-tensioning.

- In the four specimens without stirrups with full lateral load (in which all central beams failed in shear), a great enhancement of capacity was found for shorter shear span lengths, similar to the single beam tests. Furthermore, when comparing the capacity with the equivalent single beam, the average increase was a remarkable 140%, meaning that in all cases the capacity of the beam was at least doubled by the frictional restraint due to the lateral prestressing (see Figure 4.49).

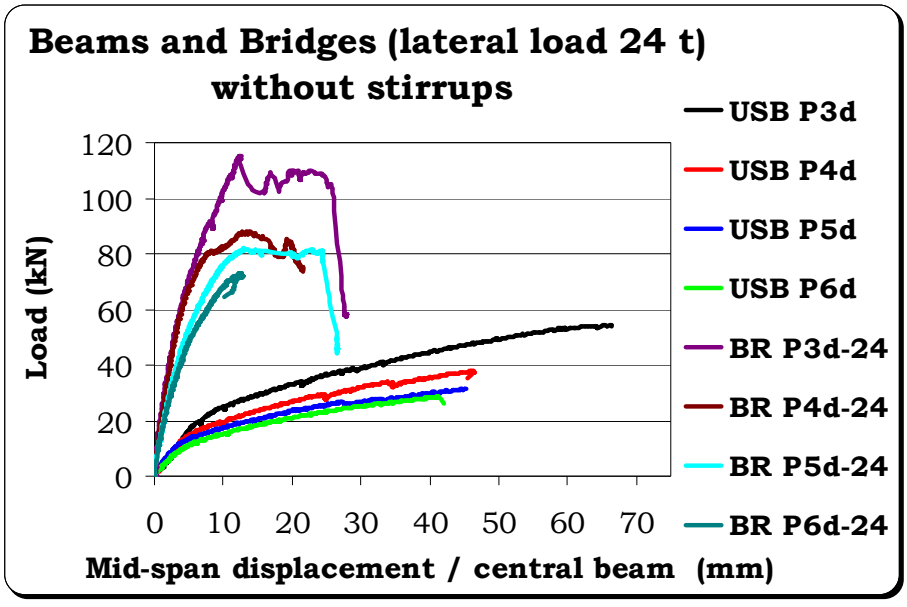

Figure 4.49: Load-displacement plot for the small-scale beams and bridges without stirrups

- The lateral confinement proved very effective even in the case of reduced lateral pressure. A most notable finding was that, even in the case of a bridge without stirrups, loaded at the worst case shear span and with a lateral force reduced to 25%, the capacity was enhanced by about 40% compared to the single beam case (see Figure 4.50).

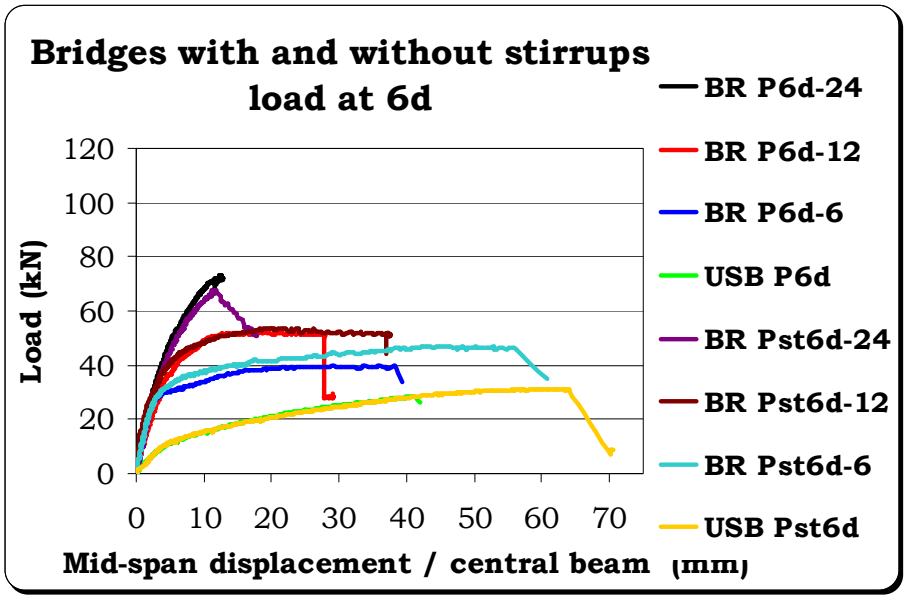

Figure 4.50: Load-displacement plot for the small-scale bridges and beams loaded at 6d

- Stirrups had no effect in increasing the beam capacity when either full and half lateral load was applied, as the lateral confinement was so effective that in these specimens the gap between shear and flexural capacity was minimized. However, in the specimen in which the lateral prestress was reduced to one quarter, the bridge containing stirrups underwent a ductile flexural failure at a load about 8kN higher than the one with no stirrups. This means that, should the lateral confinement in the real bridge be heavily compromised, a shear strengthening of the loaded beam by using the deep embedment technique, for example, could ensure that the flexural capacity of the loaded beam is reached as a ductile failure, rather than a catastrophic shear failure.

4.5 Large-scale beams (ULB)

As discussed in Chapter 2, size effect in shear can be significant and it is necessary to validate the findings of the previous tests on small-scale specimens for real size beams. Four unstrengthened large-scale prestressed beams, with the layout described in Chapter 3, were tested at 4 and 6 times the effective depth, respectively, to confirm the trend of an increasing capacity for reduced shear span length, observed in the small-scale PSC beam.

4.5.1 Test observations

Figures 4.51 to 4.56 show the four unstrengthened large-scale beams at failure, with the load-displacement plots shown in Figure 4.57.

Figure 4.51: ULB P4d at failure

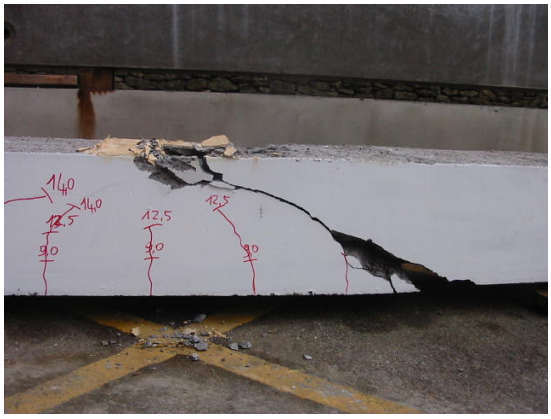

Figure 4.52: ULB P6d at failure

Figure 4.53: ULB Pst4d at failure

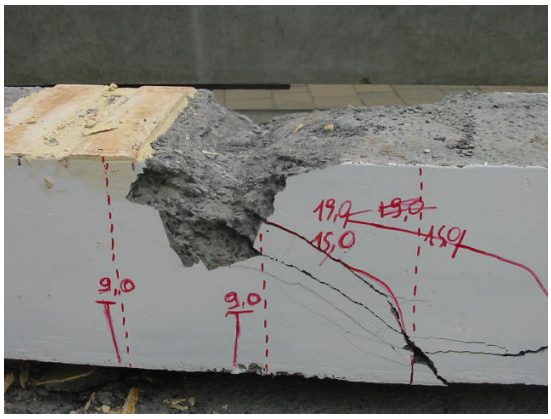

Figure 4.54: ULB Pst6d at failure

In both specimens ULB P4d and ULB Pst4d, the first flexural cracks started to appear in the central zone at an applied load of about 125kN, propagating upwards

as load was increased. Flexural cracks then formed over a wider area until two single diagonal shear cracks appeared in both shear zones at an applied load of 215kN. In specimen ULB P4d, without stirrups, the two shear cracks kept increasing in width until brittle shear failure occurred in the left span at 295.9kN (see Figures 4.51 and 4.55). In specimen ULB Pst4d, with stirrups, the diagonal cracks increased in width considerably but were limited by the stirrups until flexural failure occurred at a load of 351.0kN (see Figures 4.53 and 4.55).

Figure 4.55: ULB P4d (bottom) and Pst4d at failure

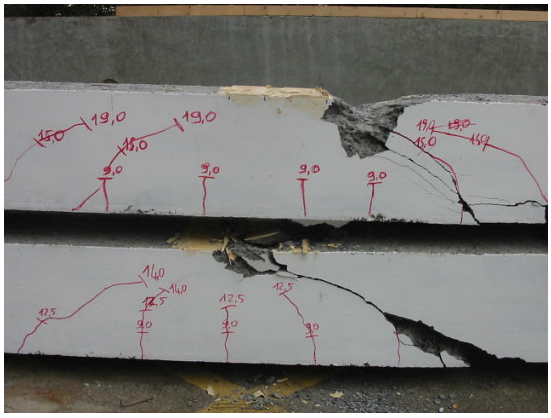

Figure 4.56: ULB P6d (bottom) and Pst6d at failure

In specimens ULB P6d and ULB Pst6d the flexural cracks appeared at about 90kN, while the diagonal shear cracks formed soon after the load reached 140kN, in both spans.

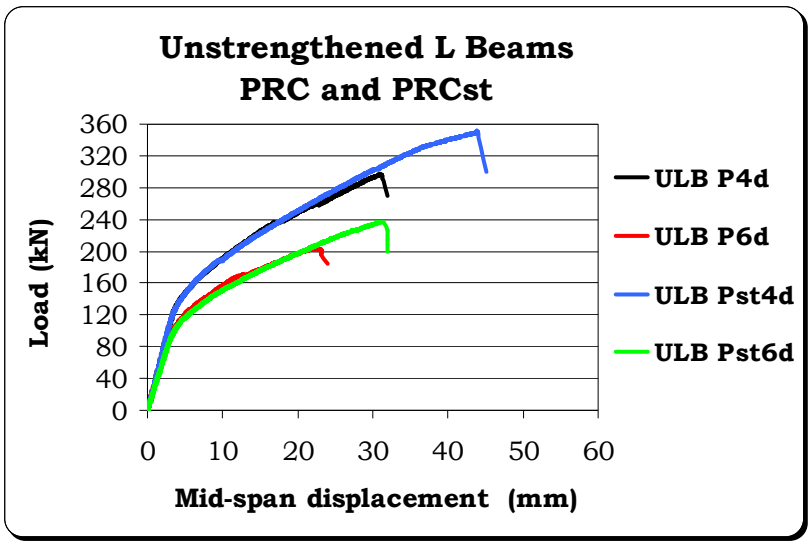

Figure 4.57: Load-displacement plot for the unstrengthened large-scale beams

The beam without stirrups failed in brittle shear at a load of 203.4kN in the right-hand span (see Figures 4.52 and 4.56), while the beam containing stirrups could sustain a higher load until the failure occurred in flexure at 236.6kN (see Figures 4.54 and 4.56). However, signs of an incipient shear failure were present in the specimen, confirming that even for prestressed beams of real size the shear capacity reduces with the increase of shear span length.

4.5.2 Discussion

From the observation of the test results, it is clear that the large-scale PSC beams with and without stirrups followed exactly the same behaviour of the equivalent small-scale beams in terms of enhancement of shear capacity for decreasing shear span, confirming that an extrapolation of the results from the small to large scale is possible. Despite their low percentage within the cross-section, the stirrups proved to be effective in preventing shear failure leading to a flexural failure.

4.6 Comparison with code provisions

4.6.1 General comparison of test results with codes

Tables 4.2 and 4.3 summarize, for the unstrengthened beams and bridges, respectively, the test results and the predictions from the Network Rail assessment standard NR/GN/CIV/025 (2006) and the Eurocode 2 (2004), where all safety factors have been set to unity.

In the tables, P is the value at each of the two point loads, i.e. half of the total vertical load applied; $P_{cr,fl}$ is the first flexural cracking load, $P_{cr,sh}$ is the first diagonal shear cracking load, P_{ult} is the peak ultimate failure load and P_{slip} is the load at which the central beam started to slip from its neighbouring beams in the bridge specimens. No values for the first flexural and shear cracking load are reported for the bridge specimens, as it was not possible to observe crack formation in the central beams covered by the neighbouring beams.

For the flexural capacity, in terms of both the first cracking load and the ultimate load, the predictions given by NR/GN/CIV/025 (2006) and Eurocode 2 (2004) are virtually coincident, with a maximum difference of less than 2% between them;

therefore, Eurocode 2 (2004) prediction only is used in Table 4.2 for the first flexural cracking load, representing the general code prediction.

From Table 4.2 is seen that, for both RC and PSC beam specimens, the theoretical first flexural cracking load and the ultimate flexural load match closely with the actual values, confirming that the flexural theory for reinforced concrete beams, employed by codes, is very accurate.

Table 4.2*:* Actual and predicted capacity for the unstrengthened test beams (in kN)

Specimen	***a/d***	***Act*** $P_{cr,fl}$	***Pred*** $P_{cr,fl}$	***Act*** $P_{cr,sh}$	***Actual*** P_{ult}	***Pred EC*** P_{ult}	***Pred NR*** P_{ult}
	Small-scale Beams - RC						
USB R3d	3	6.0	5.0	22.5	23.5 (shear)	21.0 (s)	20.5 (s)
USB R4d	4	5.5	3.8	23.0	25.1 (shear)	21.0 (s)	20.6 (s)
USB R5d	5	4.0	3.0	20.0	21.4 (shear)	21.1 (s)	20.7 (s)
USB R6d	6	3.0	2.5	20.0	21.7 (shear)	21.2 (s)	20.8 (s)
USB Rst3d	3	6.0	5.0	22.5	31.5 (shear)	27.9 (s)	30.6 (s)
USB Rst4d	4	5.5	3.8	23.0	33.8 (shear)	28.0 (s)	30.7 (s)
USB Rst5d	5	4.0	3.0	20.0	28.3 (shear)	28.1 (s)	30.8 (s)
USB Rst6d	6	3.0	2.5	20.0	28.4 (shear)	28.2 (s)	29.7 (f)
	Small-scale Beams - PSC						
USB P3d	3	18.0	16.0	34.5	54.4 (shear)	29.5 (s)	29.0 (s)
USB P4d	4	15.0	12.2	30.0	37.9 (shear)	29.6 (s)	24.1 (s)
USB P5d	5	12.0	9.9	26.0	31.3 (shear)	29.6 (s)	21.2 (s)
USB P6d	6	10.0	8.3	23.0	28.5 (shear)	29.7 (s)	19.4 (s)
USB Pst3d	3	18.0	16.0	34.5	54.5 (shear)	27.9 (s)	39.0 (s)
USB Pst4d	4	15.0	12.2	30.0	46.4 (flex)	28.0 (s)	34.1 (s)
USB Pst5d	5	12.0	9.9	26.0	37.9 (flex)	28.1 (s)	31.3 (s)
USB Pst6d	6	10.0	8.3	23.0	31.2 (flex)	28.2 (s)	29.5 (s)
	Large-scale Beams - PSC						
ULB P4d	3	125.0	129.8	215.0	295.9 (sh)	227.7 (s)	236.8 (s)
ULB P6d	4	90.0	87.3	140.0	203.4 (sh)	229.7 (s)	185.4 (s)
ULB Pst4d	5	125.0	129.8	215.0	351.0 (flex)	258.6 (s)	348.3 (s)
ULB Pst6d	6	90.0	87.3	140.0	236.5 (flex)	241.5 (f)	241.5 (f)

Figure 4.58 shows the actual to predicted capacity for all unstrengthened tests in graphical form. The majority of the results are above the line of exact prediction, as the codes are generally conservative. It is also evident that codes are not able to

predict the capacity of the bridge specimens accurately, due to their inability to account for the lateral prestressing, so the predictions for such bridges are extremely conservative.

Table 4.3: Actual and predicted capacity for the test bridges (in kN)

Specimen	a/d	Actual P_{slip}	Actual P_{ult}	Pred EC P_{ult}	Pred NR P_{ult}
	Small-scale Bridges - PSC - Full lateral load				
BR P3d-24	3	91.7	115.4 (shear)	29.5 (s)	29.0 (s)
BR P4d-24	4	79.8	88.0 (shear)	29.6 (s)	24.1 (s)
BR P5d-24	5	63.9	82.0 (shear)	29.6 (s)	21.2 (s)
BR P6d-24	6	55.4	73.1 (shear)	29.7 (s)	19.4 (s)
BR Pst6d-24	6	57.5	67.5 (flexure)	28.2 (s)	29.5 (s)
	Small-scale Bridges - PSC – 50% of Full lateral load				
BR P6d-12	6	37.5	52.9 (shear)	29.7 (s)	19.4 (s)
BR Pst6d-12	6	37.5	53.5 (flexure)	28.2 (s)	29.5 (s)
	Small-scale Bridges – PSC—25% of Full lateral load				
BR P6d-6	6	27.5	39.6 (shear)	29.7 (s)	19.4 (s)
BRPst6d-6	6	22.0	47.1 (flexure)	28.2 (s)	29.5 (s)

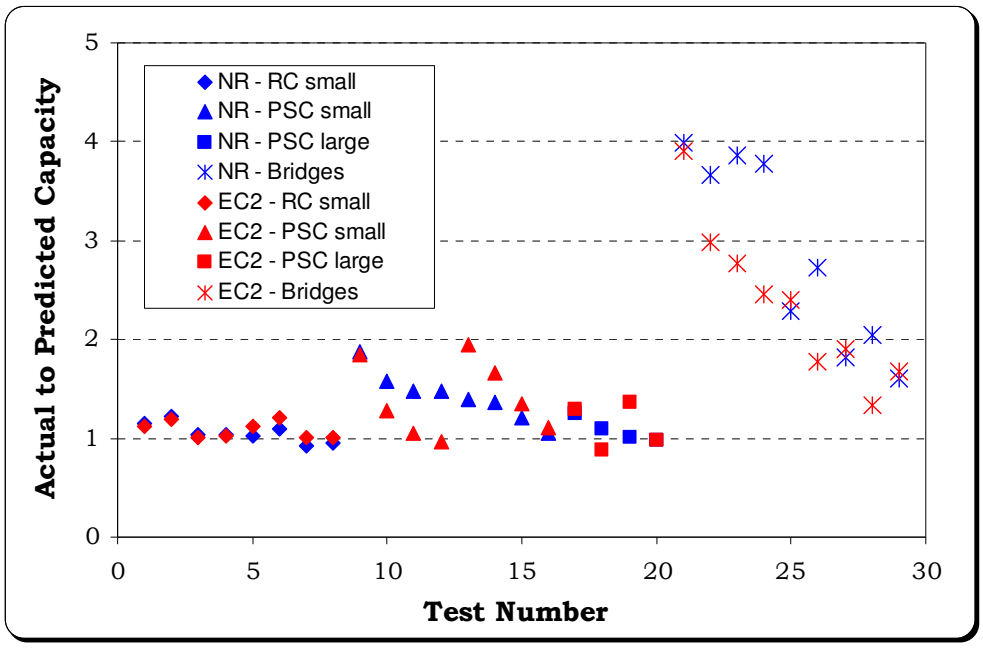

Figure 4.58: Ratio of test results to code predictions for all specimens

The test results for the specimens failed in shear are plotted against the code predictions in terms of shear stress capacity in Figure 4.59, where the shear stress

is equal to the shear force V divided by bd_s, where for all specimens b is the beam width and d_s is the effective depth to the centroid of the tensile reinforcement. When all specimens are considered, the ratio of the experimental to predicted capacity ranges from 0.89 to 3.98, with an average of 1.57 and 1.72 and a coefficient of variation (CoV) of 45% and 54% for the EC2 and NR code provisions, respectively. However, if only the beams are considered, average and CoV of the actual to predicted capacity equal to 1.22 and 23% for the EC2 and 1.21 and 20% for the NR assessment code, respectively.

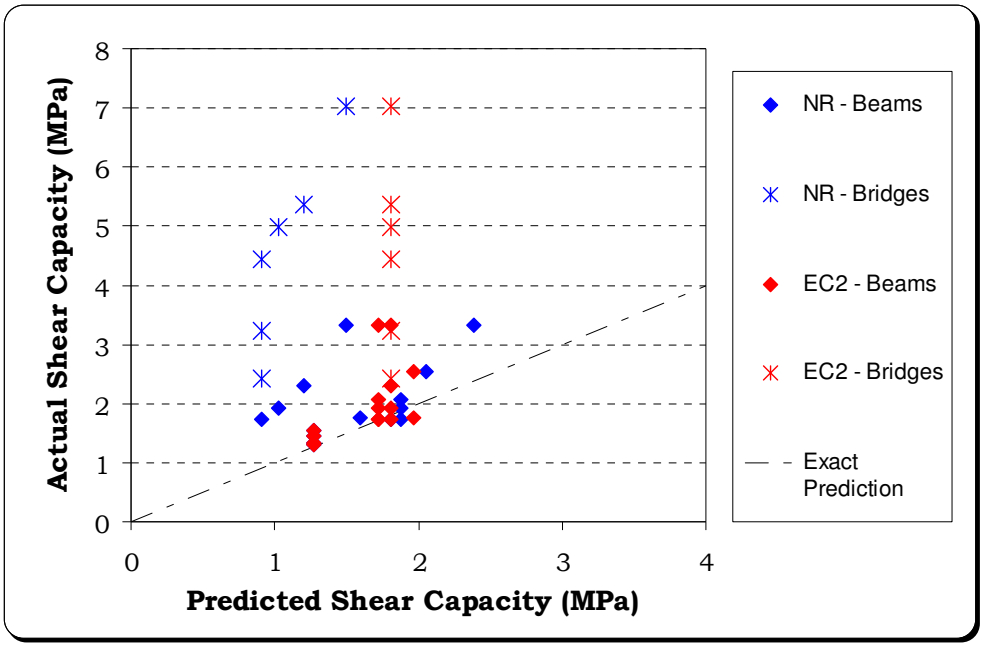

Figure 4.59: Test results and shear predictions for the specimens failed in shear

In the following sections, the ability of the codes in predicting the influence of the various parameters investigated in the test regime is assessed, i.e. the effect of prestressing, the effect of the shear span length, the size effect (if any), the presence of stirrups and the effect of lateral prestressing (for the bridge specimens only).

4.6.2 Beams

Figure 4.60 shows the code predictions, compared with the test results, for all RC and PSC beams that failed in shear.

It is evident that both codes are very accurate for RC beams, both with and without stirrups, with an average and CoV for the actual to predicted capacity, respectively, of 1.09 and 7.3% for the EC2 and of 1.06 and 8.6% for the NR code.

For prestressed beams, both codes are quite conservative. However, the NR code is more accurate, with an average and CoV of the actual to predicted capacity of 1.28 and 16.8% respectively, while for EC2 gives the average is 1.34 and the CoV is 26.1%. As it will be shown later, the main problem of the EC2 approach is that it does not take into account the effect of the shear span length on the shear capacity.

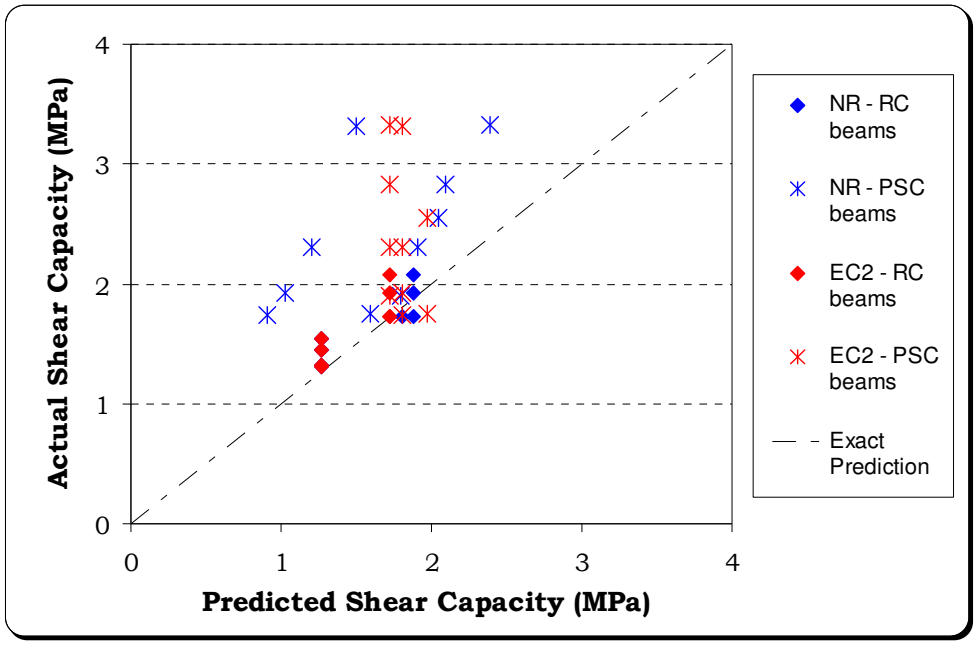

Figure 4.60: Shear predictions for the RC and PSC beams that failed in shear

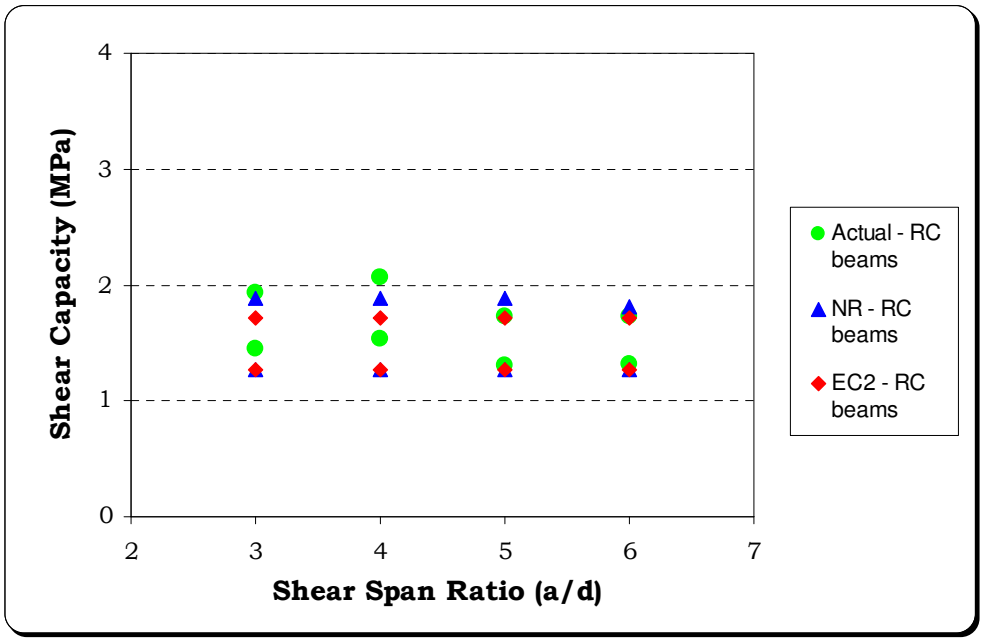

Figure 4.61: Shear predictions for the RC beams

The effect of the shear span length can be examined with the aid of Figures 4.61 and 4.62, which refer to RC and PSC beams, respectively. For RC beams, the change in capacity with the shear span length, disregarded by codes, appears to be negligible and the slight differences in the tests may well be within experimental error. Code predictions for all RC beams are accurate and sufficiently conservative.

However, as shown in Figure 4.62, for both small- and large-scale prestressed beams the shear span length is clearly a key factor in dictating the actual shear capacity. In this respect, despite its excessive conservativeness, the NR code is theoretically more correct as it takes into account the decrease of shear capacity due to co-existent bending moment which decompresses the prestressed section for longer span lengths, a concept ignored in the EC2 provisions. This means that EC2 provisions are very conservative for spans up to 4*d* but can become dangerously unconservative for longer shear spans as it is the case for specimens USB P6d and ULB P6d (see Table 4.2).

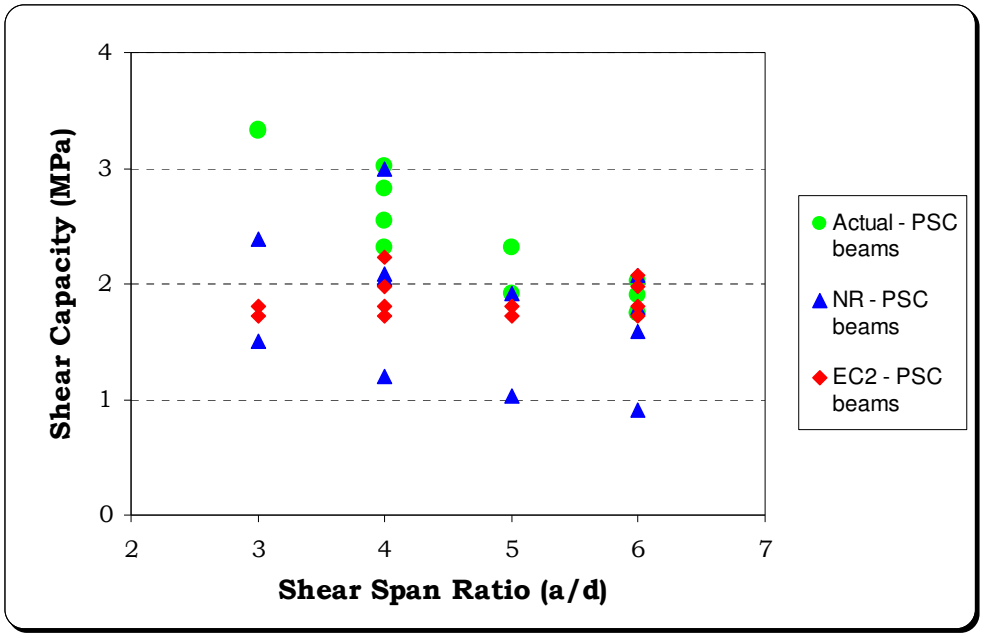

Figure 4.62: Shear predictions for all the PSC beams

To evaluate the effect of the beam size over the shear capacity, Figure 4.63 shows the actual to predicted capacity for both the small- and the large-scale prestressed beams loaded at 4*d* and 6*d* that failed in shear. In terms of actual results, the shear stresses at failure at 4*d* were 2.31MPa and 2.55MPa for the small- and large-scale beams, respectively, while for the beams loaded at 6*d* the shear stresses at failure

were almost identical (1.74MPa and 1.75MPa), indicating that for the beams tested the size effect was very marginal, as no reduction in shear capacity due to the beam size was encountered.

When considering the EC2, the average actual to predicted capacity is 1.12 for the small-scale beams and 1.09 for the large-scale beams, so there is no change in the shear prediction due to the beam size. However, with the NR code, the average actual to predicted capacity is 1.52 for the small-scale beams and 1.17 for the large-scale beams, meaning that the formula of the NR assessment code for PSC beams, that does not include any size effect factor (in contrast with the NR code formula for RC beams), actually appears to be excessively conservative for small size beams but reasonably accurate for larger specimens, of a comparable size to those used in practice.

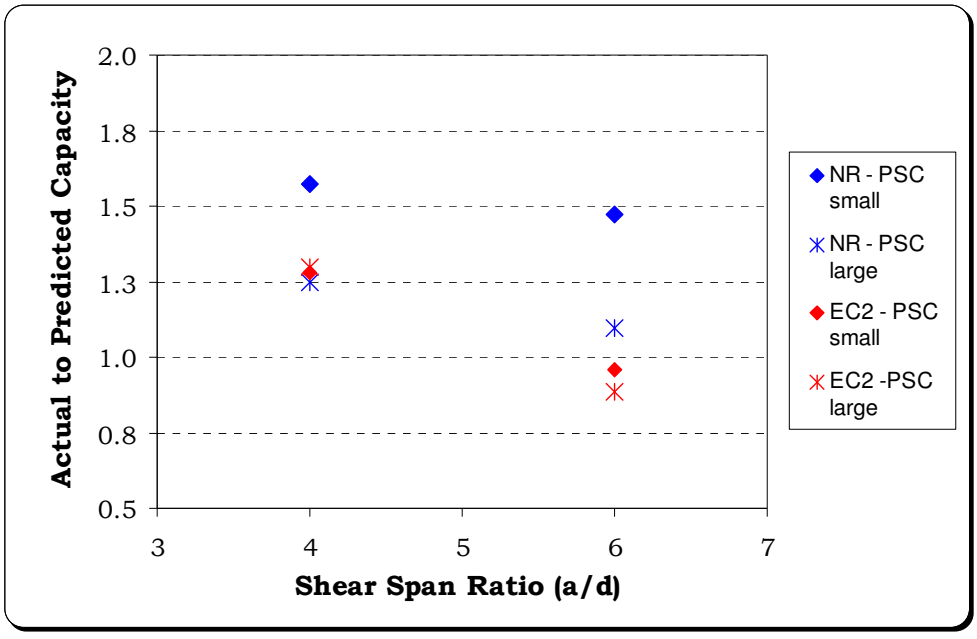

Figure 4.63: Capacity of the PSC beams loaded at 4d and 6d that failed in shear

The ability of the codes to evaluate the contribution of the stirrups is evaluated with the aid of Figures 4.64 and 4.65, which show the actual to predicted capacity for the RC and PSC beams, respectively. When considering the RC beams with stirrups, the actual to predicted average and CoV are equal to 1.11 and 7.0% for the NR code and 1.09 and 6.9% for the EC2 code, respectively, both very accurate. However, the EC2 predictions, which employ a variable angle truss model, are accurate only when the minimum allowed inclination for the compression struts is

chosen ($\cot\theta = 2.5$), otherwise they will be very conservative. With the NR code, the predictions can become slightly uncoservative for high values of the shear span. As discussed previously in the chapter, the actual average increase of capacity due to the presence of the stirrups was 7.6kN, while the average predicted increase from codes was 7.4kN for the EC2 and 10.1kN for NR code, showing the latter to be slightly unconservative in this case.

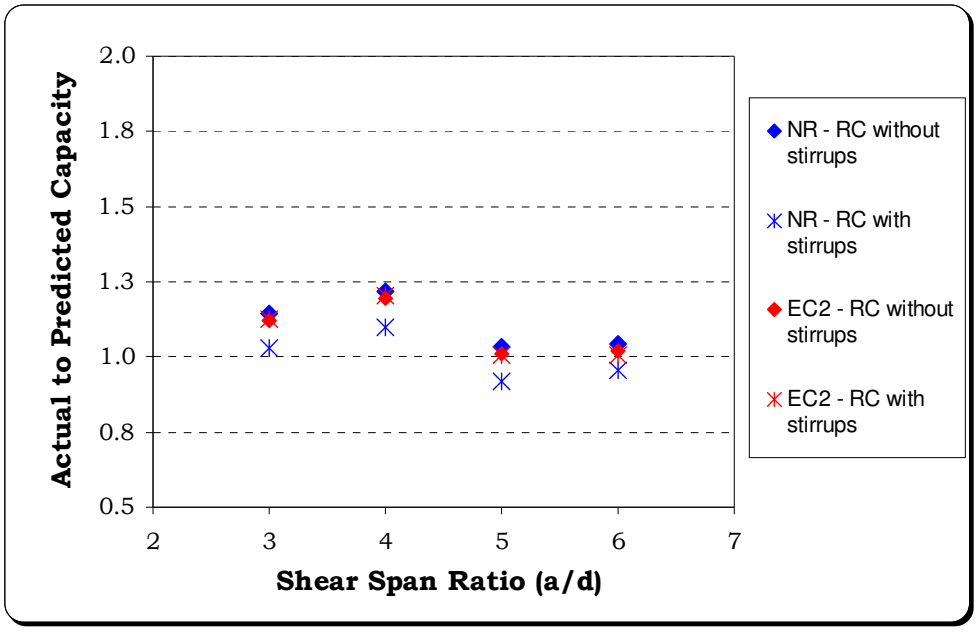

Figure 4.64: Actual to predicted capacity for all the RC beams

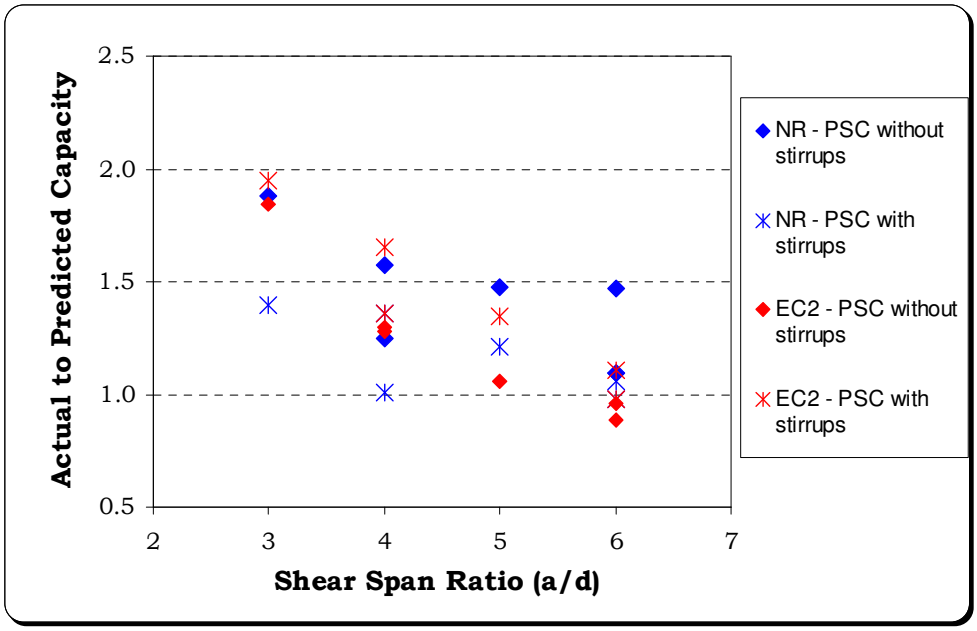

Figure 4.65: Actual to predicted capacity for all the PSC beams

Five out of the six prestressed beams with stirrups actually failed in flexure, although shear failure was predicted by the codes for five of them and flexural failure was expected only for specimen ULB Pst6d (see Table 4.2). Therefore, in the case of PSC beams with stirrups, the performance of the code cannot be judged only on the basis of the actual to predicted capacity, as the actual failure mode could not be predicted. Nevertheless, the NR code predictions were more accurate, with an average of 1.17 and a CoV of 14.1% for the actual to predicted capacity; an average of 1.40 and a CoV of 23.3% were found for the EC2 code.

The lack of ability of the codes to predict these flexural failures stems from the somewhat unexpected increase of shear capacity experienced by the prestressed beams when loaded at shear spans shorter than 5*d*. Apart from the beam loaded at 3*d*, where the stirrups were not effective due to the arching action being predominant, in all other cases the increase in capacity due to stirrups was at least as effective as the codes predicted.

4.6.3 Bridges

Figure 4.66 shows the capacity of the four small-scale bridges loaded at 3, 4, 5 and 6 times the effective depth compared with the capacity of the equivalent single prestressed beams and the code predictions.

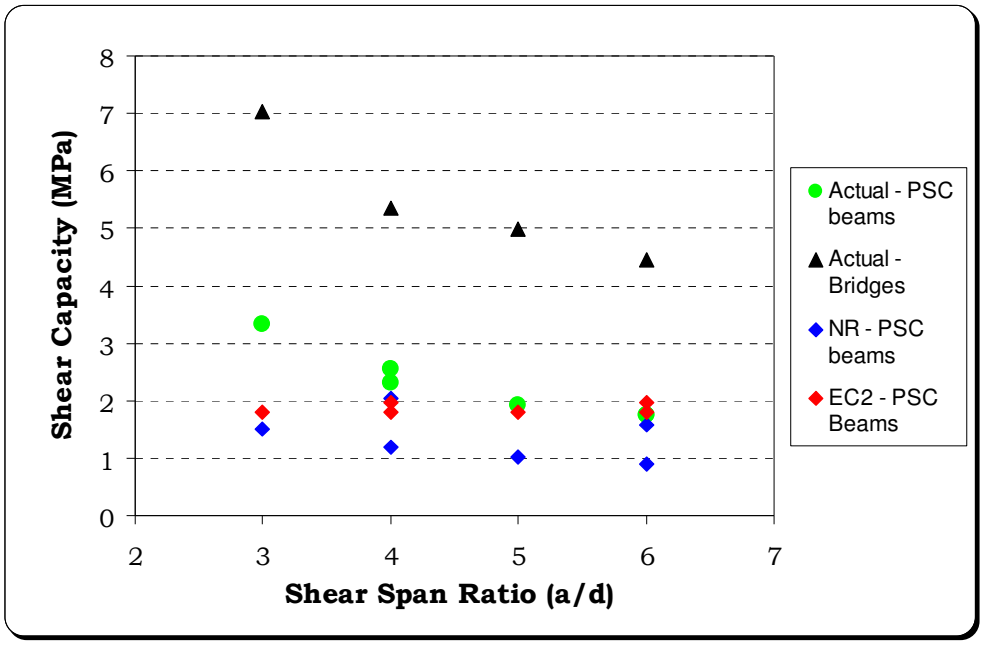

Figure 4.66: Shear capacity of the small-scale bridges with full lateral prestressing

As discussed previously, the failure in these specimens occurred in the central beam after it slipped with respect to its neighbouring beams, with ultimate loads much higher than the equivalent single beam. Codes cannot predict this large increase of capacity due to the lateral prestressing because, after the longitudinal and transverse distribution of the railway load to the beam, the assessment analysis is performed on the individual beams considered to be acting alone independently with no lateral confinement, and hence no lateral distribution of load. From the plot, it can be seen how for the bridge specimens there is a very clear decreasing trend for the shear capacity when the shear span length increases, in a similar manner to the behaviour of the small- and large-scale prestressed beams.

The effect of the lateral prestressing on the shear capacity of the small-scale bridges loaded at 6*d* is shown in Figure 4.67. The code predictions for the single beams, equivalent to a bridge specimen with no lateral prestressing, are indicated for comparison.

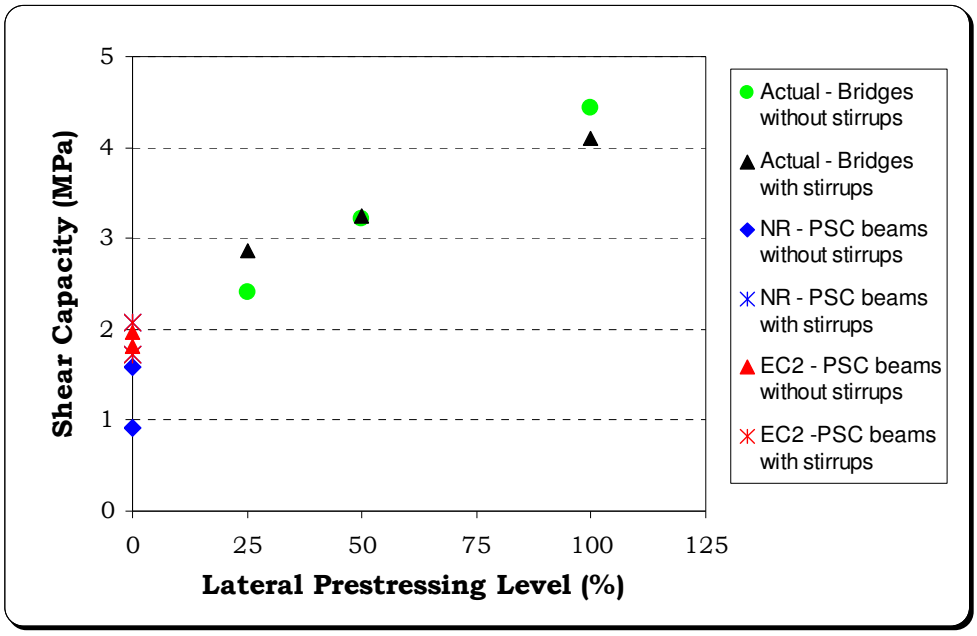

Figure 4.67: Shear capacity of the small-scale bridges with reduced lateral prestressing loaded at 6d

The plot shows a clear pseudo-linear descending trend for the capacity of the beams in the bridges when the lateral load is reduced to half and to a quarter of the full lateral prestressing. A most notable finding is that, in the bridge specimen with

25% of the full lateral load, the stirrups were effectively able to change the failure of the critical central beam from shear to flexure, indicating an actual increase in capacity of 7.5kN, in good agreement with the predicted increase due to the stirrups according to the codes in the case of a single beam. Even when compared to the less conservative code predictions for the capacity of the single beam, the capacity of the specimen with 25% of the full lateral load was 33% higher.

4.6.4 Concluding remarks

From the comparison of the test results on all unstrengthened specimens with the provisions of Eurocode 2 (2004) and the Network Rail assessment standard NR/GN/CIV/025 (2006), the following can be concluded:

- Both codes are able to accurately predict the behaviour and capacity of RC beams, with and without stirrups.

- For prestressed beams, codes predictions are not as accurate, especially at short shear spans. The NR code, despite being excessively conservative for small-scale beams, is able predict the decrease of shear capacity for increasing shear span lengths, while the EC2 code, which does not take into account this effect, can be unconservative for long shear spans. The shear span dependency renders all prestressed beams critical in shear at long spans but, at the same time, allows ductile flexural failure to occur with the introduction of only small amount of transverse reinforcement.

- Codes are unable to predict the enhancement in ultimate capacity found in the laterally prestressed bridge specimens due to their inability to account for the confining and load distribution effects of the lateral prestressing. Therefore, in order to assess these bridges appropriately, the code provisions should be improved by considering an assessment methodology which is able to take into account the beneficial effects of the lateral confinement. This issue will be addressed in Chapter 6. The test results on the specimens strengthened with the deep embedment technique, applicable when shear deficiencies are encountered, are presented in the following Chapter 5.

Chapter 5
Test Results and Discussion - Strengthened Specimens

5.1 Introduction

The test results on the small- and large-scale specimens strengthened with the deep embedment technique, designed and described in Chapter 3, are summarised in the following sections, together with the bond tests on the strengthening bars.

As deep embedment is a novel technique, the various guidelines for strengthening concrete members with FRP described in Chapter 2 do not contain any provision for calculating the shear capacity of concrete elements containing deep embedded bars, so no actual comparison between codes and test results on the strengthened specimens is possible. However, a simple truss-based method to calculate the shear enhancement due to the deep embedded bars that can be implemented into codes will be developed and discussed in Chapter 6.

5.2 Bond tests

5.2.1 Test observations

The results of the bond tests for the different bar types, adhesives and embedment lengths, following the test programme described in Chapter 3, are summarised in Table 5.1 in terms of average bond strength and failure mode, while Figure 5.1 presents images of typical bars following pull-out. The bond strength at failure for the short embedment tests, taken as the average along the bonded length, is equal to:

$$\tau_{bu} = \frac{T_u}{\pi\, d_b l_b} \tag{5.01}$$

where T_u is the maximum measured tensile load during the test, d_b is the bar diameter and l_b is the bonded length.

Figure 5.1: Bars after pull-out failure: (a) Steel, (b) Glass, (c) Carbon, (d) Aramid

The failure modes encountered were interlaminar shear (IS) between the bar core and the sanded/coated surface, which occurred in most FRP bars (see Figures 5.1b, c and d), shearing in the resin adhesive layer (SR, which occurred for the steel bars below their yield load, see Figure 5.1a), yielding of the steel bars (BY) and rupture of the FRP bars (BR), which occurred when the embedment length was greater than a specific threshold representing the yield capacity of steel or the ultimate capacity of the FRP.

Table 5.1: Summary of bond test results

Bar Type	**Average bond strength** (MPa) – **Failure mode**				
	l_b=15 mm	l_b=30 mm	l_b=45 mm	l_b=60 mm	l_b=75 mm
	Non-sag epoxy (Hilti 500)				
Steel 8	37-SR	36-BY	27-BY	20-BY	16-BY
Carbon 7.5	36-IS	32-IS	28-IS	24-IS	25-IS
Carbon 6	33-IS	30-IS	27-IS	23-IS	21-IS
Glass 9	25-IS	27-IS	24-IS	20-IS	16-BR
Aramid 7.5	17-IS	14-IS	10-IS	07-IS	07-IS
	Low-viscosity epoxy (Araldite)				
Steel 8	37-SR	27-SR	26-BY	21-BY	16-BY
Carbon 7.5	33-IS	22-IS	28-IS	30-IS	31-IS
Glass 9	36-IS	04-IS	27-IS	22-IS	25-BR
Aramid 7.5	26-IS	20-IS	18-IS	17-IS	13-IS
	Medium-strength paste (Hilti 150)				
Steel 8	10-SR	17-SR	26-BY	21-BY	16-BY
Carbon 7.5	17-IS	17-IS	16-IS	19-IS	19-IS
Glass 9	16-IS	16-IS	17-IS	17-IS	17-IS
Aramid 7.5	07-IS	06-IS	08-IS	08-IS	05-IS

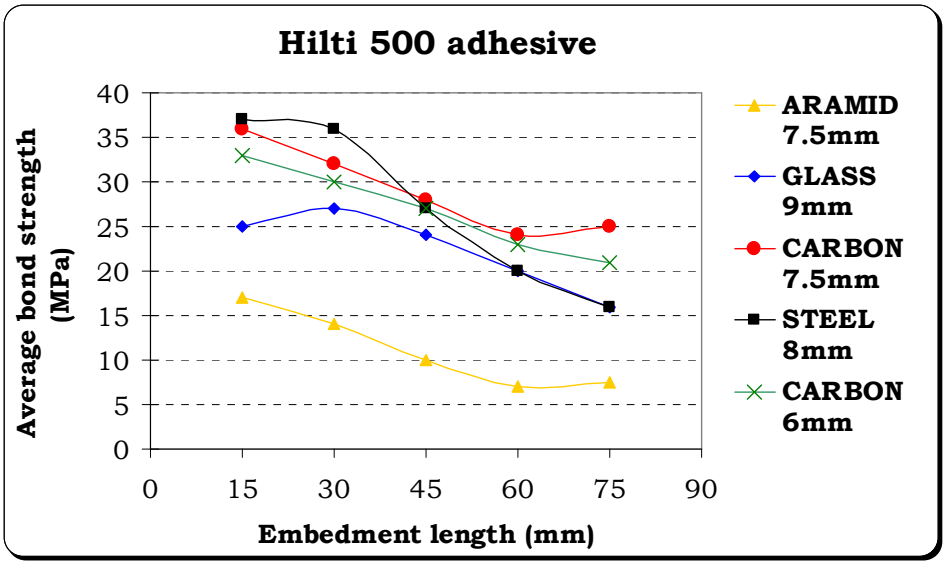

Figure 5.2: Bond capacities of the strengthening bars - Hilti 500 adhesive

The bond strength is shown in graphical form in Figures 5.2, 5.3 and 5.4 for the three adhesives. Note that the values of bond strength for the steel bars which yielded (BY) or the glass bars which ruptured (BR) represent the equivalent average bond stress corresponding to the tensile yield capacity or rupture for the particular bonded length.

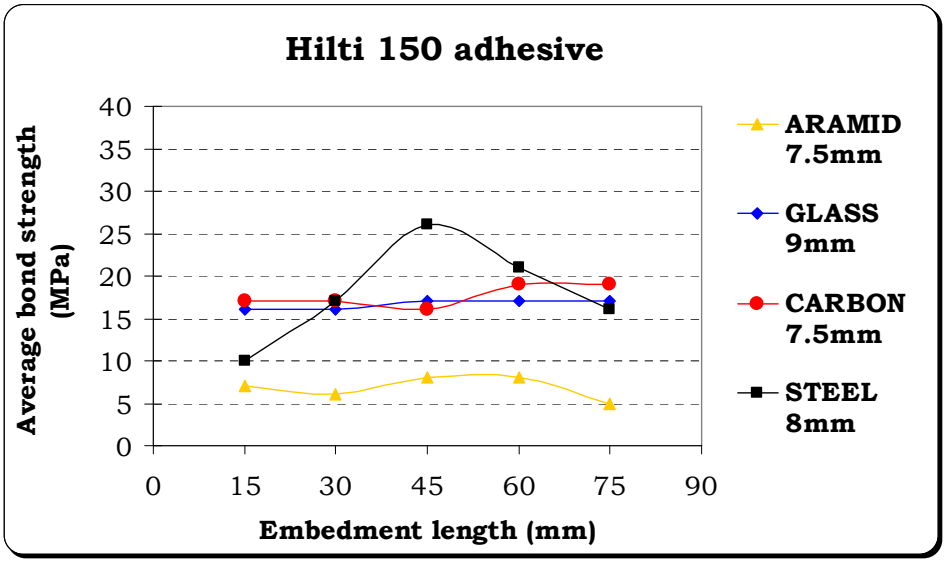

Figure 5.3: Bond capacities of the strengthening bars - Hilti 150 adhesive

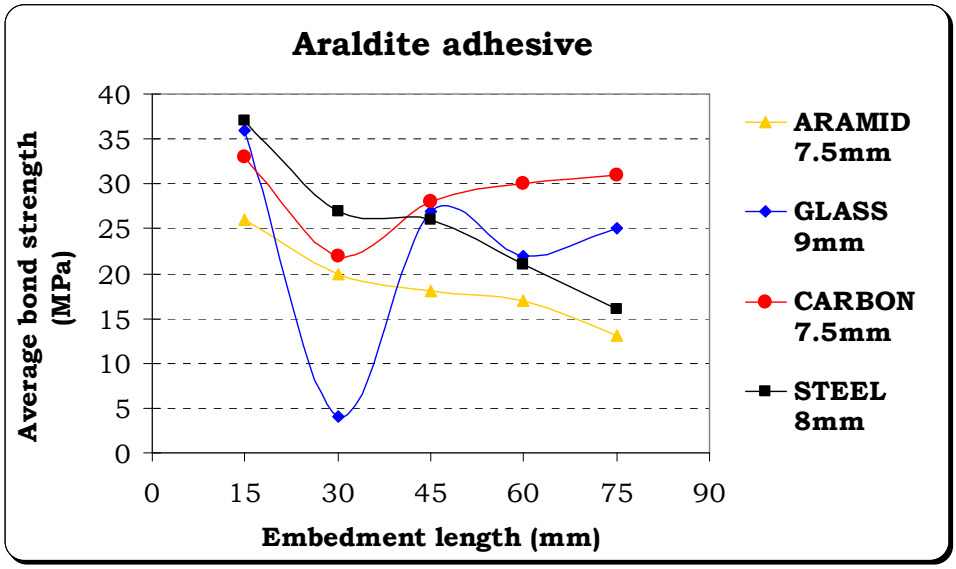

Figure 5.4: Bond capacities of the strengthening bars - Araldite adhesive

In all tests, the readings of the two strain gauges in the middle of the bar and within the clearance hole were practically identical, confirming the bars were effectively unbonded along the clearance hole. Generally, the system proved to be very effective with both steel and FRP bars and the bond capacities obtained were substantial, especially with the Hilti 500 and Araldite adhesives. Indeed, for appropriate values of the embedment length, bond was sufficient to yield the steel bars and snap the glass FRP bars, whose yield or ultimate tensile capacities are much lower than aramid and carbon, for appropriate values of the embedment length (see Figure 5.5).

Figure 5.5: Rupture of the glass bar at (Hilti 500 adhesive – 75mm bonded length)

The steel tests showed an increase in capacity with increased capacity of the adhesive, resulting in weaker bond with the Hilti 150; this may be explained by the fact that, when the steel yield stress could not be reached, bond failures in the steel bars occurred for shearing in the resin in a plane close to the tip of the surface ribbing (see Figures 5.1a and 5.3), so the capacity was guided by the adhesive.

Typically, for the FRP bars the results showed a decreasing bond strength with increased embedment length, with the exception of the Hilti 150 adhesive where bond strength was approximately constant. The low value obtained with the glass bar and Araldite adhesive at 30mm (see Figure 5.4) was probably due to an incorrectly prepared resin mix which led to an unusually low bond resistance.

The aramid bars offered a much lower bond capacity than the other bars, and this is due to their poor surface treatment, as the slight sand coating easily debonded from the core; the only partial exception is in the case of the Araldite resin, probably because the very low viscosity of this adhesive resulted in a better bond with the FRP bar as the adhesive more easily filled the smallest of voids.

A typical relationship between the bond stress and the slip at the test end is shown in Figure 5.6, showing the response of the 7.5mm diameter carbon bars with the Hilti 500 adhesive for the various embedment lengths.

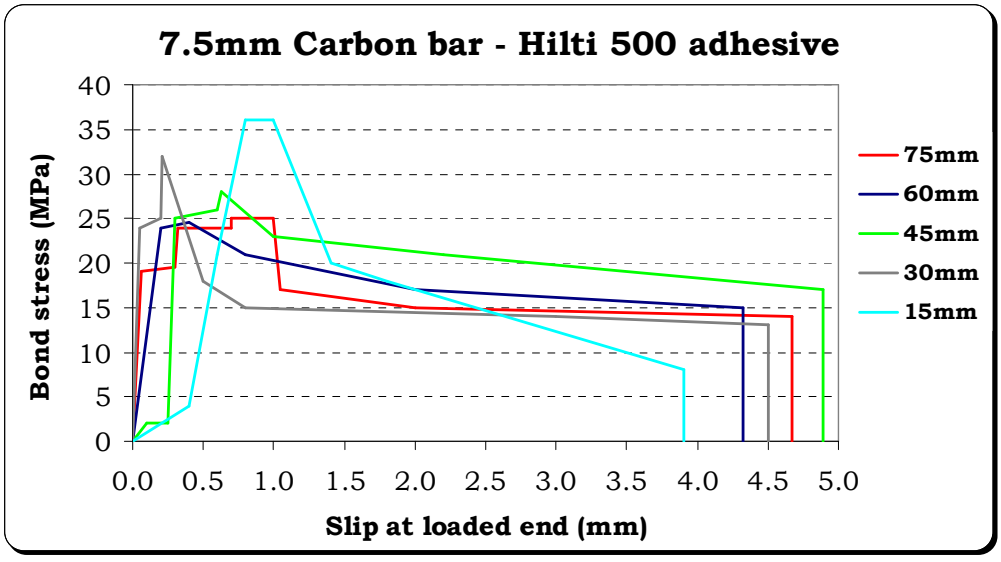

Figure 5.6: Typical bond-slip response from pull-out test

In the bond-slip plots, after the peak bond stress there was a drop in capacity, but this was generally not as sudden as other research on the bond behaviour of EB or NSM systems often suggest. Following the peak value a descending capacity was exhibited without oscillations, suggesting that a frictional resistance remained without mechanical interlock; this is further confirmed by the smooth surface observed in the FRP bars after debonding.

The shape of the bond-slip response was similar for all FRP bars using the Hilti 500 adhesive, with a significant bond stress sustained for values of slip in excess of 3mm in all cases. Slightly less ductile behaviour was obtained with the Araldite adhesive, where the values of the maximum slip did not exceed 2mm. Tests with the Hilti 150 adhesive showed a descending capacity after the peak, rather than a sudden drop, and a similar ductility to the Hilti 500; however, the peak loads were generally lower.

5.2.2 Discussion

From the analysis of the test results it appears that the bars bonded with the proposed deep embedment technique offer an efficient means of transferring load into concrete.

It is evident that the surface roughness of the bar is a key parameter for the effectiveness of the system, as the aramid bars, whose sand coating was poor, offered the worst bond performance. The detachment of the fibre spiral or sand grains and the shearing off of the surface typically caused the bond failure of the FRP bars. No major differences were noted between the other FRP bars and deformed steel, proving that the system has the potential of being effective with both FRP and steel.

With regards to the adhesives, results suggest that the non-sag Hilti 500 and the low-viscosity Araldite were the most effective, leading to values of bond strength in excess of 20MPa for all the bonded length investigated. However, the advantage over the Hilti 150 was reduced for longer embedment lengths. This implies that for short bond lengths the higher tensile strength of the Araldite and Hilti 500 adhesives plays a role in ensuring a higher bond capacity is obtained, while for longer embedment lengths the bond strength is more dependant on the surface treatment of the bar.

The post-peak bond behaviour exhibited a great ductility, especially in the case of the Hilti 500 adhesive, where a sustained bond stress of over 15MPa for values of slip in excess of 3mm was recorded for all embedment lengths when carbon bars were used. Therefore, as the non-sag Hilti 500 adhesive gave the best results and is particularly suitable for this strengthening methodology, in which vertical injections from the soffit are required, it was decided to proceed with using the Hilti 500 for shear strengthening in combination with the carbon and steel bars. This combination not only offers the best performance, but also provides a strengthening system containing bars with an elastic modulus considerably higher than that of aramid and glass, a desirable property to avoid excessive opening of the shear cracks.

5.3 Small-scale beams (SSB)

As discussed in Chapter 3, a total of ten tests were performed on small-scale specimens strengthened with the deep embedment technique using steel or carbon bars and the Hilti 500 adhesive.

5.3.1 Prestressed specimens

To evaluate the effectiveness of the proposed methodology, two initial tests were performed inserting one 7.5mm carbon or one 8mm steel bar, spaced at 0.7d, in the shear zone of prestressed beams without stirrups loaded at a shear span of 4d, where a gap of 6.5kN exists between the shear capacity of the unstrengtened specimen (USB P4d) and its flexural capacity (see Chapter 4).

The two specimens SSB P4d-C7.5@0.7d and SSB P4d-S8@0.7d failed in flexure, at loads of 42.1kN and 43.8kN respectively, proving that the strengthening scheme can work. In both cases, the crack pattern followed the same path as the unstrengthened specimen, as the flexural cracks formed in the constant moment zone at 15kN and the first diagonal cracks appeared at about 30kN. The presence of the strengthening bars prevented the shear crack from opening (see Figure 5.7, where the red markings indicate the position of the strengthening bars) until ductile flexural failure occurred (see Figure 5.8).

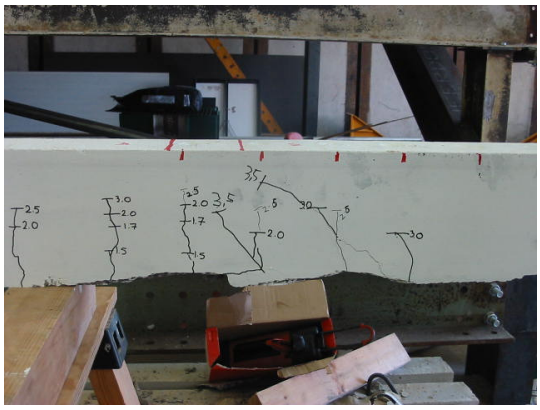

Figure 5.7: Shear cracks in SSB P4d-C7.5@0.7d

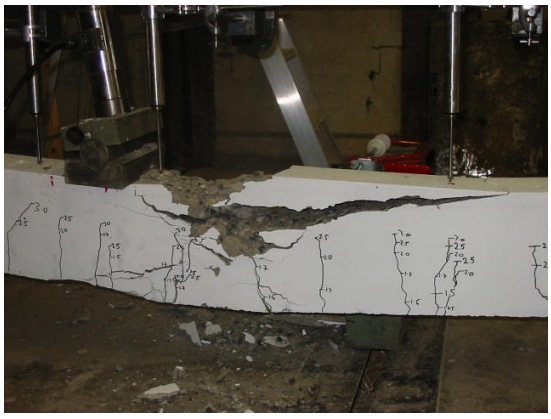

Figure 5.8: SSB P4d-S8@0.7d at failure

Four additional prestressed specimens were then tested at the same shear span length of 4*d* with a reduced amount of strengthening, using 6mm carbon or steel bars spaced at 0.7*d* and 1.0*d*. Again, all specimens failed in flexure, further confirming the effectiveness of the system. Figure 5.9 shows the load-displacement plot for the six strengthened small-scale prestressed specimens together with the equivalent unstrengthened beam loaded at 4*d*.

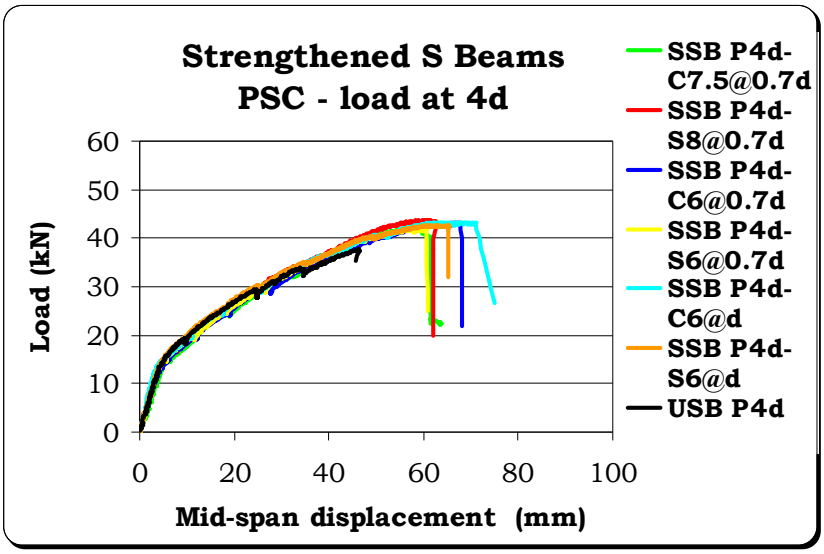

Figure 5.9: Load-displacement plot for the SSB PSC specimens

Similar to the first two specimens, multiple shear cracks formed in both shear spans of the other four beams at a load of about 30kN increasing in number as load increased. These cracks were prevented from opening further by the strengthening bars and, thus, the specimens were forced to a ductile flexural

failure. Generally, when the bar spacing was 0.7*d* a greater number of shear cracks angled at about 45° tended to form (see Figure 5.10), while one or two flatter cracks were noted in the beams with bars spaced at 1.0*d* (see Figure 5.11). This cracking pattern was somewhat similar to the unstrengthened specimen. Nevertheless, the strengthening bars crossed by the cracks were successful in preventing shear failure. It is worth pointing out that the percentage of transverse strengthening for the two specimens with 6mm bars spaced at 1.0*d* (150mm) was very low, equal to 0.171%.

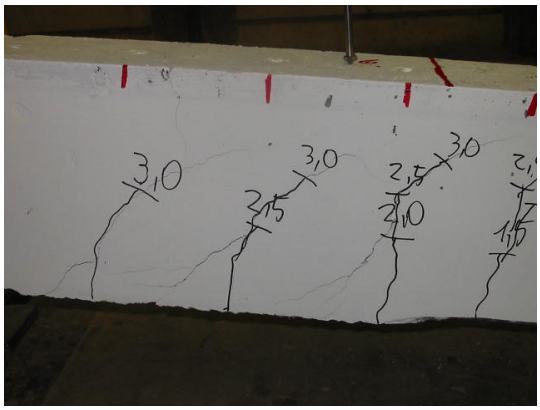

Figure 5.10: Shear cracks in SSB P4d-C6@0.7d

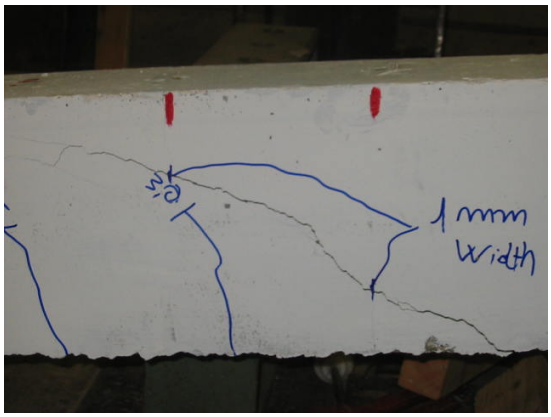

Figure 5.11: Shear cracks in SSB P4d-C6@d

5.3.2 Non-prestressed specimens

In order to further quantify the effectiveness of the system, four tests were performed on non-prestressed beams (one containing stirrups) loaded at 3*d*, where the gap between the shear and flexural capacity in the unstrengthened specimen is higher, i.e. 33kN and 25kN for beams without and with stirrups respectively. Only 6mm carbon bars were used this time, spaced at 0.7, 0.5 or 0.35*d*.

In all four tests, the behaviour was similar to the equivalent unstrengthened specimen (USB R3d) up to the appearance of the first diagonal cracks: the flexural cracks formed in the constant moment zone at 5.5kN and the first diagonal cracks appeared at about 23kN in both shear spans.

Specimen SSB R3d-C6@0.7d, with carbon bars spaced at 105mm, failed in shear at 46.4kN with a remarkable 97% increase over the equivalent unstrengthened specimen; diagonal shear cracks increased in number and width in both shear

spans (see Figure 5.12 showing the right side span at 40kN) until failure occurred in the left side span when three bars crossed by the critical crack debonded from the concrete at approximately 40, 60 and 50mm from the bottom or top edges (see Figure 5.13).

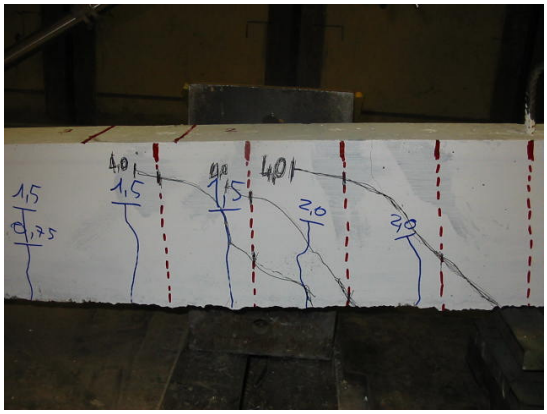

Figure 5.12: Shear cracks in SSB R3d-C6@0.7d

Figure 5.13: SSB R3d-C6@0.7d at failure

Specimen SSB R3d-C6@0.5d, where the bar spacing was 75mm, failed in shear at 50.5kN, representing an increase of 114% compared with the plain specimen. A number of relatively steep diagonal shear cracks formed in both shear spans (see Figure 5.14 showing the right side span at 42kN) and failure occurred in the left side span with four strengthening bars involved in the collapse mechanism but with the critical crack being steeper in between the two central bars that debonded at 60 and 40mm from the bottom and top edge of the beam, respectively (see Figure 5.15).

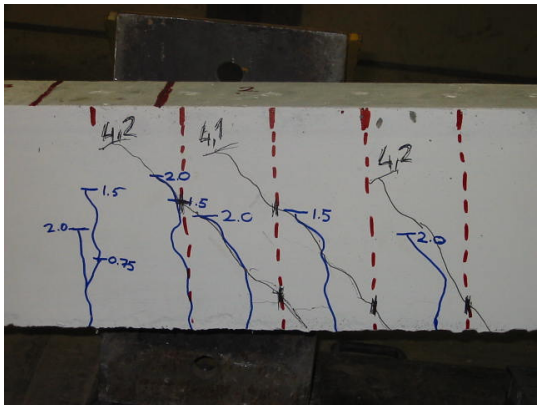

Figure 5.14: Shear cracks in SSB R3d-C6@0.5d

Figure 5.15: SSB R3d-C6@0.5d at failure

A close examination of the debonded part of the bars in the two specimens described above revealed that the bond failure occurred mostly at the adhesive-bar interface (as observed in the bond tests described in the previous section) although there were areas, nearer the concrete surface of the shear plane, where debonding occurred within the concrete itself with the adhesive and a thin ring of concrete about 1mm thick still bonded to the bar.

In specimen SSB R3d-C6@0.35d, with bars spaced at 52.5mm, a number of steep and closely spaced diagonal shear cracks started to form after 25kN in both shear span, considerably increasing in width as the load was increased (see Figure 5.16). The bars were very effective in containing the shear cracks until a relatively ductile flexural failure was initiated by crushing of the concrete in the compression zone at a load of 53.5kN. This was soon followed by the sudden formation of a very flat shear crack from the tip of the compression zone of the left side span that led to final collapse of the beam (see Figure 5.17).

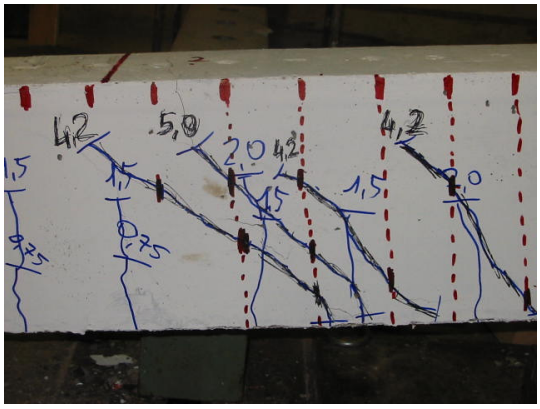

Figure 5.16: Shear cracks in SSB R3d-C6@0.35d

Figure 5.17: SSB R3d-C6@0.35d at failure

Specimen SSB Rst3d-C6@0.7d, with stirrups and strengthening bars spaced at 105mm, failed in flexure at 56.5kN in a ductile manner (see Figures 5.18 and 5.19) after the shear cracks that formed in both spans were successfully contained by the stirrups and the carbon bars. The equivalent unstrengthened specimen with stirrups (USB Rst3d) and the equivalent strengthened specimen without stirrups (SSB R3d-C6@0.7d) failed in shear at 31.5kN and 46.4kN respectively, with an increase of capacity of 8kN and 23kN respectively over the unstrengthened beam without stirrups (USB R3d). As the increased capacity of SSB Rst3d-C6@0.7d was

about 33kN over the unstrengthened specimen without stirrups, it is evident that both stirrups and carbon bars contributed fully to the shear enhancement and that the system was effective even in the presence of existing stirrups.

Figure 5.18: Shear cracks in SSB Rst3d-C6@0.7d

Figure 5.19: SSB Rst3d-C6@0.7d at failure

Figure 5.20 shows the load-displacement plot for the four strengthened small-scale non-prestressed specimens together with the equivalent unstrengthened beam loaded at 3*d*.

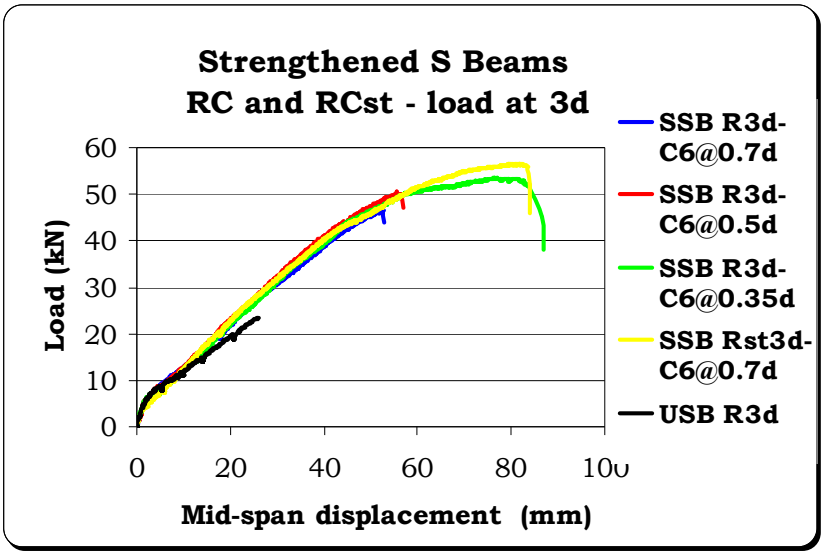

Figure 5.20: Load-displacement plot for the SSB RC and RCst specimens

5.4 Large-scale beams (SLB)

As described in Chapter 3, three of the large-scale beams were strengthened with the deep embedment technique using 7.5mm carbon or 8mm steel bars spaced at *d*; for the purposes of comparison, one beam was strengthened with the NSM technique using the 7.5mm carbon bars. In each specimen, three strain gauges were attached in the strengthening bars in the expected shear-critical locations.

All four specimens behaved in a very similar manner to their unstrengthened counterpart in terms of the appearance of the first flexural cracks (125kN) and the first diagonal shear cracks (between 210 and 230kN).

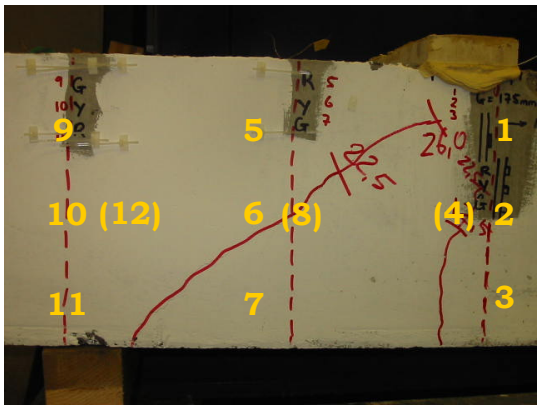

Figure 5.21: Left span of SLB P4d-2C7.5@d at failure

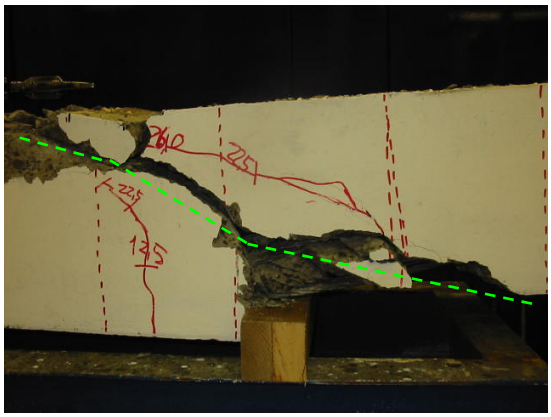

Figure 5.22: Right span of SLB P4d-2C7.5@d at failure

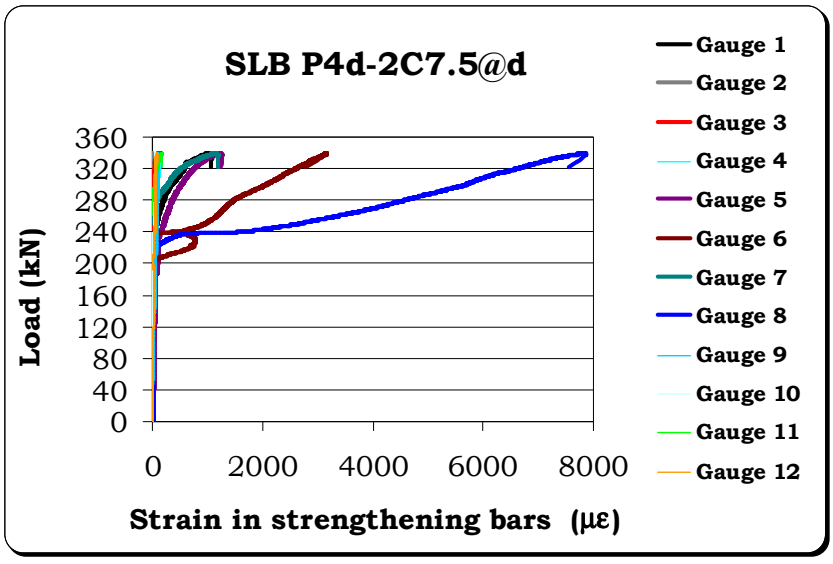

Figure 5.23: Strain gauge measurements in specimen SLB P4d-2C7.5@d

Figures 5.21 and 5.22 show both spans of specimen SLB P4d-2C7.5@d (that contained two 7.5mm carbon bars in each section, see Figure 3.22 of Chapter 3) at failure, where the location of the strain gauges on the carbon bars, that were placed on the left shear span only, have been highlighted; the numbers in brackets indicate the strain gauge on the second bar in the same cross-section. Figure 5.23 shows the strain gauge measurements.

After the appearance of the diagonal shear cracks at 215kN, strain gauges 6 and 8, located in the middle of the bar near the crack in the left span, started to record increasing strains showing both bars in the cross-section were taking load. Gauges 5 and 7, at the top an bottom of the same bar, showed a lower increase in rate of strain. The cracks in both spans grew in width but were successfully constrained by the bars until shear failure occurred in the right side at a load of 339.1kN, with an increased capacity of 43.2kN when compared to ULB P4d, a very good result given that the percentage of transverse shear reinforcement was particularly low, at only 0.076%.

Measurements showed an average value of the strain in the central zone of the critical bar in the left span (gauges 6 and 8) of over 0.004, confirming that the carbon bars in cross-section of a real size beam strengthened with the deep embedment technique can reach this value of strain, which is suggested in the literature and guidelines (ACI 440.2R, 2008; Concrete Society TR55, 2004) as a limiting criteria for FRP strain in shear in order to prevent loss of aggregate interlock.

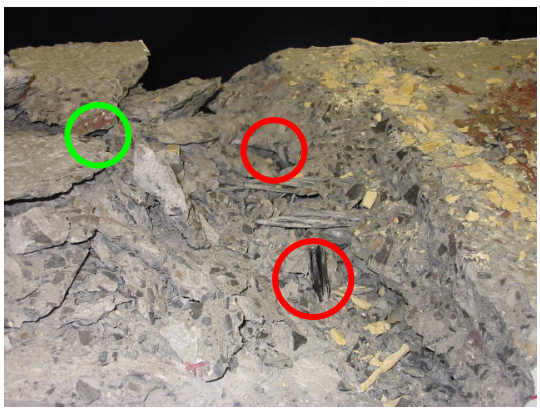

Figure 5.24: Debonded bars in SLB P4d-2C7.5@d

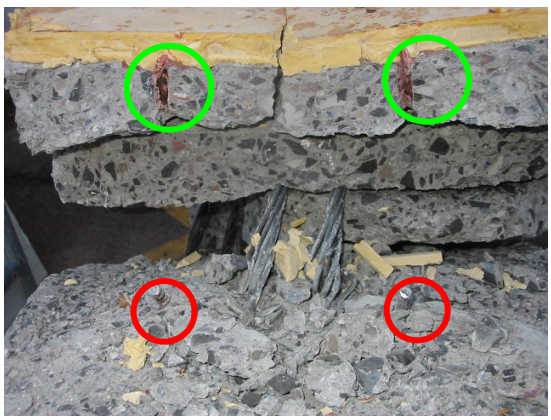

Figure 5.25: Debonded bars in SLB P4d-2S8@d

The shear failure occurred by debonding of the carbon bars from the top or bottom concrete edge with three pairs of bars involved in the mechanism (see Figure 5.22) at 50, 140 and 100mm from the top and bottom surface. Figure 5.24 shows the bars debonded at 50mm from the top concrete surface, revealing that the bond failure occurred at the bar-adhesive interface similar to the bond tests described earlier in the chapter.

Specimen SLB P4d-2S8@d, with two 8mm steel bars in each cross-section, failed in shear at 349.1kN, with an increased capacity of 53.2kN over the equivalent unstrengthened specimen, proving the system can also work with steel bars. Figures 5.26 and 5.27 show the two spans at failure and the position of the strain gauges, with reference to Figure 5.28.

After the first diagonal shear cracks formed at 210kN in both shear spans, strain gauges 1, 2 ,4 and 5 began to read strains. In the right span, the first diagonal crack was the upper one shown in Figure 5.27 passing between gauges 4 and 5. When the load reached about 300kN, a new diagonal crack formed in the right-hand span (the lower one passing between gauges 5 and 6), that was steeper in between two strengthening bars. At failure, strain gauges 4, 5 and 6 showed that the steel bar had yielded, with an average strain in excess of 0.25%. Similar to the previous specimen, the shear failure occurred by debonding of the steel bars from the top or bottom concrete surface with three pairs of bars involved in the mechanism (see Figure 5.27) at 55, 130 and 80mm from the top and bottom surface, respectively. Figure 5.25 shows the bars debonded at 55mm from the top concrete surface, highlighting the bond failure at the bar-adhesive interface.

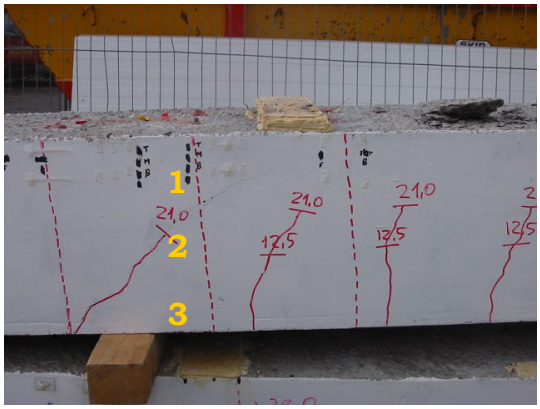

Figure 5.26: Left span of SLB P4d-2S8@d at failure

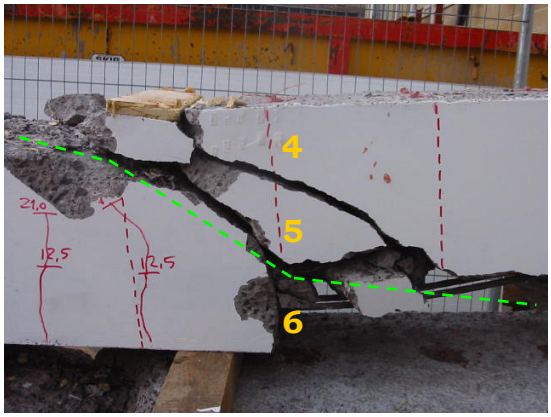

Figure 5.27: Right span of SLB P4d-2S8@d at failure

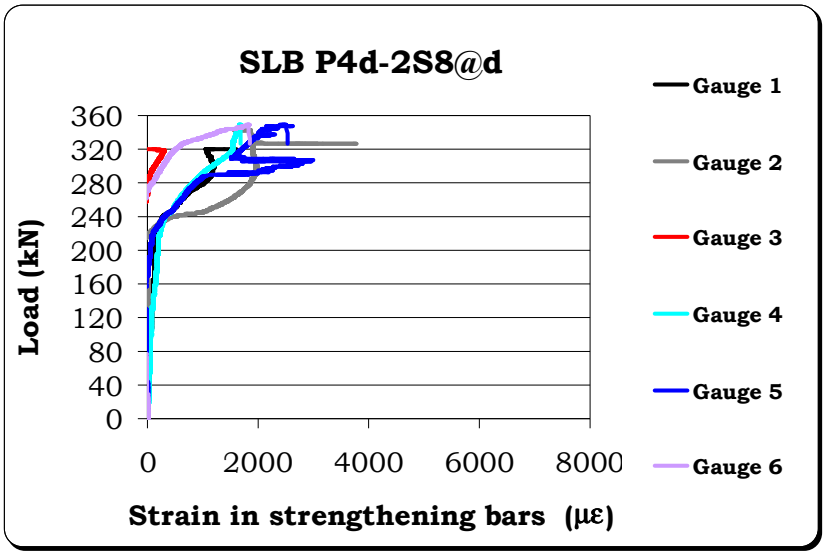

Figure 5.28: Strain gauge measurements in specimen SLB P4d-2S8@d

Photographs at failure and strain gauge measurements for specimen SLB P4d-C7.5@d, with only a single carbon bar per cross-section, are shown in Figures 5.29 to 5.31.

Figure 5.29: Left span of SLB P4d-C7.5@d at failure

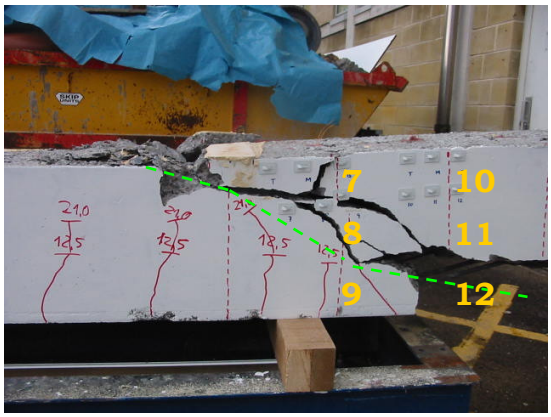

Figure 5.30: Right span of SLB P4d-C7.5@d at failure

The first diagonal cracks formed at 210kN in both shear spans. Similar to specimen SLB P4d-2S8@d, in the right span a second shear crack steeper than the previous, appeared at a load of 280kN crossing gauge 8 (see Figure 5.30). It was this latter crack that led to shear collapse at 315kN, with an increase of 19.1kN over the unstrengthened specimen, a remarkable result given the amazingly low percentage

of transverse shear reinforcement, equal to only 0.038%. This result proves the system to be effective.

The bar most heavily involved with the collapse, equipped with strain gauges 7, 8 and 9, showed an average strain at failure of 0.52%, in excess of the 0.4% limit suggested by codes. As for the two previous specimens, the shear failure occurred by debonding of the carbon bars from the top or bottom concrete surface with three bars involved in the mechanism (see Figure 5.30).

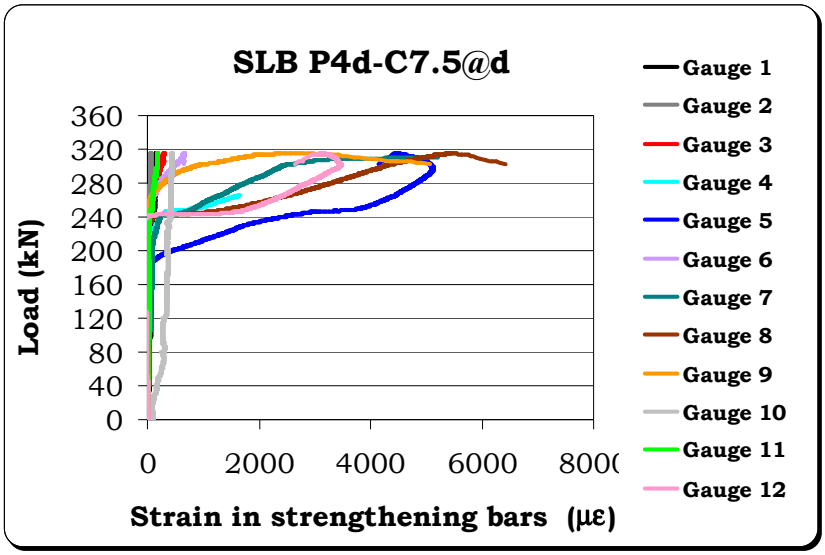

Figure 5.31: Strain gauge measurements in specimen SLB P4d-C7.5@d

Figure 5.32 shows the left span at failure for specimen SLB P4d-2C7.5N@d, strengthened with the NSM technique with two 7.5mm carbon bars on each cross-section, with the results of the strain gauge measurements shown in Figure 5.36.

After the first diagonal shear cracks appeared at about 230kN, strain gauges 3, 4, 6 and 7, located in the two bars in the same cross-section (see Figure 5.32), began to read strains. As the load increased, the critical shear crack in the left span grew in width and a sensible growth in strain was recorded in all twelve gauges, as most of them were located in close proximity to the crack. Shear failure occurred in the left-hand span at a load of 325.4kN, with an increased capacity of 29.5kN compared to the unstrengthened specimen but with a reduction of 13.7kN compared to the equivalent beam strengthened with the deep embedment technique.

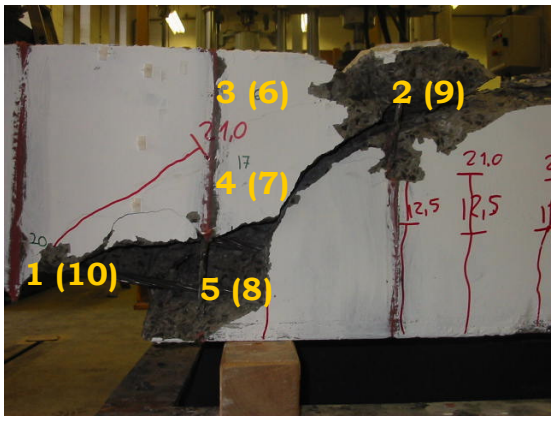

Figure 5.32: Left span of SLB P4d-2C7.5N@d at failure

Figure 5.33: Cover spalling in SLB P4d-2C7.5N@d (1)

Figure 5.34: Cover spalling in SLB P4d-2C7.5N@d (2)

Figure 5.35: Cover spalling in SLB P4d-2C7.5N@d (3)

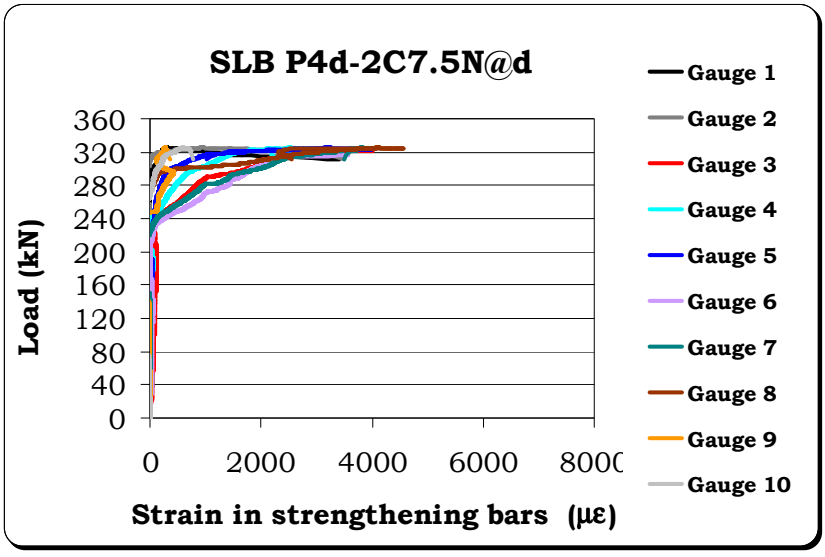

Figure 5.36: Strain gauge measurements in specimen SLB P4d-2C7.5N@d

Although the NSM system significantly enhanced the shear capacity, the deep embedded system offered better performance; this can be explained by the fact that the failure in the beams with NSM bars involved some spalling of the concrete side cover, particularly at the ends of the shear crack in the bar anchorage locations, preventing the bars from developing full bond capacity (see Figures 5.33 to 5.35). Strain gauge readings on the bars crossed by the critical cracks revealed that at failure the carbon bars had reached an average strain of 0.35%.

Figure 5.37 shows the load-displacement plot for the four strengthened large-scale beams specimens together with the equivalent unstrengthened beams loaded at 4*d*.

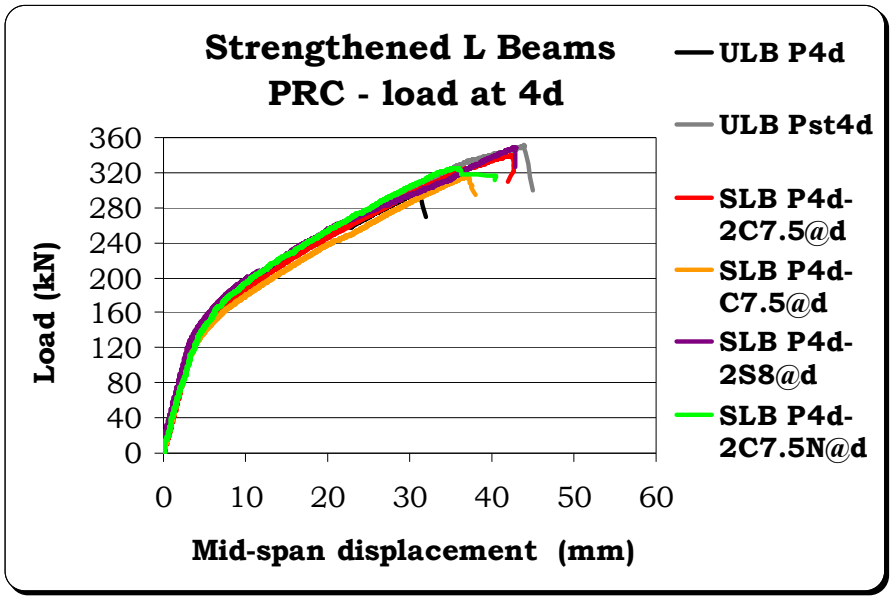

Figure 5.37: Load-displacement plot for the SLB specimens

5.5 Discussion and concluding remarks

From the test results on the small- and large-scale specimens strengthened with the deep embedment system, the following observation can be made:

- The proposed shear strengthening approach was shown to be a feasible and extremely effective system for both prestressed and non-prestressed beams of any size. The strengthened small-scale test specimens were either led to flexural failure or their shear capacity was enhanced by a minimum of 97% compared with the equivalent unstrengthened situation, even with a

percentage of strengthening reinforcement as low as 0.24%. The shear capacity of real-size prestressed beams could be enhanced by 15% even with a minimal percentage of strengthening reinforcement, equal to 0.08%.

- Because the strengthening is internal, shear failure occurs only when the bars debond from the concrete and, thus, a better bond capacity can be obtained compared to the NSM technique, where early separation of the concrete side cover can reduce the bond effectiveness. A series of pull-out tests have shown that the bond-slip response of the system is robust, when appropriate adhesives and aptly surfaced bars are used.

- The technique can work and be fully efficient even in the presence of existing stirrups, as the contribution to the shear capacity has been shown to be equal to the sum of the maximum contribution due to the stirrups and the strengthening bars alone in one of the small-scale specimens. This is due to the ductility of the bond-slip response of the deep embedment system, so that it is possible to rely on a sustained value of bond stress even for large crack widths (and, therefore, large slips) allowing the steel stirrups to yield.

- No major differences were found between the beams reinforced with steel bars and the ones reinforced with CFRP, but the use of FRP is suggested due to its light weight, allowing easy installation, and its corrosion resistance.

Chapter 6
Analytical Procedure

6.1 Introduction

The test results on the small-scale bridges, presented in the previous chapters, have shown that the lateral confinement offered by the lateral prestressing on these bridge types can be very effective in increasing the ultimate shear capacity of the single beam. This is ignored by the codes because no method is presently available for assessing such laterally prestressed beams; a theoretical method that explicitly models this effect is therefore desirable.

In this chapter, a unified analytical approach employing plasticity theory is applied to the single beams and bridges to produce a rational assessment tool for shear capacity predictions of these structures. The same model is then extended to the beams strengthened with the deep embedment technique and a simplified method is presented that can be easily incorporated in the existing codes of practice to assist in the design of the strengthening scheme.

6.2 Plasticity theory for concrete

6.2.1 Assumptions and formulation

As mentioned in Chapter 2, plasticity theory has been successfully applied to reinforced and prestressed concrete over many years, with excellent predictions obtained (Nielsen, 1999; Nielsen and Bræstrup, 1978; Ibell et al., 1997a, 1997b, 1997c, 1998a, 1998b, 1999). Indeed, most of the provisions of Eurocode 2 (2004) are based on lower-bound plasticity solutions.

Although plasticity may not immediately appear to be applicable to concrete structures due to their possible lack of ductility, the adoption of an appropriate effectiveness factor υ to the compressive concrete strength can overcome this

problem. It is not possible for a concrete structure to undergo large deformations at a constant stress level, which is a condition of the rigid-plastic behaviour assumed in the plasticity theory, because the stress-strain curve for concrete in compression has a relatively short falling branch beyond its ultimate strength. However, if we use for the strength a value appropriately lower than the peak and assume the concrete can withstand this 'effective' stress indefinitely, plasticity theory can be used.

While lower-bound methods are well suited to design situations as they provide safe estimates of the structural strength, it is often difficult to optimise the solution in the case of more complex structures. Therefore, it is believed that upper-bound methods, which consider the actual mechanism of collapse, offer a greater potential in the case of assessment, especially when the solutions can be analytically minimised and an 'exact' solution found.

The objective of an upper-bound analysis is to predict the shape of the yield lines at failure, defined as lines dividing rigid blocks of concrete along which discontinuities of displacement occur. The internal energy dissipated along the yield lines is equated to the external work done by the loads acting over the rigid blocks, which can translate or rotate according to the assumed compatible mechanism. Minimisation of the collapse load reveals the optimum shape of the yield lines.

As mentioned in Chapter 2, in plasticity theory the concrete is assumed to obey the modified Mohr-Coulomb failure criterion (shown in Figure 2.5), with sliding failure occurring when the motion has a component parallel to the yield line and separation failure occurring when the motion is perpendicular to the yield line. The internal angle of friction is equal to $\varphi = 37°$ for normal concrete (Nielsen, 1999). The tensile strength of concrete is very low and its ductility in tension extremely limited; therefore, it is prudent to disregard it and adopt the modified Mohr-Coulomb criterion with zero tension cut-off. The steel bars (longitudinal and transverse) are assumed to carry axial tension forces only, with any dowel effect ignored.

The energy dissipated along the yield lines in the concrete structure is directly related to the resultant relative displacement δ between two concrete blocks in a zone of discontinuity (see Figure 6.1). The resultant is inclined at an angle α to the yield line and can vary in magnitude and direction along the yield lines, subject to compatibility requirements.

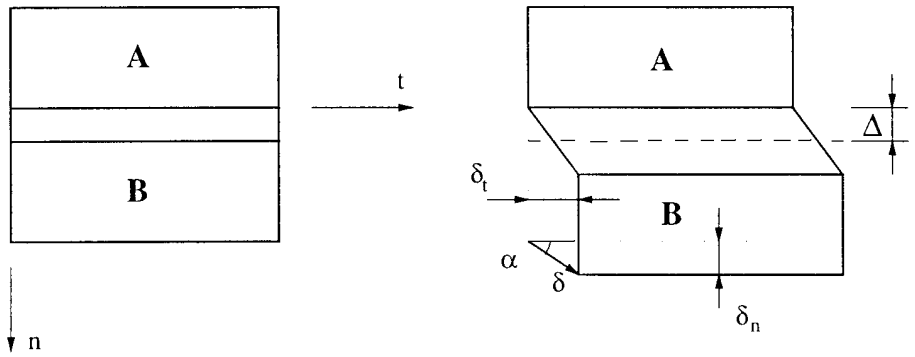

Figure 6.1: Discontinuity between two concrete rigid blocks under relative displacement (after Ibell et al., 1997c)

When the modified Mohr-Coulomb criterion is written in terms of principal stresses and the corresponding dissipation per unit volume of concrete is considered by multiplying the principal stresses by the principal strains for both conditions of plane stress and plane strain, it can be demonstrated analytically (Nielsen, 1999) that, if all the plastic strain flow is assumed to occur in a thin layer of thickness Δ between the blocks (see Figure 6.1) and the tensile strength of the concrete is disregarded, the energy dissipation per unit length of yield line is equal to:

$$ED_{c,unit} = \delta \left(\frac{1 - \sin\alpha}{2}\right) b f_c \tag{6.01}$$

where f_c is the compressive strength of the concrete, b is the width of the concrete block and the angle α to the discontinuity is comprised between $-\pi/2$ and $\pi/2$. It can also be shown that if conditions of plane strain exist, the angle α to the discontinuity must not be lower than φ, while for plane stress conditions there is no such limit. In practical terms, the difference is explained by the fact that in plane strain protruding aggregates must slide over each other for the displacement to take place, and this is not possible when the relative displacement is lower than the internal friction angle. However, there is no out of plane restraint in plane stress conditions, hence the aggregates are free to slide sideways even for values lower than φ.

The energy dissipated in the longitudinal and transverse reinforcement is the product of the yield force in the reinforcement at the discontinuity position and the component of the relative displacement between the concrete blocks in the axial direction of the bars. No energy is assumed to be dissipated by shear or bending in

the steel. Therefore, the total energy dissipation, ED, is found by summing that due to concrete, ED_c, integrated along the shear lines of discontinuity, and that of the steel, ED_s:

$$ED_c = \int_l \delta \left(\frac{1 - \sin a}{2}\right) b f_c dx \tag{6.02}$$

$$ED_s = \sum_n A_{si} f_{yi} \delta_{si} \tag{6.03}$$

where l is the total length of the discontinuity, n is the total number of steel bars crossed by the discontinuity and δ_{si} is the notional length that each bar, i, has stretched.

6.2.2 Upper-bound approaches for beams in shear

Most of the early work investigating the possibilities of utilising the theory of plasticity for the determination of the shear strength of reinforced concrete beams has been conducted in Denmark by Nielsen and his research group (Nielsen, 1999).

For beams with and without stirrups subjected to four point loading, upper-bound and lower-bound solutions have been formulated by Nielsen and Bræstrup (1975). For beams with constant shear reinforcement degree, $\psi = A_{sv} f_{yw} / bsf_c$, they considered a simple displacement field where the central part of the beam, I, undergoes a relative downward vertical displacement δ with respect to part II along two straight symmetrical yield lines (see Figure 6.2).

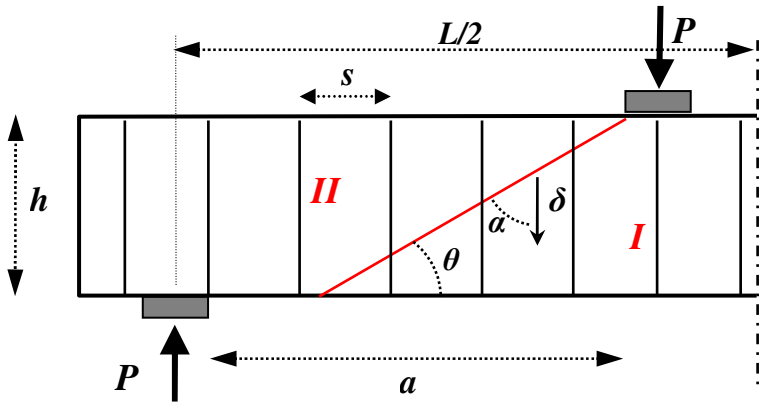

Figure 6.2: Symmetrical shear failure mechanism with straight yield lines and vertical displacement

Equating the external work done $WD = P\delta$ to the sum of the internal energy dissipation in the concrete $ED_c = 0.5bf_c(1-\cos\theta)\delta\,(h/\sin\theta)$ and that in the stirrups $ED_s = A_{sf}f_{yw}\,h\cot\theta\,\delta/s$ and minimizing the solution with respect to the angle θ, it is found that:

$$\cot\theta = \frac{1 - 2\psi}{2\sqrt{\psi(1-\psi)}} \tag{6.04}$$

and the capacity is

$$\frac{\tau}{f_c} = \frac{P}{bhf_c} = \sqrt{\psi(1-\psi)} \tag{6.05}$$

which is a solution valid for $(h/a) \le \tan\theta \le \infty$. When $(h/a) = \tan\theta$, the yield line runs from the load to the support; the corresponding shear reinforcement degree is equal to:

$$\psi_0 = \frac{\sqrt{a^2 + h^2} - a}{2\sqrt{a^2 + h^2}} \tag{6.06}$$

and the capacity becomes:

$$\frac{P}{bhf_c} = \frac{1}{2}\left[\sqrt{1+\left(\frac{a}{h}\right)^2} - \frac{a}{h}\right] + \psi\frac{a}{h} \tag{6.07}$$

When $\tan\theta = \infty$ the yield line is vertical and both ψ and τ/f_c are equal to 0.5, which is the upper limit of the shear capacity.

When the effectiveness factor υ is applied to the concrete strength, the shear capacity becomes:

$$\frac{P}{bhf_c} = \frac{1}{2}\upsilon\left[\sqrt{1+\left(\frac{a}{h}\right)^2} - \frac{a}{h}\right] + \psi\frac{a}{h} \qquad \text{for } \psi/\upsilon \le \psi_0 \tag{6.08}$$

$$\frac{P}{bhf_c} = \sqrt{\psi(\upsilon - \psi)} \qquad \text{for } \psi_0 \le \psi/\upsilon \le 0.5 \tag{6.09}$$

$$\frac{P}{bhf_c} = \frac{\upsilon}{2} \qquad \text{for } \psi/\upsilon \ge 0.5 \tag{6.10}$$

The same solution is obtained by maximising the results of a lower-bound model where a uni-axial diagonal compression field in the concrete struts is put in equilibrium with the stirrups and the longitudinal steel acting in tension; the solution is therefore theoretically exact.

When no stirrups are present, the minimum upper-bound is found for $(h/a) = \tan\theta$, and is equal to:

$$\frac{P}{bhf_c} = \frac{1}{2}\nu \left[\sqrt{1+(\frac{a}{h})^2} - \frac{a}{h}\right] \tag{6.11}$$

The above solutions assume that the relative displacement at failure is vertical, so there is no contribution from the longitudinal steel bars to the shear capacity. For beams without stirrups, if the relative displacement δ is assumed to be not vertical (so that $\alpha+\theta > 90°$), it can be shown (Jensen et al, 1978) that the shear capacity can depend on the degree of longitudinal reinforcement $\Phi = A_{sl}f_{yl}/bhf_c$ and is equal to:

$$\frac{P}{bhf_c} = \frac{1}{2}\nu \left[\sqrt{4\frac{\Phi}{\nu}(1-\frac{\Phi}{\nu})+(\frac{a}{h})^2} - \frac{a}{h}\right] \qquad \text{for } \Phi/\nu \le 0.5 \tag{6.12}$$

$$\frac{P}{bhf_c} = \frac{1}{2}\nu \left[\sqrt{(1+(\frac{a}{h})^2} - \frac{a}{h}\right] \qquad \text{for } \Phi/\nu \ge 0.5 \tag{6.13}$$

Therefore, when the degree of longitudinal reinforcement is sufficiently high it does not influence the shear capacity of the beam, according to the theory of plasticity.

When stirrups are present, the most general solution is given by (Nielsen et al., 1978):

$$\frac{P}{bhf_c} = 2\nu\sqrt{\frac{\psi}{\nu}(1-\frac{\psi}{\nu})}\sqrt{\frac{\Phi}{\nu}(1-\frac{\Phi}{\nu})} \qquad \text{for } \psi_0 \le \psi/\nu \le 0.5 \text{ and } \Phi/\nu \le 0.5 \tag{6.14}$$

$$\frac{P}{bhf_c} = \frac{1}{2}\nu \left[\sqrt{4\frac{\Phi}{\nu}(1-\frac{\Phi}{\nu})+(\frac{a}{h})^2} - \frac{a}{h}\right] + \psi\frac{a}{h} \qquad \text{for } \Phi/\nu \le 0.5 \text{ and } \psi/\nu \le \psi_0 \tag{6.15}$$

$$\frac{P}{bhf_c} = \frac{1}{2}\nu \left[\sqrt{1+(\frac{a}{h})^2} - \frac{a}{h}\right] + \psi\frac{a}{h} \qquad \text{for } \Phi/\nu \ge 0.5 \text{ and } \psi/\nu \le \psi_0 \tag{6.16}$$

In (6.14), if $\psi/\nu \ge 0.5$ and $\Phi/\nu \ge 0.5$, the second and third factors, respectively, are replaced by 0.5.

Following an extensive test campaign it was found (Nielsen, 1999) that for beams containing a sufficient amount of stirrups (i.e. where the degree of vertical reinforcement ψ is not lower than $\nu\psi_0$, 0.05ν or $0.16/\sqrt{f_c}$), the effectiveness factor can be taken as:

$$\upsilon = 0.8 - \frac{f_c}{200} \qquad \text{for RC beams} \qquad (6.17)$$

$$\upsilon = (0.8 - \frac{f_c}{200})(1 + 2.2\frac{\sigma_{cp}}{f_c}) \qquad \text{for PSC beams} \qquad (6.18)$$

where σ_{cp} is the average concrete stress due to prestressing after all losses, f_c is the compressive cylinder strength of the concrete (in MPa) and υ should not exceed unity. Expression (6.17) has been implemented in Eurocode 2 (2004) where, conservatively, 0.8 has been replaced with 0.7.

For beams without transverse reinforcement, the following formula was proposed (Nielsen, 1999) which accounts for the size effect, the amount of longitudinal reinforcement and the shear span depth:

$$\upsilon_0 = (\frac{3.5}{\sqrt{f_c}})(0.27 + \frac{0.27}{\sqrt{h}})(0.15\frac{A_{sl}}{bh} + 0.58)(1 + 0.17(\frac{a}{h} - 2.6)^2)(1.1 + 0.81\sigma_{pe} / f_{yl}) \qquad (6.19)$$

The above expression is valid for $5 < f_c < 60$ (in MPa), $0.08 < h < 0.7$ (in metres), $A_{sl}/bh < 4.5\%$ and $a/h < 5.5$; σ_{pe} is the stress in the prestressing steel after all losses and f_{yl} is the yield strength of the prestressing steel.

6.2.2.1 Sliding in cracks

Zhang (1997) developed a theory for beams without stirrups from the observation that shear failure is usually characterised by the formation of a critical shear crack leading to sliding failure. The sliding strength of concrete can be substantially reduced at a crack location, and so the resulting yield line in this crack may be more critical than those predicted by the classic plasticity theory.

The load magnitude required to form shear cracks is lower for cracks near the load and higher for cracks near the support, so, for different shear span lengths, the cracking load curve takes the shape shown in Figure 6.3. However, the load required to develop a sliding failure in a crack varies depending on the position of the crack, because for a crack close to the support the crack angle is flatter and the capacity is lower than for a crack starting closer to the load, as illustrated in the shear capacity curve of Figure 6.3. The intersection of the curves provides the critical crack position where a crack may form and develop into a shear failure discontinuity at the minimum load-carrying capacity. If the curves do not intersect the capacity is represented by the minimum value of the capacity curve.

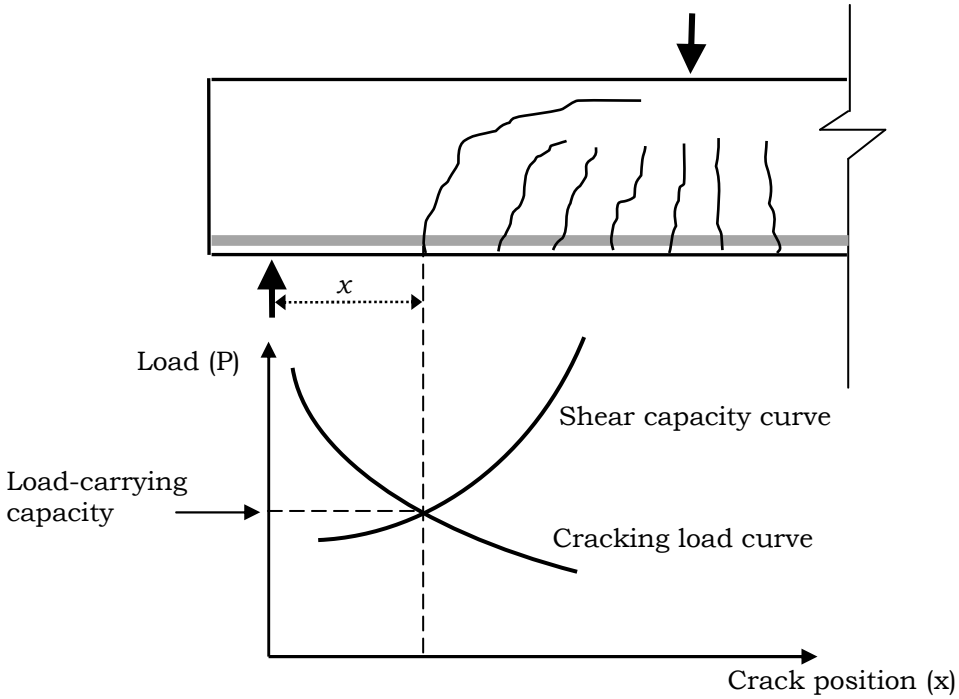

Figure 6.3: Cracking and capacity curves for beams without shear reinforcement according to Zhang's (1997) theory of sliding in cracks

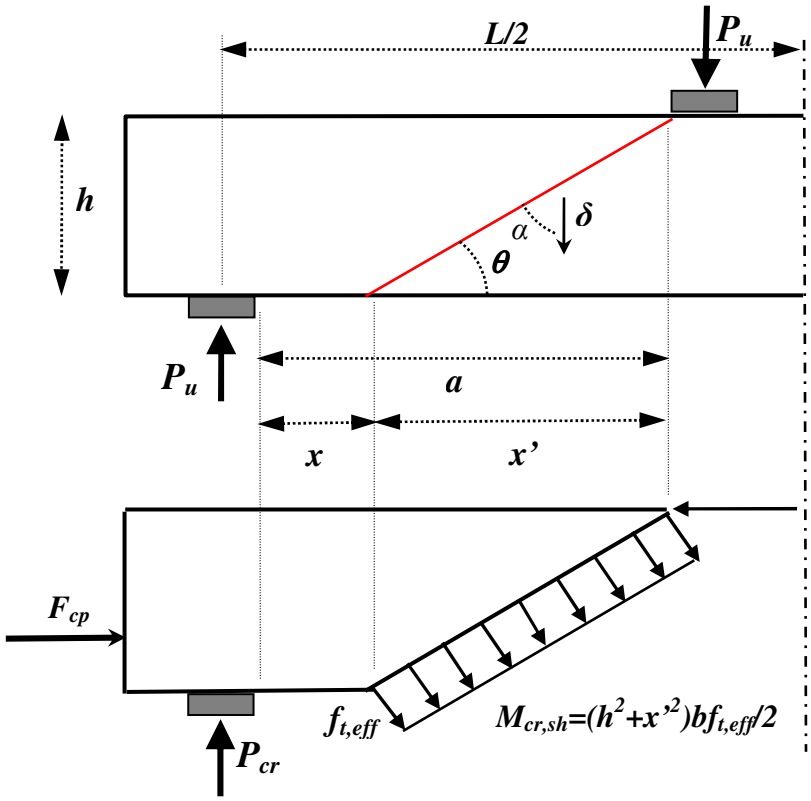

Figure 6.4: Shear capacity and shear cracking capacity according to Zhang's (1997) theory

The shear capacity curve is calculated assuming a straight yield line and a vertical relative displacement, which implies the longitudinal reinforcement is sufficiently strong (as discussed previously). With reference to Figure 6.4, for different values of the yield line position $x = a\text{-}x'$ the minimised critical capacity P_u is given by:

$$P_u = \frac{1}{2} bhf_c v \left[\sqrt{1+\left(\frac{a-x}{h}\right)^2} - \frac{a-x}{h}\right] \tag{6.20}$$

The value of x is found by equating equation (6.20) with the following expression for the cracking load:

$$P_{cr} = \frac{1}{2} bhf_{t,eff} \frac{\left(\frac{a-x}{h}\right)^2 + 1}{(l_o / 2h) + a/h} \tag{6.21}$$

where l_o is the length of the loading platen and $f_{t,eff}$ is the effective concrete tensile strength, assumed equal to:

$$f_{t,eff} = 0.6 f_t \left(\frac{h}{0.1}\right)^{-0.3} \tag{6.22}$$

where $f_t = 0.26\, f_c^{2/3}$ is the concrete tensile strength in MPa and h is in metres. As shown in Figure 6.4, the shear cracking load of (6.21) is found from a moment equilibrium about the tip of the crack assuming that the shear cracking moment $M_{cr,sh}$ along the yield line is evaluated from an equivalent plastic tensile stress distribution neglecting the depth of the compression zone. The value of x that satisfies both (6.20) and (6.21) is that representing the critical shear capacity.

If the beam is prestressed, the critical capacity is still given by equation (6.20), while the cracking load is found from (see Figure 6.4):

$$P_{cr} = \frac{1}{2} bhf_{t,eff} \frac{\left(\frac{a-x}{h}\right)^2 + 1}{(l_o / 2h) + a/h} + \frac{F_{cp} d_p / h}{(l_o / 2h) + a/h} \tag{6.23}$$

where d_p is the distance from the top concrete face to the centroid of the prestressing force.

According to Zhang (1997), the effectiveness factor v to be used for beams without stirrups is equal to the product of v_0 and v_s, where v_0 is the effectiveness factor if the concrete is uncracked and is equal to:

$$v_0 = \lambda \frac{3.5}{\sqrt{f_c}} 0.27\left(1+\frac{1}{\sqrt{h}}\right)(0.15\rho + 0.58)\left(1 + 2\frac{\sigma_{cp}}{f_c}\right) \tag{6.24}$$

where λ is a constant factor depending on the loading type and σ_{cp} is the average concrete stress due to prestressing after all losses; the limits of validity of the various factors are the same as those in (6.19). The factor υ_s, taken equal to 0.5, is the reduction in capacity of cracked concrete and represents the maximum reduction in the cohesion in a crack observed experimentally from push-off tests (Zhang, 1997), while no substantial change in the friction angle was observed in the cracked concrete. Crack sliding is assumed as a plane strain problem, so the angle α to the discontinuity must not be lower than φ.

The theory of sliding in cracks is particularly suited to slender beams where the likelihood of shear failures occurring in cracked zones is maximum, while for shorter spans the classic theory may be more appropriate. Nielsen (1999) pointed out that the theory of sliding in cracks is important since, even if the tensile strength of concrete is disregarded, a sliding strength remains in the cracks and, in the most conservative case, it is possible to rely on the classic solution where the yield line goes from load to support but with an effectiveness factor reduced from υ_0 to $\upsilon_0\upsilon_s$.

Hoang and Nielsen (1998) extended the theory of sliding in cracks to lightly reinforced beams, defined as beams where the degree of transverse reinforcement ψ is lower than $\upsilon\psi_0$, 0.05υ or $0.16/\sqrt{f_c}$. In such beams, according to the classic plasticity theory the diagonal stress field at failure has a very low inclination and therefore the effective concrete stress has to be transferred through a series of possibly heavily cracked concrete regions; the initiation of sliding failures in cracks is therefore likely, leading to lower capacities than in beams with a sufficient amount of stirrups. In fact, codes of practice that employ the variable angle truss model limit the value for $\cot\theta$ ensuring a minimum amount of stirrups is provided.

Therefore, for lightly reinforced beams it may be prudent to calculate the shear capacity using the theory of sliding in cracks. The cracking load curve is still given by (6.21) while the shear capacity curve is given by:

$$P_u = \frac{1}{2} bhf_c\upsilon \left[\sqrt{1+\left(\frac{a-x}{h}\right)^2} - \frac{a-x}{h}\right] + \psi\frac{a-x}{h} \qquad (6.25)$$

where the degree of transverse reinforcement has been taken into account. However, the theory treats the stirrups in a 'smeared' approach while in lightly reinforced beams stirrups are often excessively far apart. To take into account finite

stirrup spacing, the distance $x' = a-x$ has to be replaced by Ns, where s is the stirrup spacing and N is the number of stirrups in the distance x'; conservatively, a value of $a-x-s$ can be assumed when stirrups spacing is large. Also, to take into account the fact that the stirrups act over an effective depth d_s rather than the whole section depth h, the second term in the right-hand side of the equation should be multiplied by d_s/h. Hoang and Nielsen (1998) suggested that it is prudent to adopt the crack sliding approach for values of the shear reinforcement degree up to $0.25v_0$, because for higher degrees yielding of stirrups at failure has not been detected, indicating that crack sliding did not take place.

6.2.2.2 Other upper-bound models

Ashour (2000) presented a solution for simply supported RC deep beams in shear where the shape of the yield line, that goes from load to support, is a hyperbola, and a relative rotation is assumed between the rigid blocks *I* and *II* (see Figure 6.5). The energy dissipated in the concrete in the mechanism of Figure 6.5 is equal to:

$$ED_c = \left(\frac{1-\sin\alpha}{2}\right) bvf_c L_c \omega r \tag{6.26}$$

where L_c is the chord length of the yield line, r is the distance between the midpoint of the chord and the instantaneous centre of rotation O' and ω is the notional relative rotation. When the instantaneous centre O' lies inside a circle of diameter equal to L_c, the yield line turns into two straight segments that intersect at the instantaneous centre (Ashour, 2000).

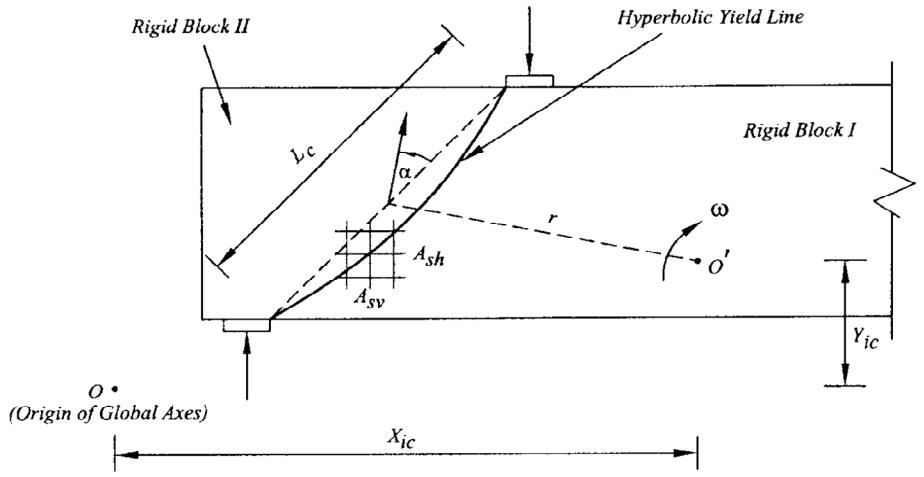

Figure 6.5: Shear failure involving hyperbolic yield lines (after Ashour, 2000)

However, when the main longitudinal reinforcement is sufficiently strong that it does not yield at failure, the instantaneous centre lies at its level. In this case, by equating the energy dissipation due to the concrete and the transverse reinforcement with the external work done, the solution is:

$$\frac{P}{bhf_c} = \frac{1}{|X_{ic}|}\left[\frac{\upsilon}{2h} L_c r(1 - \sin\alpha) + \sum_{i=1}^{N} \frac{A_{vi} f_{vi}}{bhf_c} |X_i - X_{ic}|\right] \tag{6.27}$$

where X_i and X_{ic} are the horizontal coordinate of each transverse bar crossing the yield line and of the instantaneous centre of rotation, respectively. By varying the position of the instantaneous centre along the horizontal line of the bottom longitudinal reinforcement, the minimum value of the shear capacity can be obtained. Using an effectiveness factor of υ = 0.5, good correlation was found with a range of test results in literature on deep beams with shear span ratio of 0.28 to 2. A parametric study (Ashour, 2000) revealed that, when the degree of longitudinal reinforcement Φ is greater than 0.1, its influence over the shear capacity becomes negligible. Also, it was found that the influence of the stirrups is greater when the shear span increases.

Ibell et al. (1997a, b, c; 1998a, b; 1999) developed an analytical tool for the assessment of concrete beam-and-slab structures employing an upper-bound plasticity model able to account for the different failure patterns observed experimentally on a series of small- and large-scale bridge models. For the single beams, the shear failure mechanism model is shown in Figure 6.6, where the beam is divided into five horizontal layers.

At each level through the beam depth an ordinate is chosen and a line is drawn from each point to the next representing the yield line discontinuity. The two separated rigid beam blocks are assumed to rotate by η_1 and η_2 and the right hand block can move horizontally by u_h. The geometry of the yield line is varied by moving the x-ordinates and then, for each configuration, by selecting various values of the relative rotations and displacement. The energy dissipated in the concrete and in the longitudinal and transverse steel, calculated using (6.02) and (6.03), is divided by the work done by the external loading and the ratio is finally minimised numerically to obtain the shear capacity.

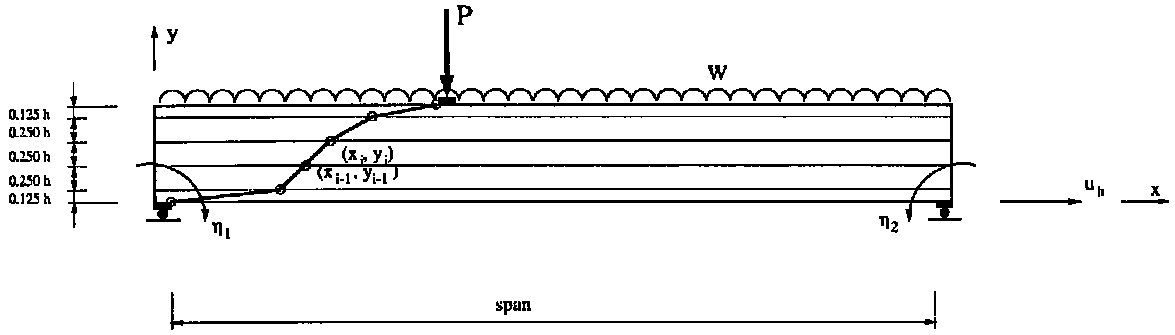

Figure 6.6: Shear failure mechanism model (after Ibell et al., 1997c)

Ibell et al (1997b) proposed a formula to calculate the concrete effectiveness factor for RC beams, as a function of the percentage of longitudinal and transverse reinforcement, concrete strength, shear span length and size effect. For slender beams with $a/d > 2.5$, the proposed effectiveness factor is:

$$\upsilon = 0.35(\sqrt{0.35 + 0.32\rho_s})(\sqrt{1 + 1.5\rho_{sv}})(2.4 - 0.04 f_{cu})(0.2 + 0.2(a/d))^{1.5}(0.35\sqrt{1 + \frac{1000}{h}}) \quad (6.28)$$

where $0.8 < \rho_s = A_s/bd < 4$, $\rho_{sv} = 100A_{sv}/bs < 0.6$, $20 < f_{cu} < 45$ (f_{cu} is the cubic characteristic concrete strength in MPa) and $80 < h < 700$ (with h in mm). For beams subject to a concentrated load, it was found that the critical shear failure mechanism generally involves only a vertical relative displacement between the rigid blocks.

6.3 Analysis of the unstrengthened beams

Table 6.1 summarizes the degrees of vertical and longitudinal reinforcement and the effectiveness factors for the small-scale, large-scale and real beams of the reference bridge when assumed to be loaded at 3, 4, 5 and 6d, with and without stirrups. The effectiveness factors are calculated with the formulae described in the previous section for beams in shear under concentrated loads according to the classic theory (Nielsen, 1999), the theory of sliding in cracks with $\lambda = 1.2$ (Zhang, 1997) and the formula proposed by Ibell et al. (1997b). For the real beams, the degree of vertical reinforcement is 0.014 but it reduces to 0.010 if the stirrups spaced laterally in excess of d are disregarded in accordance with NR/GN/CIV/025 (2006), as discussed in Chapter 3.

Table 6.1: Reinforcement degrees and effectiveness factors for all beams

Specimen	Ψ *(vert)*	Φ *(long)*	v_0 *(classic)*	v *(sliding)*	v *(Ibell et al.)*
	Small-scale RC beams				
USB R3d	NA	0.199	0.304	0.243	0.219
USB R4d	NA	0.199	0.320	0.243	0.307
USB R5d	NA	0.199	0.398	0.243	0.403
USB R6d	NA	0.199	0.540	0.243	0.508
USB Rst3d	0.012	0.199	0.550	0.243	0.239
USB Rst4d	0.012	0.199	0.550	0.243	0.335
USB Rst5d	0.012	0.199	0.550	0.243	0.434
USB Rst6d	0.012	0.199	0.550	0.243	0.554
	Small-scale PSC beams				
USB P3d	NA	0.199	0.522	0.208	0.219
USB P4d	NA	0.199	0.549	0.208	0.307
USB P5d	NA	0.199	0.683	0.208	0.403
USB P6d	NA	0.199	0.927	0.208	0.508
USB Pst3d	0.012	0.199	0.633	0.208	0.239
USB Pst4d	0.012	0.199	0.633	0.208	0.335
USB Pst5d	0.012	0.199	0.633	0.208	0.434
USB Pst6d	0.012	0.199	0.633	0.208	0.554
	Large-scale PSC beams (3d and 5d not tested)				
ULB P3d	NA	0.213	0.359	0.177	0.083
ULB P4d	NA	0.213	0.362	0.177	0.117
ULB P5d	NA	0.213	0.408	0.177	0.153
ULB P6d	NA	0.213	0.516	0.177	0.193
ULB Pst3d	0.019	0.213	0.670	0.177	0.094
ULB Pst4d	0.019	0.213	0.670	0.177	0.133
ULB Pst5d	0.019	0.213	0.670	0.177	0.174
ULB Pst6d	0.019	0.213	0.670	0.177	0.220
	Real PSC beams (not tested)				
P3d	NA	0.170	0.302	0.135	0.061
P4d	NA	0.170	0.310	0.135	0.085
P5d	NA	0.170	0.383	0.135	0.112
P6d	NA	0.170	0.541	0.135	0.141
Pst3d	0.014	0.170	0.671	0.135	0.066
Pst4d	0.014	0.170	0.671	0.135	0.092
Pst5d	0.014	0.170	0.671	0.135	0.122
Pst6d	0.014	0.170	0.671	0.135	0.153

From Table 6.1 it can be seen that, according to the classic theory, all beams are lightly reinforced in shear, as the degree of transverse reinforcement ψ is always lower than $\upsilon\psi_0$ and 0.05υ and, in any case, ψ is lower than $0.16/\sqrt{f_c} = 0.0226$. Therefore, in the classic theory, the effectiveness factors for the beams containing stirrups should actually be taken as equal to their counterpart without stirrups, i.e. $\upsilon = \upsilon_0$ from (6.19). The theory of sliding in cracks may then be applied to the beams with stirrups, too, in accordance with Hoang and Nielsen (1998).

All beams are over-reinforced in flexure as the degree of longitudinal reinforcement Φ is always > 0.5υ, when the theory of sliding in cracks is considered (and as observed experimentally). This is also in accordance with the aforementioned findings of Ashour (2000), who reported minimal influence of the longitudinal reinforcement over the shear capacity for $\Phi > 0.1$, a condition met in all cases here. Hence, it is reasonable to assume that the longitudinal reinforcement would not have yielded at shear failure and that therefore the models where the relative displacement is vertical are appropriate.

6.3.1 Small-scale RC beams

6.3.1.1 Beams without stirrups

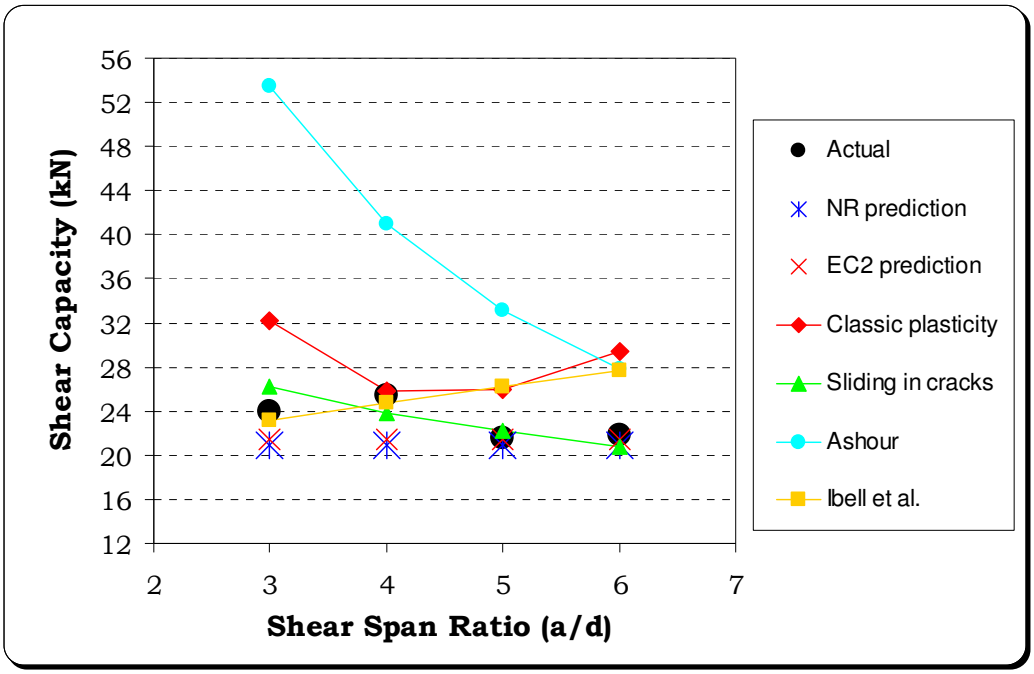

Figure 6.7: Shear predictions for the small-scale RC beams without stirrups

The ultimate shear capacity V_u of the RC beams without stirrups is calculated with all the various plasticity-based models described in the previous section; model predictions are compared with test results and code predictions in Figure 6.7. From the plot, it appears that when the effectiveness factors as suggested by the various authors are considered, the theory of sliding in cracks is the one rendering the most consistent and accurate predictions for shear spans up to $6d$ and it correctly reflects the slight decrease in capacity for increasing spans. This is mainly because this theory incorporates the effect of the shear span so that the effectiveness factor does not depend on the shear span ratio, unlike in the other models.

When the effectiveness factors are disregarded, the results offered by the classic plasticity theory, the model of Ibell et al. (1997b) and the model of Ashour (2000) are practically coincident at all shear spans, showing that these models are equivalent in this case and it is the effectiveness factor which gives the different results. In particular, apart from the model of Ashour where a constant value of 0.5 has been considered for v, which is probably too high and inadequate for beams with no stirrups, predictions are very accurate at $4d$, a value where the influence of the span length in the effectiveness factor formulae is minimal. Hence, it appears that in both (6.19) and (6.28) the factor depending on the shear span ratio is not very accurate especially for shear span lengths in excess of $4d$.

Table 6.2: Best-fit value of the effectiveness factor for the RC beams without stirrups

Specimen	$\boldsymbol{v_{1.00}}$ *(Ashour)*	$\boldsymbol{v_{1.00}}$ *(classic)*	$\boldsymbol{v_{1.00}}$ *(Ibell et al.)*
USB R3d	0.224	0.226	0.226
USB R4d	0.311	0.316	0.316
USB R5d	0.326	0.332	0.332
USB R6d	0.392	0.401	0.401
Mean $v_{1.00}$	*0.313*	*0.319*	*0.319*
	$\boldsymbol{v}$ *(Ashour)*	$\boldsymbol{v}$ *(classic)*	$\boldsymbol{v}$ *(Ibell et al.)*
Mean v	*0.500*	*0.390*	*0.359*
Mean v (no a/h)	*0.500*	*0.304*	*0.307*

Table 6.2 shows the best-fit value of the effectiveness factor $v_{1.00}$ to obtain exact predictions for the three models; when the mean is considered and compared with the mean of the proposed v, with and without the shear span effect, it is seen that

more conservative predictions would be obtained if the influence of the shear span ratio were disregarded in the expression for the effectiveness factor.

6.3.1.2 Beams with stirrups

For the small-scale RC beams with stirrups, the predictions from all plasticity models are shown in Figure 6.8, where the theory of sliding in cracks is actually the one modified by Hoang and Nielsen (1998) for lightly reinforced beams, as described in the previous section. For the purpose of comparison between the various models (and also because all these beams failed in shear), in the plots only the shear predictions are shown, although, especially for spans in excess of 4*d*, in some cases the shear predictions were so high that the flexural capacity would have governed.

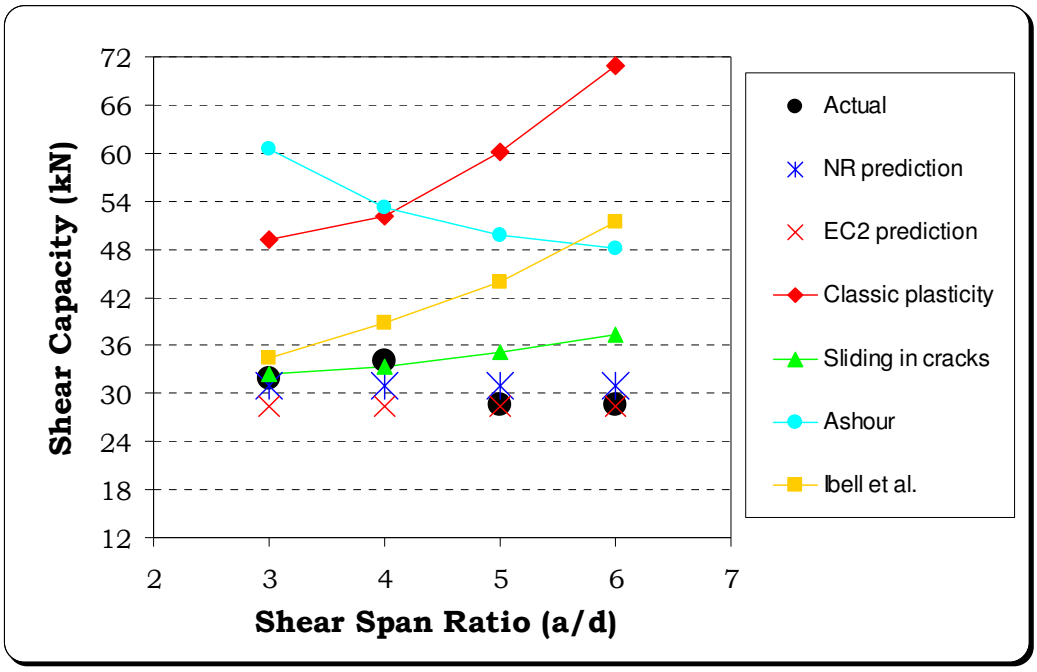

Figure 6.8: Shear predictions for the small-scale RC beams with stirrups

It is evident that predictions are, in general, excessively unconservative, with the theory of crack sliding still being the most accurate. The classic plasticity theory and the model by Ibell et al. (1997b) suffer from the same issue found in the beams without stirrups, i.e. the excessively high value of the effectiveness factor for increasing shear span length, giving a trend of capacity which is actually the inverse of that found in the test campaign, although the latter model is much more satisfactory. The same incorrect trend is found, to a lesser extent, in the theory of

sliding in cracks, while the main problem in the model by Ashour (2000) is that an effectiveness factor of 0.5 is generally too high for these beams.

In the shear capacity formulation of the classic solution and the theory of sliding in cracks, defined by (6.07) and (6.25) respectively, the contribution of the stirrups to the shear capacity is directly proportional to the shear span length a (or to $x' = a-x$). However, the assumption that the critical shear crack is straight is not necessarily correct for very lightly reinforced beams because, as observed experimentally, the cracks often deviate and become steeper in the space in between two consecutive stirrups and the contribution to the capacity may be different; this phenomenon is particularly relevant for spans in excess of $4d$, where the theoretical shear crack at failure is longer and there is greater opportunity for a critical shear crack to steepen.

Proposed model for beams with stirrups

A new model is proposed for beams with stirrups, that will also be implemented for the analysis of the strengthened beams later in the chapter. Starting from the hypothesis of the theory of sliding in cracks, i.e. that a beam would fail in shear with a yield line of projected length equal to x' if unreinforced in shear (see Figure 6.9), it is assumed that the presence of the transverse reinforcement, spaced at s, can displace the yield line making it steeper between two bars, thus leading to a higher internal energy dissipation. Two possible mechanisms, still involving vertical relative displacement between the two beam parts, are considered: one tri-linear (symmetric) and one bi-linear (see Figure 6.9). In the first case, the yield line is permitted to steepen in between two bars centred with respect to x', while in the second case the yield line can steepen in between the first two bars encountered, with one bar coincident with the edge of the yield line.

With reference to the symbols in Figure 6.9, the solution is found by varying the angle β from the initial value of θ (corresponding to the unstrengthened capacity V_c) and calculating, for each new value of β, the capacity V_{tot} due to the new shape of the yield line until the difference between V_{tot} and the capacity of the unstrengthened beam V_c equals the maximum contribution to the shear capacity offered by the stirrups crossed by the new yield line, V_s, where the capacity of each stirrup is equal to $V_{si} = A_{si}f_{yi}$. All stirrups intersected at a distance l_b from the top or bottom concrete edge (defined as the necessary "bond" length for the bar to be

effective) lower than (h-d_s) are disregarded and do not contribute to V_s as it means the crack can pass outside the bar.

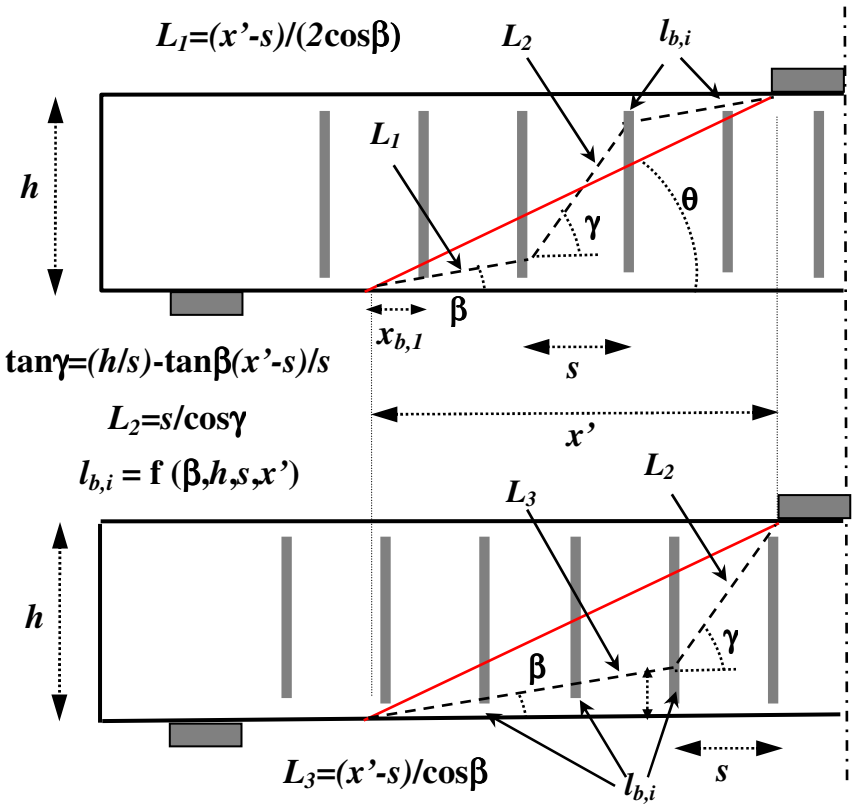

Figure 6.9: Proposed model for the shear capacity of beams with stirrups

Practically, this model considers that a lightly reinforced beam behaves exactly like an unstrengthened beam until shear cracking occurs, and that the stirrups deviate the minimum energy yield line until a point after which there can not be any more equilibrium between the surplus of shear force that can be carried by the stirrups and the increased demand of dissipation in the concrete. As the angle β decreases, the total energy dissipation in the concrete increases but the number of stirrups that can contribute to the capacity decreases, until equilibrium is achieved.

It can be easily shown by geometrical and trigonometrical considerations from Figure 6.9 that, for both mechanisms, all the unknown parameters can be expressed as a function of the angle β only; therefore, a spreadsheet where β is varied from the initial value of θ at steps of 0.5° is sufficient to obtain an optimised solution. Depending on the relative position between the stirrups and the yield line and on the amount of concrete cover, the first or the second mechanism will be the

critical. With the same hypothesis of the yield line steepening between two bars, all other possible mechanisms would render solutions lying between these two.

In the first mechanism, the ultimate shear capacity of the beam is given by:

$$V_{tot} = \frac{1}{2} \nu b f_c ((1 - \cos\gamma) L_2 + 2(1 - \cos\beta) L_1) \tag{6.29}$$

with

$$L_1 = \frac{x' - s}{2\cos\beta} \tag{6.30}$$

$$L_2 = \frac{s}{\cos\gamma} \tag{6.31}$$

$$\tan\gamma = \frac{h}{s} - \frac{x' - s}{s}\tan\beta \tag{6.32}$$

In the second mechanism, the expressions for L_2 and $\tan\gamma$ are identical, and the capacity is:

$$V_{tot} = \frac{1}{2} \nu b f_c ((1 - \cos\gamma) L_2 + (1 - \cos\beta) L_3) \tag{6.33}$$

with

$$L_3 = \frac{x' - s}{\cos\beta} \tag{6.34}$$

Finally, the 'bond' lengths l_b, equal to the distance from the concrete edge to the point where each stirrup is intersected by the yield line, are found as follows. For the first mechanism, the l_b of the two stirrups centred with respect to x' is:

$$l_{b,c} = \frac{x' - s}{2}\tan\beta \tag{6.35}$$

while the l_b of the other stirrups, symmetrically numbered in ascending order from the nearest to the edge of each side of the yield line, is:

$$l_{b,1} = x_{b,1}\tan\beta \tag{6.36}$$

$$l_{b,2} = (x_{b,1} + s)\tan\beta \tag{6.37}$$

$$l_{b,3} = (x_{b,1} + 2s)\tan\beta \tag{6.38}$$

$$l_{b,i} = (x_{b,1} + (i - 1)s)\tan\beta \tag{6.39}$$

where

$$x_{b,1} = \frac{x'-s}{2} - (\frac{ns}{2} - s) \tag{6.40}$$

with

$$n = int(\frac{x'}{s}) \qquad \text{when int}(\frac{x'}{s}) \text{ is an even number} \tag{6.41}$$

$$n = int(\frac{x'}{s}) + 1 \qquad \text{when int}(\frac{x'}{s}) \text{ is an odd number} \tag{6.42}$$

$$n = int(\frac{x'}{s}) - 1 \qquad \text{when } \frac{x'}{s} \text{ is an exact odd integer} \tag{6.43}$$

In the second mechanism there are no central bars so there is no $l_{b,c}$ and the formulae for $l_{b,i}$ are identical to the above, but here:

$$x_{b,1} = x'-sn \tag{6.44}$$

$$n = int(\frac{x'}{s}) \qquad \text{when } \frac{x'}{s} \text{ is not an exact integer} \tag{6.45}$$

$$n = int(\frac{x'}{s}) - 2 \qquad \text{when } \frac{x'}{s} \text{ is an exact integer} \tag{6.46}$$

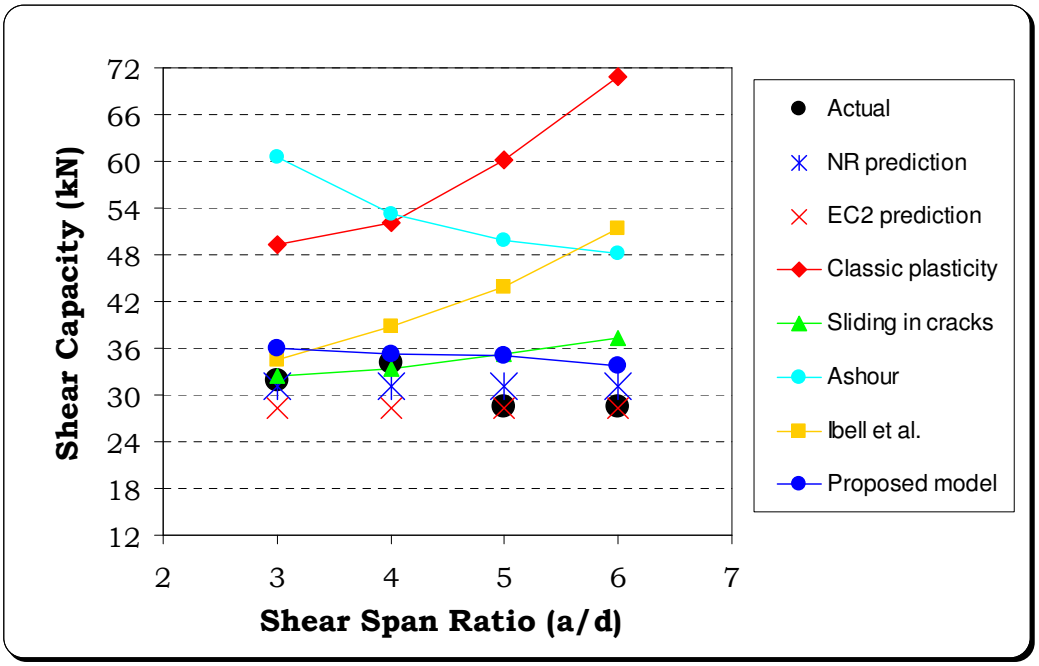

Figure 6.10: Shear predictions for the small-scale RC beams with stirrups including the proposed model

The predictions from the proposed model are compared with all the others in Figure 6.10. Although slightly unconservative, the proposed model can correctly capture the trend of reduction of capacity for increasing shear spans, with a mean of actual to predicted of 0.879 and a CoV of 6% only, compared with a mean of 0.896 and a CoV of 12% found with the crack sliding theory modified by Hoang and Nielsen (1998).

The validity of the assumptions of the proposed model is evident when looking, for example, at the failure mechanism observed in specimen USB Rst6d (see Figure 4.18), where the critical shear plane was tri-linear, with the steepest branch in the middle. Overall, for the small-scale RC beams with stirrups the codes still offer more conservative predictions for shear spans in excess of 4*d*.

6.3.2 Small-scale PSC beams

Figures 6.11 and 6.12 show the predictions for the ultimate capacity of the prestressed small-scale beams without and with stirrups, respectively, where only the classic plasticity theory and the theory of sliding in cracks have been considered this time.

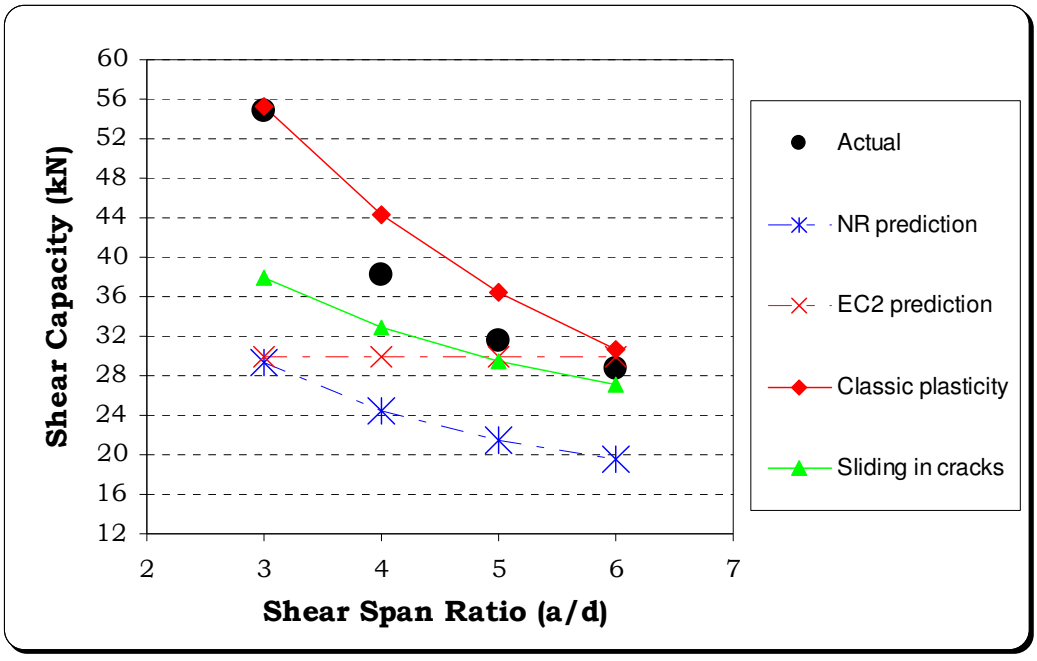

Figure 6.11: Shear predictions for the small-scale PSC beams without stirrups

When no stirrups were present, the actual test results lie in between the classic plasticity theory and theory of sliding in cracks, both more accurate than code predictions. The theory of sliding in cracks is generally more conservative and offers very good predictions for more slender beams, while the classic plasticity theory can capture almost perfectly the high shear-carrying capacity of the prestressed beam loaded at 3*d* but becomes unconservative for longer spans, corroborating the validity of the principles behind the theory of sliding in cracks.

In the beams with stirrups (see Figure 6.12) the proposed model, although still conservative up to 5*d*, results in better predictions than the theory of sliding in cracks as modified by Hoang and Nielsen (1998). It has to be noted, here, that the beams at 4, 5 and 6*d* failed in flexure and that the classic plasticity theory predictions in the plot are all flexural failures as the shear predictions were much higher; hence a direct comparison with the classic theory is not appropriate here. Nevertheless, it is clear that all models represent an improvement if compared with the excessively conservative codes.

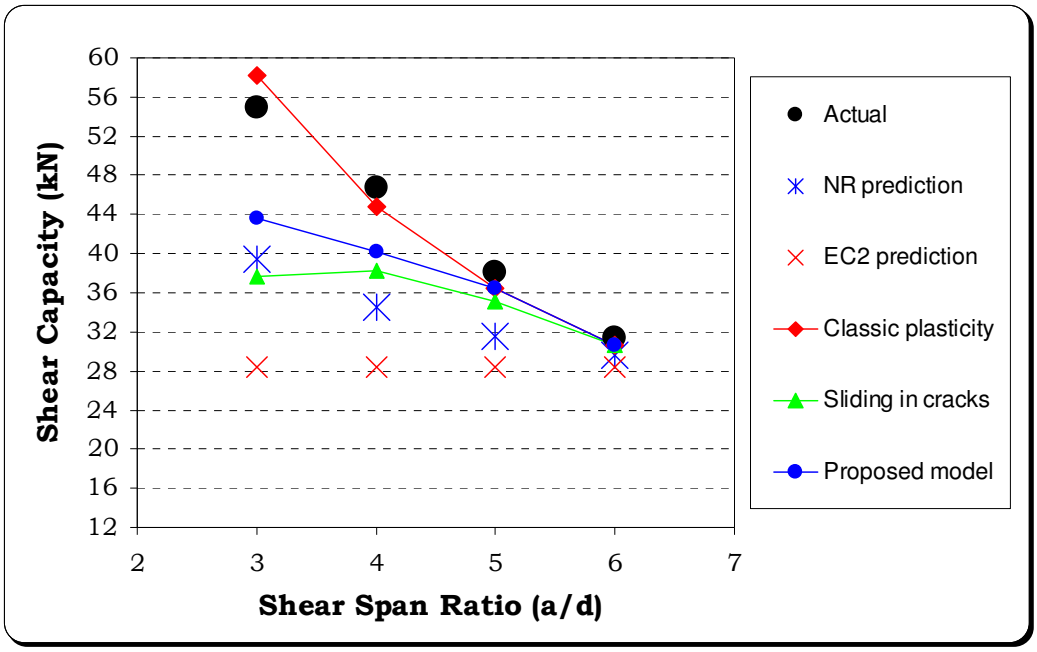

Figure 6.12: Shear predictions for the small-scale PSC beams with stirrups

6.3.3 Large-scale PSC beams

As shown in Figure 6.13, the theory of sliding in cracks is the most accurate in predicting the shear capacity of the two large-scale PSC beams without stirrups,

and the trend of predictions is consistent between the large- and the small-scale PSC beams (Figure 6.11). The classic plasticity theory goes from being unconservative for the small beams to over-conservative for the large ones. It appears that the theory of sliding in cracks can be accurate for prestressed beams of any size and it appropriately caters for the shear span effect in all cases.

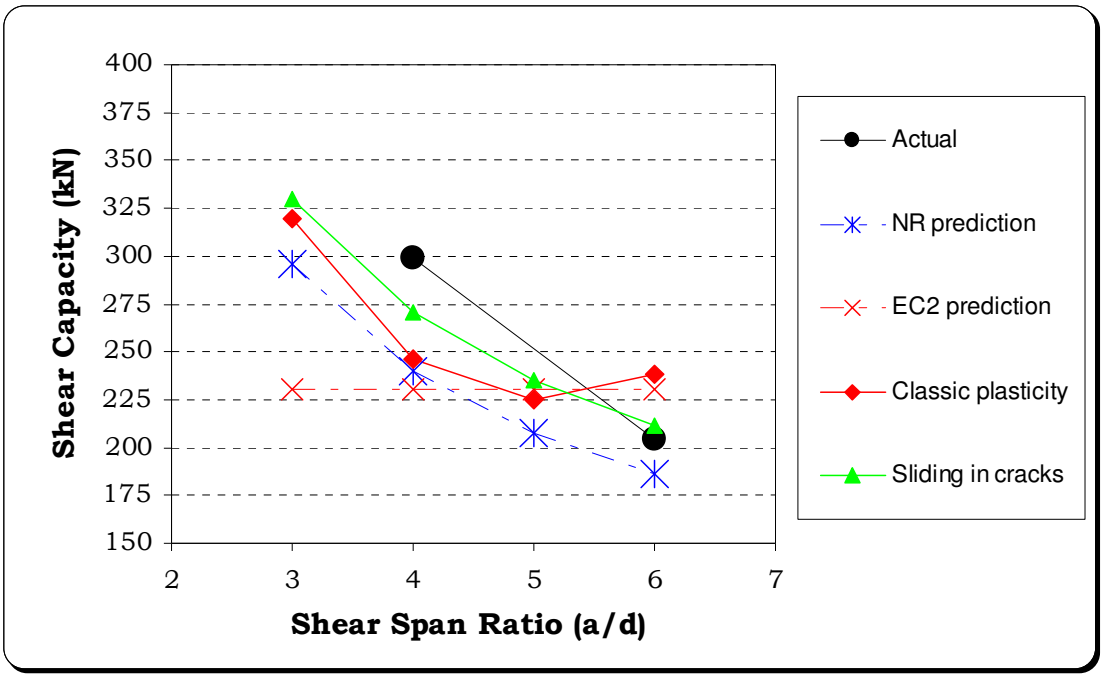

Figure 6.13: Shear predictions for the large-scale PSC beams without stirrups

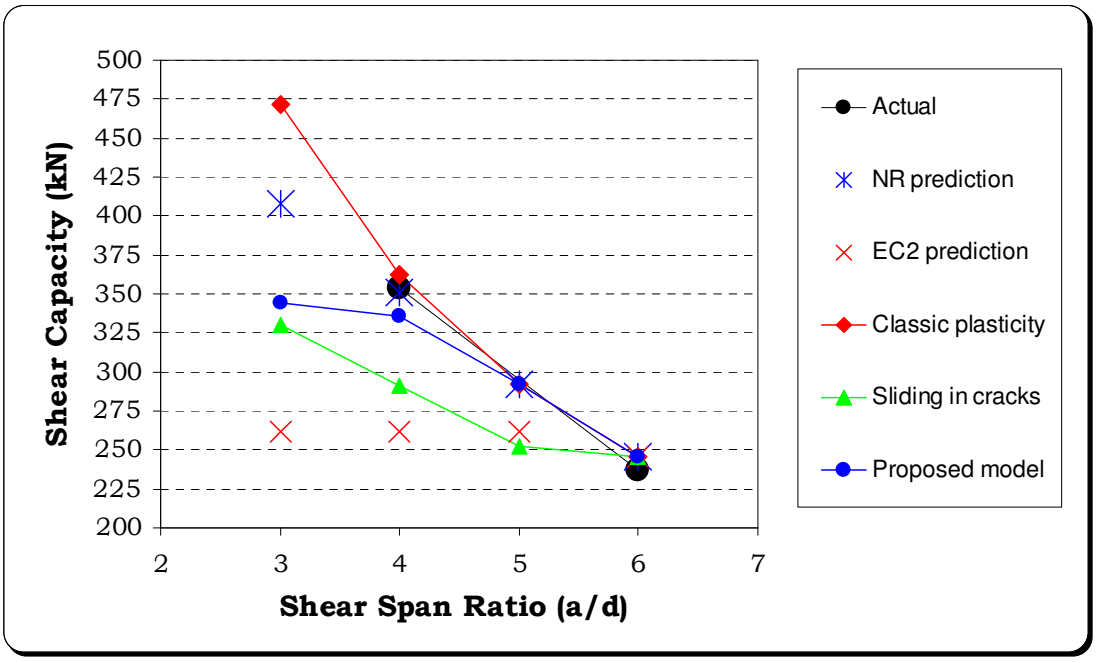

Figure 6.14: Shear predictions for the large-scale PSC beams with stirrups

For the beams with stirrups, shown in Figure 6.14, the comparisons are somewhat less significant as both beams at 4*d* and 6*d* failed in flexure. However, while the classic plasticity theory predicts flexural failure in all cases (the shear predictions are very high), the theory of sliding in cracks as modified by Hoang and Nielsen (1998) is excessively conservative. Again, the proposed model for beams with transverse reinforcement, complimentary to the theory of sliding in cracks, can offer a substantial improvement, while still appropriately remaining on the conservative side.

6.3.4 Concluding remarks

From the comparisons between the various plasticity-based models it is clear that the theory of sliding in cracks for beams without stirrups (Zhang, 1997), and the proposed model for beams with stirrups, offer the most accurate and consistent predictions for the shear capacity of RC and PSC beams of the present research project.

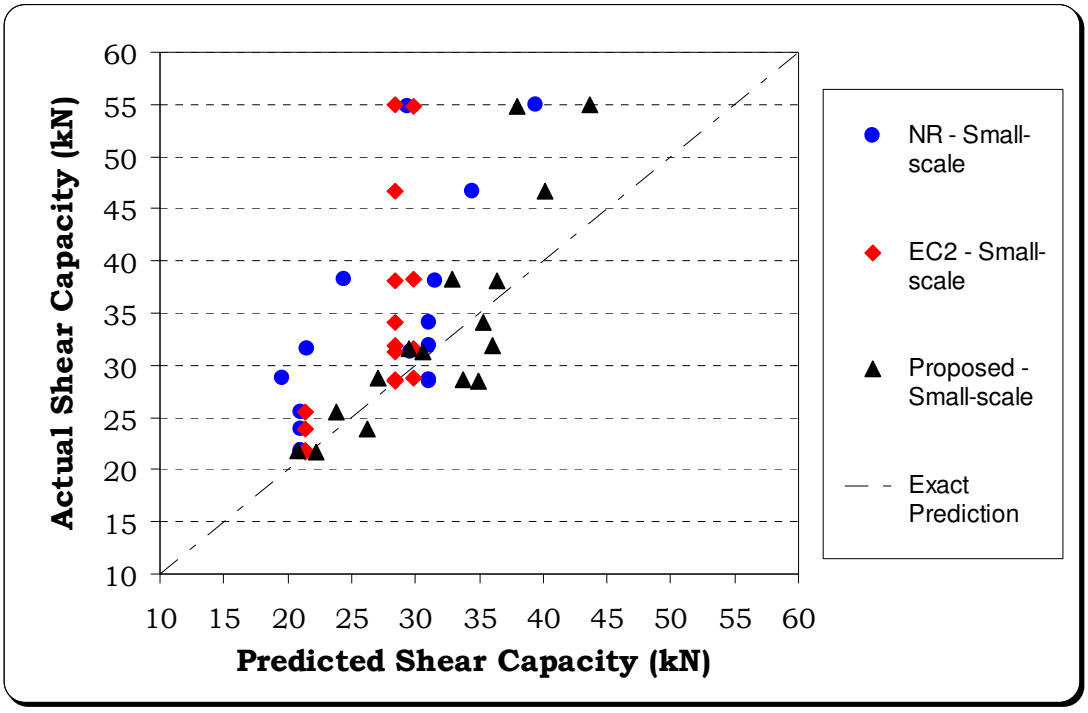

Figure 6.15: Shear predictions from codes versus proposed method - small-scale beams

In Figures 6.15 and 6.16, the predictions from the aforementioned models (in the following referred to as the proposed method) are compared with codes for the small-scale and large-scale beams, respectively. When only the RC beams are considered, the mean actual to predicted ratio is 1.09, 1.05 and 0.94 for the EC2, NR and proposed method respectively, with a CoV of 7.2, 9.1 and 9.1%, showing the proposed method gives a similar degree of accuracy than the codes for RC beams. For the small-scale PSC beams, the proposed method is much more satisfactory than codes, with a mean actual to predicted of 1.15 and a CoV of 11.4%, while the EC2 and NR codes give a mean actual to predicted of 1.40 and 1.42 and a CoV of 24.7% and 15.8%, respectively.

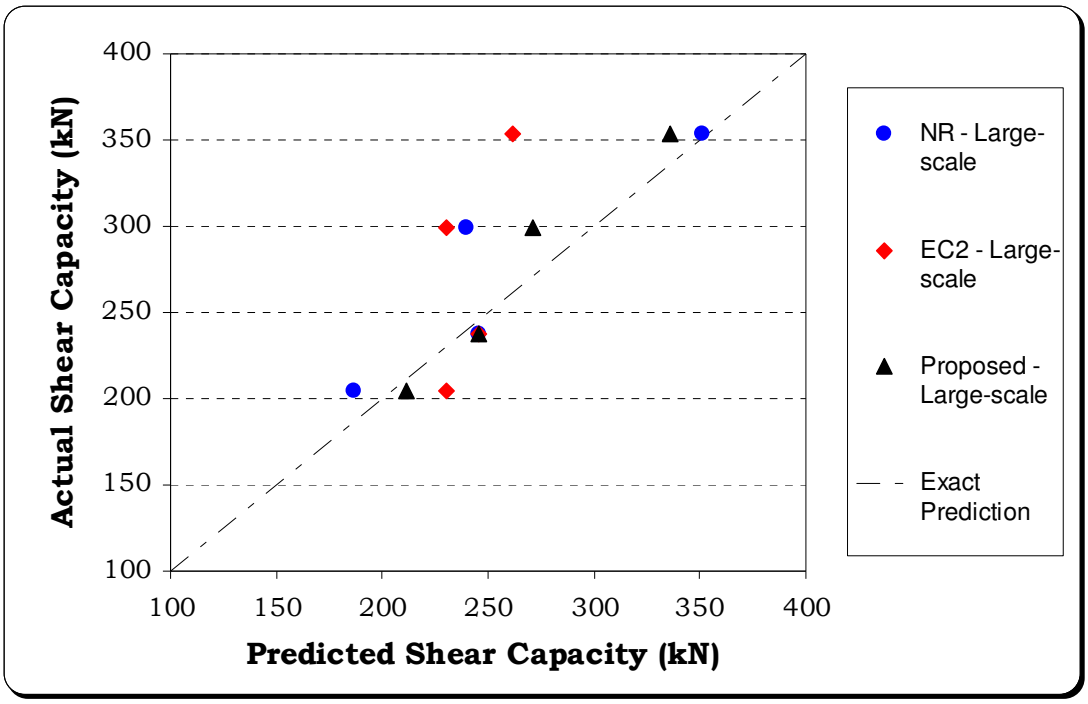

Figure 6.16: Shear predictions from codes versus proposed method - large-scale beams

Most importantly, the proposed method seems to be rather accurate for the large-scale PSC beams, as the mean of actual to predicted is 1.02 with a CoV of 5.6% only, while EC2 and NR codes have a mean actual to predicted of 1.13 and 1.08 with a CoV of 17.9% and 9.9%, respectively. When all small-scale and large-scale prestressed beams are considered together, the mean actual to predicted is 1.31 for both codes and 1.11 for the proposed method and the CoV is 24.4% and 19.3% for EC2 and NR codes and 11.6% for the proposed method. When all tested beams are considered, the proposed method results in a mean actual to predicted of 1.04 and a CoV of 13.5%, while EC2 and NR codes give 1.22 and 1.20 for the mean and

23.1% and 20.0% for the CoV; finally, if only the beams that failed in shear are counted, the mean actual to predicted for the proposed method is 1.04 with a CoV of 15.2%, while EC2 and NR codes give 1.20 and 1.23 for the mean and 24.5% and 21.0% for the CoV, respectively.

Therefore, it has been shown that the proposed upper-bound plasticity method, which is based on the theory of sliding in cracks (Zhang, 1997) for the beams without stirrups, modified for the beams with stirrups, is able to offer better shear predictions than the current codes in all cases of PSC beams of small and large size, with and without stirrups. The method is particularly appropriate for slender prestressed beams, which represent the object of this research project, and forms the basis of the analysis of the laterally-prestressed beams forming the bridge deck, described in the following section.

6.4 Analysis of the small-scale bridges

6.4.1 Elastic stage

As described in Chapter 3, the small-scale bridges were reproduced using five of the small-scale PSC beams, prestressed transversely by four equally spaced external loads (see Figure 3.10). The test results, presented in Chapter 4, have shown that all specimens behaved elastically as a whole slab until the static friction between the vertically loaded central beam and its two neighbouring ones was mobilized, meaning that up to a certain value of the applied vertical load (the 'slipping' load) the loaded beam is fully constrained by the other beams and only a fraction of the vertical load is directly transferred to its supports.

In the actual bridges, where the load is distributed through the ballast at 15° from the vertical according to the assessment code, this arrangement can represent both situations where the train load under one rail covers the width of a single beam or when the whole track load covers the width of three beams (see Figure 3.2). In fact, the cast-in concrete placed in between the beams has a non-zero cohesion and a friction angle of approximately 37° against the lower figures of the sand used in the tests, rendering the test assumption appropriately conservative.

To compare the initial stress state due to the lateral prestressing in the test specimens with that in the reference bridge, and to assess the percentage of the

applied vertical load that is directly transferred to the support of the loaded beam against that needed to be transferred through friction laterally, a series of FE models (using the software ALGOR ©, 2008) of both the small-scale and actual bridges were built using plate elements rigidly connected, which represent the situation before the lateral friction is fully mobilized and the central beams slip.

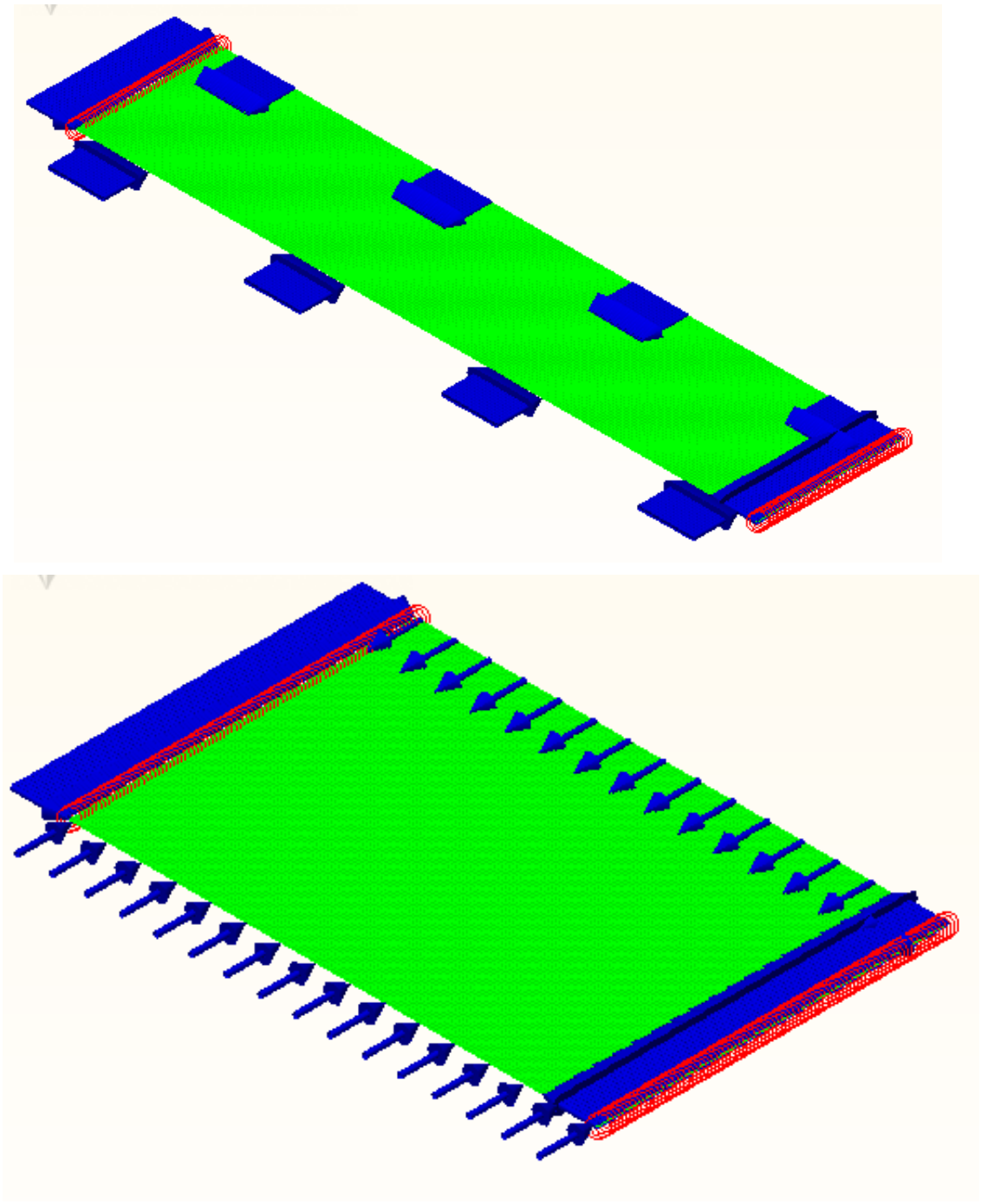

Figure 6.17: Elastic FE model of the small-scale (top) and the actual (bottom) bridge, showing transverse and longitudinal prestressing loads

In the FE element models (see Figures 6.17 and 6.18), all the prestressing loads were appropriately inserted in the mesh, and the change of longitudinal prestressing force due to the progressive debonding of tendons towards the supports in the actual bridges was appropriately accounted for. A model was built for each position of the applied test loads and, at 6*d*, for the three values of the lateral prestressing considered in the test regime, i.e. full, half and a quarter of the actual lateral load.

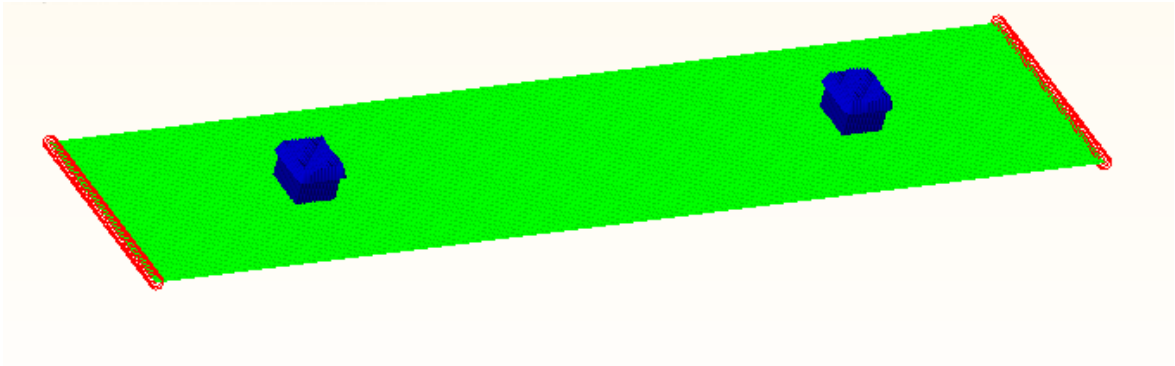

Figure 6.18: Typical vertical loading over the elastic FE model of the small-scale bridges (loads at 3d shown only)

Figure 6.19 shows the distribution of lateral stress in the small-scale bridges due to the full transverse prestressing after all losses. In the actual bridge, which contains ten beams, this distribution becomes fairly uniform after the first two lateral beams as the end anchorage effects disappear.

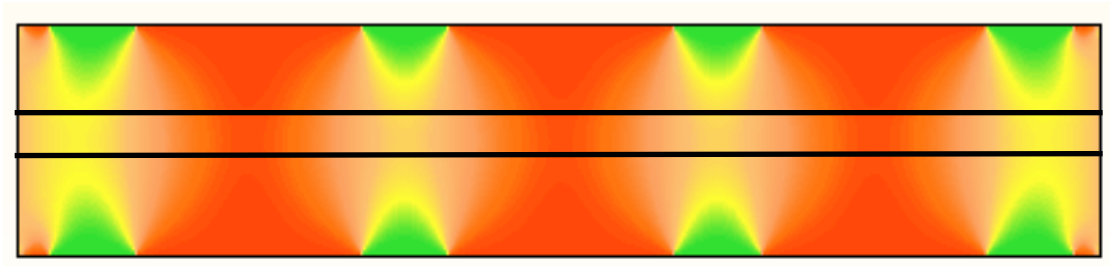

Figure 6.19: Lateral compressive stresses due to full transverse prestressing in the small-scale bridges

From the plot, it appears that it is a reasonable approximation to assume that the central beam of the small-scale test specimens is subjected to a uniform lateral

pressure, as the peaks of stress behind the lateral loading platens are highly reduced when the central beam, delimited by the two black lines in the figure, is reached.

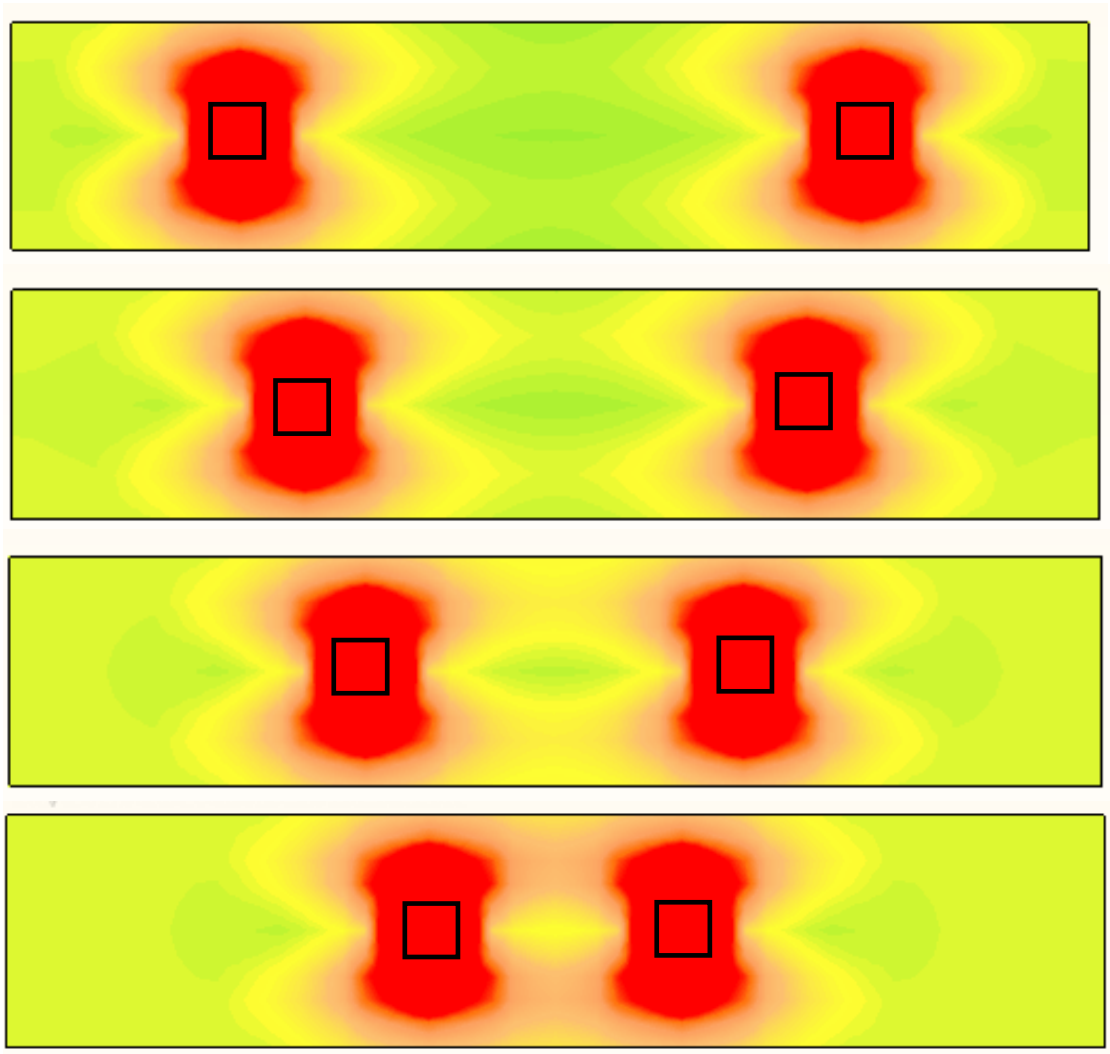

Figure 6.20: Transverse average vertical shear stress through thickness in the small-scale bridges due to loads at 3, 4, 5 and 6d (top to bottom, respectively)

As far as the distribution of the vertical loads is concerned, the models show that in the small-scale bridges the percentage of the applied load directly transferred to the support of the loaded central beam is approximately 20% in all cases (i.e. it is equal between the five beams); from Figure 6.20, showing the transverse shear stress distribution for the patch loads at 3, 4, 5 and 6*d* respectively, it is evident that even at 3*d* the specimen is slender enough for the lateral transfer to occur entirely within the span, hence fully by lateral friction through the neighbour beams.

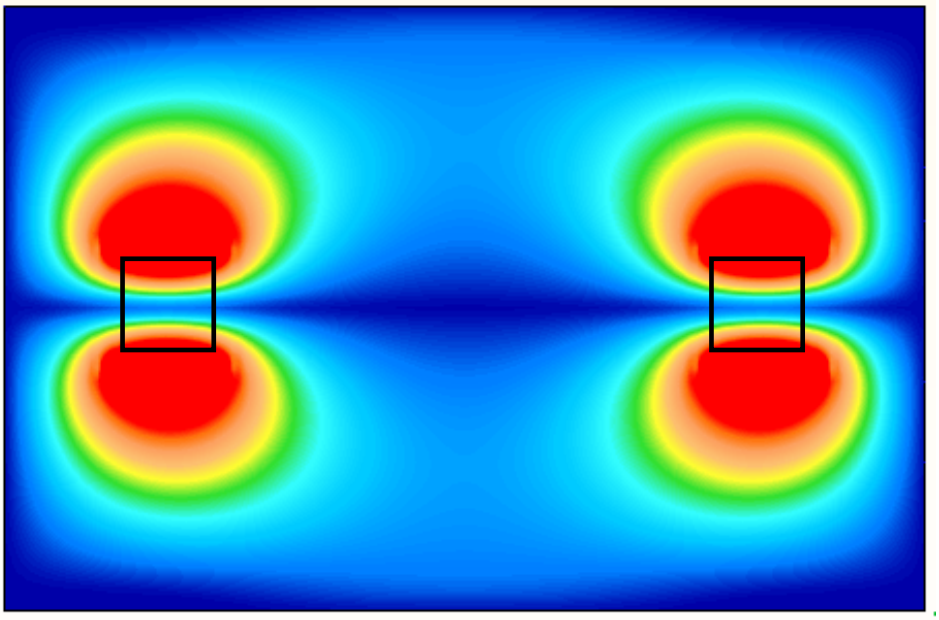

Figure 6.21: Transverse average vertical shear stress through thickness in the actual bridges due to patch loading applied at 3d

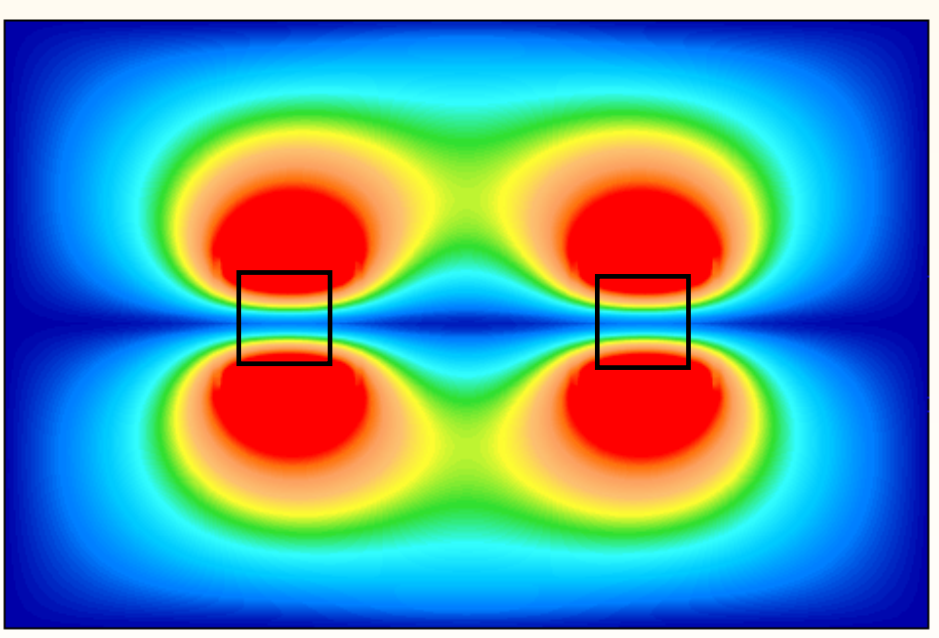

Figure 6.22: Transverse average vertical shear stress through thickness in the actual bridges due to patch loading applied at 6d

In the actual bridges, the percentage of load transferred directly to the support of the loaded beams varies slightly when the vertical patch loads are applied at 3, 4, 5 and 6*d*. From the models, it is found that the support reactions of each of the two central beams of the actual bridges vary from 10% for loading at 6*d* (representing equal distribution between the ten beams) to a maximum of 13% for loading at 3*d*,

meaning that in the latter case a lower proportion of the total vertical load is transferred through lateral friction. Figures 6.21 and 6.22 show the transverse shear stress distribution in the elements of the actual bridges when the load patches are applied, symmetrically, at 6d and 3d respectively. The plots clearly indicate that, at 6d, the whole of the load has to be carried through lateral friction, while at 3d a small proportion of it goes straight to the supports.

From the above considerations it is shown that the test specimens seem, qualitatively, to be able to model the actual bridges appropriately especially with respect to the stress state in the vicinity of the vertically loaded central beam. The scheme is slightly conservative for short shear spans, as in the real bridges a higher proportion of the loads would be directly transferred to the support of the loaded beam; this is due to the different ratio between the overall length and width of the deck in the two cases.

6.4.2 Slipping load

Test results showed that failure was always initiated by slipping of the loaded central beam relative to its neighbouring beams. A simple equilibrium model is used to predict the slipping load P_s..

It is considered that the initiation of the slip between the central beam and its neighbouring ones occurs when the demand of lateral shear stress that needs to be transferred by friction from the loaded beam, q_f, exceeds the maximum frictional resistance, q_u, that depends on the level of lateral load N, the lateral beam surface hL and the internal angle of friction of the interface material φ (see Figure 6.23).

For each level of the applied load up to slipping, the shear stress that needs to be carried by friction can be thought as the cause of the restraint to the deflection that the central beam experience when acting as a whole slab (δ_{bridge}) opposed to the deflection that the loaded beam would experience if acting alone (δ_{beam}) with no lateral friction. Assuming the frictional resistance to be uniformly distributed along the beam span with L = 2600mm, the Young's modulus of the adopted concrete E = 37000MPa and h = 190mm, the restraint of deflection due to friction $\delta_{friction}$ can be expressed as:

$$\delta_{friction} = \frac{5 q_f h L^4}{384 EI} \tag{6.47}$$

where I is the second moment of area of the beam and q_f is the frictional pressure in MPa.

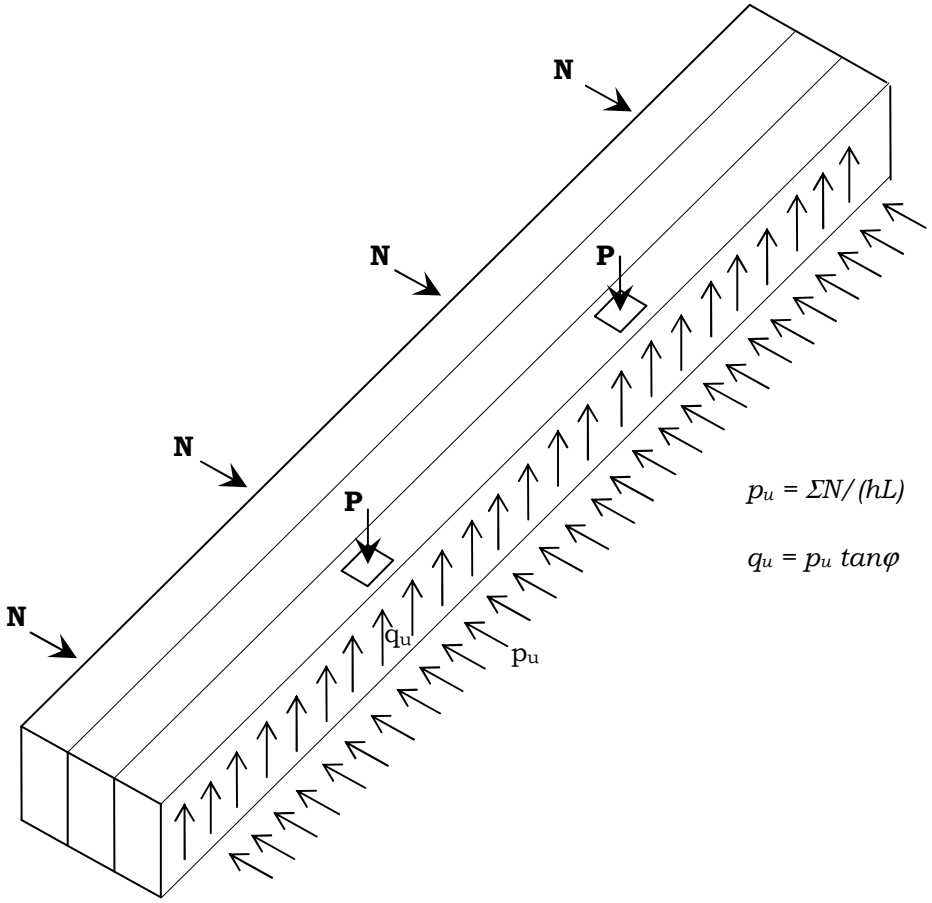

Figure 6.23: Frictional resistance due to the lateral prestressing

The mid-span deflection of the bridge as a whole slab δ_{bridge} is taken, for each specimen at different values of the applied load P, from the deflections predicted by the FE model previously described, which compared well with the test measurement in the transducers at mid-span of the central beam; for each value of the applied load, the mid-span deflection of the beam if acting alone is calculated from:

$$\delta_{beam} = \frac{PL^3}{6EI}\left(\frac{3a}{4L} - \left(\frac{a}{L}\right)^3\right) \tag{6.48}$$

where a is the shear span length.

The demand of shear stress to be carried by friction q_f is then evaluated, for increasing values of the applied load, with the (6.47) and the level of the applied load P at which q_f reaches the maximum frictional resistance q_u represents the theoretical slipping load P_s.

Table 6.3: Observed and calculated slipping loads for the small-scale bridge specimens

Specimen	***Lateral ΣN*** *(kN)*	***φ*** *(°)*	***Actual P_s*** *(kN)*	***Calc P_s*** *(kN)*
BR P3d-24	240	28	91.7	93.0
BR P4d-24	240	28	79.8	74.0
BR P5d-24	240	28	63.9	63.0
BR P6d-24	240	28	55.4	56.0
BR Pst6d-24	240	28	57.5	56.0
BR P6d-12	120	30	37.5	30.0
BR Pst6d-12	120	30	37.5	30.0
BR P6d-6	60	36	27.5	19.0
BR Pst6d-6	60	36	22.0	19.0

Table 6.3 compares the theoretical and observed slipping loads for the small-scale bridges, as reported in Chapter 4. The table shows that, despite the rather simplistic model that assumes the distribution of the lateral pressure to be perfectly uniform, the correlations are good, especially in the case of full lateral loading. When the lateral load is reduced to half and a quarter, respectively, the predictions are slightly over conservative. However, given the inherent uncertainties in the local frictional behaviour of the sand (whose friction angle has been shown to vary with the applied normal load) and the relatively accurate figure obtained for specimen BR Pst6d-6, the one with the lowest slipping load, the correlations are considered sufficiently accurate and appropriately safe.

6.4.3 Flexural capacity

As described in Chapter 4, the ultimate failure of the bridge specimens always occurred in the loaded central beam, with the others remaining virtually undamaged. It was clear then that the 3-dimensional effect able to increase the capacity was the lateral pressure provided by the neighbouring beams. The model proposed to evaluate the ultimate flexural capacity is shown in Figure 6.24, where the central beam is subject to self weight per unit length p, the test load P and a uniformly distributed vertical uplift per unit length equal to $q_u h = (\Sigma N/L)\ tan\varphi$ due to the lateral prestressing, assumed to be constantly sustained up to failure.

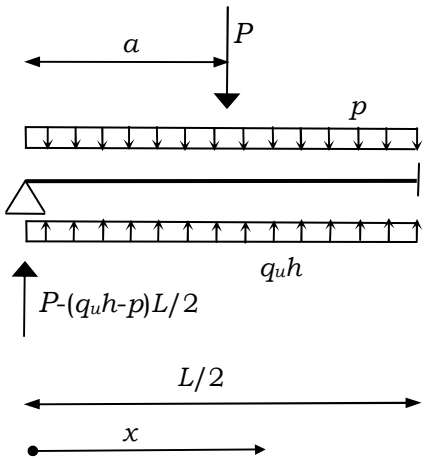

For $0 \le x \le a$

$M(x) = (P-q_u hL/2+pL/2)x + (q_u h-p)x^2/2$

For $a \le x \le L/2$

$M(x) = (P-q_u hL/2+pL/2)x + (q_u h-p)x^2/2-P(x-a)$

Figure 6.24: Evaluation of the flexural capacity of the small-scale bridges

The minimised ultimate flexural capacity $P_{u,f}$ is found to be equal to:

$$P_{u,f} = \frac{M_u + (q_u h - p)(\frac{aL}{2} - \frac{a^2}{2})}{a} \quad (6.49)$$

where M_u = 29.1kNm is the ultimate moment capacity of the prestressed beams.

Table 6.4 compares the theoretical ultimate loads in flexure for the small-scale bridges with the actual ultimate capacities, presented in Chapter 4.

Table 6.4: Calculated flexural capacity for the small-scale bridge specimens

Specimen	***Lateral ΣN*** *(kN)*	***φ*** *(°)*	***Actual P_u*** *(kN)*	***Calc $P_{u,f}$*** *(kN)*
BR P3d-24	240	28	115.4 (shear)	109.2
BR P4d-24	240	28	88.0 (shear)	92.1
BR P5d-24	240	28	82.0 (shear)	80.1
BR P6d-24	240	28	73.1 (shear)	70.1
BR Pst6d-24	240	28	67.5 (flexure)	70.1
BR P6d-12	120	30	52.9 (shear)	52.2
BR Pst6d-12	120	30	53.5 (flexure)	52.2
BR P6d-6	60	36	39.6 (shear)	44.0
BR Pst6d-6	60	36	47.1 (flexure)	44.0

The correlations are remarkably good. The flexural failure of the three specimens with stirrups (BR Pst6d-24, BR Pst6d-12 and BR Pst6d-6) seem to be predicted

with errors of 4%, 3% and 7% only. In all other specimens, it is seen that the flexural predictions are very close to the actual shear failure. In fact, as discussed in Chapter 4, in most bridge specimens the shear failures were fairly ductile, often involving some crushing of the concrete in compression, proving that the lateral confinement could enhance the load-carrying capacity of the beam up to the point of being close to avoiding shear failure at all.

6.4.4 Shear capacity

6.4.4.1 Bridges with beams without stirrups

For the analysis of the shear capacity of the bridges, an upper-bound approach is proposed which is an extension of those successfully employed for the analysis of the single beams, with the aim of taking into proper account the frictional component provided by the lateral prestressing.

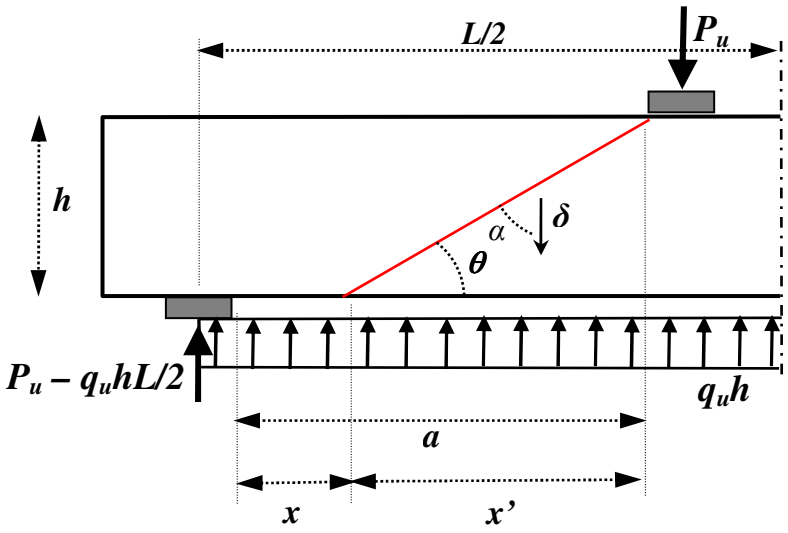

Figure 6.25: Upper-bound mechanism for the shear capacity of the critical bridge beam

The proposed upper-bound model for the shear capacity of the bridges is shown in Figure 6.25, where the central part of the beam undergoes a relative downward vertical displacement δ with respect to the outer zone along two straight symmetrical yield lines, and the lateral pressure provided by the lateral prestressing is modelled as a uniformly distributed vertical uplift per unit length equal to $q_u h = (\Sigma N/L)\ tan\varphi$ (which in the figure is shown below the beam but actually acts on its

side faces). It is to be noted that there is no need to consider a 3-dimensional 'slab-like' failure mechanism, as this sort of failure was not encountered.

Equating the external work done by the loads in the central part of the beam to the sum of the internal energy dissipation in the concrete, the following expression is found:

$$P_u\delta - q_u h(L/2 - a + 0.5h\cot\theta)\delta = 0.5f_c(1-\cos\theta)bh\delta/\sin\theta \tag{6.50}$$

After substituting $\tau_u = P_u/(bh)$ and with the position of the discontinuity defined by:

$$\sin\theta = \frac{1}{\sqrt{1+\cot^2\theta}} \tag{6.51}$$

the expression for the ultimate shear capacity can be written:

$$\frac{\tau_u}{f_c} = \frac{1}{2}\sqrt{1+\cot^2\theta} - \left(\frac{1}{2} - \frac{q_u h}{2bf_c}\right)\cot\theta + \frac{q_u h}{bf_c}\left(\frac{L-a}{2h}\right) \tag{6.52}$$

When (6.52) is minimized with respect to $\cot\theta$, after a series of mathematical manipulations and having defined:

$$\xi = \frac{q_u h}{2f_c b} \tag{6.53}$$

it is found that:

$$\cot\theta = \frac{1-2\xi}{2\sqrt{\xi(1-\xi)}} \tag{6.54}$$

and the capacity becomes, including the concrete effectiveness factor ν:

$$\frac{\tau_u}{f_c} = \sqrt{\xi(\nu-\xi)} + \frac{q_u h}{bf_c}\left(\frac{L-a}{2h}\right) \tag{6.55}$$

which is a solution valid for $(h/a) \le \tan\theta \le \infty$ and for $\cot\theta \ge 0$. Hence, as in (6.54) the denominator is always positive, the solution is valid for $1-2\xi \ge 0$, i.e. for $\xi \le 0.5\nu$, which is always largely satisfied for the possible orders of magnitude of lateral pressures encountered in these bridges.

When $(h/a) = \tan\theta$, the yield line runs from the load to the support and the corresponding value of ξ is equal to:

$$\xi_0 = \frac{\sqrt{a^2+h^2} - a}{2\sqrt{a^2+h^2}} \tag{6.56}$$

Therefore, when ξ is lower than ξ_0, which is always the case in the bridges considered in the present study, the capacity is that corresponding to $(h/a) = \tan\theta$:

$$\frac{\tau_u}{f_c} = \frac{1}{2}\upsilon \left[\sqrt{1+\left(\frac{a}{h}\right)^2} - \frac{a}{h}\right] + \frac{q_u h(L-a)}{2bf_c h} \tag{6.57}$$

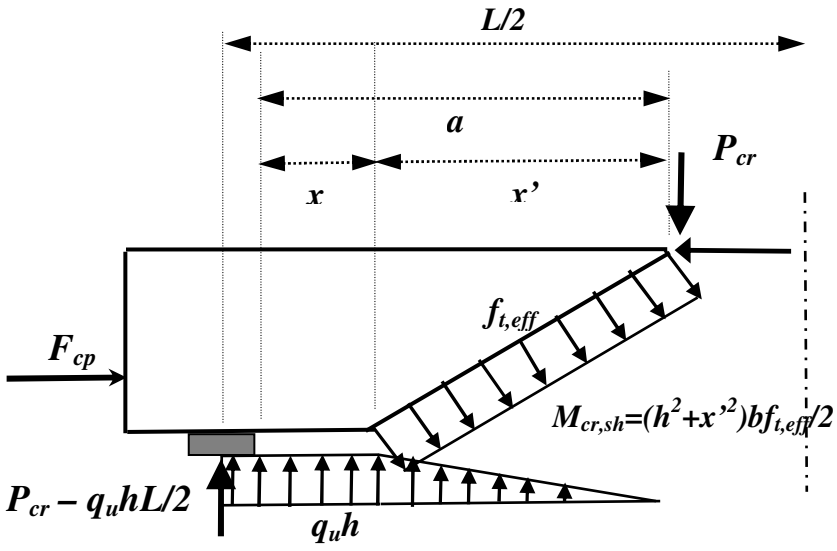

Figure 6.26: Shear cracking capacity of the critical bridge beam

When the approach suggested by the theory of sliding in cracks is adopted (which is theoretically admissible because ξ is lower than ξ_0), for different values of the yield line position $x = a\text{-}x'$ the minimised critical capacity is given by:

$$\frac{\tau_u}{f_c} = \frac{1}{2}\upsilon \left[\sqrt{1+\left(\frac{a-x}{h}\right)^2} - \frac{a-x}{h}\right] + \frac{q_u h(L-a)}{2bf_c h} \tag{6.58}$$

and the value of x is found by equating (6.58) with the following expression for the cracking load, found from moment equilibrium about the tip of the crack (see Figure 6.26):

$$\frac{\tau_{cr}}{f_c} = \frac{1}{2}\frac{f_{t,eff}}{f_c}\frac{\left(\frac{a-x}{h}\right)^2+1}{\frac{l_o}{2h}+\frac{a}{h}} + \frac{F_{cp}d_p/(bh^2 f_c)}{\frac{l_o}{2h}+\frac{a}{h}} + \frac{q_u hL}{2f_c bh} - \frac{q_u h}{f_c b}\frac{\left(\frac{l_0}{2}+x\right)\left(a+\frac{l_0}{4}-\frac{x}{2}\right)}{h\left(\frac{l_0}{2}+a\right)} - \frac{q_u h}{f_c b}\frac{(a-x)^2}{3h\left(\frac{l_o}{2}+a\right)} \tag{6.59}$$

where l_o is the length of the loading platen, $f_{t,eff}$ is the effective concrete tensile strength defined in (6.22) and d_p is the distance from the top concrete face to the centroid of the prestressing force after all losses.

The value of x that satisfies both (6.58) and (6.59) is that representing the critical shear capacity, with the effectiveness factor υ equal to $\upsilon_0\upsilon_s$, where υ_s = 0.5 and υ_0 is given by (6.24).

Figures 6.27 and 6.28 show the predictions for the ultimate flexural and shear capacity of the small-scale bridges containing beams without stirrups with full and reduced lateral prestressing, respectively, where both the proposed models obeying the classic plasticity theory and the theory of sliding in cracks have been considered for the shear predictions.

The results for the bridges with full lateral prestressing tested at different shear spans show that the proposed approach is able to predict the ultimate capacity with great accuracy in all cases, forming the basis of a realistic approach for such structures which is not considered by the codes. In particular, similarly to the single small-scale PSC beams, the actual test results lie in between classic plasticity theory and the theory of sliding in cracks, with the latter being generally more accurate and appropriately conservative for the more slender cases. As mentioned previously, most of these specimens failed in a mixed shear-flexural mode, which is also confirmed by the predictions.

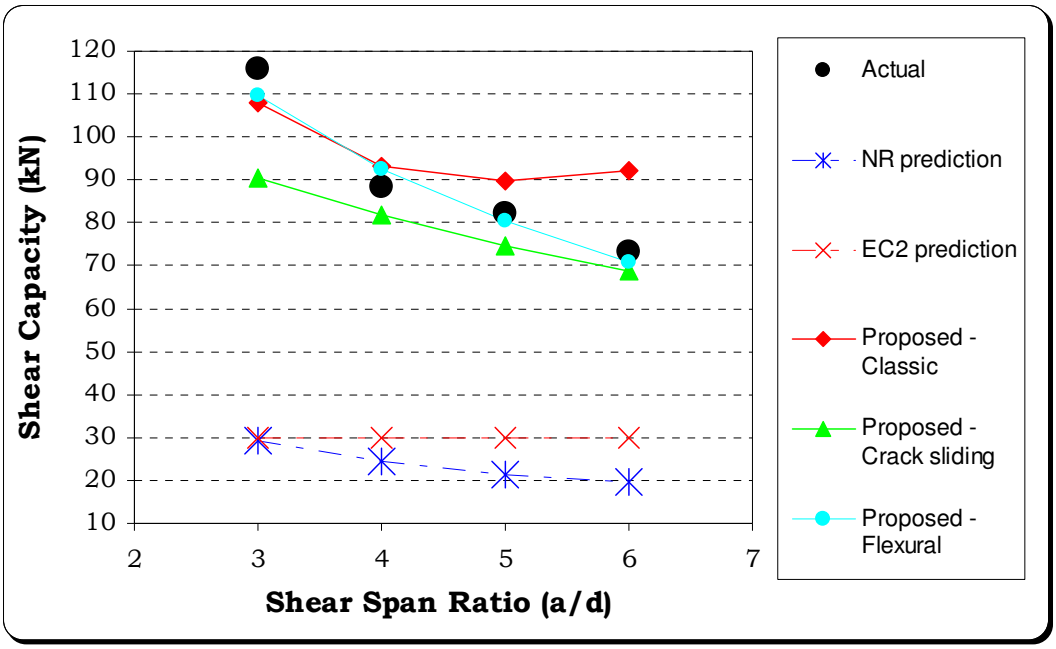

Figure 6.27: Predictions for the small-scale bridges with full lateral prestressing

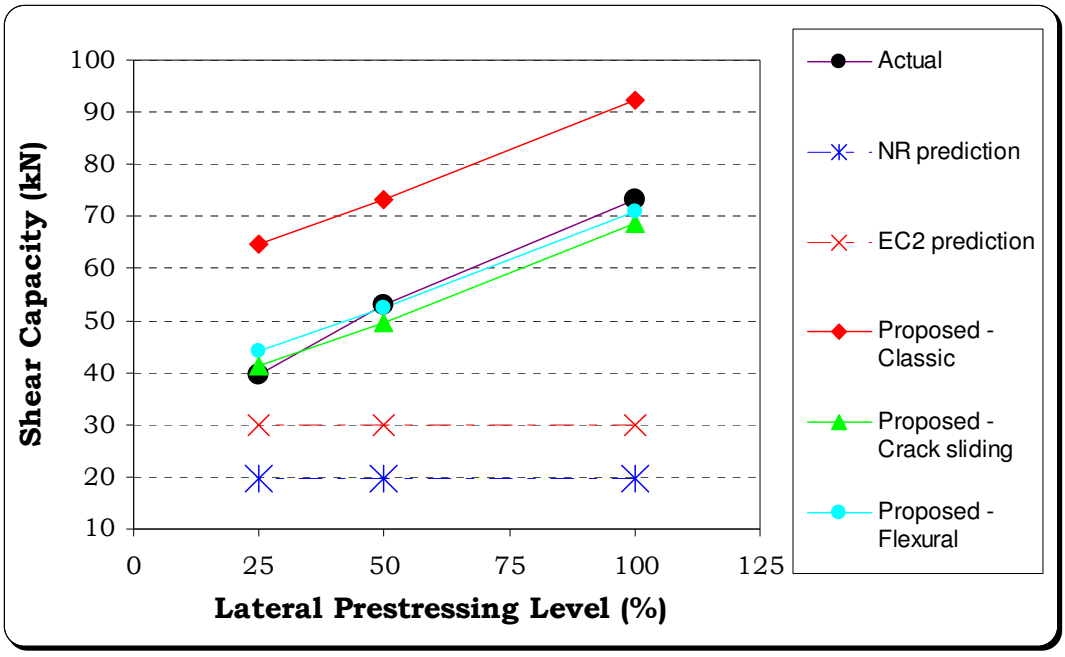

Figure 6.28: Predictions for the small-scale bridges with reduced lateral prestressing

For the beams with reduced lateral prestressing, all tested at 6*d* and failing in shear, the proposed method in its crack sliding form is shown to be consistently reliable, and it clearly appears to be the right approach for the shear assessment of these structures.

6.4.4.2 Bridges with beams with stirrups

For bridges containing beams with stirrups, the proposed model is an extension of the one described in section 6.3.1.2 for single beams, based on the crack sliding approach. Analytically it can be shown that the method is applicable when:

$$\xi + \psi \leq \frac{\sqrt{a^2 + h^2} - a}{2\sqrt{a^2 + h^2}} \tag{6.60}$$

where $\psi = A_{sv} f_{yw} / bsf_c$ is the degree of vertical reinforcement and ξ is defined in (6.53). The limit in (6.60) is always verified for the bridges considered in the present project, both small-scale and real. In any case, when the limitation in (6.60) is not verified, the approach is conservative.

As discussed in section 6.3.1.2, the model considers that the beam would fail in shear with a yield line of projection length equal to *x'* if unreinforced in shear (in accordance with the theory of sliding in cracks), and the presence of the transverse reinforcement displaces the yield line making it steeper between two bars according

to the two possible mechanisms shown in Figure 6.9. The solution is found numerically by varying the angle β from the initial value of θ until $V_{tot} - V_c = V_s$, where all expressions are the same as defined in (6.29) to (6.46), with the exception that (6.29) and (6.33) are now substituted, respectively, by (6.61) and (6.62) below:

$$V_{tot} = \frac{1}{2} vbf_c((1 - \cos\gamma)L_2 + 2(1 - \cos\beta)L_1) + \frac{q_u h(L - a)}{2h} \tag{6.61}$$

$$V_{tot} = \frac{1}{2} vbf_c((1 - \cos\gamma)L_2 + (1 - \cos\beta)L_3) + \frac{q_u h(L - a)}{2h} \tag{6.62}$$

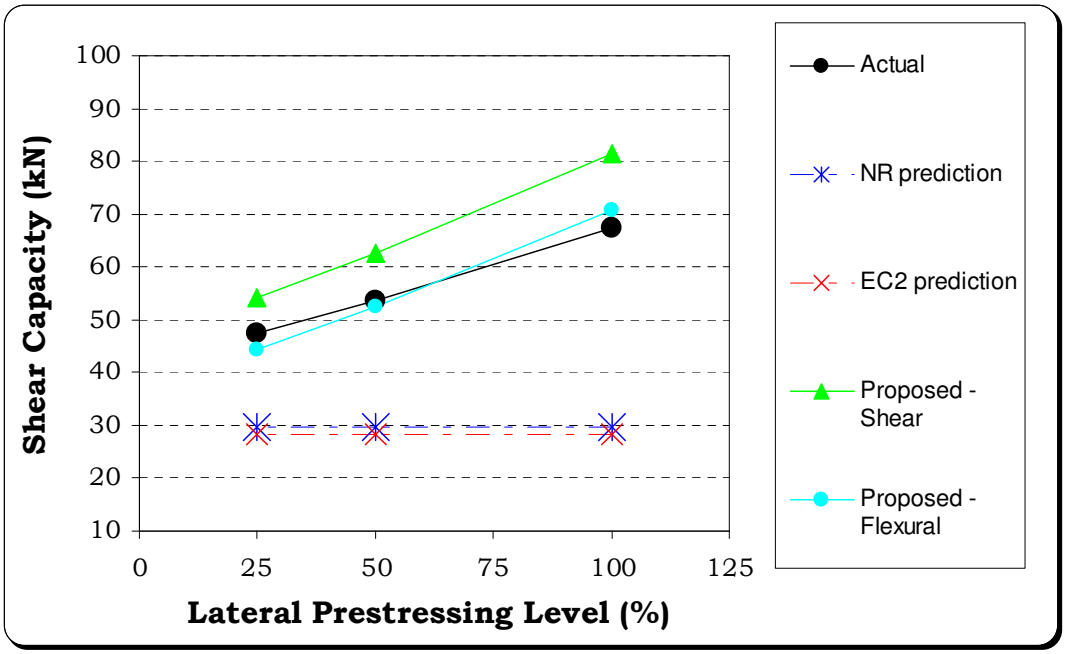

Figure 6.29: Predictions for the small-scale bridges containing beams with stirrups

Figure 6.29 shows the predictions for the ultimate flexural and shear capacity of the small-scale bridges containing beams with stirrups with the proposed method. For all these specimens a direct comparison with the shear capacity is not appropriate as they failed in flexure; indeed, the model correctly predicted the flexural failure for these beams, with good correlation.

6.4.5 Concluding remarks

The analytical approach adopted to evaluate the behaviour of the small-scale bridge specimens at both the elastic and ultimate stage has been shown to be accurate and consistent with the test observations.

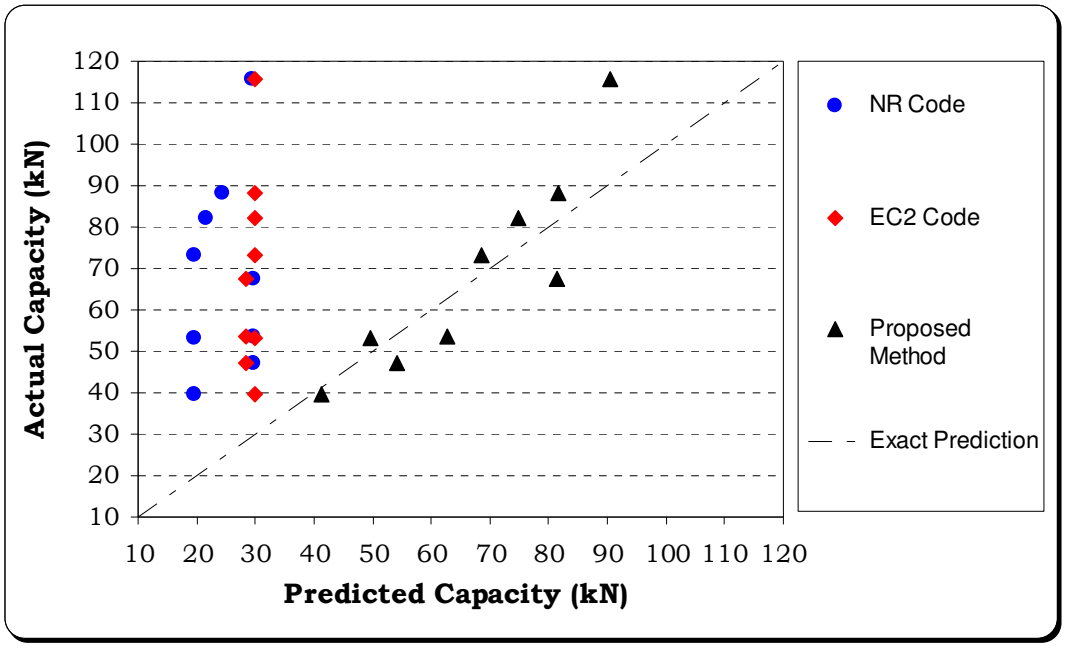

Figure 6.30: Predictions from codes and proposed method for the small-scale bridges

In Figure 6.30, the ultimate capacity predictions for all specimens from the proposed method and the codes are shown. When all specimens are considered together, the mean actual to predicted ratio is 2.34, 2.84 and 1.01 for the EC2, NR and proposed method respectively, with a CoV of 31.5, 31.5 and 13.6%. When only those whose beams failed in shear are counted, the proposed method gives a mean actual to predicted ratio of 1.09 with a CoV of 8.6%.

6.5 Analysis of the strengthened beams

6.5.1 Introduction

As discussed in Chapter 2, the existing guidelines for the shear strengthening of concrete with FRP have been developed for externally bonded (EB) applications, and only more recent studies have dealt with the near-surface mounted (NSM) system. Both techniques have been proven successful in increasing the shear capacity of concrete members; however, a series of drawbacks have been identified, which can reduce the effectiveness of these systems.

The bond-slip response of side-bonded EB applications has a relatively low ductility, so it is likely that the peak shear forces that can be resisted by the FRP

cannot be sustained until the stirrups yield, rendering the hypothesis of summing the stirrups and FRP contribution unconservative (Mohamed Ali et al., 2006). In the NSM system, the fracture energy in the bond-slip response is much higher and it has been shown (Rizzo and De Lorenzis, 2009a) that, when an appropriate value of the bond strength is chosen, a simple rigid-plastic bond-slip model can be successfully employed and the peak of the FRP contribution can still be reached after the stirrups have yielded. On the other hand, as also observed in the present experimental campaign, the NSM technique may suffer from early detachment of the side concrete cover containing the FRP bars, preventing the strengthening system from reaching its full bond capacity.

In Chapter 5 it has been shown that the deep embedment technique, in addition to being conveniently applicable in all situations where there is no access to the sides of the member, can overcome the two issues described above. The bond-slip response, obtained from pull-out tests, appears sufficiently ductile, with a fracture energy comparable to or higher than that encountered in the NSM case, and the strengthening is fully internal, so the bond capacity of the system can always be relied upon, unlike in the NSM case, where additional failure mechanisms may need to be catered for.

6.5.2 Modelling considerations

With reference to Figure 6.31, showing a beam containing both stirrups and strengthening bars, if the critical diagonal shear crack opens following a vertical downward movement between the two concrete parts, coherently with the critical failure mechanisms discussed in the unstrengthened situation, all crossed bars and stirrups are subject to the same imposed elongation, equal to the crack width w, that increases with the shear force.

Each closed stirrup of length h_s crossed by a crack is initially subject to a strain equal to $\varepsilon_s = w/h_s$; with $\varepsilon_s = \sigma_s/E_s = V_s/(E_s A_s)$. The relation between the shear force resisted by a stirrup V_s and the crack width w is linear:

$$V_s = w\frac{E_s A_s}{h_s} \tag{6.63}$$

where A_s is the total area of each stirrup leg. When the stirrup yields, the shear force $V_s = V_{sy} = f_y A_s = \varepsilon_y E_s A_s$ remains constant for increasing crack widths, until the stirrups reach the ultimate strain ε_u, usually of the order of 0.05-0.1.

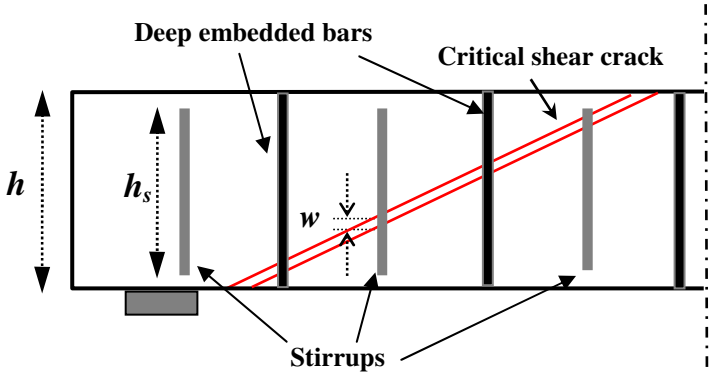

Figure 6.31: Interaction between stirrups and deep embedded bars

For the deep embedded bars, the crack width is equal to the sum of the slips at the loaded end (i.e. at the crack location) for the two parts of the bar each side of the crack. The ultimate bond capacity is guided by the part of the bar on the shortest side, so the bond capacity for a bar is given by:

$$V_f = (\pi d_b)\tau_b l_b = \varepsilon_f E_f A_f \tag{6.64}$$

where d_b is the bar diameter, l_b is the bonded length on the shortest side of the crack, τ_b is the average bond stress relative to l_b (a function of the bar slip via the bond-slip diagram obtained from tests), ε_f is the strain in the bar, E_f is the Young's modulus of the bar and A_f is the area of the bar.

The strain in the embedded bar is related to the crack width through the bond-slip curve; unfortunately, while for the stirrups the calculation of the V-w relation is simple, for the deep embedded bars the value of the average bond stress τ_b is different for each bonded length, so a bond-slip curve for several values of the bonded length is needed. Based on the fact that, from the pull-out test campaign presented in Chapter 5, the bond-slip behaviour of the deep embedded bars has been found to be particularly ductile, it is proposed that a rigid-plastic bond-slip behaviour is adopted with an 'effective' value of the average bond stress, computed from the pull-out test results by limiting the ultimate slip at 2.5mm and maintaining the fracture energy equal to the value of the measured bond-slip curves (as shown in Figure 5.6). In this way, for the bars and the adhesive used in the strengthened test (6 and 7.5mm carbon bars, 8mm steel bars and the Hilti 500 adhesive), an effective bond stress of approximately 20MPa is found as an average value for the five bonded lengths tested (15 to 75mm).

Although it is possible that for longer bonded lengths than those tested in the present research project the effective bond stresses may result in bond stresses lower than 20MPa, in practice for bonded lengths in excess of 75mm the bar capacity V_f is limited by a strain limit, set equal to 0.004 for the deep embedded FRP bars and equal to the yield strain for the deep embedded steel bars. This upper limit of 0.004 is proposed as a limiting value for the strain of the FRP bars in shear in accordance with the maximum strain magnitudes found in the large-scale tests at failure (see Chapter 5) and also coherently with the existing recommendations of the current guidelines for externally bonded systems (Concrete Society TR55, 2004; ACI 440.2R, 2008).

There is no guarantee that the sum of the capacities of all deep embedded bars can be sustained even after the stirrups have yielded and the crack width keeps increasing. This is because the strain levels would be different in the various deep embedded bars intersected since, for the same crack width, the strain levels in a bar would depend on its effective embedment length, i.e. on the relative position of the crack with respect to the concrete edge and some may go beyond 0.004. On the other hand, this strain limit is somewhat conventional and has been originally proposed for externally bonded FRPs. So, while there is still insufficient test evidence to confirm whether for the deep embedment technique it may be higher, the assumption is appropriately prudent for the bars object of the present study, whose ultimate strain is never lower than 0.016.

Therefore, in the analysis it appears sensible to rely on the maximum capacity of a deep embedded bar given by (6.64) but still conservatively adopt the 0.004 limit. When stirrups are present, it may be advisable to perform a shear force-crack width analysis to confirm that the peak capacity of the deep embedded bars is reached for a value of crack width comparable to that corresponding to the stirrups at yield; if this is not the case, the strain required from the deep embedded bars for the maximum capacity to be additive may be excessive.

6.5.3 Upper-bound analysis

The upper-bound model derived for the analysis of all strengthened beams is conceptually the same as described in section 6.3.1.2 for the beams with stirrups,

where the contribution of the deep embedded bars is appropriately catered for as explained in the following.

Assuming, according to the theory of sliding in cracks, that the equivalent unstrengthened beam would fail in shear with a yield line of projection length equal to *x'*, the strengthening bars (and the stirrups, if present) would displace this yield line according to the two mechanisms in Figure 6.32, which is similar to Figure 6.9 but shows deep embedded bars, bonded all along the beam depth, rather than stirrups (where a concrete cover of 30mm exists).

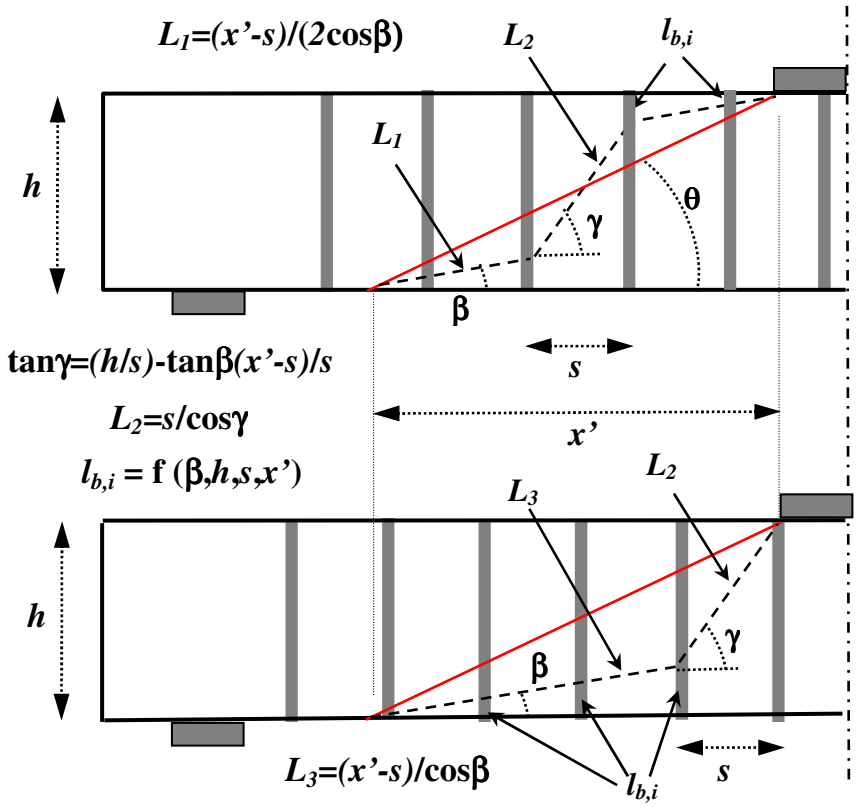

Figure 6.32: Upper-bound model for the shear capacity of the strengthened beams

The solution is found by varying the angle β in steps, starting from the initial value of $\beta = \theta$ (which corresponds to the unstrengthened capacity V_c) and calculating, for each β-value, the capacity V_{tot} due to the new mechanism until the difference between V_{tot} and V_c equals the sum of the maximum capacity of each deep embedded bar and stirrup intersected at a distance $l_{b,i}$ from the top or bottom concrete edge in the mechanism. Therefore, the role of the strengthening bars is to allow a displacement of the critical yield line from the position of minimum energy

to a position where the increase in dissipation can be guaranteed by their bond capacity.

The maximum capacity of each stirrup intersected by the yield line, if present, is $V_{si} = A_{si}f_{yi}$. The maximum capacity of each deep embedded bar is given by the bond-related relation:

$$V_f = (\pi d_b)\tau_b l_b \tag{6.64}$$

with the effective bond stress τ_b assumed equal to 20MPa, as discussed in the previous section. The capacity is limited to:

$$V_{f,max} = 0.004E_f A_f \tag{6.65}$$

for deep embedded FRP bars and to:

$$V_{f,max} = f_y A_f \tag{6.66}$$

for deep embedded steel bars, where f_y is the steel yield stress. In all cases, the optimized solution is easily found numerically with the aid of an appropriate spreadsheet, where all unknowns are a function of the angle β and the capacity is given by the lowest between the first or the second mechanism, in accordance with the formulae of previously defined (6.29) to (6.46).

Table 6.5 shows the actual and predicted capacities for all strengthened beams. For each category (small-scale RC, small-scale PSC and large-scale PSC), the table contains the results of the equivalent unstrengthened to facilitate the comparison.

In the small-scale PSC beams, the gap between shear and flexural failure was quite small, so the strengthening was effective in all cases leading each beam to ductile flexural failure. Therefore, although the predictions for these beams are accurate, they are of minor significance, as an actual comparison between shear capacities cannot be made. For both the small-scale RC beams and the large-scale PSC beams, where the gap between shear and flexure was higher and the effectiveness of the strengthening could be appreciated, the model is consistently accurate and appropriately conservative.

When only the RC beams are considered, the mean actual to predicted ratio is 1.09 with a CoV of 7.4%, while for the large-scale beams the mean actual to predicted ratio is 1.11 with a CoV of 2.7%. If only the beams which failed in shear and which were strengthened with the deep embedment technique are considered, the mean

actual to predicted ratio is 1.11 with a CoV of 2.9%, confirming the validity of the model.

Table 6.5: Upper-bound predictions for the strengthened beams (all loads in kN)

Specimen	***a/d***	***Actual P_{ult}***	***Pred P_{ult}***
	Small-scale RC		
USB R3d	3	23.5 (shear)	25.9 (shear)
SSB R3d-C6@0.7d	3	46.4 (shear)	40.7 (shear)
SSB R3d-C6@0.5d	3	50.5 (shear)	47.4 (shear)
SSB R3d-C6@0.35d	3	53.5 (flexure)	54.6 (shear)
USB Rst3d	3	31.5 (shear)	35.6 (shear)
SSB Rst3d-C6@0.7d	3	56.5 (flexure)	47.3 (shear)
	Small-scale PSC		
USB P4d	4	37.9 (shear)	32.4 (shear)
SSB P4d-C7.5@0.7d	4	42.1 (flexure)	44.3 (flexure)
SSB P4d-S8@0.7d	4	43.8 (flexure)	44.3 (flexure)
SSB P4d-C6@0.7d	4	43.2 (flexure)	44.3 (flexure)
SSB P4d-S6@0.7d	4	41.9 (flexure)	44.3 (flexure)
SSB P4d-C6@d	4	43.3 (flexure)	42.3 (shear)
SSB P4d-S6@d	4	42.7 (flexure)	42.3 (shear)
	Large-scale PSC		
ULB P4d	4	295.9 (shear)	268.2 (shear)
SLB P4d-2C7.5@d	4	339.1 (shear)	302.6 (shear)
SLB P4d-C7.5@d	4	315.0 (shear)	291.0 (shear)
SLB P4d-2S8@d	4	349.1 (shear)	303.7 (shear)
SLB P4d-2C7.5N@d	4	325.4 (shear)	302.6 (shear)

It is noted that while the predictions for the beams containing only deep embedded bars are generally very accurate, for the specimen SSB Rst3d-C6@0.7d (the only one containing both stirrups and FRP) the predicted increase in capacity with respect to the plain specimen is 21.4kN, a bit over conservative if compared with the observed minimum increase of 33kN (as it failed in flexure). As discussed above, the model prediction in the table is the lower between the two upper bound mechanisms of Figure 6.32, that in most cases give similar figures. However, for these specimens the predicted increase in capacity resulted in 21.4kN and 29.0kN respectively for the two mechanisms, with the second closer to the actual capacity.

6.5.4 Simplified methodology

Based on the findings of the experimental campaign and on the previous modelling considerations, a simplified method is proposed to assist in the design of the deep embedment strengthening scheme which can be easily incorporated into existing codes.

The increase in capacity attributable to the strengthening bars, to be added to the steel and concrete contributions from the codes, is calculated from a 45° truss analogy:

$$V_f = \frac{\sigma_f A_f}{s} z \tag{6.67}$$

where s is the bar spacing, σ_f is a stress limit for the bars and the effective lever arm, z, equals:

$$z = h - l_{b,max} \tag{6.68}$$

where $l_{b,max}$ is defined below. The stress limit σ_f is equal to the yield strength for the steel bars and to the product $\varepsilon_f E_f$ for carbon bars, where E_f is the elastic modulus of the FRP bar and $\varepsilon_f = 0.004$ is the proposed strain limit value previously discussed.

The required anchorage length at each end of the embedded bars is found by rearranging (6.64), with the force in each bar being given by $\sigma_f A_f$:

$$l_{b,max} = \frac{\sigma_f A_f}{\pi d_b \tau_b} \tag{6.69}$$

where the value of the bond stress is taken equal to 20MPa, as previously discussed.

The validity of the proposed formulation is reinforced by the ductility of the bond-slip response of the deep embedment system, so it is possible to rely on a sustained value of bond stress even for large values of the crack widths (and then large slips). On the other hand, the formula is conservative, because all bars crossed by the 45° crack whose bonded length l_b is below $l_{b,max}$ are disregarded, whereas in reality they would contribute with a capacity equal to (6.64); in practice, the value of $l_{b,max}$ would be sufficiently small that the contribution of any bar with smaller lengths may be disregarded without appreciable error.

Table 6.6 compares the predicted values for V_f from the above formulation with the actual V_f, taken as the difference between the actual shear capacity of the strengthened beam and the capacity of its unstrengthened counterpart. When only the beams strengthened with the deep embedment technique that failed in shear are considered, the truss model seems to predict V_f with reasonable accuracy, with a mean of actual to predicted of 1.13 and a CoV of 19.4%, which is not unduly high given the extreme simplicity of the approach. From the table, it is also clear that the prediction for the beam strengthened with NSM is unsafe, as the full bond capacity of the bars could not be developed in this specimen.

Table 6.6: Predictions from the simplified truss model for the strengthened beams (all loads in kN)

Specimen	***Actual* P_{ult}**	***Pred* P_{ult} (EC2)**	***Pred* P_{ult} (NR)**	***Actual* V_f**	***Pred* V_f**
	Small-scale RC				
USB R3d	23.5 (sh)	21.0 (sh)	20.5 (sh)	n/a	n/a
SSB R3d-C6@0.7d	46.4 (sh)	36.3 (sh)	35.9 (sh)	22.9	15.4
SSB R3d-C6@0.5d	50.5 (sh)	42.5 (sh)	42.1 (sh)	27.0	21.5
SSB R3d-C6@0.35d	53.5 (flex)	51.7 (sh)	51.3 (sh)	30.0	30.8
USB Rst3d	31.5 (sh)	27.9 (sh)	30.6 (sh)	n/a	n/a
SSB Rst3d-C6@0.7d	56.5 (flex)	43.3 (sh)	46.0 (sh)	25.0	15.4
	Small-scale PSC				
USB P4d	37.9 (sh)	29.6 (sh)	24.1 (sh)	n/a	n/a
SSB P4d-C7.5@0.7d	42.1 (flex)	44.3 (flex)	44.3 (flex)	≥4.2	20.2
SSB P4d-S8@0.7d	43.8 (flex)	44.3 (flex)	44.3 (flex)	≥5.9	21.3
SSB P4d-C6@0.7d	43.2 (flex)	44.3 (flex)	39.4 (sh)	≥5.3	15.4
SSB P4d-S6@0.7d	41.9 (flex)	44.3 (flex)	40.1 (sh)	≥4.0	16.1
SSB P4d-C6@d	43.3 (flex)	40.3 (sh)	34.8 (sh)	≥5.4	10.8
SSB P4d-S6@d	42.7 (flex)	40.8 (sh)	35.3 (sh)	≥4.8	11.2
	Large-scale PSC				
ULB P4d	295.9 (sh)	227.7 (sh)	236.8 (sh)	n/a	n/a
SLB P4d-2C7.5@d	339.1 (sh)	272.2 (sh)	281.3 (sh)	43.6	44.5
SLB P4d-C7.5@d	315.0 (sh)	250.0 (sh)	259.0 (sh)	19.1	22.2
SLB P4d-2S8@d	349.1 (sh)	277.7 (sh)	286.8 (sh)	53.6	50.0
SLB P4d-2C7.5N@d	325.4 (sh)	272.2 (sh)	281.3 (sh)	29.9	44.5

When the V_f from the model is added to the concrete and shear capacity from codes to form the code predictions, the results for the prestressed beams are rather

conservative, but this is mostly due to the over-conservativeness of the codes for the unstrengthened case. However, when the beams which failed in shear are considered, the CoV is only 2.5% and 2.7% for the EC2 and NR code predictions, respectively, which means that it is possible safely to design a shear strengthening scheme for realistically-sized structures using this simplified approach.

6.5.5 Concluding remarks

The upper-bound plasticity approach adopted to evaluate the capacity of the beams strengthened with the deep embedment technique has been shown to render accurate predictions for all specimens considered in the present research project. As the method is fully consistent with the analytical approach proposed for the unstrengthened single beams and bridges, it represents an ideal complement and a complete assessment tool for such types of bridge and, in general, for every concrete beam suspected to be deficient in shear.

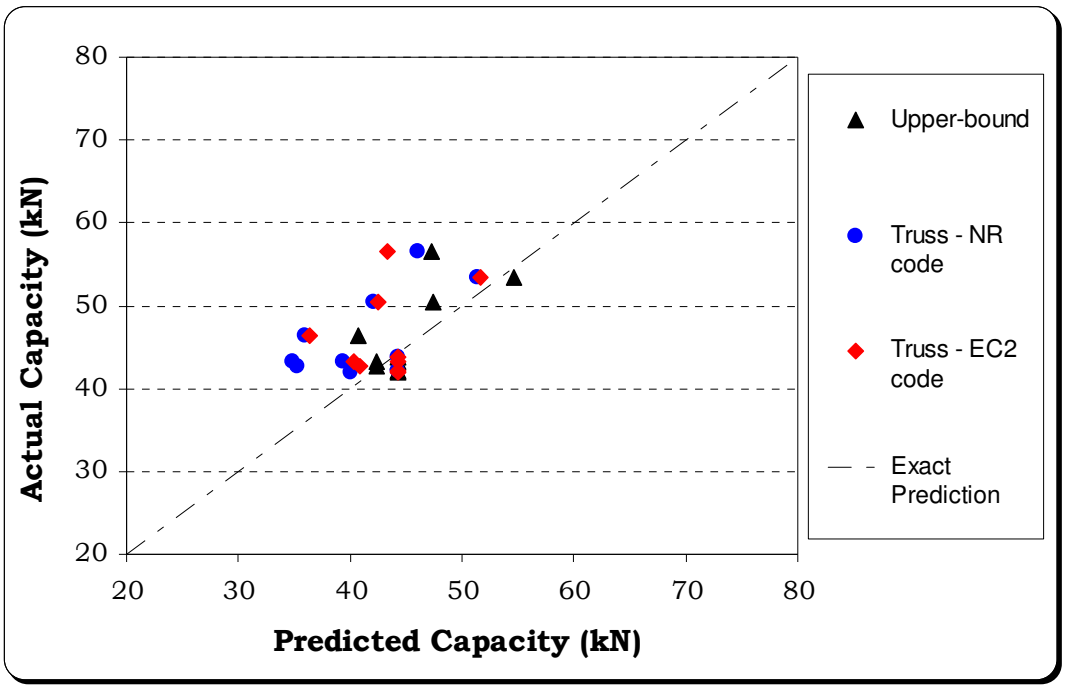

Figure 6.33: Ultimate capacity predictions for the strengthened small-scale beams

However, for a rapid estimate of the amount of deep embedded bars needed in designing a strengthening scheme, the simplified method, based on the truss analogy, can be used safely. Figures 6.33 and 6.34 show the predictions for the strengthened small-scale and large-scale beams, respectively, using the upper-

bound approach and the simplified method with the Eurocode and Network Rail assessment code.

Although from the results it may appear that, especially for the large-scale beams, the predictions are a bit too conservative, it must be remembered that all strengthened tests on the prestressed beams have been performed at $4d$ to ensure the gap between shear and flexural failure was not too small in the unstrengthened case, but actually the beams were critical in shear for longer shear spans, where the code predictions for the unstrengthened case were much more accurate.

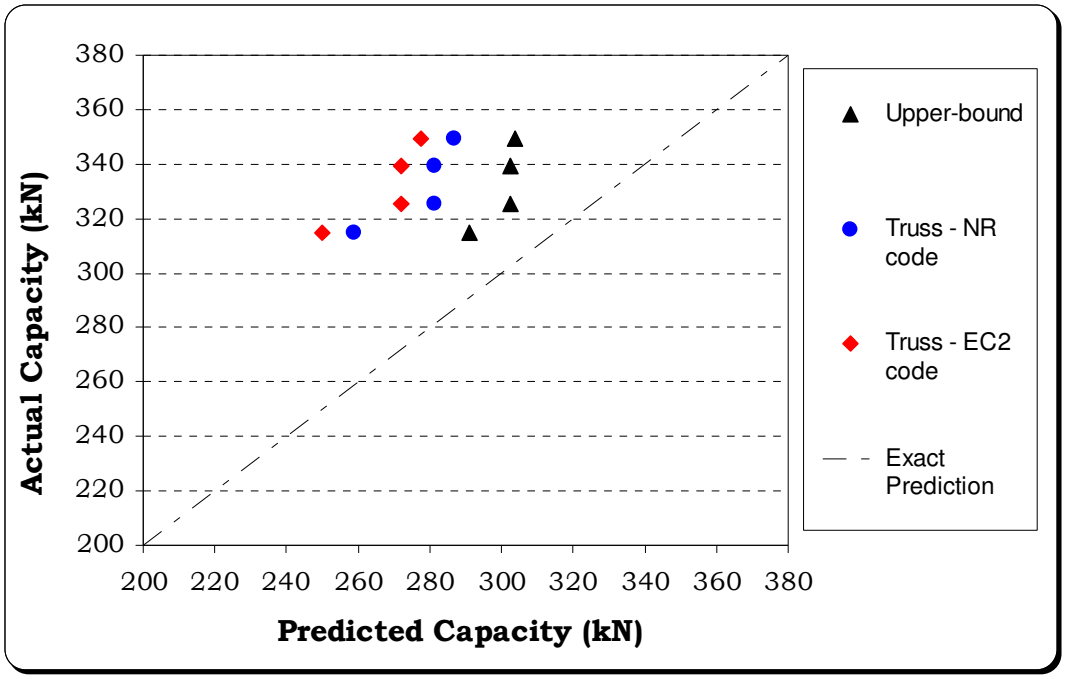

Figure 6.34: Ultimate capacity predictions for the strengthened large-scale beams

6.6 Conclusions

A unified analytical approach employing upper-bound models based on the plasticity theory has been developed and applied to small- and large-scale single beams and bridges to produce an assessment tool for prestressed concrete rectangular bridge beams when post-tensioned transversely and made contiguous within a deck. The same model has been successfully extended to the specimens strengthened with the deep embedment technique. The analytical approach adopted has been shown to be accurate and consistent with the test observations, forming the basis of a rational assessment procedure for these types of bridge. In addition, a simplified method has been presented that can be easily incorporated

into existing codes of practice to assist in the design of the proposed deep embedment strengthening scheme.

Chapter 7
Shear Assessment and Strengthening Example

7.1 Introduction

In the previous chapters, it has been shown that the provisions of the assessment codes are excessively conservative for the bridges considered in the present study, as no method is given to properly evaluate the beneficial contribution of the lateral prestressing. Furthermore, no viable existing shear strengthening technique is available for the beams of such bridges, where only access from the soffit is possible.

As shown in Chapter 5, a novel strengthening technique, the deep embedment of FRP or steel bars, has been validated through testing. It would permit the problem of shear strengthening of such structures to be overcome.

In Chapter 6, a series of analytical models, based on the upper-bound theorem of plasticity theory, have been developed that match well with the behaviour of a large number of small-scale and large-scale specimens with and without stirrups, for different levels of lateral prestressing and in both unstrengthened and strengthened situation. A simple model, easily incorporated in the current codes, has been developed for the design of the strengthening scheme.

In order to demonstrate the practical applicability of the proposed methodology to a real structure, the shear assessment and strengthening procedure is applied to the existing prestressed concrete railway bridge described in Chapter 3, which formed the basis for the design of the laboratory test specimens.

7.2 Assessment and strengthening example

7.2.1 Load analysis

As detailed in Chapter 2, the assessment calculations of existing bridges in UK are performed in accordance with the NR/GN/CIV/025 (2006) code for railway structures and the BD 44/95 (1995) code for highway structures; the two documents are perfectly equivalent in terms of provisions for calculating the flexural ad shear resistance of the structural elements.

The safe load capacity of a railway bridge is defined by the Route Availability number (RA) of its most critical elements when subject to a load associated with the permissible speed of the route at the bridge location, which is taken equal to 60mph for the bridge in discussion. As shown in the flowchart of Figure 2.20, the live load to be applied to the bridge, to be multiplied by the appropriate dynamic factor, is that corresponding to 20 British Standard Units (BSU), represented, for each track, by a series of axle loads of 200 and 150kN and a distributed load of 65kN/m. The assessment load effects, S^*_A, are derived from the nominal loads multiplied by the load partial factors γ_{fL} and γ_{f3}. The RA number of the bridge is then given by:

$$RA = 20 \times \frac{R^*_A - S^*_{A,P}}{S^*_{A,L}} - 10 \tag{7.01}$$

where $S^*_{A,P}$ and $S^*_{A,L}$ are the permanent and live load effects, respectively, and R^*_A is the factored resistance under the critical load effect (shear, bending, etc.).

All geometric properties of the prestressed beams of the reference bridge have been presented in Chapter 3. The assessment load effects due to permanent and live loads (bending moment and shear) are calculated at mid-span and at the sections at 3, 4, 5 and 6d from the support, in line with the locations analysed during the experimental campaign. Furthermore, the beams contain several tendons that are debonded towards the support so the ultimate flexural capacity is not the same across all sections.

The permanent loads acting on a single beam are the dead load (1645kg/m), the ballast (405kg/m) and the relevant proportion of load from the track (240kg/m). When multiplied for the corresponding partial factors γ_{fL} (equal to 1.15, 1.75 and

1.2, respectively) and for γ_{f3} = 1.1, a total distributed permanent load of 31.8kN/m is obtained at the ULS over the beam.

The live load from each rail, distributed transversely at 15° through the ballast, covers the whole width of the beam, so the load on a beam is half the nominal EUDL live load on a track, multiplied at ULS by γ_{fL} = 1.4 and γ_{f3} = 1.1. The dynamic factor, calculated in accordance with NR/GN/CIV/025 (2006), is equal to 1.286 for bending and 1.191 for shear. The critical live load combination at ULS is the sum of the vertical and the horizontal effects (traction, braking, nosing and centrifugal); for the shear and bending of the single beam, however, only the nosing gives a contribution in the form of an additional vertical component of 55kN at ULS, calculated by multiplying the transverse load on the track by the distance between the top of the rail and the top of the beams divided by the spacing of the rails.

Table 7.1 summarizes the maximum shear V and corresponding bending moment M at ULS on a single beam due to both permanent and live loads at the sections at 3, 4, 5 and 6d; also shown is the maximum bending moment at mid-span.

Table 7.1: Assessment load effects (bending and shear) on the existing reference bridge beams

Section	M_{perm} (kNm)	V_{perm} (kN)	M_{live} (kNm)	V_{live} (kN)
3d	343	160	1340	741
4d	436	141	1710	715
5d	519	121	2100	691
6d	589	100	2410	667
Mid-span	748	0	2450	150

7.2.2 Assessment

The shear resistance of a concrete beam according to the assessment code NR/GN/CIV/025 (2006) has been defined in Chapter 2, by (2.40) to (2.49). In order to compare the code provisions with the predictions of the upper-bound model developed in the present research project, the ultimate (unfactored) shear capacities of each single real bridge beam loaded at 3, 4, 5 and 6d are shown in Figure 7.1, where both cases with and without stirrups are considered.

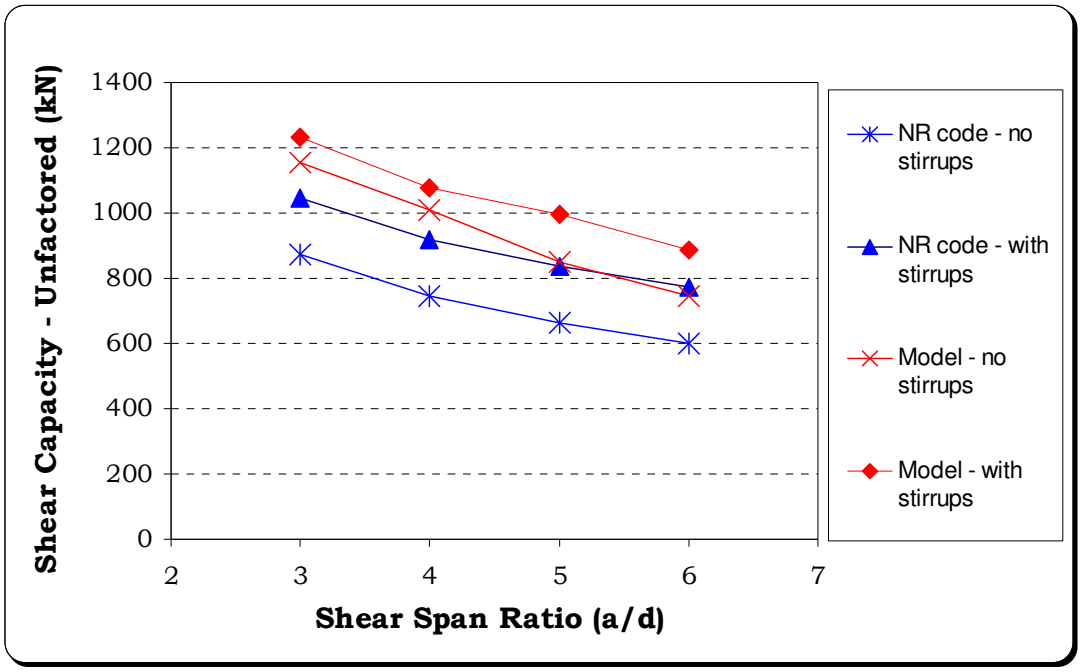

Figure 7.1: Ultimate shear capacity predictions for the real beams

From the plots, it is seen that the predictions from the proposed model are around 15 to 25% higher than the assessment code, and the gap is smaller for longer shear spans; this is in good agreement with the findings presented in Chapter 6 for the small- and large-scale specimens, proving the model is consistent and can correctly capture the size effect. The model also predicts the stirrups to be more effective at long shear spans.

Figure 7.2 shows the available shear capacity at ULS, defined as the ultimate factored shear capacity minus the factored shear force due to the permanent loads, calculated for the each single real beam with both the assessment code and the proposed model, where the same factors γ_{mc} = 1.5 and γ_{ms} = 1.15 have been applied to the concrete resistance f_c and to the stirrup yield stress f_y in the various formulae of the upper-bound model.

From the graph, where the shear demand from the assessment load effect corresponding to 20 BSU is also depicted, is clear that, although the predictions from the model are higher than the corresponding to the code, in all cases the shear capacity is lower than that required for the beams to have a RA number of 10. Therefore, if the effect of the lateral prestressing is disregarded, the bridge is theoretically unable to safely carry 20 BSU at 60mph. It is worth noting that the model predictions at 3d and 4d are identical. This is due to the fact that, when the

material safety factors are applied to the concrete in the upper-bound model and the projection *x'* is calculated, the critical crack at 3*d* is particularly steep and the angle *a* to the discontinuity (see Figure 6.4) is lower than *φ*; however, it has to be not lower than *φ* to satisfy the plane strain conditions assumed for crack sliding problems, so the angle to the discontinuity is limited to *φ* and the overall capacity is reduced.

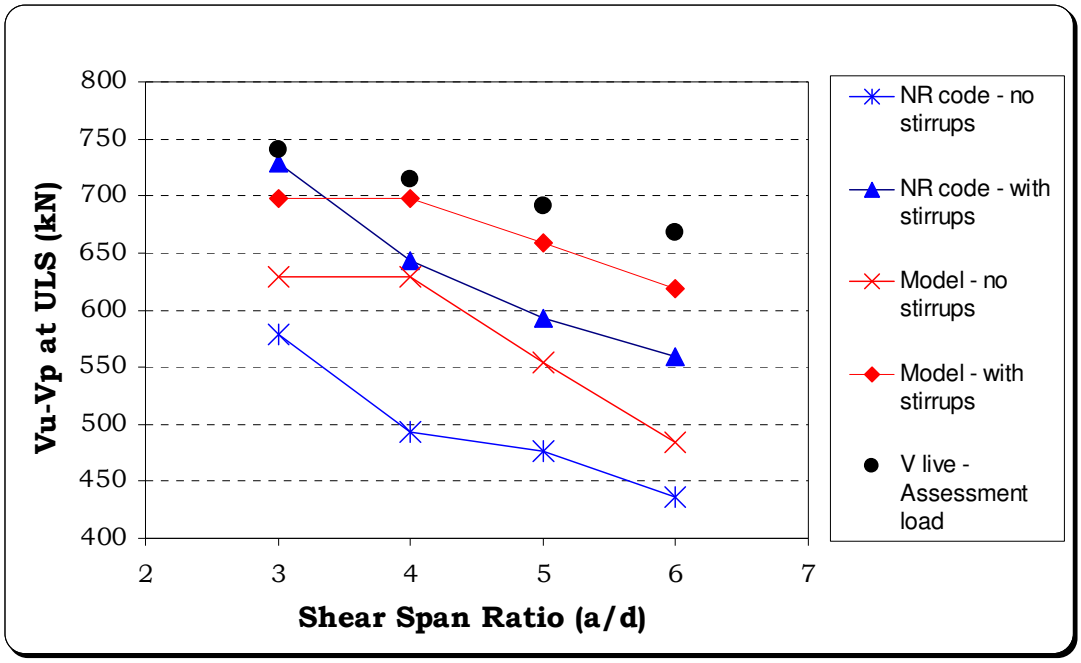

Figure 7.2: Available shear capacity at ULS for the single real beams

When the lateral prestressing (factored by γ_{fL} = 0.87) is considered and its effect evaluated using the proposed upper-bound model with a friction angle of 37°, assumed for the concrete to concrete interface, the increase in shear capacity is substantial. In Figure 7.3, the available shear capacity at ULS for the real bridges with only 25% of the full lateral prestressing is shown and compared with the capacity from the code and the assessment load effect. The equivalent live load leading to flexural failure is also shown for both single beams and bridges.

The graph indicates that a mere 25% of the lateral prestressing is theoretically sufficient to ensure the bridge is able to carry at least 20 BSU at 60mph, even if the contribution of the stirrups is completely disregarded. When compared to the single beam, the increase in shear capacity due to the lateral prestressing is around 30%, very similar to the increase found in the small-scale test specimens in Chapter 6.

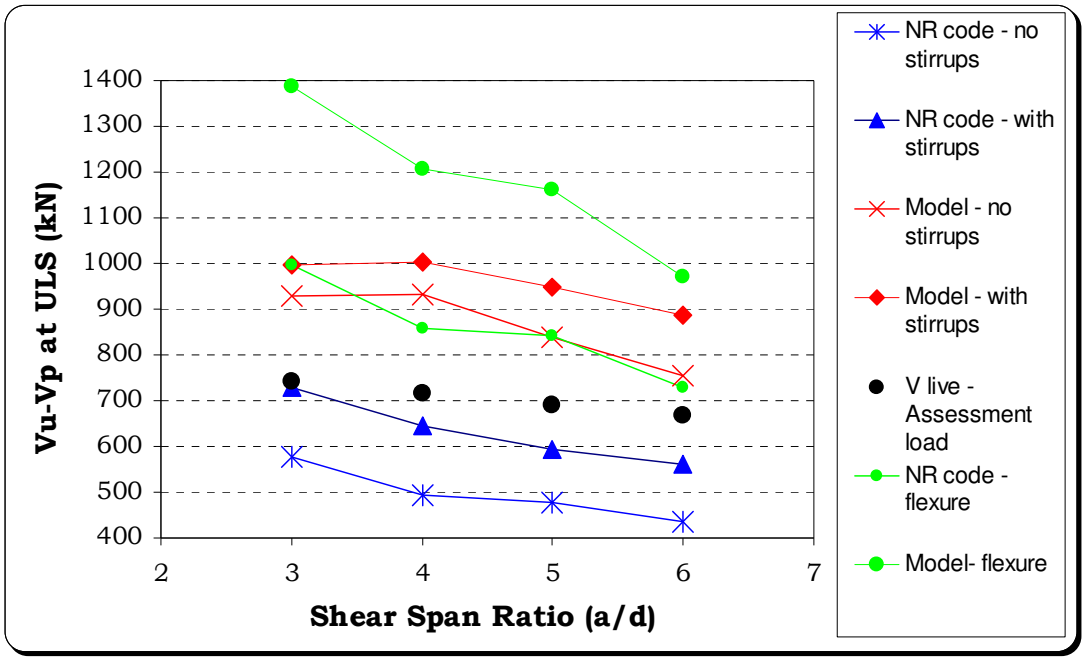

Figure 7.3*:* Available shear capacity at ULS for the real bridges with 25% of the lateral prestressing

Table 7.2*:* Route Availability (RA) number at 60mph for the reference bridge

	Without Stirrups		**With Stirrups**	
Section	*Code*	*Model*	*Code*	*Model*
3d (no lateral load)	RA5	RA6	RA9	RA8
4d (no lateral load)	RA3	RA7	RA8	RA9
5d (no lateral load)	RA3	RA6	RA7	RA9
6d (no lateral load)	RA3	RA4	RA6	RA8
3d (25% lateral load)	-	RA15	-	RA15
4d (25% lateral load)	-	RA15	-	RA15
5d (25% lateral load)	-	RA14	-	RA15
6d (25% lateral load)	-	RA12	-	RA15

Table 7.2 shows the RA number of the bridge, calculated using (7.01), according to both the assessment code and the upper-bound model, with and without considering the stirrups. The results show that, unless the effect of the lateral prestressing is completely ignored, the bridge may have a shear capacity well in excess of that calculated using the assessment code. It is also confirmed that, in general, sections farther away from the support are critical for the shear resistance of prestressed beams; this means that, if the lateral prestressing is lost or conservatively ignored in the assessment process, the zone where the shear

strengthening is needed the most would be between 4 to 6 times the effective depth of the section, rather than close to the supports.

7.2.3 Strengthening

The assessment calculations have shown that, if the lateral prestressing is lost or disregarded, according to both the assessment code and the upper-bound model the beams are theoretically unable to safely carry 20 BSU at 60mph, and may need to be strengthened in shear using the deep embedment technique.

The amount of strengthening can be designed using the simplified methodology described in Chapter 6, where the increase in the shear force V_f required from the strengthening bars in order to obtain a RA number of 10 at each section is shown in Table 7.3. Note that V_f is calculated as the difference between the assessment load effect (see Table 7.1) and the corresponding available shear capacity at ULS for the single beam according to the NR/GN/CIV/025 (2006) code (see Figure 7.2).

Table 7.3: Required increase of shear capacity for the real beams (in kN)

Section	Without Stirrups	With Stirrups
3d (no lateral load)	163	12.6
4d (no lateral load)	222	71.5
5d (no lateral load)	215	98.7
6d (no lateral load)	231	108

The table shows that it is necessary for the strengthening bars to increase the shear capacity by 108kN, if their contribution is additive to that of the stirrups; if, very conservatively, the stirrups contribution is completely disregarded, the bars have to provide an increase of 231kN.

In order to evaluate the V_f contribution, the formulae (6.67) to (6.69) in Chapter 6 are used, but appropriate safety factors are adopted at ULS, in line with those of the assessment code NR/GN/CIV/025 (2006) and those of the UK guidelines for strengthening (Concrete Society TR55, 2004), presented in Chapter 2. Therefore the capacity V_f offered by the deep embedment bars at ULS is equal to:

$$V_f = \frac{\sigma_{f,D} A_f}{s} z \tag{7.02}$$

where s is the bar spacing, $\sigma_{f,D}$ is the design stress for the bars and the effective lever arm z is equal to:

$$z = h - l_{b,max,D} \tag{7.03}$$

with

$$l_{b,max,D} = \frac{\sigma_{f,D} A_f}{\pi d_b \tau_{b,D}} \tag{7.04}$$

In the above expressions, the design stress $\sigma_{f,D}$ is equal to the yield stress divided by γ_{ms} = 1.15 for the steel bars and to the product $\varepsilon_f E_{f,D}$ for CFRP bars, where $E_{f,D}$ is the elastic modulus of the FRP bars divided by the factors γ_E = 1.1 and γ_{mm} = 1.05 (related to the loss in elastic stiffness over time and to the manufacturing process, respectively), while ε_f = 0.004 is the strain limit value. The design bond stress, for both steel and FRP bars, is taken equal to 20MPa divided by the safety factor for the adhesive γ_{mA} = 4 recommended in Concrete Society TR55 (2004), so $\tau_{b,D}$ = 5MPa.

Using the same bars adopted in the large-scale test specimens (7.5mm diameter CFRP bars or 8mm diameter steel bars), from (7.02) to (7.04) and from the bar properties defined in Chapter 3, it may be shown that if two bars at 150mm c/c or four bars at 300mm c/c are inserted in the shear zone of the real beam, the increase in shear capacity V_f is equal to 112kN or 120kN for the CFRP and steel bars, respectively. This means that, if the contribution of the stirrups can be summed to that of the deep embedded bars, a percentage of transverse strengthening as little as 0.065% may suffice in enhancing the shear capacity of the bridge from RA 6 to RA 10. If the contribution of the stirrups is disregarded, the amount of strengthening has to be doubled; still, the required percentage of transverse strengthening would be 0.130%, certainly not a value excessively high.

Having designed the amount of deep embedded bars with the simplified methodology based on the truss analogy, it is possible to calculate the shear capacity of the strengthened beams using the upper-bound analysis for single beams described in Chapter 6. In the upper-bound analysis, the same safety factors used for the simplified methodology are applied to the elastic modulus of the FRP bars and to the bond stress and both cases of beams with and without stirrups are considered. When the stirrups are included, four CFRP bars at 300mm c/c are assumed in the cross-section; if the stirrups are disregarded, the analysis refers to four CFRP bars at 150mm c/c.

Table 7.4 shows the theoretical shear capacity of the real beams strengthened with CFRP bars at the ULS according to the upper-bound model. For comparison, also shown is the value of shear resistance obtained from summing V_f from the truss analogy with the shear capacity from the assessment code. In the table, the ultimate shear capacities of the strengthened beams are presented by subtracting the shear resistance needed for factored permanent loads and are compared with the assessment load effects due to live load only, to provide a gauge of live-load resistance. In the upper-bound analysis, the increase in shear capacity due to the deep embedded bars V_f is calculated as the difference between the ultimate capacities of the strengthened and the corresponding unstregthened model.

Table 7.4*:* Shear capacity of the strengthened real beams at ULS (in kN)

Section	**Shear Capacity**		**V_f**		**V_{live}**
With Stirrups	*Truss*	*Model*	*Truss*	*Model*	
3d	840	754	112	76	741
4d	756	774	112	76	715
5d	705	755	112	96	691
6d	672	735	112	116	667
Without Stirrups	*Truss*	*Model*	*Truss*	*Model*	
3d	802	758	224	150	741
4d	717	779	224	150	715
5d	700	742	224	188	691
6d	660	718	224	233	667

From the table it can be seen that, apart from the section at 3*d*, the total shear predictions from the simplified truss methodology are conservative, although the predicted increase in capacity due to the deep embedded bars, constant in the truss, varies with the shear span in the upper-bound model due to the fact that flatter shear cracks intercept a higher number of bars. It appears that the amount of strengthening bars designed using the simplified methodology is sufficient to enhance the shear capacity of the real beams in such a way that they are, at any section, in excess of the assessment load effect at ULS.

7.3 Outline of proposed methodology

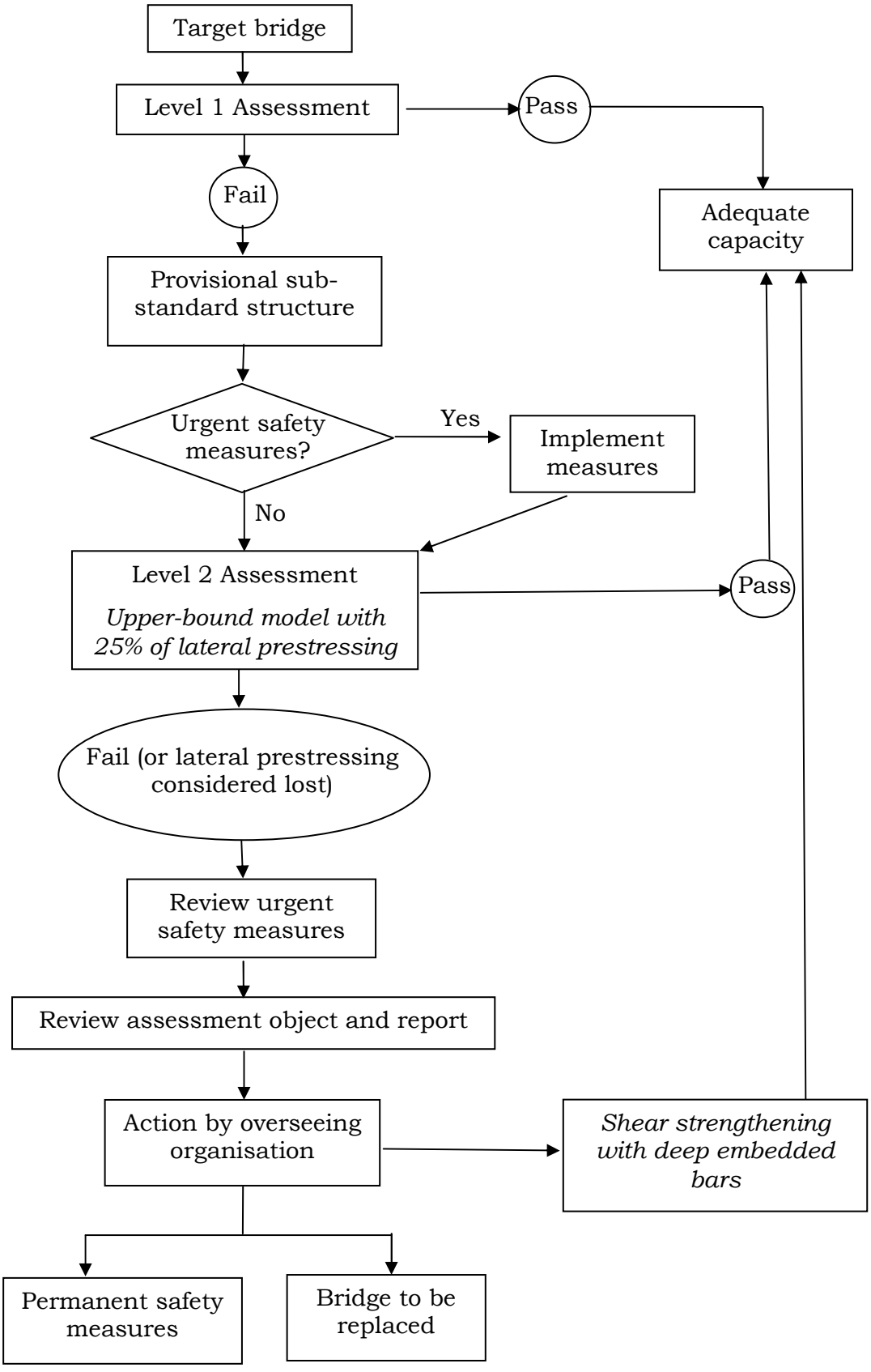

Figure 7.4: Application of the proposed assessment procedure

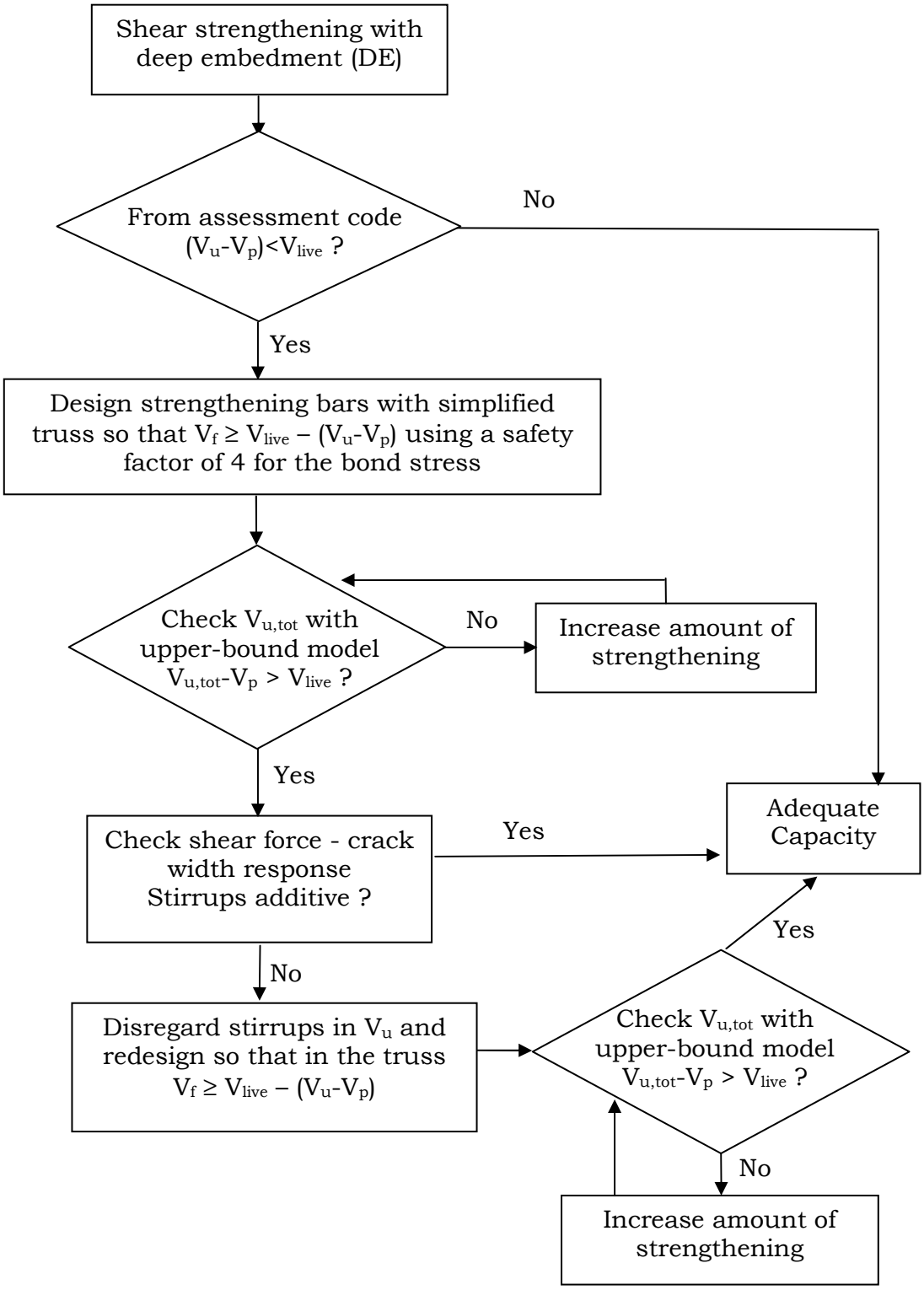

Figure 7.5: Application of the proposed strengthening procedure

From the experimental and analytical work presented in the previous chapters and on the basis of the example discussed in relation to the existing reference bridge,

the proposed assessment procedure for these bridges is illustrated in Figure 7.4, which represents an update of the flowchart of the NR/GN/CIV/025 (2006) code (Figure 2.19 in Chapter 2). When the bridge fails the assessment and a decision is taken to strengthen the structure with the deep embedded technique, the procedure summarized in the flowchart of Figure 7.5 is proposed.

7.4 Conclusions

A unified methodology, based on the experimental and analytical work presented in the previous chapters, has been proposed to conveniently assess and strengthen in shear existing prestressed concrete bridges accessible from the soffit only following the principles of the UK assessment codes.

The proposed assessment method, derived from the upper-bound theorem of plasticity, represents a major improvement as it can appropriately take into account the enhancement in capacity due to the lateral prestressing, potentially saving many structure from being sub-standard.

When the assessed capacity is inadequate, it has been shown that an appropriate shear strengthening scheme can easily be designed and checked, and it is likely that a realistically small number of strengthening bars will be sufficient to enhance the shear capacity up to the required level.

Chapter 8
Conclusions and Recommendations

8.1 Conclusions

A bridge may be assessed to be sub-standard even if its actual strength is sufficient to sustain the specified assessment load, because the methods used are unnecessarily conservative. Therefore, it is important that realistic assessment methods are employed, so that the cost associated with strengthening or replacing the structure can be avoided. On the other hand, when a bridge is indeed sub-standard, it is important that appropriate and cost-effective strengthening techniques are available. In this way, the life of the structure can be extended.

An issue identified by various bridge owners has been the shear capacity of prestressed concrete bridge beams post-tensioned together transversely and made contiguous within a deck, for which traditional methods of analysis, which neglect the lateral prestressing, would lead to shear assessment failures, as these beams often contain a low percentage of stirrups. The priority of this research project, therefore, has been to develop a realistic shear assessment tool and a viable shear strengthening technique for these bridges where only access from the soffit is possible.

This research has comprised an extensive series of large- and small-scale laboratory tests on beam and bridge specimens. Twenty-nine tests on unstrengthened specimens were carried out, studying variables like the level of longitudinal prestressing, the level of lateral prestressing, the shear span to depth ratio and the presence of internal stirrups. A novel shear strengthening technique, the deep embedment system, has been validated through fourteen beam tests and sixty-five bond tests where five different bar types and three adhesives were considered.

The experimental testing demonstrated that the collapse mechanism of these bridges involves the loaded beam only, but the lateral prestressing offers a great enhancement to the beam capacity, which can be substantially greater than that

found using traditional methods even if 75% of the initial lateral prestressing is lost, as codes are unable to account for the confining and load distribution effects of the lateral prestressing. The results also showed that, for both small- and large-scale specimens, the length of the shear span has a great influence over the shear capacity of prestressed beams, which are critical in shear farther away from the support than RC beams. Therefore, transverse reinforcement in PSC beams may be needed for a greater length but a relatively small amount is sufficient to lead to ductile flexural failures, as the gap between shear and flexural capacity is smaller.

The proposed shear strengthening method was shown to be feasible and extremely effective for both RC and PSC beams of any size. The strengthening procedure is quick and requires access to the soffit of the structure only, when an appropriate non-sag epoxy adhesive is adopted. Because the strengthening is internal, a better bond capacity can be obtained compared with other existing techniques. The pull-out tests showed that the bond-slip response of the system is ductile and robust, so it is possible to rely on a sustained value of bond stress even for large crack widths, when stirrups have already yielded, allowing the technique to be fully efficient even in the presence of existing stirrups. As no major differences were found between the beams strengthened with CFRP and steel bars, the use of FRP is suggested owing to its light weight, allowing easy installation, and its corrosion resistance.

The use of the plasticity theory is very well suited to the assessment of concrete bridges, as it can accurately take into account the actual manner in which a bridge behaves during collapse. Therefore, a unified analytical approach, based on the upper-bound theorem of plasticity, was developed and applied to single beams and bridges to produce a rational assessment tool for shear capacity predictions. It was shown that the proposed upper-bound method is able to offer better shear predictions than Eurocode 2 and the Network Rail assessment code for both small- and large-scale prestressed beams, with and without stirrups. Most importantly, the model is able to accurately and consistently predict the behaviour of the bridge specimens at both the elastic and ultimate stage, therefore representing an appropriate approach to the assessment of such bridges.

The upper-bound model was then extended to specimens strengthened using the deep embedment technique, rendering accurate predictions for both small- and large-scale specimens strengthened with steel or CFRP bars, therefore representing an ideal complement to the analytical assessment tool for such bridges. In addition,

a simplified method, based on the truss analogy and combined with codes, was developed to assist in the design of the strengthening scheme, giving predictions only slightly less accurate than the upper-bound model, and generally on the safe side.

To demonstrate its practical applicability, the shear assessment and strengthening procedure was applied to an existing prestressed concrete railway bridge. It was shown that the theoretical shear capacity of the bridge, when only 25% of the lateral prestressing is considered and when the same safety factors used by the assessment code are assumed, is around 30% in excess of that calculated using the assessment code. If the lateral prestressing is disregarded, a realistically small number of strengthening CFRP bars will be sufficient to enhance the shear capacity to the required level.

The objectives of the research project have been fully met. It is now possible to analytically assess existing longitudinally- and laterally prestressed concrete bridges for shear capacity in a rational manner, and then to devise and determine the capacity of a practical shear strengthening system if the bridge turns out to actually be understrength.

8.2 Recommendations

- It is recommended that the assessment of the typology of bridges which have been the subject of the present research should be undertaken following the procedure illustrated in the flowchart of Figure 7.6, where the same safety factors of the NR/GN/CIV/025 (2006) code are adopted.
- When shear strengthening is required, it is recommended that the deep embedment technique is adopted using FRP bars, with the amount of strengthening designed and checked with the procedure illustrated in the flowchart of Figure 7.7.
- There is potential for the assessment method developed here to be extended to other structures prestressed both longitudinally and/or laterally or, for example, to be used for voided structures, where lateral distribution is critical.

- The effectiveness of the deep embedment system relies on the bond between the resined bars and the concrete, and its practical application requires a non-sag adhesive. Further bond tests and application trials may be required if bar and adhesive types different from those considered in the present research are to be adopted.
- Only one small-scale specimen was tested that contained both stirrups and deep embedded bars. Therefore, to confirm that the enhancement of shear capacity due to deep embedded bars can be additive with that of the existing stirrups, further tests on large-scale beams may be needed.
- In addition to the bridges considered in the present research project, the deep embedment strengthening technique could have many applications when there are issues of punching shear, such as in the case of pier heads, or when shear strengthening of elements such as columns and corbels is needed. Fundamental research into these issues would be both feasible and useful to society.

References

AASHTO LFRD (2004). *Bridge design specifications and commentary.* Second edition. American Association of State Highway and Transportation Officials, Washington D.C.

AASHTO LFRD (2008). *Bridge design specifications and commentary.* Fourth edition. American Association of State Highway and Transportation Officials, Washington D.C.

ACI 318-02 (2002). *Building code requirement for structural concrete and commentary*. ACI Committee 318, American Concrete Institute, Farmington Hills, Michigan.

ACI 318-05 (2005). *Building code requirement for structural concrete and commentary*. ACI Committee 318, American Concrete Institute, Farmington Hills, Michigan.

ACI 318-08 (2008). *Building code requirement for structural concrete and commentary*. ACI Committee 318, American Concrete Institute, Farmington Hills, Michigan.

ACI 440R (2007). *Report on fiber-reinforced polymer (FRP) reinforcement for concrete structures*. ACI Committee 440, American Concrete Institute, Farmington Hills, Michigan.

ACI 440.2R (2002). *Guide for the design and construction of externally bonded FRP systems for strengthening concrete structures*. ACI Committee 440, American Concrete Institute, Farmington Hills, Michigan.

ACI 440.2R (2008). *Guide for the design and construction of externally bonded FRP systems for strengthening concrete structures*. ACI Committee 440, American Concrete Institute, Farmington Hills, Michigan.

ALGOR v23 (2008). Algor, Inc., Pittsburgh, PA, USA.

ANDERSON, N. S. and RAMIREZ, J. A. (1989). *Detailing of stirrup reinforcement*. ACI Structural Journal, Vol. 86, No. 5, pp. 507-515.

ASHOUR, A. F. (2000). *Shear capacity of reinforced concrete deep beams*. Journal of Structural Engineering, Vol. 126, No. 9, pp. 1045-1052.

BATCHELOR, B. D. V. and KWUN, M. (1981). *Shear in reinforced concrete beams without web reinforcement.* Proceeding of the ASCE Journal of Structural Division, Vol. 107, No. 5, pp. 907-921.

BAZANT, Z. P., YU, Q., GERSTLE, W., HANSON, J. and JU, J. W. (2007). *Justification of ACI 446 proposal for updating ACI code provisions for shear*

design of reinforced concrete beams. ACI Structural Journal, Vol. 104, No. 5, pp. 601-610.

BD 21/01 (2001). *The assessment of highway bridges and structures (DMRB 3.4.3)*. The Highways Agency, HMSO, London.

BD 44/95 (1995). *The assessment of concrete highway bridges and structures (DMRB 3.4.14)*. The Highways Agency, HMSO, London.

BD 79/06 (2006). *The management of sub-standard highway structures (DMRB 3.4.18)*. The Highways Agency, HMSO, London.

BD 84/02 (2002). *Strengthening of concrete bridge supports using fibre reinforced polymers (DMRB 1.3.16)*. The Highways Agency, HMSO, London.

BD 85/08 (2008). *Strengthening highway structures using externally bonded fibre reinforced polymer (DMRB 1.3.18).* The Highways Agency, HMSO, London.

BENTZ, E. C., VECCHIO, F. J. and COLLINS, M. P. (2006). *Simplified modified compression field theory for calculating shear strength of reinforced concrete elements*. ACI Structural Journal, Vol. 103, No. 4, pp. 614-624.

BIANCO, V., BARROS, J. A. O. and MONTI, G. (2009). *Three dimensional mechanical model for simulating the NSM FRP strips shear strength contribution to RC beams*. Engineering Structures, Vol. 31, No. 4, pp. 815-826.

BLASCHKO, M. (2003). *Bond behaviour of CFRP strips glued into slits*. Proceedings of the sixth international symposium on non-metallic (FRP) reinforcement for concrete structures (FRPRCS-6), July, Vol. 1, pp. 205-214, Singapore.

BOUSSELHAM, A. and CHAALLAL, O. (2008). *Mechanisms of shear resistance of concrete beams strengthened in shear with externally bonded FRP*. Journal of Composites for Construction, Vol. 12, No. 5, pp. 499-512.

BRESTLER, B. and SCORDELIS, A. C. (1963). *Shear strength of reinforced concrete beams*. Proceedings of the ACI Journal, Vol. 60, No. 1, pp. 51-72.

BROWN, M. D., BAYRAK, O. and JIRSA, J. O. (2006). *Design for shear based on loading conditions.* ACI Structural Journal, Vol. 103, No. 4, pp. 541-550.

BS 5400-4 (1990). *Steel, concrete and composite bridges. Part 4: Code of practice for design of concrete bridges*. British Standard Institution, London.

BS 8110-1 (1997). *Structural use of concrete. Part 1: Code of practice for design and construction*. British Standard Institution, London.

CEB-FIP MODEL CODE (1993). *International recommendations for the design and construction of concrete structures*. Comité Euro-International du Béton, Thomas Telford, London.

CHEN, J. F. and TENG, J. G. (2001). *Anchorage strength models for FRP and steel plates bonded to concrete*. Journal of Structural Engineering, Vol. 127, No. 7, pp. 784-791.

CHEN, J. F. and TENG, J. G. (2003a). *Shear capacity of fiber-reinforced polymer-strengthened reinforced concrete beams: fiber reinforced polymer rupture*. Journal of Structural Engineering, Vol. 129, No. 5, pp. 615-625.

CHEN, J. F. and TENG, J. G. (2003b). *Shear capacity of FRP-strengthened RC beams: FRP debonding*. Construction and Building Materials, Vol. 17, No. 1, pp. 27-41.

CHOI, K.-K., PARK, H.-G. and WIGHT, J. K. (2007). *Unified shear strength model for reinforced concrete beams – Part I: Development*. ACI Structural Journal, Vol. 104, No. 2, pp. 142-152.

CHOI, K.-K. and PARK, H.-G. (2007). *Unified shear strength model for reinforced concrete beams – Part II: Verification and simplified method*. ACI Structural Journal, Vol. 104, No. 2, pp. 153-161.

CIDAR (2006). *Design guideline for RC structures retrofitted with FRP and metal plates: beams and slabs*. Draft 3, The University of Adelaide. Cited in *Lima and Barros* (2007).

CIRIA Report C595 (2004). *Strengthening metallic structures using externally-bonded fibre-reinforced polymers*. Construction Industry Research and Information Association, London, pp. 234.

CLADERA BOHIGAS, A. (2002). *Shear design of reinforced high-strength concrete beams*. PhD Thesis, Departament d'Enginyeria de la Construcciò, Universitat Politècnica De Catalunya, Barcelona.

CLADERA, A. and MARI', A. R. (2006). *Shear design of prestressed and reinforced concrete beams*. Magazine of Concrete Research, Vol. 58, No. 10, pp. 713-722.

CLADERA, A. and MARI', A. R. (2007). *Shear strength in the new Eurocode 2. A step forward?*. Structural concrete, Vol. 8, No. 2, pp. 57-66.

CNR DT-200 (2004). *Guide for the design and construction of externally bonded FRP systems for strengthening existing structures – Materials, RC and PC structures, masonry structures*. Advisory Committee on Technical Recommendations for Construction, National Research Council, Rome.

CNR DT-201 (2005). *Guide for the design and construction of externally bonded FRP systems for strengthening existing structures – Timber structures*. Advisory Committee on Technical Recommendations for Construction, National Research Council, Rome.

CNR DT-202 (2005). *Guide for the design and construction of externally bonded FRP systems for strengthening existing structures – Metallic structures*. Advisory Committee on Technical Recommendations for Construction, National Research Council, Rome.

COLLINS, M. P., MITCHELL, D., ADEBAR, P. and VECCHIO, F. J. (1996). *A general shear design method*. ACI Structural Journal, Vol. 93, No. 1, pp. 36-45.

COLLINS, M. P. and KUCHMA, D. (1999). *How safe are our large, lightly reinforced concrete beams, slabs and footings?* ACI Structural Journal, Vol. 96, No. 4, pp. 482-490.

COLOTTI, V., SPADEA, G. and SWAMY, R. N. (2004). *Analytical model to evaluate failure behaviour of plated reinforced concrete beams strengthened for shear*. ACI Structural Journal, Vol. 101, No. 6, pp. 755-764.

CONCRETE SOCIETY TR49 (1998). *Design guidance for high strength concrete*. Technical Report, The Concrete Society, Camberley, UK, pp. 168.

CONCRETE SOCIETY TR55 (2004). *Design guidance for strengthening concrete structures using fibre composite materials.* Second edition. Technical Report, The Concrete Society, Camberley, UK, pp. 102.

CONCRETE SOCIETY TR57 (2003). *Strengthening concrete structures using fibre composite materials: acceptance, inspection and monitoring*. Technical Report, The Concrete Society, Camberley, UK, pp. 48.

CP 110 (1972). *The structural use of concrete. Part 1: Design, materials and workmanship*. The Council for Codes of Practice, British Standards Institution, London.

CSA COMMITTEE A 23.3 (2004). *Design of concrete structures*. Canadian Standards Association, Mississauga, pp. 214.

DE LORENZIS, L. and NANNI, A. (2001). *Shear strengthening of reinforced concrete beams with near-surface mounted fiber-reinforced polymer rods*. ACI Structural Journal, Vol. 98, No. 1, pp. 60-68.

DE LORENZIS, L. and NANNI, A. (2002). *Bond between near-surface mounted fiber-reinforced polymer rods and concrete in structural strengthening*. ACI Structural Journal, Vol. 99, No. 2, pp. 123-132.

DE LORENZIS, L., LUNDGREN, K. AND RIZZO, A. (2004). *Anchorage length of near-surface mounted fiber-reinforced polymer bars for concrete strengthening – experimental investigation and numerical modeling*. ACI Structural Journal, Vol. 101, No. 2, pp. 269-278.

DE LORENZIS, L. and GALATI, D. (2006). *Effect of construction details on the bond performance of NSM FRP bars in concrete.* Proceedings of the second fib Congress, Federation Internationale du Béton, June, Naples, paper ID 10-24 (on CD-ROM), pp. 12.

DE LORENZIS, L. and TENG, J. G. (2007). *Near-surface mounted FRP reinforcement : an emerging technique for strengthening structures*. Composites Part B: Engineering, Vol. 38, No. 2, pp. 119-143.

DIAS, S. J. E. and BARROS, J. A. O. (2005). *Shear strengthening of RC beams with near-surface-mounted CFRP laminates*. Proceedings of the seventh international symposium on non-metallic (FRP) reinforcement for

concrete structures (FRPRCS-7), ACI SP-230, November, Vol. 1, pp. 807-816, Kansas City.

DIAS, S. J. E. and BARROS, J. A. O. (2006). *NSM CFRP laminates for the shear strengthening of T section RC beams.* Proceedings of the second fib Congress, Federation Internationale du Béton, June, Naples, paper ID 10-58 (on CD-ROM), pp. 12.

DIN 1045-1 (2001). *Reinforced and prestressed concrete structures – Part 1: Design.* Deutsches Institut für Normung (DIN), Berlin.

DUTHINH, D. (1999). *Sensitivity of shear strength of reinforced concrete and prestressed concrete beams to shear friction and concrete softening according to modified compression field theory.* ACI Structural Journal, Vol. 96, No. 4, pp. 495-508.

EL-ARISS, B. (2007). *Behavior of beams with dowel action.* Engineering Structures, Vol. 29, No. 6, pp. 899-903.

EL-BADRY, M. M. (1996). *Advanced composite materials in bridges and structures – Second international conference.* The Canadian Society for Civil Engineering.

EUROCODE 2 (2004). *Design of concrete structures. Part 1-1: General rules and rules for buildings.* BS EN 1992-1-1, British Standard Institution, London.

fib BULLETTIN 14 (2001). *Externally bonded FRP reinforcement for RC structures.* Technical Report, Federation International du Béton, July.

fib BULLETTIN 35 (2006). *Retrofitting of concrete structures bonded by FRPs with emphasis on seismic applications.* Technical Report, Federation International du Béton, April.

GASTEBLED, O. J. and MAY, I. M. (2001). *Fracture mechanics model applied to shear failure of reinforced concrete beams without stirrups.* ACI Structural Journal, Vol. 98, No. 2, pp. 184-190.

GE/RT/8006 (2000). *Interface between rail vehicle weights and underline bridges.* Issue 1, Railway Group Standards, Railtrack PLC (now Network Rail), London.

GRANDE, E., IMBIMBO, M. and RASULO, A. (2007). *Experimental behaviour of RC beams strengthened in shear by FRP sheets.* Proceedings of the eight international symposium on non-metallic (FRP) reinforcement for concrete structures (FRPRCS-8), July, Patras, paper ID 5-10 (on CD-ROM), pp. 9.

HARRIS, S. (2004). *Fire resistance of epoxy-grouted steel rod connections in laminated veneer lumber (LVL).* MEng Thesis, Fire Engineering Research report 04/7, June, Department of Civil Engineering, University of Canterbury, Christchurch, New Zealand.

HILLERBORG, A. (1983). *Analysis of one single crack.* Fracture Mechanics of Concrete, Developments in Civil Engineering, Elsevier Science Publishers, Amsterdam, pp. 223-249.

HILTI Inc. (2008a). *HIT-RE 500 Epoxy adhesive anchoring system*. Product Technical Guide 2008. Online at http://www.us.hilti.com, last accessed 15-09-2008.

HILTI Inc. (2008b). *HIT-ICE/HIT-HY 150 Adhesive anchoring system*. Product Technical Guide 2008. Online at http://www.us.hilti.com, last accessed 15-09-2008.

HOANG, L. C. and NIELSEN, M. P. (1998). *Plasticity approach to shear design*. Cement and Concrete Composites, Vol. 20, No. 6, pp. 437-453.

HOULT, N. A. and LEES, J. M. (2009). *Efficient strap configurations for the shear strengthening of reinforced concrete T-beams*. Journal of Composites for Construction, Vol. 13, No. 1, pp. 45-52.

HUGHES BROTHERS Inc. (2008). *Aslan 100 GFRP rebar / Aslan 200 CFRP rebar*. Technical Data Sheet. Online at http://www.hughesbros.com/Aslan_FRP.html, last accessed 15-09-2008.

HUNTSMAN ADVANCED MATERIALS (2007). *Araldite LY 5052 / Aradur 5052*. Technical Data Sheet. Online at http://www.huntsman.com, last accessed 15-09-2008.

IBELL, T. J., MORLEY, C. T. and MIDDLETON, C. R. (1997a). *A plasticity approach to the assessment of shear in concrete beam-and slab bridges.* The Structural Engineer, Vol.75, No. 19, pp. 331-338.

IBELL, T. J., MORLEY, C. T. and MIDDLETON, C. R. (1997b). *Shear assessment of concrete beam-and-slab structures.* Final Highways Agency Contract Report, Cambridge University Engineering Department.

IBELL, T. J., MORLEY, C. T. and MIDDLETON, C. R. (1997c). *A generalised collapse analysis method for concrete bridges.* Technical Report CUED/D – Structural/TR 166, Cambridge University Engineering Department.

IBELL, T. J., MORLEY, C. T. and MIDDLETON, C. R. (1998a). *Shear assessment of concrete beam-and-slab bridges*. Proceedings of the Institution of Structural Engineers, Structures and Buildings, Vol. 128, No. 3, pp. 386-391.

IBELL, T. J., MORLEY, C. T. and MIDDLETON, C. R. (1998b). *An upper-bound plastic analysis for shear.* Magazine of Concrete Research, Vol. 50, No. 1, pp. 67-74.

IBELL, T. J., MORLEY, C. T. and MIDDLETON, C. R. (1999). *Strength and behaviour in shear of concrete beam-and-slab bridges.* ACI Structural Journal, Vol. 96, No. 3, pp. 386-391.

JACKSON, P. and SALIM, S. W. (2006). *Web crushing in EN 1992.* The Structural Engineer, Vol. 84, No. 23-24, pp. 50-57.

JELIC, I., PAVLOVIC, M. N. and KOTSOVOS, M. D. (1999). *A study of dowel action in reinforced concrete beams*. Magazine of Concrete Research, Vol. 51, No. 2, pp. 131-141.

JENSEN, J. F., NIELSEN, M. P., BRÆSTRUP, M. W. and BACH, F. (1978). *Nogle plasticitetsteoretiske bjælkeløsninger (Some plastic solutions concerning the load-carrying capacity of reinforced concrete beams)*. Technical University of Denmark, Structural Research Laboratory, Copenhagen, Report No. R-101, pp. 50.

KANI, G. N. J. (1967). *How safe are our large reinforced concrete beams?* ACI Journal, Vol. 64, No. 3, pp. 128-141.

KELLER, C., TUE, N. V. and ZINK, M. (2002a). *Influence of prestressing forces on the shear capacity - Part 1: Beams without shear reinforcement.* LACER No. 7, pp. 287-296, University of Leipzig.

KELLER, C., TUE, N. V. and ZINK, M. (2002b). *Influence of prestressing forces on the shear capacity - Part 2: Beams with shear reinforcement.* LACER No. 7, pp. 297-306, University of Leipzig.

KELLER, C. (2004). *Shear bearing capacity after inclined cracking.* LACER No. 9, pp. 8, University of Leipzig.

KHALIFA, A., GOLD, W. J., NANNI, A. and AZIZ, A. M. I. (1998). *Contribution of externally bonded FRP to shear capacity of RC flexural members*. Journal of Composites for Construction, Vol. 2, No. 4, pp. 195-202.

KOTSOVOS, M. D. (1988). *Compressive force path concept: basis for reinforced concrete ultimate limit state design*. ACI Structural Journal, Vol. 85, No. 1, pp. 68-75.

KOTSOVOS, M. D. and BOBROWSKI, J. (1993). *Design model for structural concrete based on the concept of the compression force path.* ACI Structural Journal, Vol. 90, No. 1, pp. 12-20.

KOTSOVOS, M. D. (2007). *Concepts underlying reinforced concrete design: time for reappraisal*. ACI Structural Journal, Vol. 104, No. 6, pp. 675-684.

KREFELD, W. J. and THURSTON, C. W. (1966). *Studies of the shear and diagonal tension strength of simply supported reinforced concrete beams.* ACI Journal, Vol. 63, No. 4, pp. 451-477.

KUCHMA, D. A., SUN, S. and HAWKINS, N. M. (2006). *Shear design and behaviour of high-strength concrete bridge girders.* Proceedings of the second fib Congress, Federation Internationale du Béton, June, Naples, paper ID 2-29 (on CD-ROM), pp. 11.

KUCHMA, D. A., HAWKINS, N. M., KIM, S.-H., SUN, S. and KIM, K. S. (2008). *Simplified shear provisions of the AASHTO LFRD bridge design specifications.* PCI Journal, Vol. 53, No. 3, pp. 53-73.

KUPFER, H. (1964). *Erweiterung der Mörsc'schen fachwerkanalogie mit hilfe des prinzips von minimum der formänderungsarbeit.* CEB Bulletin 40, Paris, pp. 44-57. Cited in *Regan* (1993).

LEE, T. K. and AL-MAHAIDI, R. (2008). *An experimental investigation on shear behaviour of RC T-beams strengthened with CFRP using photogrammetry*. Composite Structures, Vol. 82, No. 2, pp. 177-184.

LEONHARDT, F. and WALTHER, R. (1962). *Shubversuche an enfeldrigen Stahlbetonbalken mit und ohne Schubbewehrung*. Deutscher Ausschuß für Stahlbeton (DAfStb), Report No. 151, Ernst and Sohn, Berlin. Cited in *Zink* (2000).

LEUNG, K. Y., CHEN, Z., LEE, S., NG, M., XU, M. and TANG, J. (2007). *Effect of size on the failure of geometrically similar concrete beams strengthened in shear with FRP strips*. Journal of Composites for Construction, Vol. 11, No. 5, pp. 487-496.

LI, B. and NGOC TRAN, C. T. (2008). *Reinforced concrete beam analysis supplementing concrete contribution in truss models*. Engineering Structures, Vol. 30, No. 11, pp. 3285-3294.

LIMA, J. L. T. and BARROS, J. A. O. (2007). *Design models for shear strengthening of reinforced concrete beams with externally bonded FRP composites: a statistical versus reliability approach*. Proceedings of the eight international symposium on non-metallic (FRP) reinforcement for concrete structures (FRPRCS-8), July, Patras, paper ID 5-2 (on CD-ROM), pp. 10.

LU, X. Z, TENG, J. G., YE, L. P. and JIANG, J. J. (2005). *Bond-slip models for FRP sheets/plates externally bonded to concrete*. Engineering Structures, Vol. 27, No. 6, pp. 920-937.

LU, X. Z., CHEN, J. F., YE, L. P., TENG, J. G. and ROTTER, J. M. (2009). *RC beams shear-strengthened with FRP: stress distributions in the FRP reinforcement*. Construction and Building Materials, Vol. 23, No. 4, pp. 1544-1554.

MAEDA, T., ASANO, Y., SATO, Y., UEDA, T. and KAKUTA, Y. (1997). *A study on bond mechanism of carbon fiber sheet*. Proceedings of the third international symposium on non-metallic (FRP) reinforcement for concrete structures (FRPRCS-3), Vol. 1, pp. 279-285, Sapporo.

MARTI, P. (1985). *Basic tools of reinforced concrete beam design.* ACI Journal, Vol. 82, No. 1, pp.46-56.

MATTHYS, S. and TRIANTAFILLOU, T. C. (2001). *Shear and torsion strengthening with externally bonded FRP reinforcement*. Proceedings of the international workshop on composite in construction, pp. 203-210, July, Capri, Italy.

MOHAMED ALI, M. S., OEHLERS, D. J. and SERACINO, R. (2006). *Vertical shear interaction model between external FRP transverse plates and internal steel stirrups*. Engineering Structures, Vol. 28, No. 3, pp. 381-389.

MOHAMED ALI, M. S., OEHLERS, D. J. and GRIFFITH, M. C. (2008). *Shear transfer across cracks in FRP strengthened RC members*. Journal of Composites for Construction, Vol. 12, No. 4, pp. 416-424.

MONTI, G. and LIOTTA, M. (2007). *Tests and design equations for FRP-strengthening in shear*. Construction and Building Materials, Vol. 21, No. 4, pp. 799-809.

MÖRSCH, E. (1909). *Concrete-steel construction* (English translation of *Der eisenbetonbau*). McGraw-Hill, New York.

MOSALLAM, A. S. and BANERJEE, S. (2007). *Shear enhancement of reinforced concrete beams strengthened with FRP composite laminates*. Composites Part B: engineering, Vol. 38, No. 5-6, pp. 781-793.

MOUKWA, M. (1996). *Molecular structure and properties of thermosetting resins used in advanced composite materials. In El-Badry* (1996), pp. 83-90.

MUTTONI, A. and FERNANDEZ RUIZ, M. (2008). *Shear strength of members without transverse reinforcement as function of critical shear crack width.* ACI Structural Journal, Vol. 105, No. 2, pp. 163-172.

NAGLE, T. J. and KUCHMA, D. A. (2007). *Shear transfer resistance in high-strength concrete girders.* Magazine of Concrete Research, Vol. 46, No. 8, pp. 611-620.

NANNI, A., DI LUDOVICO, M. and PARRETTI, R. (2004). *Shear strengthening of a PC bridge girder with NSM CFRP rectangular bars*. Advances in Structural Engineering, Vol. 7, No. 4, pp. 97-109.

NIELSEN, M. P. and BRÆSTRUP, M. W. (1975). *Plastic shear strength of reinforced concrete beams*. Technical Report No. 3, Bygningsstatiske Meddelelser, Vol. 46, pp. 61-99.

NIELSEN, M. P., BRÆSTRUP, M. W., JENSEN, B. C. and BACH, F. (1978). *Concrete plasticity, beam shear - shear in joints - punching shear.* Special Publication of Danish Society for Structural Science and Engineering, Lyngby, pp. 129.

NIELSEN, M. P. and BRÆSTRUP, M. W. (1978). *Shear strength of prestressed concrete beams without web reinforcement.* Magazine of Concrete Research, Vol. 30, No. 104, pp. 119-128.

NIELSEN, M.P. (1999). *Limit analysis and concrete plasticity*. Second edition, CRC Press, London, pp. 936.

NR/CS/CIV/032 (2004). *Managing existing structures*. Issue 1, Network Rail, London.

NR/SP/CIV/035 (2004). *Assessment of structures*. Issue 2, Network Rail, London.

NR/GN/CIV/025 (2006). *The structural assessment of underbridges*. Issue 3, Network Rail, London.

OEHLERS, D. J., RASHID, R. and SERACINO, R. (2008). *IC debonding resistance of groups of FRP NSM strips in reinforced concrete beams*. Construction and Building Materials, Vol. 22, No. 7, pp. 1574-1582.

OH, B. H. and KIM, K. S. (2006). *Experimental investigation on the shear behaviour of full-scale post-tensioned prestressed concrete bridge girders.* Proceedings of the second fib Congress, Federation Internationale du Béton, June, Naples, paper ID 13-18 (on CD-ROM), pp. 11.

PARK, J.-W. and KUCHMA, D. (2007). *Strut-and-tie model analysis for strength prediction of deep beams*. ACI Structural Journal, Vol. 104, No. 6, pp. 657-666.

PAULAY, T., PARK, R. and PHILLIPS, M. H. (1974). *Horizontal constructions joints in cast in place reinforced concrete*. ACI Special Report SP 42, pp. 599-616.

PELLEGRINO, C. and MODENA, C. (2008). *An experimentally based analytical model for the shear capacity of FRP-strengthened reinforced concrete beams*. Mechanics of Composite Materials, Vol. 44, No. 3, pp. 231-244.

PRIESTLEY, M., SEIBLE, F. and CALVI, G. (1996). *Seismic design and retrofit of bridges*. John Wiley and Sons, New York, pp. 704.

REINECK, K.-H. (1991). *Ultimate shear force of structural concrete members without transverse reinforcement derived from a mechanical model.* ACI Structural Journal, Vol. 88, No. 5, pp. 592-602.

REINECK, K.-H. (2001). *Basis for the shear design in DIN 1045-1 for members of structural concrete with web reinforcement.* Bauingenieur No. 76, pp. 168-179, Springer Verlag, Berlin.

RITTER, W. (1899). *Construction techniques of Hennebique.* Schweizerische Bauzeitung, Vol. 33, No. 7, pp. 59-61, Zürich.

RIZZO, A. and DE LORENZIS, L. (2009a). *Modeling of debonding failure for RC beams strengthened in shear with NSM FRP reinforcement*. Construction and Building Materials, Vol. 23, No. 4, pp. 1568-1577.

RIZZO, A. and DE LORENZIS, L. (2009b). *Behavior and capacity of RC beams strengthened in shear with NSM FRP reinforcement*. Construction and Building Materials, Vol. 23, No. 4, pp. 1555-1567.

SCHLAICH, J., SCHAFER, K. AND JENNEWEIN, M. (1987). *Toward a consistent design of structural concrete.* PCI Journal, Vol. 32, No. 3, pp. 74-150.

SENA CRUZ, J. M. and BARROS, J. A. O. (2002). *Bond behaviour of carbon laminate strips into concrete by pull-out bending tests*. Proceedings of the international symposium 'Bond in concrete – from research to standards', Budapest, pp. 614-621.

SERACINO, R., JONES, N. M., ALI, M. S. M., PAGE, M .W. and OEHLERS, D. J. (2007). *Bond strength of near-surface mounted FRP strip-to-concrete joints*. Journal of Composites for Construction, Vol. 11, No. 4, pp. 401-409.

SHIELD, C., FRENCH, C. and MILDE, E. (2005). *The effect of adhesive type on the bond of NSM tape to concrete*. Proceedings of the seventh international symposium on non-metallic (FRP) reinforcement for concrete structures (FRPRCS-7), ACI SP-230, November, Vol. 1, pp. 355-372, Kansas City.

SIA CODE 262 (2003). *Concrete structures*. Swiss Society of Engineers and Architects, Zürich.

SIREG S.p.A. (2008). *Arapree Rod / Carbopree Rod*. Technical Data Sheet. Online at http://www.sireg.net/rods.html, last accessed 15-09-2008.

SONNENBERG, A. M. C. and AL-MAHIDI, R. (2007). *Investigation of dowel shear in RC beams using photogrammetry.* Magazine of Concrete Research, Vol. 59, No. 9, pp. 621-626.

SWAMY, R. N. and QURESHI, S. A. (1974). *Shear behaviour of reinforced concrete T beams with web reinforcement.* Proceeding of the Institution of Civil Engineers, Part 1 – Design and construction, Vol. 57, No. 2, pp. 35-49.

SWAMY, R. N. and ANDRIOPOULAS, A. D. (1974). *Contributions of aggregate interlock and dowel forces to the shear resistance of reinforced beams with web reinforcement.* ACI Special Report SP-42, American Concrete Institute, Detroit, Michigan, pp.129-166.

TÄLJSTEN, B. and CAROLIN, A. (2007). *Beams strengthened in shear by EBR – design model*. Proceedings of the eight international symposium on non-metallic (FRP) reinforcement for concrete structures (FRPRCS-8), July, Patras, paper ID 5-11 (on CD-ROM), pp. 10.

TAYLOR, H. P. J. (1974). *The fundamental behaviour of reinforced concrete beams in bending and shear.* ACI Special Report SP 42, pp. 43-77.

TENG, J. G., CHEN, J. F., SMITH, S. T. and LAM, L. (2003). *Behaviour and strength of FRP-strengthened RC structures: a state-of-the-art review*. Proceedings of the Institution of Civil Engineers, Structures and Buildings, Vol. 156, No. 1, pp. 51-62.

TIMOSHENKO, S. P. (1983). *History of strength of materials: with a brief account of the history of theory of elasticity and theory of structures*. Courier Dover Publications, New York, 452 pp.

TRIANTAFILLOU, T. C. (1998). *Shear strengthening of reinforced concrete beams using epoxy-bonded FRP composites*. ACI Structural Journal, Vol. 95, No. 2, pp. 107-115.

TRIANTAFILLOU, T. C. and ANTONOPOULOS, C. P. (2000). *Design of concrete flexural members strengthened in shear with FRP*. Journal of Composites for Construction, Vol. 4, No. 4, pp. 198-205.

TUREYEN, A. K. and FROSCH, R. J. (2003). *Concrete shear strength: another perspective*. ACI Structural Journal, Vol. 100, No. 5, pp. 609-615.

TUREYEN, A. K., WOLF, T. S. and FROSCH, R. J. (2006). *Shear strength of reinforced concrete T-beams without transverse reinforcement.* ACI Structural Journal, Vol. 103, No. 5, pp. 656-663.

VALERIO, P. and IBELL, T. J. (2003). *Shear strengthening of existing concrete bridges*. Proceedings of the Institution of Civil Engineers, Structures and Buildings, Vol. 156, No. 1, pp. 75-84.

VECCHIO, F. J. and COLLINS, M. P. (1986). *The modified compression field theory for reinforced concrete elements subjected to shear.* ACI Structural Journal, Vol. 83, No. 2, pp. 219-231.

VECCHIO, F. J. (2000). *Analysis of shear-critical reinforced concrete beams.* ACI Structural Journal, Vol. 97, No. 1, pp. 102-110.

von RAMIN, M. and MATAMOROS, A. B. (2006). *Shear strength of reinforced concrete members subjected to monotonic loads.* ACI Structural Journal, Vol. 103, No. 1, pp. 83-92.

WALRAVEN, J. C. (1981). *Fundamental analysis of aggregate interlock.* ASCE Journal of the Structural Division, Vol. 107, No. 11, pp. 2245-2270.

WATANABE, F. and KABEYASAWA, T. (1998). *Shear strength of RC members with high-strength concrete.* High strength concrete in seismic regions, ACI Special Report SP-176, American Concrete Institute, Farmington Mills, Michigan, pp.379-396. Cited in *von Ramin and Matamoros* (2006).

WHITEHEAD, P. A. (2002). *Shear strength of concrete containing fibre-reinforced-plastic reinforcement.* PhD Thesis, Department of Architecture and Civil Engineering, University of Bath, Bath, UK.

WOLF, T. S. and FROSCH, R. J. (2007). *Shear design of prestressed concrete: a unified approach.* Journal of Structural Engineering, Vol. 133, No. 11, pp. 1512-1518.

ZARARIS, P. D. and PAPADAKIS, G. C. (2001). *Diagonal shear failure and size effect in RC beams without web reinforcement.* Journal of Structural Engineering, Vol. 127, No. 7, pp. 733-742.

ZARARIS, P. D. (2003). *Shear strength and minimum shear reinforcement of reinforced concrete slender beams.* ACI Structural Journal, Vol. 100, No. 2, pp. 203-214.

ZARARIS, I. P., KARAVEZIROGLOU, M. K. and ZARARIS, P. D. (2006). *Shear strength of reinforced concrete T-beams.* ACI Structural Journal, Vol. 103, No. 5, pp. 693-700.

ZHANG, J.-P. (1997). *Diagonal cracking and shear strength of reinforced concrete beams.* Magazine of Concrete Research, Vol. 49, No. 178, pp. 55-65.

ZINK, M. (2000). *Diagonal shear cracking in slender concrete beams.* LACER No. 5, pp. 305-332, University of Leipzig.

ZSUTTY, T. C. (1971). *Shear strength prediction for separate categories of simple beam test.* Proceeding of the ACI Journal, Vol. 68, No. 2, pp. 138-143.